THE SUBSURFACE NATURE OF MERCURY AND MARS FROM THERMAL MICROWAVE EMISSION

Thesis by
Jeffrey Nicholas Cuzzi

In Partial Fulfillment of the Requirements
for the Degree of
Doctor of Philosophy

California Institute of Technology
Pasadena, California

1973

(Submitted November 29, 1972)

> "Perhaps we are never
> by mountain, wood, or common stream
> far from the dust of one who laughed
> with nothing left to lose."
>
> Canyon 68–69

ACKNOWLEDGEMENTS

Dr. Duane Muhleman has consistently provided fruitful scientific direction and moral support in great abundance, and much of this work, including the Mars spectrum paper, originated with his suggestions.

Dr. Glenn Berge has always been generous with his considerable grasp of all phases of the experimental work. His aid has been essential in overcoming many obstacles, and his continued interest in this work has been greatly appreciated.

Dr. Bruce Murray and Dr. Laurence Soderblom have been sources of continuing motivation and enthusiasm, and the completion of this project owes much to their encouragement. I am also indebted to Solomon Giles for his perspective and timely wisdom.

My wife Eileen has weathered the hardest times with a patience and balance she would never admit to, and significantly aided my progress by typing the original manuscript.

The author was supported by a National Aeronautics and Space Administration Traineeship from 1967-1970, and thereafter support for this work was under NASA grants NGL-05-002-003 and NGR-005-002-114. Work done at the Owens Valley Radio Observatory was supported under NSF grant 30400X1 and ONR contract N00014-67-A-0094-0019.

ABSTRACT

Detailed numerical modeling techniques are applied to the analysis of microwave observations of Mercury and Mars. The model calculations include the effects of orbital-axial resonance and dependence of regolith properties (e.g. specific heat and thermal conductivity) on temperature in the case of Mercury, and for the effects of seasonally varying CO_2 frost caps in the case of Mars. Variations of geocentric aspect from one observation period to the next are treated for both planets. The dielectric properties of the subsurfaces of these planets are treated as independent of temperature and homogeneous with depth and location on the planet.

Observations of Mercury were made at 3.71, 6, and 18 cm, and previously published observations at .31, .33, and 3.75 cm are also employed in the analysis. The Mercury data appear to be consistent with the presence of a dry, porous regolith in which the radiative transport of heat is important in the total thermal conductivity. The ratio of radiative to contact thermal conductivity, χ, is normally evaluated at $T = 350^\circ$ K, and it is found that these data limit χ thus defined to the range $0.4 < \chi < 1.0$. A value for the effective subsurface dielectric constant is determined from interferometric measurements at 3.71 cm presented here. This value ($\epsilon = 2.0 \pm .16$) is then corrected for the effects of surface roughness to yield a value for the dielectric constant of the regolith of $\epsilon = 2.4 \pm .3$. Final values of other parameters are:

$$\tan\Delta = \text{regolith loss tangent} = .0075 \pm .002$$

$$\gamma = \text{thermal inertia} = .0014 {}^{+.0021}_{-.0008} \text{ cal cm}^{-2}\text{deg}^{-1}\text{sec}^{-\frac{1}{2}}.$$

In a similar way, expected microwave spectra of Mars are computed using accurate aspect geometry and a thermal model that includes seasonal polar cap effects. It is found that for a range of loss tangents characteristic of dry particulate geological materials ($.003 < \tan\Delta < .015$), and for values of other surface parameters determined independently, the observable spectrum of Mars in the microwave region is "flat" from 0.1 to 21 cm to within the accuracy of the present data, and that a regolith of homogeneous, lunar-like properties is completely consistent with the existing data set when polar cap effects are considered. This result differs from that predicted by the analytical theory in common use which is in apparent conflict with the observed spectra for values of the surface parameters similar to those found for the Moon or Mercury.

Final values of other relevant parameters are:

γ = thermal inertia = $.006$ cal $\mathrm{cm}^{-2}\mathrm{deg}^{-1}\mathrm{sec}^{-\frac{1}{2}}$

ϵ = regolith dielectric constant = $2.5 \pm .3$

A = bolometric Bond albedo = .25

E = infrared emissivity = .90 .

TABLE OF CONTENTS

Appendices:

List of illustrations:

List of Tables

I. INTRODUCTION

The determination of the characteristics of planetary surfaces by remote sensing techniques is an important first step in understanding the nature and history of our planetary system. In order to begin to choose between theories of planetary evolution, it is necessary first to know the similarities and differences between the different planets in chemical composition, as evidenced in the material makeup of their surfaces; and in physical state, as evidenced by the density and inhomogeneity of their regoliths. In order to understand better the processes which acted on a planet in its geological past, and in order to intelligently design equipment for direct surface exploration, it is helpful to have some knowledge of the typical mechanical nature, or roughness, of its surface terrain. A good deal of this information is contained in the thermal emission from the planetary surface at radio wavelengths. Although the thermometric temperature prevailing on a planet's very surface is best investigated at infrared wavelengths, the lower opacity of geological materials at radio wavelengths allows radio astronomers to more readily probe beneath the surface to greater depths and investigate the regolith on a scale of centimeters to meters, encompassing phenomena of wider physical and chemical interest.

The first efforts along these lines utilized the variation of disk temperature (radio brightness integrated over the disk) with planetary phase angle (Piddington and Minnett, 1949). These workers developed a simple analytical theory which allowed the determination of the electrical characteristics of the regolith given the thermal behavior of the surface material as determined from infrared measurements. This method presupposes several simplifying conditions. These conditions include dependence of regolith temperatures only on insolation, dependence of insolation only on singly periodic diurnal rotation of the planet, and independence of the properties of the regolith on depth and temperature. The effective prevalence of these conditions in the lunar regolith has made this technique an effective tool in lunar investigations. Unfortunately, this theory has met with only limited success in attempting to explain radio observations of Mercury and Mars. In the case of Mercury, solar insolation varies in a way that is not singly periodic due to the peculiar coupling between Mercury's orbital and axial rotation rates. This requires that several harmonics be used to adequately describe the insolation and invalidates the conditions under which the simple theory is valid. In addition, the thermal parameters vary significantly with temperature at ambient Mercurian temperatures, rendering the heat equation unsuitable for analytical treatment. In the case of Mars, the existence of a tenuous carbon dioxide atmosphere buffered by seasonally varying polar caps (Leighton and Murray, 1966) causes regolith temperatures to vary in quite a different manner than would be the result of insolation variations alone. In the case of both planets, substantial changes in geocentric aspect from one observation to the next, coupled with the above considerations, will cause discrepancies between experimental data and results predicted by any theory which fails to account for these complications. Discrepancies of this sort have been pointed out by Epstein (1970,1971)and Ulich et al. (1972).

Several advantages are obtained in the use of interferometry to study the planets. In addition to yielding quantities analogous to single antenna (disk-average) measurements, and allowing one to minimize solar interference effects (particularly important in the case of Mercury), interferometric data allows a nearly unique determination of the surface dielectric constant and, in general, contains important information on the brightness distribution across the visible disk. This is discussed in detail in Appendix V. The added resolution obtainable from interferometry, when coupled with the previously mentioned inadequacies of the simple theory, requires the use of modeling methods to fully understand the available information about these planetary surfaces. It is the aim of this work to apply realistic numerical models of subsurface thermophysics to gain a reasonable understanding of the conditions prevailing in the top few meters of the surfaces of Mercury and Mars. The great usefulness of relatively sophisticated modeling techniques has been demonstrated by the planetary models of Leighton and Murray (1966), Gierasch and Goody (1968), Leovy and Mintz (1966), and Morrison (1969). The danger one must be aware of in employing modeling techniques is that of ambiguity. One constructs the most general and complete model possible and investigates how it agrees with observations of the real object under study. If a satisfactory fit is obtained one feels justified in claiming validity for the model, assuming that it includes all important physical processes that are relevant to the observations, and in using the model with caution to determine the physical parameters that best match the observations. As it is possible to draw erroneous conclusions from incomplete or overextended models it is important both to note if, how, and where the many simplifications and assumptions incorporated in any model may be expected to lead to misleading, if apparently valid, results, and also to understand the limitations of the data. Where discrepancies arise between model predictions and observed data, we are left only with speculation and must attempt to state what is the likelihood of bias, insufficiency, or inaccuracy in either model or data as opposed to the likelihood of neglect of an important physical process. Model results, in the opinion of this author, should be treated with respect and great caution due to the uniqueness difficulty.

The use of a model in analysis of the Martian subsurface is treated in Part III, and the following discussion of the model analysis of the nature of the subsurface of Mercury comprises Part II of this work.

Part II: Mercury

2.1: Mercury has been one of the more difficult planets to understand for several reasons.

(1) The peculiar 3/2 resonance of its axial to orbital rotation rates produces a heating asymmetry locked to the planet's surface. This was discussed by Soter and Ulrichs (1967) and by Morrison and Sagan (1968). The magnitude of this effect is enhanced by the extremely high eccentricity of Mercury's orbit and the net effect is of some regions receiving more than twice the total insolation as others at the same latitude. This dependence of apparent temperature on planetary longitude has rendered conventional "phase effect" analyses, which assume longitudinal independence of average temperature, inaccurate. In addition, classical thermal models such as have been successful in interpreting lunar radio data (Wesselink, 1948; Jaeger and Harper, 1950) fail to account for temperature dependence of the thermal parameters; the thermal conductivity (K_T) and specific heat (C). The variations in thermal conductivity were recently experimentally investigated for particulate materials in a vacuum by Watson (1964) and by Wechsler and Glaser (1965). It was found that under these conditions the effective thermal conductivity takes the form

$$\begin{aligned} K_T &= K_c + BT^3 \\ &= K_c + K_r \end{aligned}$$

where K_c is the contact, or phonon, thermal conductivity and is independent of temperature in the case where it is limited by conduction across grain boundaries (Watson, 1964; Wechsler, Glaser, and Fountain, 1972). The results of Watson (1964) showed that over a range of chemical compositions and grain sizes no higher value of contact conductivity than $\sim 10^{-5}$ to 10^{-6} cal cm^{-1} sec^{-1} deg^{-1} is observed for particulate materials in a vacuum ($\sim 10^{-5}$ - 10^{-6} mm Hg). Wechsler and Glaser (1965) have shown that the effective thermal conductivity of particulate material is independent of gas pressure for pressures less than $\sim 10^{-1}$ mm Hg ($\sim 10^{-1}$ mbar). Presence of a gas in the pores of a sample will increase the thermal conductivity by a factor of about 2 at 1 mbar (Wechsler and Glaser, 1965) and by a factor of about 10 at 6 mbar (Fountain and West, 1970). The relative contribution of the radiative conductivity will thus be small for ambient gas pressures greater than about 10^{-1} mbar (for a temperature range of 100-700°K and particle sizes in the range 10-100μ). Thus determination of the relative importance of the contact and radiative thermal conductivities is a sensitive test for the presence of a non-zero ambient gas pressure.

The radiative effect is discussed theoretically by Winter (1972) and by Clegg, Bastin, and Gear (1966) and is due to radiative transport of thermal energy between and through individual grains. Linsky (1966) and Troitskii (1967) demonstrated that a marginally observable effect at microwave frequencies was produced under lunar conditions when radiative heat transfer was considered, and it was early recognized that if Mercury's subsurface were at all similar to that of the Moon the much higher ambient temperatures prevailing in the Mercurian subsurface would produce a much larger and possibly observable "heating hysteresis" effect (Morrison and Sagan, 1968). Linsky (1966) gives a good discussion of the most readily observable result of this which is an increase with depth of the mean temperature. The argument goes qualitatively as follows: At each depth, the mean diurnal heat flux in or out must be equal to zero in the steady state.

$$\langle F(z) \rangle = \langle K_T \frac{\partial T}{\partial z} \rangle = 0 \quad .$$

If $K_T = K_c + BT^3$, and $B > 0$, K_T during the day is much larger than at night. Consequently for $\left\langle K_T \frac{\partial T}{\partial z} \right\rangle = 0$ to hold, $\frac{\partial T}{\partial z}$, or the thermal gradient, during the day is small and negative, and during the night is large and positive. Consequently the mean thermal gradient is positive and the mean temperature increases with depth. The situation may also be regarded as a greenhouse effect (Morrison and Klein, 1970) in which heat flows downward more readily during the day under conditions of high thermal conductivity than it flows upward at night under conditions of low conductivity.

The problem of modelling the behavior of the Mercurian subsurface including the effects of temperature-dependent thermal conductivity was first treated by Morrison (Morrison and Sagan, 1968). Although this treatment was an important step and was the first to determine the observable effects of variable parameters, it has led to inconsistent results with different sets of data. Morrison and Klein (1970), and Morrison (1970), demonstrate that the apparent increase in mean microwave brightness temperature with wavelength from .3 to 6.0 cm is consistent with a particulate subsurface in which the radiative contribution is of equal importance to the contact contribution to K_T. Denoting

$$\chi = \frac{BT^3}{K_c} \text{ at } T = 350^\circ K \quad ,$$

their conclusions indicate a value of $\chi \cong 1.0$. Epstein et al. (1970), however, whose .3 cm mean temperature is critical to the conclusions of Morrison and Klein, believe that their observations of Mercury over several years and many phase angles provide a somewhat better fit to Morrison's $\chi = 0$ models (no radiative conductivity). In addition, the .3 cm mean temperature of Epstein et al. has been questioned by Ulich et al. (1972) whose recent measurements at .3 cm with a new absolute calibration scheme indicate no decrease of mean temperature from values determined at 3-6 cm; a result consistent again with $\chi = 0$ or no radiative term. If interpreted as a true mean temperature of 373°K, the result of Ulich et al. is inconsistent both with the upper limit on thermal inertia determined from the infrared observations of Murray (1967) and with lunar analogy. In an attempt to resolve some of these inconsistent results, a new model has been devised similar in many ways to that of Morrison, but less simplified and designed for different usage.

The need for a new model arises from the finer spatial resolution needed for use in forward calculation of interferometric data. A full and preferably fine-scale brightness map composed of many grid points over the disk is needed to compute a Fourier Transform, and the method of Morrison of choosing a representative mid-latitude at which the temperature is nearly equal to the disk-average to compute effective disk temperature is insufficient. Another factor is the geocentric aspect of the planet. Mercury's high orbital inclination ($\sim 7^\circ$) causes the subearth point to vary over a latitude range of $\sim\pm 15^\circ$ on the surface of the planet, and the consequent variation of the apparent temperature distribution was felt to be a potentially important effect. This situation will also affect disk-average predictions, although to a lesser extent. The problem of the true orientation of the disk to the projected interferometer baseline has also to be considered. This was dealt with in two parts; finding the true orientation of the planet with respect to celestial north and determining the variations due to baseline rotation across the planet with changing hour angle.

2.2: Summary of Results on the Study of Mercury

The detailed numerical analysis undertaken here enables us to understand the available data, both previously published and taken as part of this study, quite satisfactorily in the light of a lunar-like subsurface. Interferometric data at high resolution were used to obtain a rather well-determined value for the subsurface dielectric constant ($\epsilon = 2.4 \pm .3$), from which the effects of surface roughness have been removed using the established similarity in surface roughness of Mercury to the Moon as determined from radar observations. Disk-average observations over a large range of wavelengths are consistent with a particulate subsurface in which the ratio of radiative to contact conductivity is in the range $0.4 < \chi < 1.0$. A rather significant biasing in the interferometric data was discovered which prevented the accuracy in determination of these values from being improved greatly, but this discrepancy is not believed to be due to anomalous surface processes. It is shown that the apparent discrepancies previously mentioned were due mainly to inadequate techniques of analysis or to uncertainty in flux calibration. It is believed that none of the presently existing data are indicative of a subsurface nature or thermal behavior significantly different from that which would be expected of the Moon, were it placed in the orbit of Mercury with the resonant rotation rate of Mercury.

3.1: Thermal Model

The surface of the planet is assumed to be represented by a grid of surface elements having centers at the intersections of meridians and latitude circles. Meridians spaced every 15° of longitude or one hour of time were used, and latitude circles used were taken every 10° from the pole to the equator. The pole of rotation was taken co-incident with the pole of the orbit (Peale, 1969) and use was made of the ensuing symmetry between north and south latitudes. The longitude co-ordinate system increases to the west (left-handed) with zero chosen to be the sub-solar longitude at perihelion, or the "hot pole" of Soter and Ulrichs (1967). At each grid point, the subsurface was divided into 20 plane-parallel slabs of constant temperature, the top 10 being of 7.5 cm thickness and the lower 10 being of 30.0 cm. The heat equation

$$\rho\, C[T(z)]\, \frac{\partial T(z,t)}{\partial t} = \frac{\partial}{\partial z}\left[K_T\, [T(z)]\, \frac{\partial T}{\partial z}\right]$$

was expanded assuming K_T of the form

$$K_T = K_c + K_r(T) = K_c + BT^3$$

and $C(T) = -.034T^{\frac{1}{2}} + .008T - .0002T^{3/2}$ (Winter and Saari, 1969). The equation then becomes non-linear:

$$\rho C(T)\, \frac{\partial T(z,t)}{\partial t} = \frac{\partial}{\partial z}\left[(K_c + BT^3)\, \frac{\partial T(z,t)}{\partial z}\right]$$

or

$$\rho C(T)\, \frac{\partial T(z,t)}{\partial t} = \frac{\partial}{\partial z}\left[K_c \frac{\partial T}{\partial z} + BT^3\, \frac{\partial T}{\partial z}\right]$$

$$\rho C(T)\,\frac{\partial T(z,t)}{\partial t} = K_c\,\frac{\partial^2 T(z,t)}{\partial z^2} + \frac{\partial^2}{\partial z^2}\left[\frac{BT^4(z,t)}{4}\right] \qquad (3.1.1)$$

Using the implicit algorithm of Crank and Nicholson (1947) this non-linear equation was put into incremental form in the following way:

$$\rho C(T)\;\frac{T_j^{n+1} - T_j^n}{\Delta t} = \frac{K_c}{2\Delta z^2}\left[\delta^2 T_j^{n+1} + \delta^2 T_j^n\right] + \frac{B}{8\Delta z^2}\left[\delta^2 (T^4)_j^{n+1} + \delta^2 (T^4)_j^n\right]$$

where

$$\delta^2 f_j^n = f_{j-1}^n - 2f_j^n + f_{j+1}^n \qquad (3.1.2)$$

and the indices j and n refer respectively to the j^th depth layer and the n^th time step. Linearizing by the following approximations

$$(T^4)_j^{n+1} \approx (T^4)_j^n + 4(T^3)_j^n\left[T_j^{n+1} - T_j^n\right]$$

and substituting

$$w_j = T_j^{n+1} - T_j^n$$

the equation reduces to

$$\frac{\rho C(T) w_j}{\Delta t} = \frac{K_c}{2\Delta z^2}\left[\delta^2 T_j^{n+1} + \delta^2 T_j^n\right] + \frac{B}{8\Delta z^2}\left\{\delta^2\left[(T^4)_j^n + 4(T^3)_j^n\, w_j\right] + \right.$$

$$\left. + \,\delta^2 (T^4)_j^n\right\}$$

rearranging terms

$$\frac{\rho C(T) w_j}{\Delta t} - \delta^2\left\{\left[\frac{K_c}{2\Delta z^2} + \frac{B}{2\Delta z^2}\,(T^3)_j^n\right] w_j\right\} = \frac{K_c}{\Delta z^2}\,\delta^2\;T_j^n + \frac{B}{4\Delta z^2}\,\delta^2 (T^4)_j^n$$

using (3.1.2), we then get a set of equations of the form

$$A_n\, w_{j-1} + B_n\, w_j + C_n\, w_{j+1} = D_n$$

where the quantities A_n, B_n, C_n, D_n are known at time step n + 1 and T_i^{n+1} is to be determined using $T_i^{n+1} = T_i + w_i$. The entire set of J equations (j = 1,J) must be solved simultaneously to yield all w_i. This slight computing inconvenience is offset by the greater stability of this method and the higher accuracy obtained. Where normal "explicit" algorithms yield error terms of $0(\Delta z^2 + \Delta t)$ this method yields an error term of $0(\Delta z^2 + \Delta t^2)$. The set of coefficients A_n, B_n, and C_n forms a tri-diagonal matrix and the vector $\bar{w}$ may easily be obtained by matrix inversion methods. The algorithm used time steps on the order of one to several days without producing destructive oscillations in the solution, which was helpful in minimizing computing expenses. The boundary condition at the surface was solved independently. The equation of conservation of flux in the top layer

$$-E\sigma\ T_1^4 + H_0(\theta,\varphi,t)(1-A) + \frac{K_T(T_2 - T_1)}{\Delta z} = 0$$

where σ is the Stephan-Bolzmann constant, H_0 is the insolation function, and A is the bolometric Bond Albedo,* was iterated many times per day over the longer orbit step relevant to all layers, and mean top layer temperature and energy flux per unit time were obtained. This mean temperature was then used as a boundary condition in solving for all T_i^{n+1}. It was found that this method of treating the surface was quite adequate, in that the final determination of T_1 (along with all T_i) never changed the initial guess by more than a few degrees. Below the J^{th} layer the temperature was assumed constant at T_J^n. The net "diurnal" heat flux into each layer was computed and the solution was considered to have converged when this value at all layers was less than the value thought to be typical for heat flux

---

* E is the radiometric emissivity

from the interior of the Earth or Moon. This was found to require between five to eight diurnal periods of iteration. An ad hoc extrapolation method was used to speed convergence. It is difficult to estimate uncertainties on model temperatures, particularly in the case of Mercury where the analytical theory in common use for computing temperature structure is totally inadequate, but by analogy to the Mars model which uses the same algorithm and is more readily checked, an accuracy of better than 2% on all temperatures is estimated. A more complete discussion of the analytical theory and its use is given in Part III (Sec. 9.1).

Accurate treatment of the insolation function $H_0(\theta,\varphi,t)$ is as important as satisfactory treatment of temperature dependent parameters. There is no clear distinction between Mercury's "day" and its "year" due to the 3/2 resonance effect, and the diurnal period is actually two "years" (176 days) long. This day was divided into 40 steps chosen at equal intervals in true anomaly. This choice produces a favorable distribution of total time spent in each step, which is small when temperatures are relatively high and changing rapidly (near perihelion) and large at aphelion when temperatures are lower and change more slowly. The insolation scheme used may be written

$$H_0(\theta,\varphi,t)\,\Delta t_i = \frac{S_0}{R_i^2}\,\Delta t_i\,\cos\theta\,\cos(\varphi-\lambda_{ss}^i)\,F(\theta,\varphi,\lambda_{ss}^i)$$

where
S_0 = Solar constant at 1 A.U.
R_i = heliocentric distance for i^{th} step
Δt_i = time spent in i^{th} step
θ = latitude

φ = planetocentric longitude measured west from sub-solar longitude at perihelion

λ^i_{ss} = sub-solar longitude for i^{th} step

and $F\left(\vartheta, \varphi, \lambda^i_{ss}\right)$ = a function designed to account for the finite size of the Sun.

Δt_i and λ^i_{ss} are computed analytically for the nominal true anomaly of each step using relations due to Liu (1970 * , 1972) :

$$t(f) = \frac{P_o}{2\pi}\left[\frac{\pi}{2} - \sin^{-1}\left[\frac{e + \cos f}{1 + e\cos f}\right] - \frac{e(1 - e^2)^{\frac{1}{2}}\sin f}{1 + e\cos f}\right]$$

$$\varphi(f) = \lambda_{ss}(f) = \frac{P_o}{P_r}\left[\frac{\pi}{2} - \sin^{-1}\left[\frac{e + \cos f}{1 + e\cos f}\right] - \frac{e(1 - e^2)^{\frac{1}{2}}\sin f}{1 + e\cos f}\right] - f$$

where f is the true anomaly (orbital angle measured from perihelion). P_o is the orbital period, P_r is the rotational period, e is the orbit eccentricity, t is the time at which such positioning occurs, and λ_{ss} is the sub-solar longitude at such time and orbit position using the previously mentioned zero definition. The pole of rotation was assumed to be coincident with the pole of the orbit. There are good theoretical (Peale, 1966; Ward, 1972) and empirical (Smith, 1972) grounds for this assumption.

As the angular diameter of the Sun as seen from Mercury at perihelion is nearly 2° some care was taken to accurately treat the effective area

---

* There is a sign error in Liu's published equations which is removed by a change of variable. The above equations require no such change.

visible and effective zenith angle when the Sun was partly covered by the horizon. The situation is described in Fig. 1.

If $dA = 2y dx = 2\sqrt{R^2 - x^2}\, dx$

letting $R = 1$,

$$dA = 2\sqrt{1 - x^2}\, dx$$

$$A(x^*) = \int_{-1}^{x^*} dA$$

where $A(x^*)$ is the total area covered by the horizon when its edge is at an angular separation of x^* from the center of the Sun. The effective solar intensity is then

$$I(x^*) = I_o \left[1 - \int_{-1}^{x^*} 2\sqrt{1 - x^2}\, dx \right]$$

$$= I_o \left[1 - A(x^*) \right]$$

where $$A(x^*) = N\left[x^*\sqrt{1 - x^{*2}} + \sin^{-1} x^* + \pi/2 \right]$$

(N is a normalization constant)

Letting $\xi = R + x = 1 + x$ be the angular extent of coverage by the horizon, $x^* = \xi^* - 1$ and

$$I(\xi^*) = I_o\left[1 - N\left[(\xi^* - 1)\sqrt{2\xi^* - \xi^{*2}} + \sin^{-1}(\xi^* - 1) + \frac{\pi}{2}\right]\right]$$

or

$$I(\xi^*) = I_o\left[1 + N\left[(1 - \xi^*)\sqrt{2\xi^* - \xi^{*2}} + \sin^{-1}(1 - \xi^*) - \pi/2\right]\right]$$

using the criterion that

$$A(\xi^*) = 1 \text{ at } \xi^* = 2 \text{ (whole disk covered)}$$

we determine

$$N = 1/\pi \quad .$$

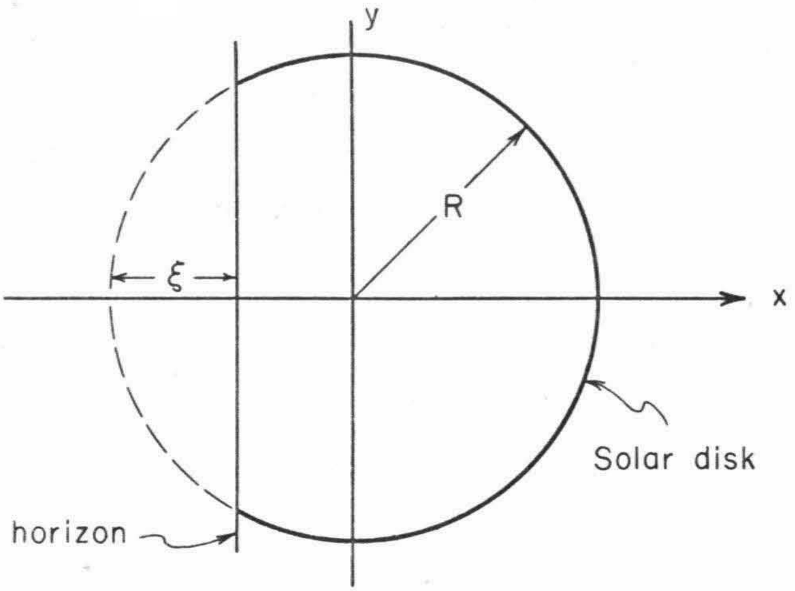

Fig. 1: The solar disk partially obscured by the horizon. $x = \xi - R$.

The parameter ξ is readily determined to be

$$\xi = 2\left[\frac{ZA(\theta,\varphi,t) - 89^\circ 09'}{1^\circ 42'}\right]$$

where $ZA(\theta,\varphi,t)$ is the local zenith angle of the center of the solar disk and 1° 42' is the solar diameter seen from Mercury at perihelion. The "effective" zenith angle of the visible portion was then redefined to be

$$ZA' = 90^\circ - \frac{51'}{2}(x+1)$$

causing the effective centroid of the Sun to set half as fast as the Sun itself and to be at zenith angle 90° when the Sun had completely set. This elaborate technique was felt to be necessary for satisfactory treatment of the situation at the poles, where one-half of the Sun is always visible, and also of the curious double sunrise/double sunset phenomena at the warm poles noted by Soter and Ulrichs (1967) when the Sun spends quite a lot of time near the horizon. The function previously denoted $F(\theta,\varphi,t)$ is simply the function

$$\frac{I(\xi^*(\theta,\varphi,t))}{I_o} .$$

The result of these computations is a four-dimensional map of temperature along and in the subsurface as a function of latitude, planetocentric longitude, depth and time or orbital position. In order to compute observable quantities of relevance, it is necessary to compute them over the temperature distribution in evidence as seen from the Earth at the time of observation. Previous efforts have not taken this problem under consideration fully. The first attempt(Morrison, 1969) took the important step of defining apparent temperature as a function both of phase and sub-earth longitude.

Unfortunately this work did not treat the large orbital inclination of the planet which can cause displacement of the subearth point from the equator by as much as $\pm 15^\circ$ of latitude as may be seen in Fig. 2. Obviously this effect is of great importance where accurate brightness distributions are needed and may even affect disk-average predictions in extreme cases. A series of co-ordinate transformations (derived in Appendix II and somewhat different than those used to do the same job for Mars) is used to relate the coordinates in which the observables are calculated to those in which the subsurface physical temperatures are determined. In order to utilize this useful technique, it is necessary to know the celestial co-ordinates of the rotation axis of the planet as accurately as possible. Small errors in the assumed right ascension of the pole (which is not as well defined as its declination) will produce large errors in the transformed co-ordinates. Use was made of the claim by Peale (1966) that the spin axis must be in the plane defined by the pole of Mercury's orbit and the pole of the invariable plane (closely approximated by Jupiter's orbit) and must be separated by less than a degree from one or the other of those two pole positions. Peale indicates that proximity to the orbit pole is the more likely state, but as the two possible positions are separated by $\sim 7^\circ$, the geometry was worked out for both possibilities in the hope of being able to distinguish between them from the data. The derivation of Mercury's probable alternative pole positions is shown in Appendix III. The geocentric aspect results were checked against ephemeris tabulation of position angle of the lighted crescent midpoint and phase angle. The method described for reproducing the geocentric aspect of the planet is valid for any date for which ephemerides exist and was used in forward

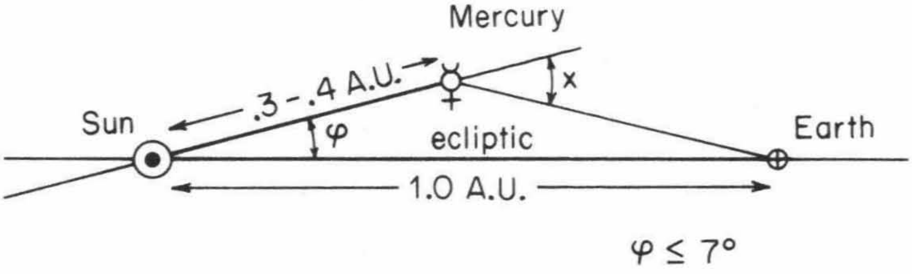

Fig. 2: Geometry of the Earth and Mercury is schematically indicated as it would prevail near inferior conjunction. The angle x is equal to the subearth latitude or planetocentric declination of the Earth.

calculation of observable radio brightness temperatures and interferometric visibility functions to understand data taken at several wavelengths on several different dates. This was accomplished by numerical solution of the radiative transfer problem in the subsurface, as described in detail in Sec. 9.1 and Appendix IV. The only difference here is the larger depth step size used for Mercury. There still are three subsurface layers in one "folding length" or 1/e attenuation length of the Mercurian diurnal thermal wave. Brightness temperature maps obtained in orthogonal polarizations were then used to compute observables using a program originally written by Olav Hansen (1970) which carefully accounts for "serrations" along the edge of the supposedly round disk produced by the grid spacing of 1/25 of the planetary diameter and thus decreases the effect of the grating appearance on the computed visibility functions. As it happened, the effects of baseline rotation were unimportant in the only interferometric data taken as Mercury at the time of observation was quite close ($\sim 3^\circ$) to the Celestial Equator. Consequently, the approximation was made of computing observables using a non-rotating east-west baseline. This was checked by doing the full rotating-baseline calculation once and was found to be accurate to 0.1% in the visibility function for all values of β (= baseline in wavelengths × planetary radius in radians. See Appendix V).

3.2: Parameters Used in the Models:

Models were computed using a range of parameters to determine which set best fit the observations. Thermal models were computed using the following parameter values:

ρ = subsurface density = 1.0, 1.5 gm cm^{-3}

$\gamma = \sqrt{K_c \rho C}$ = contact thermal inertia

= .001, .002 cal cm^{-2}deg^{-1} sec$^{-\frac{1}{2}}$

A = bolometric Bond Albedo = .06

χ = ratio of $K_r/K_c = \frac{BT^3}{K_c}$ at T = 350° K

= 0.0, 0.4, 1.0, 1.5

E = radiometric emissivity = 0.94

and $K_r(T)$ and $C(T)$, as described earlier, were taken to be of the form

$$K_T(T) = K_c + BT^3 = K_c + K_r(T)$$
$$C(T) = -.034\, T^{\frac{1}{2}} + .008\, T - .0002 T^{3/2}$$

The values used for χ are consistent with those obtained by Watson (1964) for crushed quartz particles of dimension approximately 100 microns or less, in a vacuum. One of the least well-determined of these parameters is the contact thermal inertia, $\gamma_c = \sqrt{K_c \rho C}$. Measurements of the dark side temperature by Murray (1967) gave an upper limit of 150° K, which has since been revised to 140° K (Murray , 1968). This represents an upper limit of $\gamma_t = .006$, where γ_t contains both contact and radiative thermal conductivity. In an attempt to improve on the limits of γ_t, we may utilize the calibration-independent result of Epstein et al. (1970):

$$\delta/\lambda = 1.3^{+1.4}_{-0.8}$$

where δ is interpreted in the light of the linear theory (Piddington and Minnett, 1949) as

$$\delta = L_e/L_t = \frac{\text{electrical skin depth}}{\text{thermal skin depth}} \quad .$$

This result is based on a five-parameter fit to the extensive phase data of Epstein et al., and is presumably sufficient to establish limits on γ_t.

Solving for γ_t, we get

$$\gamma_t = \frac{C\sqrt{\Omega}}{(\delta/\lambda)\ 2\pi\sqrt{2\epsilon}} \quad \frac{\rho}{\tan\Delta}$$

Ω = diurnal rotation rate

C = Specific heat

ϵ = dielectric constant

ρ = density

$\tan\Delta$ = electrical loss tangent

We use a value for ϵ of $\epsilon = 2.4$ (see next section) and utilize the empirically determined fact (Troitskii et al., 1970) that

$$\frac{\tan\Delta}{\rho} \approx \text{Constant over a wide range of densities and materials.}$$

To evaluate this constant lunar values are used, and a value of $\frac{\tan\Delta}{\rho} = 5.34 \times 10^{-3}$ is obtained. With the above values and the results of Epstein et al., we obtain the following limits on γ_t:

$$.0006 < \gamma_t < .0035$$

$$\text{best value: } \gamma_t = .0014$$

If the subsurface of Mercury is at all similar to that of the moon, which is the assumption we are testing, then

$$\frac{\gamma_t}{\sqrt{2}} \le \gamma_c < \gamma_t \quad (\text{for } 0 < \chi < 1) \text{ at } T = 350^\circ\text{K} \quad .$$

Thermal models were computed for two values of the contact thermal inertia, $\gamma_c = \sqrt{K_c \rho C}$. We used $\gamma_c = .001, .002$. This parameter can be determined best from infrared dark-side data and the difficulties of making this measurement have as yet prevented a completely satisfactory determination. Murdock and Ney (1970) obtained a value of $\gamma = .0014$ using an infrared spectral technique and fitting simple two-region models to it. The weakness of their method lies in the assumption of a constant dark-side temperature. If even a small gradient exists across the terminator, the method will produce an overestimate of γ. At the time of their observations, however, the "crescent" was on the north side of the planet; i.e. the "terminator" was not the evening terminator, but the rather sharp line dividing day from night across the pole as seen from the earth which was somewhat above the planet and looking down. Consequently the gradient across the terminator is really quite sharp. In reality however, this result should be regarded as being perhaps slightly high due to small remnant temperature gradient effects and non-linear averaging at infrared wavelengths which give higher temperatures much greater weight than lower temperatures. In addition, uncertainty in the exact geometry of the terminator will aggravate this problem. Their final result was interpreted using the model predictions of Morrison and is thus also model-dependent. A thermal inertia of .001 was used in all final models. The radio data treated here do not seem to discriminate between $\gamma = .001$ and $\gamma = .002$, but both are consistent with a particulate subsurface.

Choice of the Bolometric Bond Albedo was made as follows. The Visual Bond Albedo, A_V, is .056 (de Vaucouleurs, 1963). If we may assume that the phase integral is independent of wavelength for an airless planet such as Mercury, and there is some observational evidence for this being the case for the Moon, (Minnaert, 1961), then we may get an approximation for the Bolometric Albedo. Using geometric albedos in U,B,V,R, and I given by Harris (1961), and intensities of the smoothed solar spectrum at these effective wavelengths (Allen, 1963), an integrated value of

$$A = .07$$

is obtained. This uses a value for the phase integral for all wavelengths equal to that observed for the visual, $q = .560$. It is thus felt that values of the bolometric Albedo of .10 or .12 as suggested by Morrison (1969) and Linsky (1966) are somewhat high. In any case this will be a small effect due to the dependence of equilibrium temperature on $(1 - A)^{\frac{1}{4}}$. In an exact calculation of surface temperature, however, this should be considered. The microwave temperatures are not as sensitive to this parameter.

Morrison (1969) determined from laboratory data of Hovis and Callahan (1966) that for particles of size $< 38\mu$, the infrared emissivity is constant ($\approx .94$) with temperature. Temperature effects are due to the strictly non-grey spectrum of silicates, and vanish for dust-size particles due to the reduction in spectral contrast for small particles in the infrared. Parameters describing the dielectric nature of the surface are less well established. As the major question attacked by this work is whether or not Mercury is similar in subsurface makeup and topography to the moon, values were chosen in the range found to be typical of the lunar regolith and of a wide variety of particulate geological materials (Campbell and Ulrichs, 1969).

$$\epsilon = \text{surface dielectric constant} = 1.1\text{-}3.0$$

$$\tan\Delta = \text{electrical loss tangent} = .003\text{-}.020$$

The only definite experimental determinations to date of either of these quantities comes from radar return data ($\epsilon = 2.5\text{-}3.0$) and this value is directly correlated with mean surface roughness to an unknown extent.

4.1: 6 cm Observations

Observations of Mercury at 6 cm. wavelength were made in early January, 1971 after the conjunction of December 1970. Uncooled parametric amplifiers were used on the 90' antennas of the Owens Valley Radio Observatory operating double sideband at 4995 MHz. System temperature, assuming an antenna efficiency of 50% at this wavelength, was 340° K (geometric mean). The system gave a signal-to noise ratio of about 6 on a given one-minute fringe. Approximately 10 useable records of 15 minutes length were obtained on each of 3 separate days. All other data were afflicted with chronic interference problems or were taken when the wind speed was above 15 mph. This consistently produced sporadic amplitude fluctuations of more than 5%. All data taken during these windy periods were discarded. All records taken on a given day were then averaged as weighted by the inverse square of their formal error. In this way, we increase the effective signal to noise ratio to approximately 70 for a single daily measurement. The system was calibrated in gain and phase every 60-90 minutes on a nearby small diameter source of well known position. The flux density of this source at the epoch of observation was determined by comparison with non-variable sources of well known flux density. The flux density of the primary calibrators used was taken from Pauliny-Toth and Kellermann (1968).

S_{5000} CTA102 = 3.63 ± .06 flux units (10^{-26} watts/m^2Hz)

S_{5000} 3C48 = 5.37 ± .07 flux units

S_{5000} 3C286 = 7.48 ± .09 flux units

The extragalactic radio source NRA0530 (3C360), of a dimension unresolved by the spacings used, and close in position to Mercury during the observing period, was used as secondary instrumental calibrator. Its flux density was determined using the above primary source flux densities to be

$$S_{5000} \;\; \text{NRA0530} = 3.92 \pm .07 \text{ flux units (f.u.)}$$

The quoted errors on daily temperatures are internal errors (do not include absolute calibration uncertainty or systematic pointing errors) and are calculated from the scatter of the individual points for each day. The temperatures refer to a disk of apparent radius 6.68" of arc at a distance of .5 AU. The results, along with relevant orbital data and geometry, are shown in Table I.

TABLE I.

6 cm DATA

Date	T_B°K		Phase Angle φ	Heliocentric Longitude	Subearth Longitude λ_{se}
12/30/70	342	± 11	166°	105.4°	165
12/31/70	322	± 15	158°	111.4°	158
1/ 1/71	317	± 5	151°	117.3°	151
1/ 7/71	317	± 9	118°	149.7°	123

4.2: 18 cm Observations

Observations of Mercury at a wavelength of 18 centimeters were made before the conjunction of April 24, 1971. The Owens Valley interferometer was used at an antenna spacing of 1600 feet in order to minimize the effects of solar interference. The receivers were matched, uncooled parametric amplifiers operating double sideband at 1612 MHz. System temperature using the twin 90' antennas was about 90°K, assuming an antenna efficiency of 60%

at this wavelength. Using this configuration, the formally computed minimum detectable flux density for one 15 minute record was .02 f.u. in the absence of confusion. Consequently the observations were not noise limited, but were confusion limited. At the time of these observations, Mercury was at galactic latitude -55°. Consequently galactic confusion was not a great problem, nor were there any known discrete radio sources of importance near enough to cause confusion. Confusion, when used here, refers to erroneous results caused by convolution into our measured flux density of radio emission from sources distant from Mercury but near enough to be in either the main beam or one of the side lobes of the antenna pattern. This is a persistent difficulty at decimeter-decameter wavelengths and arises mainly from continuum non-thermal emission of countless distant radio sources. The galactic plane is a region of high confusion. At most places in the sky, however, the density of nonthermal sources is such that the minimum detectable flux density at a spacing of $\sim 2670\lambda$ is on the order of .05 - .08 flux units ($1\ \text{f.u.} = 10^{-26}\ \text{w}/\text{m}^2 - \text{Hz}$). As the expected thermal flux density from Mercury at this wavelength is only .06 - .07 f.u., this is the limiting factor which must be dealt with.

The source of greatest confusion in this case is, however, the Sun. Although Mercury was not observed closer to the sun than about 6°, at which separation the antenna response is quite low and negligible for normal sources, the high solar brightness temperature of $\sim 10^{6\circ}$K at this wavelength is quite capable of producing a significant contribution to the net observed flux density. This difficulty was surmounted by making use of the rapid relative motion of Mercury and the sun shown in Fig. 3. As noted in Appendix V,

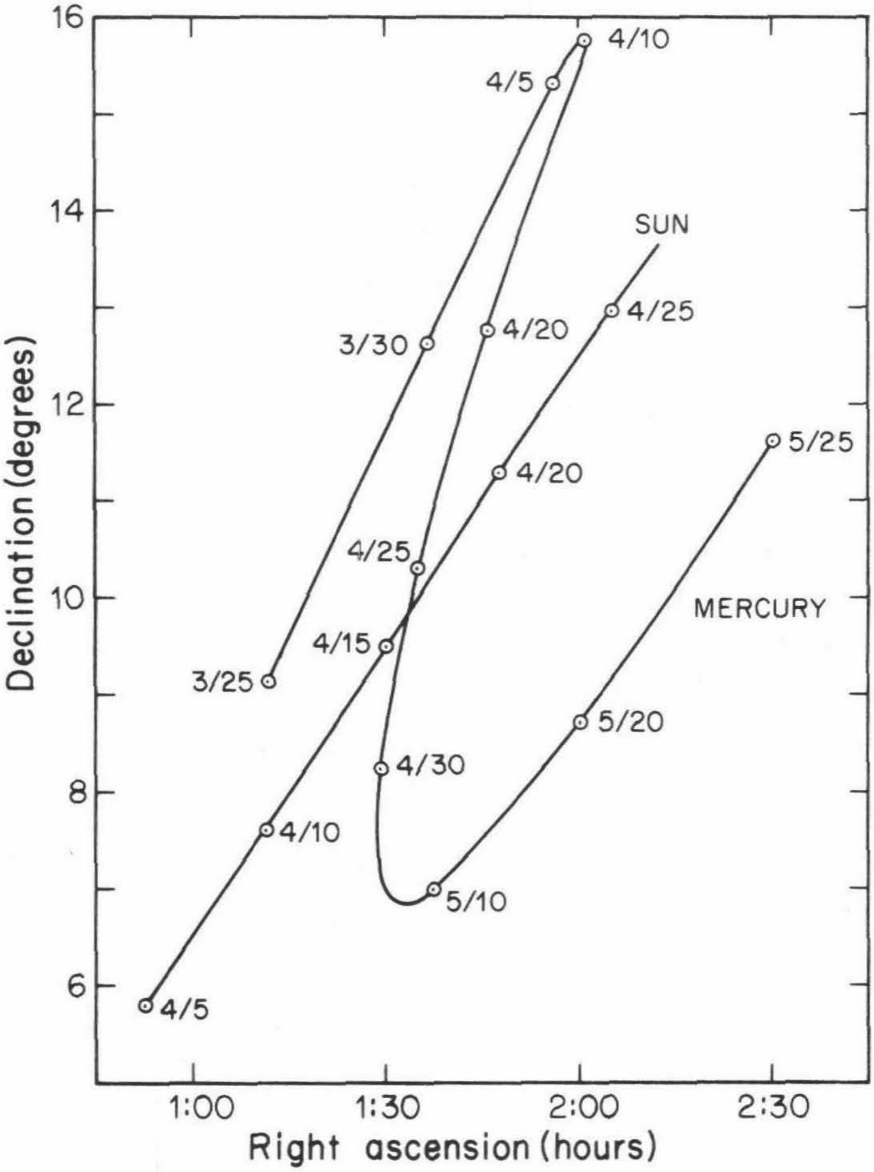

Fig. 3: Celestial positions of Mercury and the Sun , Spring 1971. The motion in right ascension is what is primarily relevant to removal of solar confusion from the observations, due to the use of an east-west baseline.

each interferometic data point is a vector, and yields both an amplitude and a phase of the signal. This phase angle rotates slowly as the effective centroid of the emission moves with respect to the main lobe of the interferometer pattern. As the phase of the central fringe is held constant (by tracking delay) relative to Mercury, we may consider Mercury to be stationary, (phase $= 0^\circ$) and the effective centroid of the sun's emission to be moving across the fringes. The phase of the response to the sun's emission rotates through a full 2π radians every time the centroid of the sun moves across one fringe. If the instantaneous vector response to the sun is denoted $\vec{S}$ and the vector response to Mercury is denoted $\vec{M}$, then

$$\vec{S} = S_o e^{i\omega_s t}$$

$$\vec{M} = M_o e^{i\varphi_o}$$

and the net response, or the result averaged over a particular record of length T is:

$$\frac{1}{T}\int_o^T \left[M_o e^{i\varphi_o} + S_o e^{i\omega_s t} \right] dt \quad .$$

When sufficient records are taken and vector averaged, the solar contribution will be greatly diminished. As the fringe spacing was 1'16" for the longest effective baseline (at transit), and the motion of the sun relative to Mercury was 45" in 15 minutes (320^s per day), the relative phase of the sun's contribution rotated through 2π radians every two records. The relative phase of the fixed background rotated through 2π radians every 3-5 records (about every hour). A total of 62 records were taken over four days, covering a net relative rotation of many lobes, or many rotations of 2π in phase.

The success of such a method is critically dependent on accurate phase data. The equipment used is intrinsically quite stable, giving formal errors of approximately .01 lobes or ~4°. It has been used to determine source positions operating single sideband by Hardebeck (1971) for which measurement highly accurate phase data is necessary. Used in a double sideband mode, the equipment is less sensitive to instrumental phase error. In addition, quite a lot of time was spent observing a phase calibrator of well-known position. This source was strong enough to allow us to neglect the solar contribution and not too distant (~10°) from Mercury. This provided a well determined instrumental phase variation curve with which the Mercury observations could be calibrated. Almost twice as much time was spent in this calibration mode as in a normal observing run. An integration time of 15 minutes was used on Mercury, and 6 minutes on the stronger calibration source. Gain calibration was achieved by tying the Mercury calibrator to several sources whose flux density is well established. The following sources and flux densities were assumed for calibration. The flux densities were obtained by interpolation of the source spectra and the errors are estimated.

3C48 $S_{1612} = 13.30 \pm .05$ f.u.
CTA21 $= 6.90 \pm .05$
3C286 $= 13.30 \pm .05$
CTA102 $= 6.40 \pm .05$

This flux scale is consistent with that given by Kellermann, Pauliny-Toth, and Williams (1969) and Day et al. (1969). Using these as primary calibrators, the flux density of the secondary calibrator, or Mercury calibrator, was determined to be: $S(P0229 + 13) = 1.31 \pm .05$ f.u. This determination had an internal error of ± .01 f.u. and consequently the flux density can be stated as accurately as the flux density of the primary calibrators. The end points of the individual vector measurements of "Mercury + confusion" and their vector average as weighted by the inverse squares of the individual formal errors are shown in Fig. 4. The quoted internal error was derived in the following manner. Vector differences between the final vector-average result and each individual measurement (R_i) are squared and summed over the data set. A circle of one standard error radius is defined in the usual fashion:

$$S^2 = \frac{\sum_i R_i^2}{N} \qquad \text{(See Fig. 10)}$$

then

$$\sigma_r = \frac{S}{\sqrt{(N-1)}} \; t_{.32} = \frac{1.06\ S}{\sqrt{(N-1)}}$$

where $t_{.32}$ is the value of the "Student's t" distribution for 62 degrees of freedom yielding the best estimate of a 68% confidence region on the basis of the given finite data set. From the symmetrical scatter of the data,

$$\sigma_x^2 \sim \sigma_y^2$$

thus

$$\sigma_r^2 = \sigma_x^2 + \sigma_y^2 \sim 2\sigma_x^2$$

and

$$\sigma_x = \frac{\sigma_r}{\sqrt{2}}$$

where σ_x is the formal internal error in amplitude (real part of F_x) and gives the quoted formal error in brightness temperature. The credibility of the

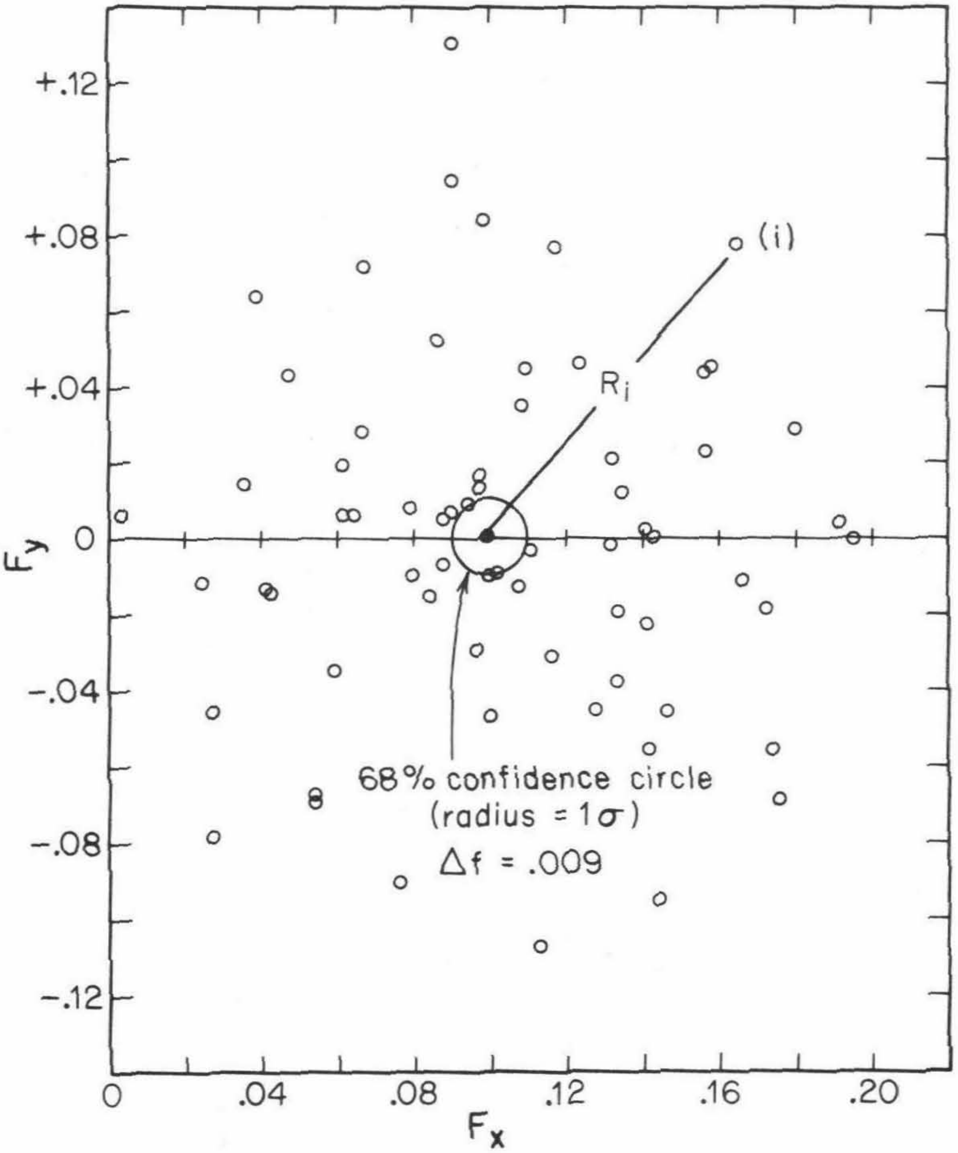

Fig. 4: Interferometric vector measurements (amplitude and phase) are shown in a plot of their x- and y- components. Individual measurements are open circles and the vector average is the solid circle. The formal one-sigma error circle is also shown. The measurements are at 18 cm.

result is strengthened by the fact that the resultant phase (imaginary part or $\tan^{-1}(F_y/F_x)$ is very close to zero. If some solar contribution remained in the final average, one would expect there to be a non-zero imaginary component, or phase. The final brightness temperature, as referred to a disk of radius 6".68 at .5 A.U., is $T_d(18\text{ cm}) = 356° \pm 22°K$ (formal error). Relevant geometric data are shown in Table II.

TABLE II.

18 cm Data

Date	φ°	Heliocentric Longitude	Sub-earth Longitude	T_B °K (Vector Average)
4/13/71	151	184	162	350
4/14/71	155	188	167	280
4/15/71	159	192	173	353
4/16/71	163	196	179	366
4/17/71	167	199	185	323

net vector average = 356° ± 22° formal error

4.3: 3.71 cm Observations

This group of data was taken from August 12-19, 1971. Although the observing run was scheduled for the favorable opposition of Mars, it happened that Mercury was also situated favorably to permit disk-resolved data to be taken. This run was the first successful use of all three Owens Valley antennas (two 90' antennas and the 130' antenna) as a three-element interferometer. The addition to the previous instrumentation at OVRO of one extra delay line and related electronics was needed to implement this very useful setup. As discussed in Appendix V, the received signal from one antenna must be delayed with respect to the received signal from the other by an amount depending upon the celestial position of the source and the position of the antennas. A similar relation holds for the third antenna in relation to the first. (See equation 3 of Appendix V). The fact that the three baselines define a closed triangle in space (in the general case) permits an important simplification to be made. The delay required to stop and maximize the fringes from the third effective baseline is identically the difference between the delays separately required to stop the fringes from the two "primary" baselines. Choosing delays relative to antenna #1 and denoting the delay inserted into the IF line of antenna #2 = τ_{21} and that for antenna #3 = τ_{31} then from equation 3 of Appendix V,

$$\tau = \frac{D_{ij} \sin \theta_{ij}}{c}$$

$$\tau_{21} = \frac{S_{21}}{c}\left[\sin d_{21} \sin \delta + \cos d_{21} \cos \delta \cos(h_{21} - H)\right] \qquad (4.3.1)$$

$$\tau_{31} = \frac{S_{31}}{c}\left[\sin d_{31} \sin \delta + \cos d_{31} \cos \delta \cos(h_{31} - H)\right] \qquad (4.3.2)$$

where

S_{ij} = baseline length

d_{ij} = baseline declination

h_{ij} = baseline hour-angle

(H, δ) = Celestial co-ordinates of source.

The requisite delay for the third baseline is

$$\tau_{32} = \frac{S_{32}}{c}\left[\sin d_{32} \sin \delta + \cos d_{32} \cos \delta \cos(h_{32} - H)\right]$$

the desired identity,

$$\tau_{32} = \tau_{31} - \tau_{21}$$

holds if and only if

$$S_{32} \sin d_{32} = S_{31} \sin d_{31} - S_{21} \sin d_{21}$$

and

$$S_{32} \cos d_{32} \cos(h_{32} - H) = S_{21} \cos d_{21} \cos(h_{21} - H) - S_{31} \cos d_{31} \cos(h_{31} - H)$$

These expressions merely denote projections on orthogonal axes of the three baselines and the "identity" is immediately obtained using the fact that the three baselines form a closed triangle. Consequently, the IF signals received from antennas 2 and 3 after being delayed by the times τ_{21} and τ_{31} to form fringes when multiplied by the IF signal from antenna # 1 may be directly multiplied to produce the desired fringes from baseline S_{32} without further manipulation. The three baseline setup is a powerful tool. Besides enabling us to gather three baseline-weeks worth of data in one week's observing time, it frees us from the loss of time due to moving antennas and reestablishing pointing correction curves. The advantages to planetary observations are even greater as Mercury, in particular, is usually only observable over a period of about a week or two. Equally important, the collection of disk average data from the shortest baseline simultaneously with highly resolved data from the longest baseline allows us to normalize the resolved data correctly and prevents the variability of total flux with time from confusing the resultant visibility function.

The two antennas forming the longest baseline were equipped with cooled degenerate parametric amplifiers operating at 8085 MHz which yielded system temperatures of less than 100°K. A crystal-mixer amplifier was used on the third antenna with a noise temperature of approximately 300°K. Our most highly resolved data had internal errors due to noise of approximately .05 flux units, as compared with approximately .2 f.u. for our short-baseline (unresolved) data taken with the two 90' antennas one of which employed the crystal-mixer amplifier.

The question of "resolution" deserves some discussion here. When applied in the above manner this term is not as intuitively meaningful as when used in other astronomical connotations. Certainly it is clear that the scale of relevant detail decreases with increase in spatial frequency or $\beta(S_\lambda)$. It may be qualitatively stated that the scale of relevant detail represented by data taken at a given baseline is about $\frac{1}{2}$ of the angular width of one fringe. Or, since the fringe width at baseline S_λ is

$$\theta = \frac{1}{S_\lambda} \text{ radians,}$$

visibility amplitude data at our longest spacing (of 3700') contains information relevant to detail with angular resolution of $\sim$3". Our shortest spacing of 300' yields an approximate resolution of 40". At the time of observation, the disk of Mercury subtended an angle of 10". Information relevant to detail on a smaller scale than 3" is potentially obtainable from phase function data, but this data for Mercury was poor and contained large ambiguities and scatter, and was not usable for this purpose. These resolutions may be regarded as spatial resolution that would be obtainable if the data were complete enough for inversion to a brightness map. System gain was calibrated every 60-90 minutes in the fashion described earlier. The absolute flux scale was derived for several sources by interpolation of source spectra using the flux density measurements of Dent and Haddock (1966), which were first corrected upwards by 7% to conform to the flux scale of Scheuer and Williams (1968), (consistent with S_{8000}(Cas A) = 629.6 f.u. (1964.4).

Calibrators used and flux densities assumed were

CTA21	S_{8000} = 2.30 f.u. (10^{-26}w/m^{2}Hz)
3C147	= 5.25
3C286	= 5.80
CTA102	= 3.33

giving a value for the secondary calibrator used for Mercury (a variable source) of

P1055 + 01 $S_{8000}(1971.62) = 3.28$ f.u.

A discussion of absolute calibration at 8000 MHz will be given in the next section. Relevant geometric data are shown in Table III, and the observed visibility function data are shown in Fig. 5.

TABLE III.

3.71 cm Data

Date	Phase Angle φ^o	Heliocentric Longitude	Sub-earth Longitude
8/12/71	123	284	239
8/13/71	126	287	248
8/14/71	129	290	257
8/15/71	132	293	264
8/16/71	135	296	270
8/17/71	138	299	276
8/18/71	141	302	283
8/19/71	145	305	290

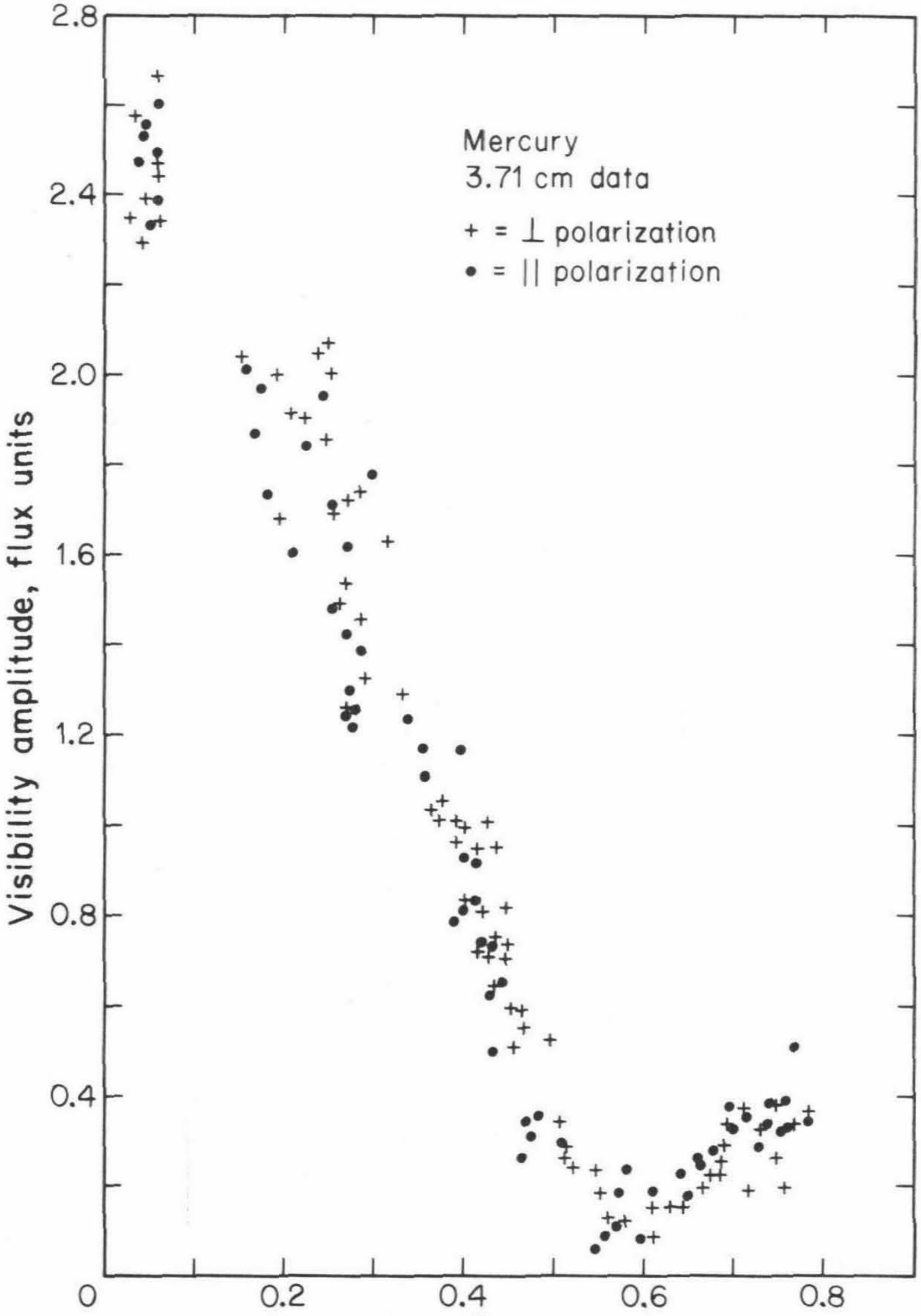

Fig. 5: Amplitude of the visibility function observed at 3.71 cm in August, 1971, given as a function of β, the normalized effective baseline. The visibility amplitude, in flux units, refers to a disk of radius 6.68" at a distance of 0.5 AU.

5. ANALYSIS

In the general case of fitting a modelled observable for "best" parameters when the observable depends on several parameters in a non-linear or complex fashion a simultaneous fitting of all parameters by linearizing the dependence relations is necessary. This is because local minima in the residuals for each parameter are intercorrelated and one wants to know the single set of parameters that best fits the data. In the case at hand, however, the situation does not warrant or require such treatment. For one thing, several different independent kinds of observables are being fit (i.e. disk measurements, visibility functions, and polarization function). The dependence of each observable on the parameter set (basically, the dielectric constant, ϵ, electrical loss tangent *, and radiative thermal conductivity parameter, χ) is different. In addition, as has been mentioned and will be further demonstrated, the effective dielectric constant is uniquely determined by the polarization curve and the best fitting χ as determined from the interferometric data is effectively independent of both dielectric constant and loss tangent. For these reasons, it was decided to independently fit the dielectric constant (ϵ) from the interferometric data and to use model computations with other disk-average data to evaluate consistency and validity of the final parameter set. This method will be shown to be quite satisfactory and to produce a consistent set of results. The parameters will be treated in order of the strength attached to the means of deriving them. The dielectric constant (ϵ)

---

* Where used here, the dielectric constant is the real part of the complex dielectric constant and the loss tangent is the ratio of the imaginary to the real part. These two parameters are used to define the absorbtion coefficient (see Appendix IV).

will first be determined. Thermal models will then be fit to the disk-average data over a large range of wavelengths and many phase angles, and extreme values of χ and $\tan\Delta$ will be ruled out. Concurrently, the value of χ that best fits the interferometric data is shown to be insensitive to variations in dielectric constant and loss tangent compatible with the disk-average data. Difficulty in matching the model to the visibility functions in detail will then be discussed. This method has the important advantage of separating well-determined parameters from poorly-determined ones, and of isolating the inconsistent data.

5.1: Determination of the dielectric constant

As shown in Appendix V, the function $(V_{\perp} - V_{\parallel})$ produced by differencing the normalized polarized visibility functions is essentially independent of everything but the dielectric constant. In particular it is independent of the physical temperature distribution and loss tangent. This is due to the first-order similarity of all planetary brightness distributions under investigation, and is shown in Appendix V. Adjacent individual data points of 15 minute length were differenced in the following fashion. Our standard observing technique alternates records taken in polarizations $\perp$ and $\parallel$ to the projected baseline. As the records are approximately 15 minutes long, the projected baseline length and thus the value of β will be slightly different even for adjacent records. In order to compute $P(\beta) = V_{\perp}(\beta) - V_{\parallel}(\beta)$, the average of the two values of β was taken. Observed fluxes were then linearly extrapolated to a corrected value at the average β and differenced. The extrapolation was along the unpolarized visibility function produced by the model for $\chi = .4$ and $\tan\Delta = .0075$. Curves produced for $\varepsilon = 1.1$, which are only very slightly polarized to begin with, were averaged to produce the unpolarized visibility function.

Choice of parameters used for this extrapolation curve is not critical as the changes in β are small between adjacent points. It was felt that using even an approximate curve for the model under consideration was more reasonable than using a uniform-disk visibility function which differs greatly from the observed curves. In any case systematic errors introduced in this fashion are of higher order than those that would be introduced by using any other extrapolation scheme. The resultant polarizations as a function of $\overline{\beta}$ are shown in Fig. 6. Using no correction to $\overline{\beta}$ produces a much more widely scattered set of points. Model visibility functions were used to match these data. Again, this is a potentially biased method but it was felt to be preferable to using "uniform disk" polarization for the following reasons. The fluxes, or data points, that are to be differenced are actually visibility amplitudes, and are different for a non-uniform disk from the real part of the complex visibility function, or simple cosine transform. The complex visibility function as derived in Appendix V is

$$\begin{aligned} C(\beta) &= V(\beta)e^{i\Phi(\beta)} \\ &= V(\beta)\cos\Phi(\beta) + iV(\beta)\sin\Phi(\beta) \\ &= V_R(\beta) + i\,V_I(\beta) \end{aligned}$$

for a uniform disk, $\Phi(\beta) = n\pi$ $(n = 0,1,2....)$ and $C(\beta) = V_R(\beta)$. However, for a non-uniform brightness distribution in general, $\Phi(\beta) \neq (0,\pi)$ and $|C(\beta)| = |V(\beta)e^{i\Phi(\beta)}| = (V_R^2 + V_I^2)^{1/2}$. This effect causes $|C(\beta)|$ to never actually go through zero, so the "zero" of $C(\beta)$ is, strictly, not

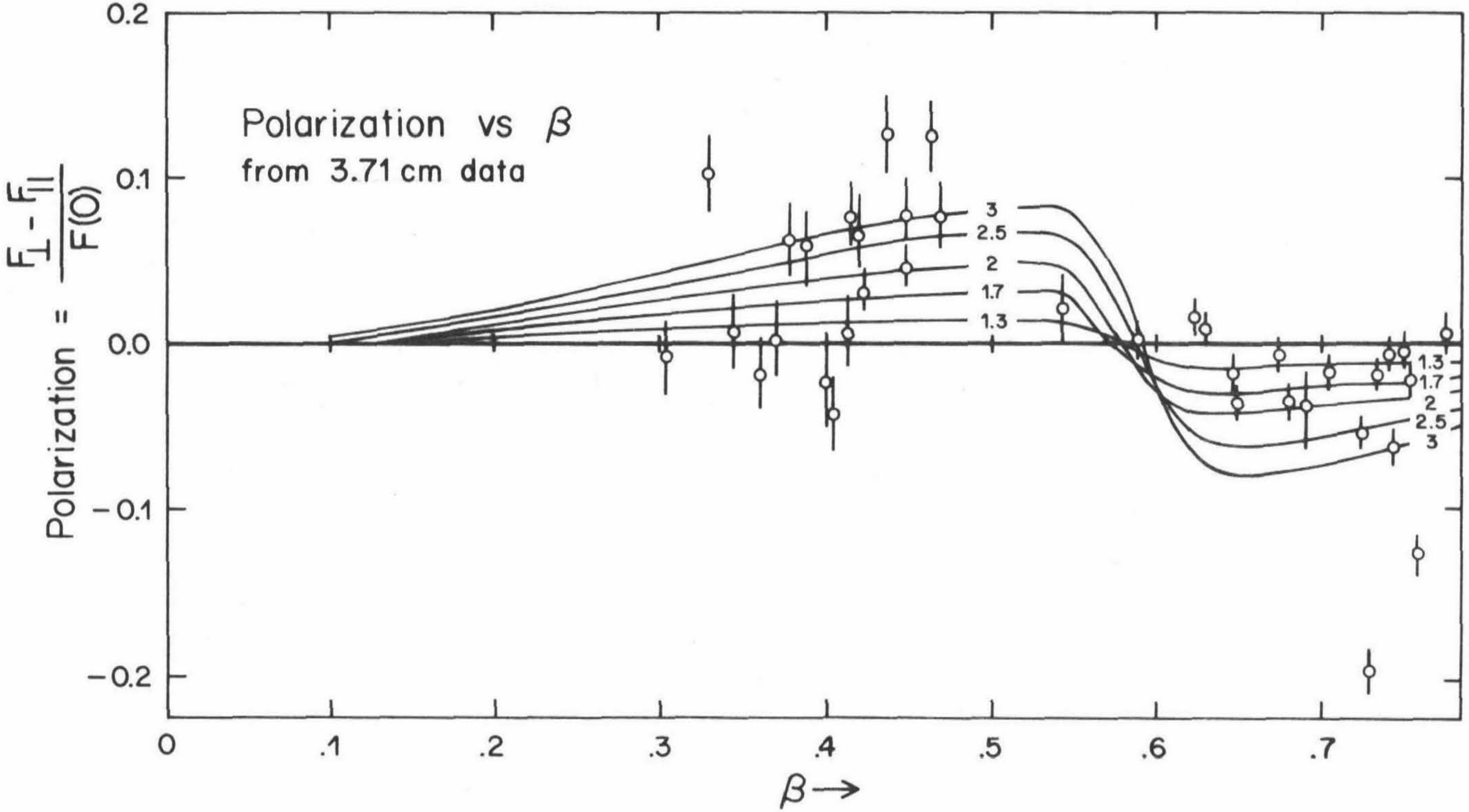

Fig. 6: Differences between the observed visibility functions in orthogonal polarizations (3.71 cm data). The smooth curves are model-generated difference functions for different values of effective dielectric constant, ϵ.

defined. In practice, it may be approximated to good accuracy but the real data that are being differenced near this arbitrarily defined zero are the numbers $|C(\beta)|$ and consequently > 0. Where the diference $(V_{R\perp} - V_{R\parallel})$ for a uniform disk shows a maximum near the "zero" of the unpolarized function V_R, the difference $|C_\perp(\beta)| - |C_\parallel(\beta)|$ actually goes to zero near this point. Without highly accurate phase data (which were not obtained) the visibility amplitudes measured may not be used to get the "real part" of the visibility function. Thus in order to avoid unnecessarily large residuals and thereby increase the accuracy of the determination of ϵ, model-computed functions were used, and visibility amplitudes were differenced directly. These curves are also shown in Fig. 6. Choice of parameters other than ϵ is not critical as variations of the polarization curve with ϵ are much greater than variations due to other parameters. This is shown in Appendix V. Residuals were computed for each of several effective dielectric constants and the best fit value and standard error ($\pm 1\sigma$) were computed using a method described in Appendix VI. The curve of residuals is shown in Fig. 7. The result obtained by fitting a parabola to the three central points of the curve of residuals is:

$$\epsilon = 2.0 \pm .16 \text{ (formal error)}$$

This is actually a lower limit on material dielectric constant as surface roughness significantly decreases polarization by statistically blurring the "hot spots" shown in Fig. 52 of Appendix V for a perfectly smooth dielectric sphere.

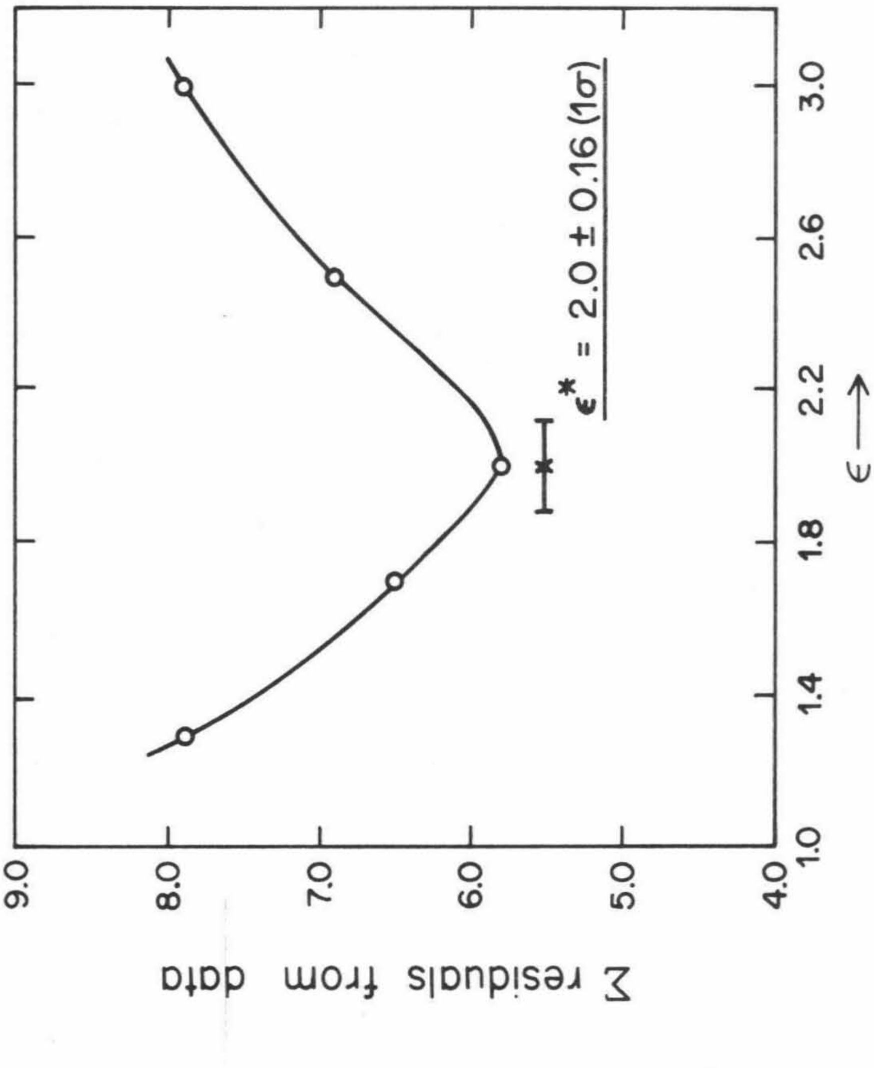

Fig. 7: Residuals relative to the 3.71 cm polarization difference data calculated for the model-generated curves shown in fig. 6 for several values of possible surface dielectric constant, ε. The best-fitting value of ε = 2.0 is shown along with its associated error. (one-sigma formal error).

It is possible to make a correction for this effect in order to use ϵ in interpreting the disk-average data which are not sensitive to smearing out of detailed brightness maps and are dependent on the dielectric constant of the bulk material constituting the subsurface. The correction is that of Hansen and Muhleman (1970). The method consists basically of dividing the surface area into facets which are tilted with respect to the smooth-surface normal. The tilt angle of a given facet is a random number with an exponential probability distribution

$$p(\theta) = \frac{1}{\sigma} e^{-\theta/\sigma} \quad . \qquad (5.1.1)$$

where σ is the "mean" or "typical" angle characterizing the roughness of the surface. The Fresnel emission coefficients are then computed for the resultant angle between the real tilted surface normal and the direction to the Earth. Visibility functions are computed by Fourier Transforming the resulting brightness maps, and the degree of depolarization for a given σ and ϵ may be computed. Typical results are shown in Fig. 8 . Using this method and a "mean tilt angle" (analogous to σ) derived from radar data, we may get an approximate value for the material dielectric constant.

Radar Data

It is beyond the scope of this thesis to discuss the many subtle details of deriving the radar backscatter law, and the reader is referred to discussions in Muhleman (1964) and Hagfors (1968). Subject to certain assumptions, it is

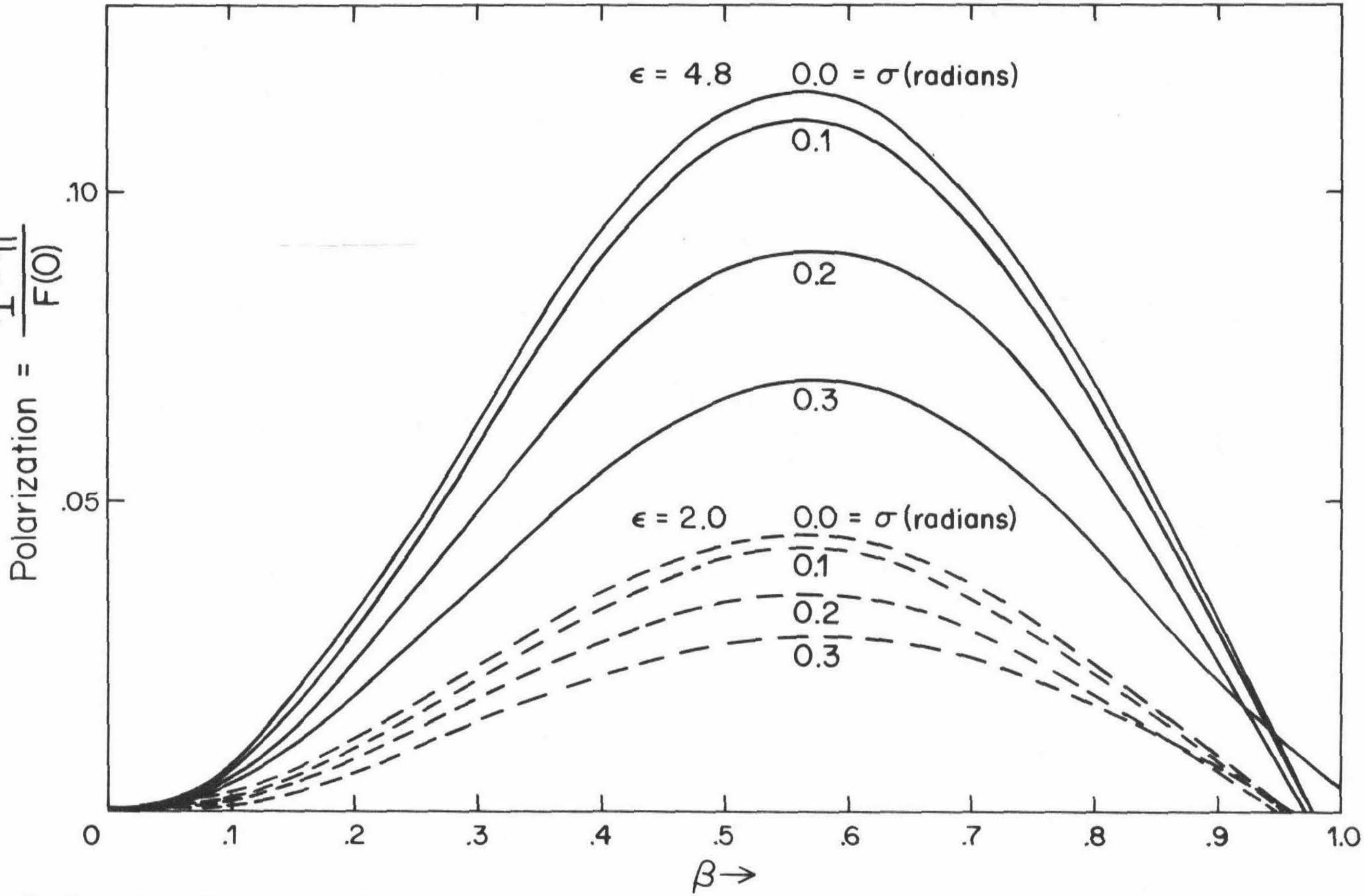

Fig. 8: The effect of surface roughness characterized by mean tilt angle σ on apparent polarization for two values of "true" surface dielectric constant, $\epsilon = 2.0$, $\epsilon = 4.8$. Curves from Hansen and Muhleman, 1970.

possible to treat a planetary surface in first approximation as a faceted reflector with facet tilt angles distributed in accord with various probability densities; one which is commonly used is the distribution (5.1.1). Great controversy is attached to this subject, and methods used by different observers vary widely. The range of derived mean tilt angle varies somewhat from method to method as well as from planet to planet. Although radar backscatter data for Mercury is rather scarce, it is currently thought that Mercury's surface is as rough as, or perhaps slightly rougher than, the Moon's (NEROC quarterly report, (1971); Hagfors and Evans, (1968); Muhleman, (1966); Pettengill et al. (1967) and definitely rougher than Venus (Goldstein, 1971; Muhleman, 1966; Pettengill, Dyce, and Campbell, 1967). We have therefore used typical lunar roughness described at 3.6 cm by $\sigma \sim 15°$ (Hagfors and Evans, 1968). In general σ is wavelength dependent and is completely analagous to the σ of equation 5.1.1. Using the results of Hansen and Muhleman, we derive a value of the effective subsurface material dielectric constant of $\varepsilon = 2.4 \pm .3$. The larger uncertainty reflects uncertainty in mean tilt angle. This value of ε is believed to be the most well-determined parameter in this investigation, and will be used in all further calculations. Although the value of ε as determined from radar measurements has previously been used for lack of any other value in calculating microwave emissivity, this is the first determination of ε from the microwave emission and thus is an important independent determination. It is likely that this value is more relevant to understanding radio emission data. The disk-average data are not as critically dependent on surface roughness as are the interferometric data and tend to be determined by the material dielectric constant, a function of specific dielectric constant of the rock type, ε_s, and the density of the bulk material. The dependence is best described by the Rayleigh mixing relationship. (Rayleigh, 1892). This result for the dielectric constant is in rather good agreement with the radar value of $\varepsilon = 2.7 \pm .2$. Radar-derived dielectric constants are generally somewhat higher than those derived by use of passive radio astronomical data (See Fig. 9). This phenomenon is possibly due in some way to the fact that radar information is due mainly to normal-incidence reflection from the front cap of the planet and thus tends to refer to material at greater depths than the radio emission (polarization) information which comes mainly from points near the limb at which material at shallow depths is being observed. In any case the discrepancy seems to be predictable and is of a similar magnitude to that found for the moon. The empirical relationship due to Troitskii et al. (1970)

$$\rho = \frac{\sqrt{\varepsilon} - 1}{a}$$

is used for $a = .5$ (their value averaged over many terrestrial materials at a wavelength of 3 cm)* to get a value for the subsurface material density of

---

* "a" is an empirical constant, called the specific polarizability by Troitskii et at. It is not clear where the difference in these values of "a" arises as the claim is made by Troitskii et al. that a lower value of "a" implies higher silica content. It does not appear feasible to use these results for any purpose beyond setting an approximate range of likely densities.

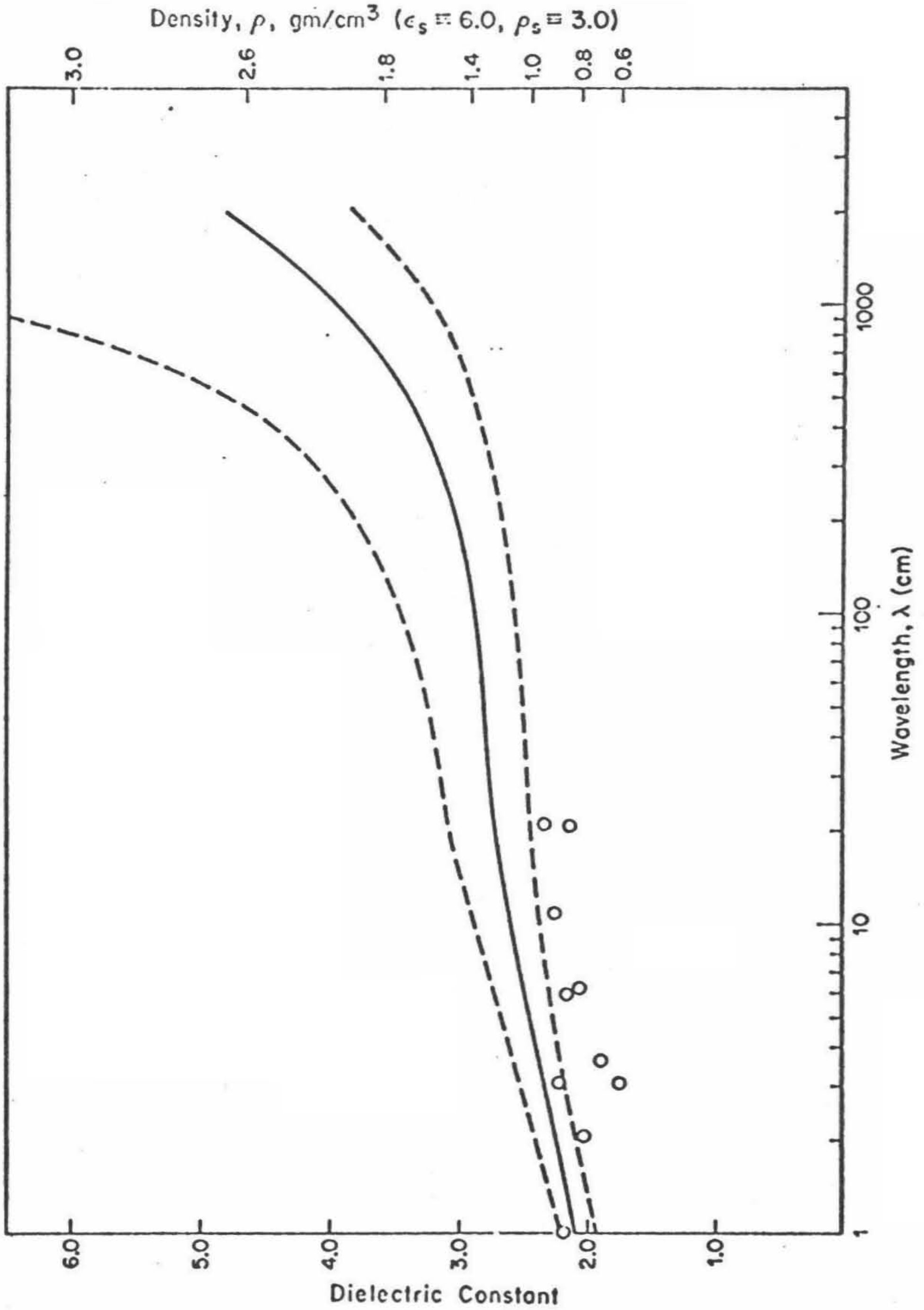

Fig. 9: Observed values of dielectric constant for the Moon as a function of wavelength. The radar values are approximated by the smooth curve, with confidence limits shown by the dashed curves. Values of ϵ obtained from radio emission data are open circles, corrected for roughness. (From Muhleman, 1972)

$$\rho = 1.12 \text{ gm cm}^{-3}$$

The measured value of "a" for a sample of lunar soil (Gold et al., 1970) is ~.35. Using this alternate value, we obtain a density of

$$\rho = 1.57 \text{ gm cm}^{-3}$$

relative to a depth of 45 - 50 cm beneath the surface.

Model results using parameters described in Section 3.2 were then used to compute observable disk average temperatures at the given dates of observation for data at several radio wavelengths. The 6.0 cm and 18.0 cm data described earlier were treated in this manner, as were selected previously published data from Klein (1968), Epstein et al. (1970), and Ulich et al. (1972). Low-error data were chosen in all cases where possible to give best discriminability. All models used constant dielectric parameters and the condition of subsurface homogeneity was assumed. These assumptions are found to be satisfactory in the analysis of the Martian subsurface (Part III) and of the lunar subsurface (Linsky, 1966). In each case, model generated brightness maps will be shown; one map of surface temperature and one map showing the apparent brightness distribution at the wavelength of observation. The great difference in appearance is due to the generally greater effective depth of origin of the microwave emission ($z_{eff} \sim 15\lambda \sim L_e$) and crudely represents the temperature distribution at this depth. Naturally, no sharp terminator is apparent in the microwave maps for this reason.

5.2: 6 cm data analysis

Theoretical brightness maps of Mercury as seen from the Earth on 1/8/71 are shown in figs. 10 and 11. The appearance of the planet did not change appreciably over the week of observation. The data are shown in fig. 12 along with model-computed disk-average temperatures for $\varepsilon = 2.5$ and several choices of χ and $\tan\Delta$. These data are clearly consistent with several values of the different parameters. Following lunar analogy until it is proven invalid, however, our conclusion here is that the data are consistent with $\varepsilon = 2.5$, $1.0 > \chi > 0.4$ and $.010 > \tan\Delta > .005$. We may rule out combinations of lower χ and higher $\tan\Delta$, or higher χ and lower $\tan\Delta$. The values of $\tan\Delta$ and χ considered likely are consistent with particulate geological materials in vacuum. The absorbtion length, or effective depth of observation, may be calculated from the expression

$$L_e = \lambda/2\pi\sqrt{\varepsilon}\tan\Delta$$

where $L_e = (k_\lambda)^{-1}$ and k_λ is derived in Appendix IV. For $\varepsilon = 2.5$ and $\tan\Delta = .0075$, we determine that these measurements pertain to material at a depth of 13.5λ, or approximately 80 cm.

5.3: 18 cm data analysis

Our measurement at 18 cm. refers to material at a much greater depth. Using the parameters considered in the previous section we find that the effective depth of observation is 13.5λ or 245cm. A certain increase in density is to be expected at this depth from lunar analogy. Figure 9 shows the

```
THE MATRIX OF SURFACE KINETIC TEMPERATURES

   0.   0.   0.   0.   0.   0.   0.   0.   0.   0.   0.   0.  83.   0.   0.   0.   0.   0.   0.   0.   0.   0.   0.   0.   0.
   0.   0.   0.   0.   0.   0.   0.   0. 365. 201.  39.  88.  88.  93.  88.  88.  89.   0.   0.   0.   0.   0.   0.   0.   0.
   0.   0.   0.   0.   0.   0. 462. 386. 303. 141.  92.  90.  90.  90.  90.  90.  90.  90.  91.   0.   0.   0.   0.   0.   0.
   0.   0.   0.   0.   0. 519. 459. 392. 170.  94.  91.  91.  91.  91.  91.  91.  91.  91.  91.  92.   0.   0.   0.   0.   0.
   0.   0.   0.   0. 531. 475. 419. 253. 100.  96.  92.  92.  92.  92.  92.  92.  92.  92.  92.  92.  92.   0.   0.   0.   0.
   0.   0.   0. 552. 511. 440. 260. 103.  98.  95.  93.  93.  93.  93.  93.  93.  93.  93.  93.  93.  93.  94.   0.   0.   0.
   0.   0. 581. 533. 471. 423. 264. 104.  99.  93.  95.  93.  93.  93.  93.  93.  93.  93.  93.  93.  93.  93.  93.   0.   0.
   0.   0. 566. 525. 476. 427. 348. 266. 184.  99.  98.  96.  93.  93.  93.  93.  93.  93.  93.  93.  93.  93.  94.   0.   0.
   0. 597. 558. 505. 432. 452. 432. 432. 269. 106. 103. 100.  94.  94.  94.  93.  94.  94.  94.  94.  94.  93.  94.  93.   0.
   0. 611. 573. 523. 434. 459. 454. 434. 270. 105. 103. 100.  94.  94.  94.  94.  94.  94.  94.  94.  94.  94.  94.  94.   0.
   0. 619. 593. 565. 536. 487. 437. 354. 271. 106. 103. 100.  94.  94.  94.  94.  94.  94.  94.  94.  94.  94.  93.  94.   0.
   0. 620. 594. 566. 537. 488. 436. 355. 272. 106. 103. 100.  94.  94.  94.  94.  94.  94.  94.  94.  94.  94.  93.  94.   0.
 644. 621. 595. 567. 538. 488. 439. 355. 272. 106. 103. 100.  94.  94.  93.  93.  94.  94.  94.  94.  94.  93.  93.  94.  93.
   0. 620. 594. 566. 527. 468. 438. 355. 272. 105. 103.  99.  93.  93.  93.  93.  93.  93.  93.  93.  93.  93.  93.  94.   0.
   0. 619. 593. 565. 536. 487. 437. 354. 271. 105. 102.  99.  93.  93.  93.  93.  93.  93.  93.  93.  93.  93.  93.  94.   0.
   0. 631. 598. 551. 533. 484. 460. 434. 270. 105. 102.  99.  93.  93.  93.  93.  93.  93.  93.  93.  93.  93.  93.  93.   0.
   0. 634. 603. 572. 530. 507. 481. 432. 268. 104. 102.  98.  92.  92.  93.  92.  92.  93.  93.  93.  93.  92.  93.  92.   0.
   0.   0. 610. 580. 552. 525. 476. 427. 265. 103. 100.  98.  92.  92.  92.  92.  92.  92.  92.  92.  92.  92.  92.   0.   0.
   0.   0. 631. 585. 546. 519. 471. 423. 262. 102.  99.  97.  91.  91.  91.  91.  91.  91.  91.  91.  91.  91.  89.   0.   0.
   0.   0.   0. 602. 565. 525. 464. 416. 258. 178.  99.  95.  91.  91.  91.  91.  91.  91.  91.  91.  91.  90.   0.   0.   0.
   0.   0.   0.   0. 590. 545. 520. 469. 428. 256. 164. 127.  69.  69.  69.  89.  89.  89.  89.  91.  88.   0.   0.   0.   0.
   0.   0.   0.   0.   0. 583. 556. 532. 494. 425. 368. 228.  88.  86.  86.  88.  88.  86.  85.  87.   0.   0.   0.   0.   0.
   0.   0.   0.   0.   0.   0. 574. 529. 495. 465. 398. 273.  83.  84.  85.  85.  85.  85.  84.   0.   0.   0.   0.   0.   0.
   0.   0.   0.   0.   0.   0.   0.   0. 527. 480. 449. 373. 232. 110.  80.  79.  78.   0.   0.   0.   0.   0.   0.   0.   0.
   0.   0.   0.   0.   0.   0.   0.   0.   0.   0.   0.   0. 350.   0.   0.   0.   0.   0.   0.   0.   0.   0.   0.   0.   0.
   0.0   3.8  11.3  18.8  26.3  33.8  41.3  48.8  56.3  63.8  71.3  90.0 120.0 150.0 180.0 210.0 240.0 270.0 300.0 330.0
 210.4 251.1 352.4 369.6 382.0 382.6 378.9 374.6 371.4 369.6 369.0 367.5 367.6 367.7 367.7 367.8 367.8 367.8 367.8 367.8
  8.6 MICRON FLUX=0.2010E-05 MICROWATTS/(SQ CM MICRON)
 11.8 MICRON FLUX=0.3185E-05 MICROWATTS/(SQ CM MICRON)
   DISK TEMP AT 20.0 MICRONS=287.69  FLUX=0.4460E-11
```

Fig. 10: Computed map of surface physical temperature of Mercury as seen from the Earth on 1/8/71. Celestial north is at the top of the map.

```
POLARIZED TEMPERATURE DISTRIBUTION

   0.   0.   0.   0.   0.   0.   0.   0.  88. 116. 143. 165. 174. 181. 177. 158.  92.   0.   0.   0.   0.   0.   0.   0.   0.
   0.   0.   0.   0.   0.   0. 132. 191. 164. 174. 196. 211. 224. 231. 232. 220. 187. 221. 143.   0.   0.   0.   0.   0.   0.
   0.   0.   0.   0.   0. 246. 211. 236. 240. 232. 249. 262. 274. 281. 287. 282. 282. 270. 278. 234.   0.   0.   0.   0.   0.
   0.   0.   0.   0. 275. 282. 250. 201. 254. 263. 283. 292. 302. 309. 316. 315. 315. 319. 313. 287. 273.   0.   0.   0.   0.
   0.   0.   0. 331. 311. 318. 330. 285. 263. 287. 300. 310. 320. 321. 323. 329. 335. 340. 343. 340. 315. 292.   0.   0.   0.
   0.   0. 274. 335. 347. 331. 301. 277. 255. 302. 312. 317. 322. 327. 333. 335. 342. 351. 357. 363. 360. 332. 256.   0.   0.
   0.   0. 323. 367. 353. 333. 313. 207. 304. 321. 320. 320. 320. 330. 340. 342. 351. 361. 368. 375. 377. 372. 315.   0.   0.
   0. 243. 357. 380. 365. 348. 333. 310. 317. 320. 323. 327. 335. 346. 352. 358. 363. 369. 376. 384. 389. 390. 374. 285.   0.
   0. 351. 400. 384. 357. 352. 357. 349. 333. 318. 326. 333. 349. 361. 367. 373. 373. 373. 391. 387. 392. 399. 395. 332.   0.
   0. 409. 417. 376. 378. 365. 363. 353. 336. 320. 328. 335. 352. 363. 370. 376. 375. 375. 391. 386. 396. 402. 405. 379.   0.
   0. 422. 431. 415. 393. 378. 359. 349. 335. 322. 329. 337. 354. 366. 371. 379. 378. 382. 377. 389. 399. 406. 411. 398.   0.
   0. 440. 434. 413. 400. 375. 360. 350. 343. 322. 329. 337. 353. 365. 371. 376. 383. 393. 390. 394. 399. 406. 412. 434.   0.
   0. 444. 435. 419. 401. 381. 361. 350. 340. 321. 329. 337. 353. 365. 371. 378. 388. 396. 401. 397. 378. 405. 412. 405.   2.
   0. 440. 434. 413. 400. 375. 369. 347. 338. 319. 327. 334. 350. 362. 369. 375. 379. 358. 357. 391. 375. 402. 438. 403.   0.
   0. 432. 431. 415. 398. 378. 358. 347. 336. 316. 325. 331. 347. 359. 366. 371. 371. 377. 372. 382. 391. 390. 433. 393.   0.
   0. 419. 428. 410. 394. 374. 364. 353. 332. 311. 321. 326. 342. 353. 361. 365. 365. 364. 372. 375. 355. 391. 393. 367.   0.
   0. 369. 420. 409. 388. 379. 367. 347. 327. 306. 315. 320. 336. 347. 355. 359. 359. 353. 366. 374. 377. 383. 380. 315.   0.
   0. 319. 423. 403. 392. 373. 360. 343. 317. 291. 297. 304. 318. 329. 334. 340. 344. 349. 357. 365. 367. 370. 354. 263.   0.
   0.   0. 353. 389. 379. 364. 352. 335. 305. 275. 293. 267. 300. 310. 318. 321. 330. 339. 346. 352. 354. 349. 291.   0.   0.
   0.   0. 303. 359. 360. 353. 335. 324. 295. 290. 265. 277. 289. 299. 308. 313. 317. 325. 330. 336. 344. 304. 278.   0.   0.
   0.   0.   0. 324. 341. 343. 339. 325. 314. 286. 259. 265. 272. 281. 289. 296. 303. 307. 309. 307. 280. 259.   0.   0.   0.
   0.   0.   0.   0. 314. 310. 323. 323. 313. 288. 266. 253. 249. 257. 264. 270. 277. 280. 275. 249. 226.   0.   0.   0.   0.
   0.   0.   0.   0.   0. 277. 250. 276. 279. 275. 259. 237. 201. 213. 230. 236. 237. 226. 199. 191.   0.   0.   0.   0.   0.
   0.   0.   0.   0.   0.   0. 177. 220. 199. 216. 222. 206. 167. 161. 171. 165. 142. 172. 103.   0.   0.   0.   0.   0.   0.
   0.   0.   0.   0.   0.   0.   0.   0. 119. 157. 135. 175. 127. 109. 112.  94.  47.   0.   0.   0.   0.   0.   0.   0.   0.
AS= 115.65905     AE=-131.31023     DE=  -8.22438
SUBSOLAR LONGIT=   4.12DEGREES
SOIL              CONDUCTIVITY=0.00200000JOULES/SEC-CM-DEG K
SPECIFIC HEAT=0.83700JOULES/GM-DEG K
DENSITY=1.50GM/CC
DIELECTRIC CONSTANT=2.5000
LOSS TANGENT=0.005
WAVELENGTH=   6.00CM
```

```
POLARIZED TEMPERATURE DISTRIBUTION

   0.   0.   0.   0.   0.   0.   0.   0. 190. 208. 238. 259. 276. 289. 293. 276. 207.   0.   0.   0.   0.   0.   0.   0.   0.
   0.   0.   0.   0.   0.   0. 205. 263. 241. 245. 270. 268. 304. 315. 320. 309. 275. 337. 224.   0.   0.   0.   0.   0.   0.
   0.   0.   0.   0.   0. 293. 274. 247. 292. 287. 302. 317. 332. 341. 347. 347. 343. 332. 236. 281.   0.   0.   0.   0.   0.
   0.   0.   0.   0. 286. 311. 323. 315. 286. 258. 321. 332. 343. 351. 356. 355. 355. 357. 348. 316. 282.   0.   0.   0.   0.
   0.   0.   0. 279. 311. 323. 325. 304. 284. 305. 327. 338. 349. 351. 352. 357. 361. 363. 361. 351. 315. 268.   0.   0.   0.
   0.   0. 210. 304. 336. 331. 304. 287. 309. 318. 331. 337. 342. 343. 352. 353. 356. 364. 364. 363. 348. 301. 197.   0.   0.
   0.   0. 261. 329. 335. 331. 313. 291. 311. 331. 332. 333. 333. 344. 353. 353. 360. 367. 364. 367. 353. 333. 251.   0.   0.
   0. 187. 312. 339. 342. 335. 328. 318. 322. 326. 331. 335. 344. 355. 360. 364. 366. 368. 370. 370. 363. 347. 335. 180.   0.
   0. 239. 329. 340. 332. 346. 343. 346. 335. 320. 330. 338. 355. 366. 372. 376. 373. 369. 372. 370. 364. 354. 325. 225.   0.
   0. 291. 343. 350. 349. 348. 351. 347. 334. 320. 330. 338. 355. 366. 372. 376. 373. 369. 369. 367. 365. 355. 334. 270.   0.
   0. 313. 355. 366. 366. 357. 345. 341. 335. 320. 329. 338. 355. 367. 371. 377. 373. 373. 365. 367. 366. 357. 339. 289.   0.
   0. 323. 359. 365. 367. 357. 346. 341. 334. 319. 328. 337. 354. 365. 370. 375. 377. 380. 375. 371. 365. 357. 340. 296.   0.
   1. 326. 360. 369. 367. 358. 346. 341. 334. 329. 328. 336. 353. 364. 370. 374. 381. 383. 385. 376. 365. 357. 343. 298.   1.
   0. 323. 359. 368. 367. 357. 346. 340. 333. 316. 327. 334. 351. 362. 368. 372. 374. 378. 371. 365. 362. 354. 337. 293.   0.
   0. 313. 355. 356. 356. 357. 345. 349. 332. 314. 325. 332. 349. 360. 366. 369. 366. 368. 359. 360. 359. 351. 332. 281.   0.
   0. 298. 333. 362. 363. 355. 351. 347. 329. 311. 322. 329. 345. 356. 363. 365. 362. 359. 360. 356. 355. 345. 324. 261.   0.
   0. 251. 345. 363. 360. 352. 353. 346. 327. 308. 314. 325. 341. 352. 354. 361. 358. 354. 357. 357. 350. 340. 312. 214.   0.
   0. 204. 329. 359. 367. 365. 355. 343. 320. 296. 304. 312. 327. 337. 342. 346. 348. 349. 351. 352. 345. 330. 263. 167.   0.
   0.   0. 262. 350. 359. 360. 352. 343. 313. 284. 294. 299. 313. 323. 330. 332. 338. 344. 346. 345. 336. 313. 232.   0.   0.
   0.   0. 235. 326. 355. 358. 346. 336. 308. 295. 280. 294. 307. 317. 327. 329. 332. 337. 337. 336. 323. 276. 176.   0.   0.
   0.   0.   0. 302. 341. 354. 353. 343. 338. 311. 282. 290. 297. 306. 315. 321. 327. 328. 326. 318. 283. 239.   0.   0.   0.
   0.   0.   0.   0. 326. 342. 359. 362. 353. 326. 302. 293. 283. 292. 300. 305. 312. 314. 306. 274. 237.   0.   0.   0.   0.
   0.   0.   0.   0.   0. 330. 313. 339. 340. 333. 314. 287. 251. 254. 278. 286. 288. 277. 236. 230.   0.   0.   0.   0.   0.
   0.   0.   0.   0.   0.   0. 267. 314. 293. 304. 306. 281. 227. 223. 236. 232. 238. 243. 166.   0.   0.   0.   0.   0.   0.
   0.   0.   0.   0.   0.   0.   0.   0. 246. 275. 298. 275. 203. 182. 194. 174. 128.   0.   0.   0.   0.   0.   0.   0.   0.
AS= 115.65905     AE=-131.31023     DE=  -6.22436
SUBSOLAR LONGIT=   4.12DEGREES
SOIL              CONDUCTIVITY=0.00200000JOULES/SEC-CM-DEG K
SPECIFIC HEAT=0.83700JOULES/GM-DEG K
DENSITY=1.50GM/CC
DIELECTRIC CONSTANT=2.5000
LOSS TANGENT=0.005
WAVELENGTH=   6.00CM
```

Fig. 11: Computed brightness temperature maps of Mercury in orthogonal polarizations for $\varepsilon = 2.5$. These maps refer to the appearance of the planet at a wavelength of observation of $\lambda = 6$ cm, on 1/8/71. Above, parallel polarization; below, perpendicular polarization.

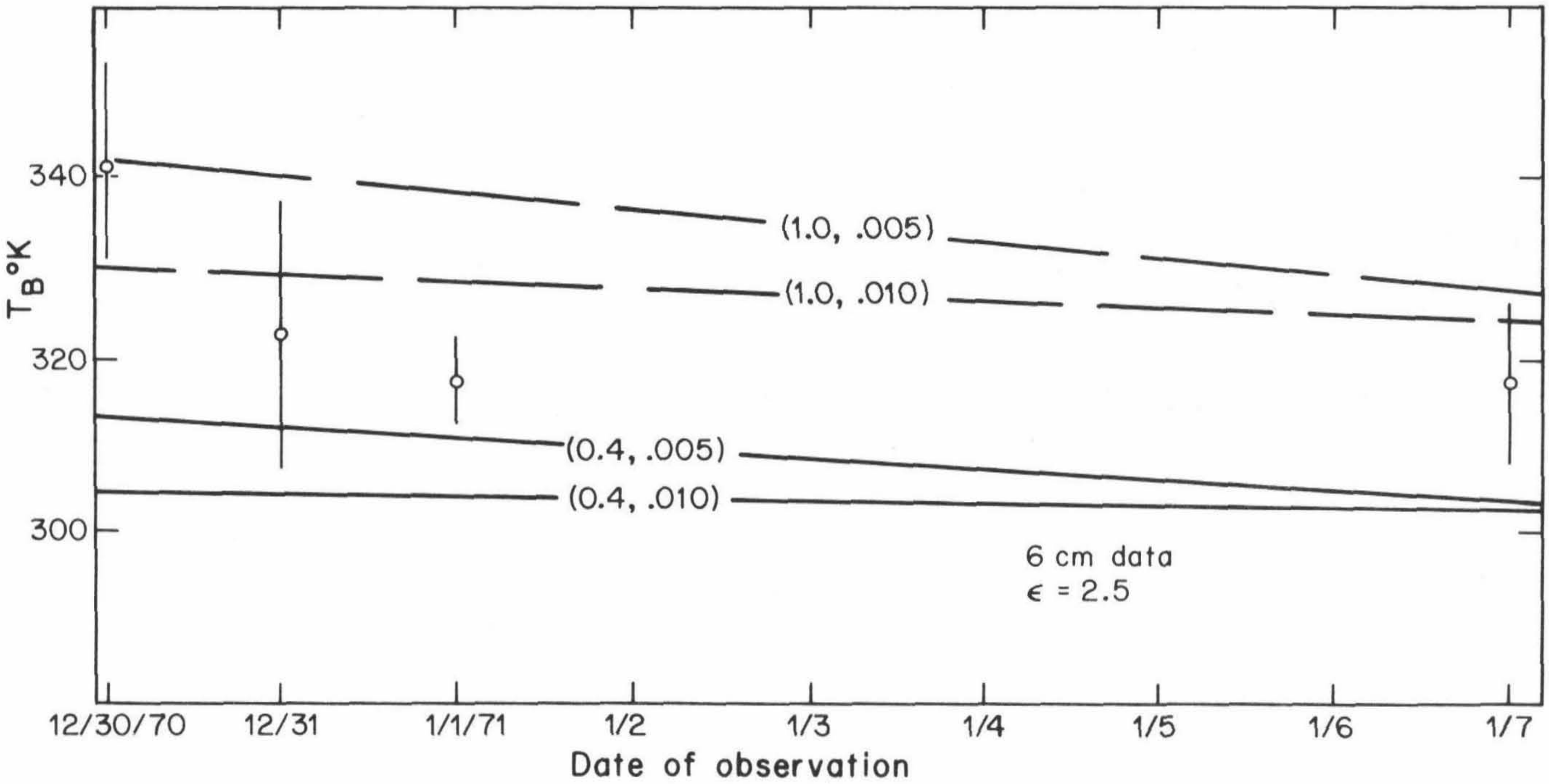

Fig. 12: Disk-average observations of the brightness temperature of Mercury at a wavelength of 6 cm. Curves shown are model-generated results, for electrical loss tangent=$\tan\Delta$=.005, .010. Solid curves: χ=.4. Dashed curves: χ= 1.0.

observed increase in radar reflectivity with wavelength for the Moon. The apparent increase in the reflectivity, although perhaps due in part to greater smoothness on the scale of a wavelength, may be interpreted as an increase in the normal reflection coefficient with depth of ~ 50% (from ~ 7% to ~ 10%). Using this relation and the value of ϵ determined for Mercury by the 3.71 cm data, one may compute the dielectric constant to be expected at $\lambda = 18$cm <u>if</u> the density gradient in the subsurface of Mercury is similar to that for the Moon. Denoting by R and E the reflection and emission coefficients ,

$$\frac{R_{18}}{R_{3.7}} = \frac{.10}{.07} \quad ; \quad \frac{E_{18}}{E_{3.7}} = \frac{.90}{.93} \quad \text{(Moon)}$$

for $\epsilon = 2.4$ (Mercury)

$$E_{3.7} = 1 - \left[\frac{1-\sqrt{\epsilon}}{1+\sqrt{\epsilon}}\right]^2 = .9494 \quad \text{(Mercury)}$$

giving $E_{18} = .92$

and consequently $\epsilon \sim 3.2$ for the emissivity and dielectric constant of Mercury at $\lambda = 18$ cm.

A small increase in $\tan\Delta$ is also to be expected. Empirically, the relation $\tan\Delta / \rho$ is found to be constant over geological materials. Using the relation

$$\rho = \frac{\sqrt{\epsilon} - 1}{a}$$

earlier defined, we find for $a = 0.5$

$$\epsilon = 2.5, \ \rho = 1.12 \text{ gm cm}^{-3}$$

$$\epsilon = 3.2, \ \rho = 1.40 \text{ gm cm}^{-3} \ .$$

Thus we might expect the material at depth ~ 250 cm to be described by $\epsilon = 3.2$, $\tan\Delta = .009$.

Results shown in fig. 13 indicate that the data refer to a material somewhat less dense than expected from rigorous use of the lunar analogy, and

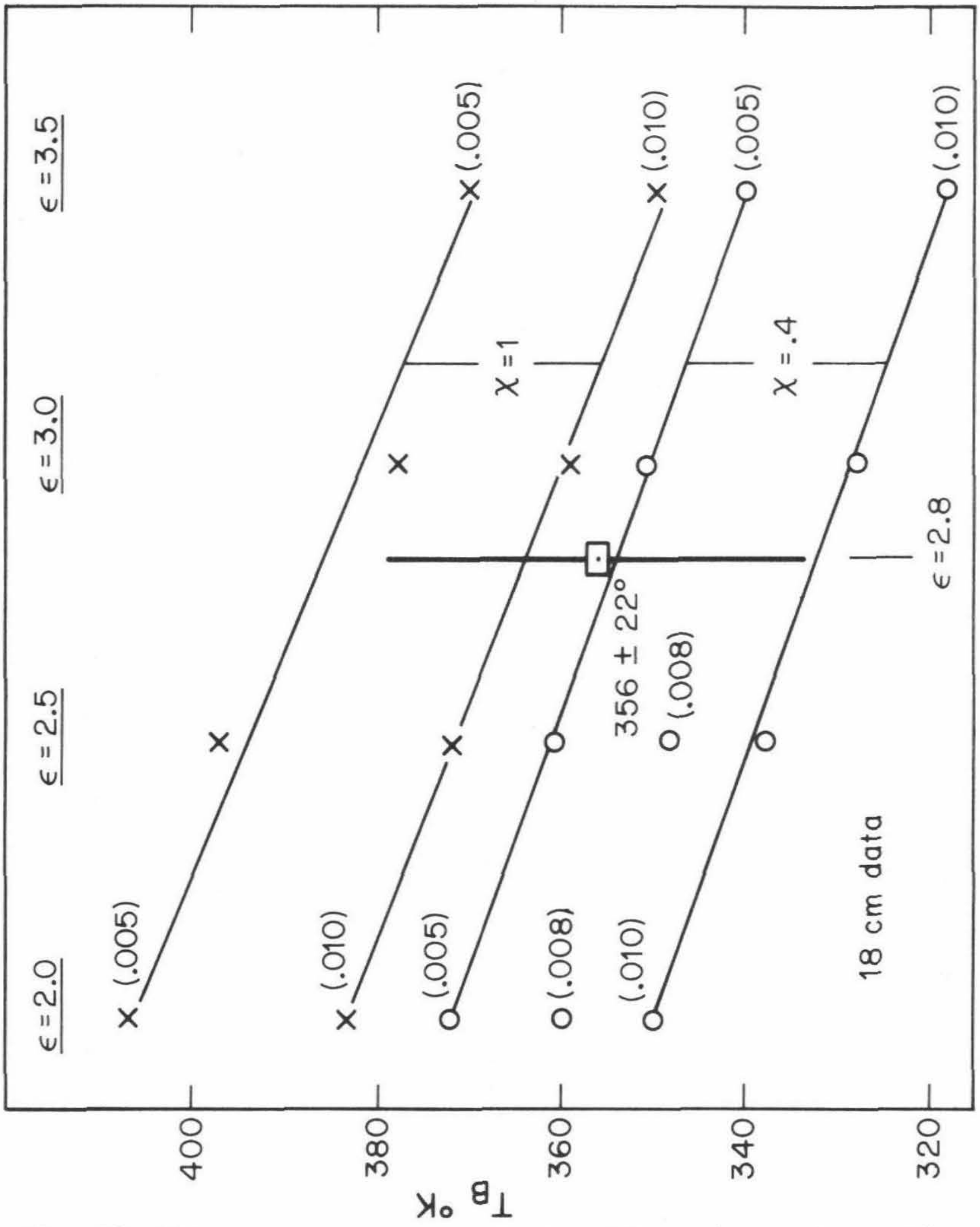

Fig. 13: Disk-average measurement at λ = 18 cm shown along with predicted values of observed brightness temperature for various values of χ, ε, and tan Δ for the date of observation (4/15/71). Values of brightness temperature shown by (x) are for χ = 1.0, and values shown by (o) are for χ = 0.4. The points are further labeled by the loss tangent and dielectric constant used in their calculation.

perhaps better described by

$$\epsilon = 3.0$$

$$\tan\Delta = .008$$

$$0.4 < \chi < 1.0.$$

Owing to the somewhat larger dielectric constant and density found typical of the upper layers of the Mercurian subsurface than for the Moon, this apparently more gradual increase with depth should perhaps not come as a surprise. The discrepancy with lunar values is, however, not large and indicates a similarly well-mixed subsurface on Mercury to a depth of at least several meters. Further support is given to the range for χ of $0.4 < \chi < 1.0$, and it may be seen again that a loss tangent greater than $\sim .020$ is not likely.

Maps of surface and apparent brightness temperatures are shown in figs. 14 and 15.

5.4: Comparison of data at millimeter wavelengths

Previously published data will now be discussed. It was mentioned that a discrepancy has arisen between the millimeter observations of the Aerospace Corporation group (see, e.g., Epstein et al., 1970) and Ulich et al. (1972). Particularly disturbing was the conclusion of Ulich et al. about the mean temperature at λ =3.1 mm determined by a simple periodic fit to their phase data (see fig. 16). The graphs are the predictions of the models of Morrison for χ =1.0 (upper) and χ =0.0 (lower). Sources of the data are shown in Table IV. The maintenance of such a high and constant mean temperature

```
THE MATRIX OF SURFACE KINETIC TEMPERATURES

  0.  0.  0.  0.  0.  0.  0.  0.  0.  0.  0.  0. 85.  0.  0.  0.  0.  0.  0.  0.  0.  0.  0.  0.  0.
  0.  0.  0.  0.  0.  0.  0.  0. 89. 89. 88. 87. 87. 86. 85. 82. 79.  0.  0.  0.  0.  0.  0.  0.  0.
  0.  0.  0.  0.  0.  0. 91. 90. 90. 89. 89. 88. 88. 87. 87. 86. 86. 84. 77.  0.  0.  0.  0.  0.  0.
  0.  0.  0.  0.  0. 90. 90. 90. 90. 90. 90. 89. 89. 89. 88. 90. 91. 90. 82. 78.  0.  0.  0.  0.  0.
  0.  0.  0.  0. 91. 91. 90. 90. 90. 90. 90. 90. 89. 91. 92. 92. 93. 90. 86. 82.112.  0.  0.  0.  0.
  0.  0.  0. 91. 91. 91. 91. 91. 91. 91. 91. 90. 90. 92. 94. 93. 92. 90. 88. 85. 82. 79.  0.  0.  0.
  0.  0. 93. 91. 91. 91. 91. 91. 91. 91. 91. 90. 90. 92. 93. 94. 91. 87. 86. 86. 84. 81.229.  0.  0.
  0.  0. 91. 91. 91. 91. 91. 91. 91. 91. 91. 92. 92. 93. 94. 94. 91. 88. 87. 86. 85. 83. 81.  0.  0.
  0. 92. 91. 91. 91. 91. 91. 91. 91. 91. 92. 93. 95. 95. 94. 95. 91. 88. 87. 87. 87. 85. 82.242.  0.
  0. 91. 91. 91. 91. 91. 91. 91. 91. 91. 92. 93. 95. 93. 92. 92. 90. 88. 87. 87. 86. 84.107.238.  0.
  0. 90. 90. 91. 91. 91. 91. 91. 91. 91. 92. 93. 95. 92. 91. 89. 88. 88. 88. 86. 85. 83. 82.230.  0.
  0. 90. 90. 90. 91. 91. 91. 91. 91. 91. 92. 93. 95. 92. 91. 89. 89. 88. 88. 87. 85. 84. 82.234.  0.
 92. 89. 90. 90. 91. 91. 91. 91. 91. 91. 92. 93. 95. 92. 91. 89. 89. 88. 88. 87. 86. 84. 82.237.358.
  0. 89. 89. 90. 90. 90. 90. 91. 91. 93. 92. 94. 95. 92. 91. 89. 89. 88. 88. 87. 86. 84. 82.240.  0.
  0. 88. 88. 89. 90. 90. 89. 91. 92. 95. 94. 95. 95. 92. 91. 89. 89. 88. 88. 87. 86. 84. 83.242.  0.
  0. 88. 88. 89. 89. 89. 89. 89. 92. 94. 94. 93. 92. 90. 90. 88. 88. 87. 87. 87. 86. 84.136.334.  0.
  0. 88. 87. 88. 89. 89. 89. 88. 91. 94. 93. 91. 89. 88. 89. 88. 87. 86. 86. 86. 86. 84.191.374.  0.
  0.  0. 86. 86. 87. 88. 88. 88. 91. 94. 92. 91. 88. 88. 88. 88. 87. 86. 85. 84. 84. 83.245.  0.  0.
  0.  0. 86. 85. 86. 87. 88. 88. 91. 93. 91. 91. 88. 88. 88. 88. 87. 86. 84. 83. 83.137.375.  0.  0.
  0.  0.  0. 83. 83. 85. 88. 90. 90. 89. 89. 88. 87. 87. 87. 87. 86. 85. 84.109.169.272.  0.  0.  0.
  0.  0.  0.  0. 84. 82. 84. 87. 90. 87. 85. 85. 85. 86. 86. 85. 84. 83.117.240.358.  0.  0.  0.  0.
  0.  0.  0.  0.  0. 78. 82. 84. 83. 84. 84. 84. 84. 84. 84. 83. 82. 82.237.405.  0.  0.  0.  0.  0.
  0.  0.  0.  0.  0.  0.177. 85. 81. 80. 82. 82. 83. 81. 81.114.205.266.358.  0.  0.  0.  0.  0.  0.
  0.  0.  0.  0.  0.  0.  0.  0.220. 74. 76. 76. 78. 98.209.306.352.  0.  0.  0.  0.  0.  0.  0.  0.
  0.  0.  0.  0.  0.  0.  0.  0.  0.  0.  0.  0.388.  0.  0.  0.  0.  0.  0.  0.  0.  0.  0.  0.  0.
   0.0   3.8  11.3  18.8  26.3  33.8  41.3  48.8  56.3  63.8  71.3  90.0 120.0 150.0 180.0 210.0 240.0 270.0 300.0 330.0
  97.3 142.7 234.3 301.3 340.3 356.9 365.2 365.6 364.3 363.0 362.3 360.6 360.7 360.8 360.9 360.9 360.9 361.0 361.0 361.0
  8.6 MICRON FLUX=0.1166E-06 MICROWATTS/(SQ CM  MICRON)
 11.8 MICRON FLUX=0.9562E-07 MICROWATTS/(SQ CM  MICRON)
  DISK TEMP AT 20.0 MICRONS=133.92   FLUX=0.2349E-12
```

Fig. 14: Computed map of surface physical temperatures on Mercury as seen from Earth on 4/15/71. Celestial north is at the top of the map.

```
POLARIZED TEMPERATURE DISTRIBUTION

   0.   0.   0.   0.   0.   0.   0.   0.  61. 145. 163. 188. 156. 172. 157. 116.  11.   0.   0.   0.   0.   0.   0.   0.   0.
   0.   0.   0.   0.   0.   0. 115. 227. 176. 223. 237. 248. 251. 238. 225. 155. 142. 133.  71.   0.   0.   0.   0.   0.   0.
   0.   0.   0.   0.   0. 203. 213. 271. 291. 301. 311. 308. 306. 304. 301. 282. 273. 235. 166. 143.   0.   0.   0.   0.   0.
   0.   0.   0.   0. 232. 272. 311. 315. 333. 346. 354. 346. 341. 344. 347. 337. 320. 257. 261. 220. 166.   0.   0.   0.   0.
   0.   0.   0. 263. 293. 341. 350. 358. 362. 369. 376. 374. 371. 367. 362. 360. 357. 344. 322. 297. 240. 222.   0.   0.   0.
   0.   0. 210. 311. 354. 373. 362. 366. 368. 367. 369. 390. 351. 386. 381. 376. 377. 372. 364. 345. 314. 273. 157.   0.   0.
   0.   0. 279. 355. 392. 391. 358. 404. 401. 357. 400. 399. 403. 355. 356. 356. 387. 378. 374. 270. 353. 224. 241.   0.   0.
   0. 245. 348. 390. 351. 400. 405. 411. 410. 409. 409. 410. 412. 408. 407. 406. 358. 351. 388. 365. 370. 353. 335. 224.   0.
   0. 291. 372. 394. 405. 409. 411. 416. 418. 420. 420. 419. 419. 415. 416. 415. 407. 403. 400. 397. 401. 378. 358. 265.   0.
   0. 337. 384. 403. 412. 416. 417. 418. 420. 423. 423. 422. 423. 420. 420. 419. 412. 404. 403. 402. 396. 388. 365. 314.   0.
   0. 365. 353. 404. 413. 418. 422. 421. 422. 426. 425. 425. 426. 423. 422. 422. 415. 414. 411. 401. 350. 382. 373. 336.   0.
   0. 366. 351. 402. 412. 416. 420. 419. 421. 426. 425. 426. 427. 424. 424. 427. 418. 418. 418. 406. 356. 385. 380. 345.   0.
   2. 353. 388. 393. 409. 413. 418. 419. 420. 426. 425. 426. 428. 425. 425. 425. 420. 415. 415. 410. 402. 394. 386. 357.   2.
   0. 355. 375. 395. 411. 413. 416. 417. 417. 423. 424. 423. 426. 424. 424. 424. 420. 415. 420. 412. 404. 351. 388. 355.   0.
   0. 342. 365. 351. 412. 412. 413. 415. 415. 419. 421. 421. 424. 422. 422. 422. 419. 419. 415. 412. 406. 358. 366. 357.   0.
   0. 307. 358. 384. 402. 402. 405. 401. 406. 412. 416. 414. 417. 413. 416. 412. 405. 405. 405. 406. 405. 358. 377. 330.   0.
   0. 257. 335. 367. 350. 393. 388. 351. 358. 405. 408. 406. 409. 404. 406. 401. 397. 393. 355. 399. 402. 388. 383. 267.   0.
   0. 207. 258. 337. 358. 372. 375. 387. 380. 394. 355. 356. 400. 358. 358. 358. 392. 386. 384. 381. 377. 370. 340. 244.   0.
   0.   0. 222. 303. 336. 356. 369. 381. 381. 381. 381. 385. 391. 391. 390. 392. 385. 378. 376. 362. 361. 345. 275.   0.   0.
   0.   0. 158. 243. 266. 274. 350. 364. 363. 362. 362. 367. 372. 375. 360. 376. 373. 365. 356. 346. 332. 300. 210.   0.   0.
   0.   0.   0. 183. 217. 273. 257. 321. 336. 337. 338. 342. 346. 352. 358. 351. 344. 328. 326. 309. 276. 251.   0.   0.   0.
   0.   0.   0.   0. 143. 189. 252. 265. 290. 309. 319. 319. 319. 321. 322. 318. 312. 307. 284. 244. 220.   0.   0.   0.   0.
   0.   0.   0.   0.   0. 105. 138. 156. 242. 247. 272. 261. 289. 278. 261. 277. 263. 243. 155. 179.   0.   0.   0.   0.   0.
   0.   0.   0.   0.   0.   0.  24. 127. 123. 168. 192. 214. 221. 225. 216. 157. 162. 135. 106.   0.   0.   0.   0.   0.   0.
   0.   0.   0.   0.   0.   0.   0.   0.   4.  89. 112. 147. 153. 172. 151. 117.  61.   0.   0.   0.   0.   0.   0.   0.   0.
AS= 153.22161      AE=  -5.65043      DE=  -4.67837
SUBSOLAR LONGIT=  18.50DEGREES
SOIL                    CONDUCTIVITY=0.002000JOULES/SEC-CM-DEG K
SPECIFIC HEAT=0.83700JOULES/GM-DEG K
DENSITY=1.50GM/CC
DIELECTRIC CONSTANT=3.0000
LOSS TANGENT=0.010
WAVELENGTH= 18.00CM
```

```
POLARIZED TEMPERATURE DISTRIBUTION

   0.   0.   0.   0.   0.   0.   0.   0. 154. 255. 309. 341. 350. 314. 300. 248. 106.   0.   0.   0.   0.   0.   0.   0.   0.
   0.   0.   0.   0.   0.   0. 204. 333. 283. 340. 353. 367. 370. 351. 342. 304. 228. 283. 137.   0.   0.   0.   0.   0.   0.
   0.   0.   0.   0.   0. 256. 280. 349. 372. 385. 357. 353. 390. 388. 384. 360. 350. 303. 218. 184.   0.   0.   0.   0.   0.
   0.   0.   0.   0. 246. 306. 358. 365. 368. 405. 416. 410. 402. 406. 408. 395. 372. 343. 255. 247. 179.   0.   0.   0.   0.
   0.   0.   0. 232. 253. 358. 375. 350. 399. 410. 420. 418. 416. 411. 405. 400. 394. 335. 344. 310. 240. 203.   0.   0.   0.
   0.   0. 152. 276. 340. 373. 393. 404. 412. 414. 419. 422. 423. 417. 410. 402. 400. 350. 374. 345. 301. 243. 114.   0.   0.
   0.   0. 211. 314. 357. 381. 399. 412. 414. 414. 420. 421. 425. 420. 416. 413. 400. 386. 374. 360. 329. 283. 183.   0.   0.
   0. 143. 270. 329. 359. 382. 358. 411. 415. 419. 422. 424. 427. 422. 415. 416. 404. 391. 381. 367. 340. 305. 252. 130.   0.
   0. 162. 240. 328. 371. 386. 357. 410. 418. 424. 427. 427. 429. 425. 423. 415. 409. 357. 387. 374. 364. 325. 276. 166.   0.
   0. 221. 301. 344. 371. 365. 395. 409. 416. 423. 426. 427. 426. 424. 423. 415. 408. 356. 366. 376. 357. 325. 266. 206.   0.
   0. 244. 308. 344. 370. 369. 402. 408. 416. 423. 425. 427. 424. 425. 422. 415. 408. 402. 392. 372. 349. 325. 292. 226.   0.
   0. 248. 306. 341. 388. 385. 355. 405. 413. 422. 424. 426. 428. 424. 423. 415. 409. 404. 354. 375. 354. 330. 298. 237.   0.
   1. 247. 303. 338. 365. 382. 356. 404. 411. 421. 423. 425. 426. 425. 423. 420. 411. 405. 357. 375. 355. 335. 333. 242.   1.
   0. 240. 257. 338. 367. 382. 395. 403. 405. 418. 422. 423. 427. 424. 422. 415. 411. 405. 358. 381. 361. 337. 304. 243.   0.
   0. 230. 263. 333. 369. 383. 394. 407. 403. 417. 421. 422. 426. 423. 422. 415. 412. 406. 355. 353. 364. 338. 304. 239.   0.
   0. 201. 275. 328. 362. 376. 388. 351. 402. 412. 418. 416. 422. 418. 415. 412. 404. 355. 392. 375. 364. 331. 295. 217.   0.
   0. 160. 252. 315. 355. 371. 376. 385. 358. 407. 415. 414. 418. 413. 413. 405. 397. 387. 382. 376. 365. 331. 264. 179.   0.
   0. 119. 231. 252. 327. 356. 372. 367. 355. 403. 407. 410. 415. 412. 410. 407. 357. 386. 376. 364. 346. 320. 263. 141.   0.
   0.   0. 173. 265. 314. 346. 369. 385. 394. 358. 400. 406. 412. 412. 409. 410. 398. 385. 370. 353. 338. 305. 208.   0.   0.
   0.   0. 115. 216. 274. 324. 360. 341. 385. 389. 390. 356. 403. 406. 405. 403. 355. 382. 368. 346. 318. 267. 153.   0.   0.
   0.   0.   0. 167. 217. 265. 318. 349. 370. 374. 378. 383. 388. 394. 399. 385. 375. 385. 345. 322. 276. 225.   0.   0.   0.
   0.   0.   0.   0. 160. 212. 268. 306. 338. 362. 375. 376. 377. 378. 375. 372. 363. 355. 324. 274. 234.   0.   0.   0.   0.
   0.   0.   0.   0.   0. 139. 182. 253. 310. 315. 347. 359. 368. 354. 358. 354. 337. 313. 257. 226.   0.   0.   0.   0.   0.
   0.   0.   0.   0.   0.   0.  76. 200. 158. 256. 266. 316. 325. 333. 322. 301. 260. 271. 150.   0.   0.   0.   0.   0.   0.
   0.   0.   0.   0.   0.   0.   0.   0.  86. 197. 225. 273. 282. 312. 286. 240. 163.   0.   0.   0.   0.   0.   0.   0.   0.
AS= 153.22161      AE=  -5.65043      DE=  -4.67837
SUBSOLAR LONGIT=  18.50DEGREES
SOIL                    CONDUCTIVITY=0.002000JOULES/SEC-CM-DEG K
SPECIFIC HEAT=0.83700JOULES/GM-DEG K
DENSITY=1.50GM/CC
DIELECTRIC CONSTANT=3.0000
LOSS TANGENT=0.010
WAVELENGTH= 18.00CM
```

Fig. 15: Computed brightness temperature maps of Mercury in orthogonal polarizations for $\epsilon = 3.0$ giving the appearance of the planet as seen from the Earth at $\lambda = 18$ cm on 4/15/71. Above; parallel polarization. Below; perpendicular polarization.

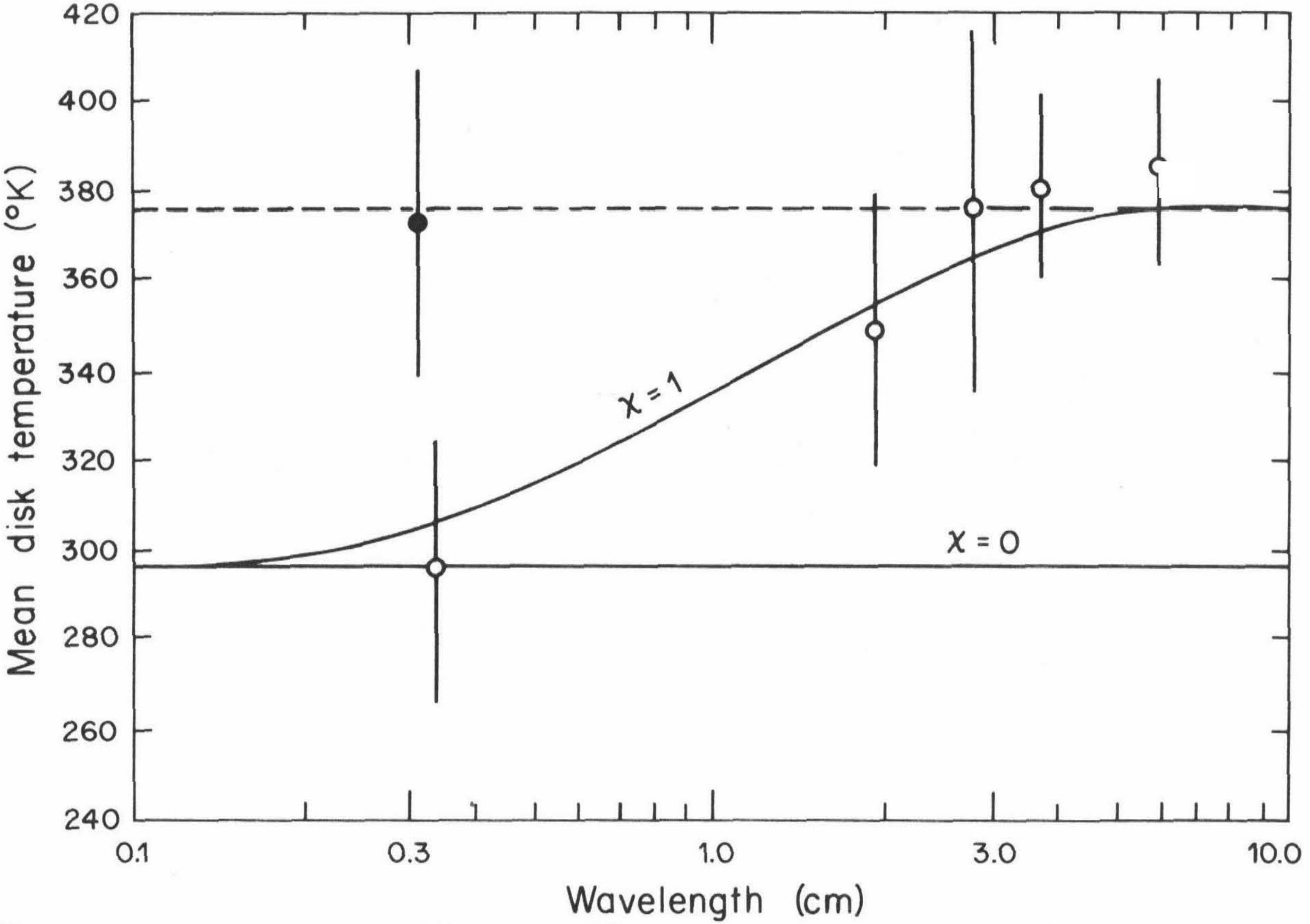

Fig. 16: Disk-average "mean" temperature of Mercury at different wavelengths (from Ulich et al., 1972). The curves are the predictions of the models of Morrison (1969) showing the increase of mean disk temperature with wavelength for $\chi = 1$ and no such increase for $\chi = 0$. The solid circle is the result of Ulich et al..

TABLE IV

REPORTED MEAN TEMPERATURES OF MERCURY

Wavelength (cm)	Mean Temperature (°K)	Reference
0.31	373 ± 35	Ulich et al., (1972)
0.33	296 ± 30	Epstein et al., (1970)
0.80	530 ± 159	*Golovkov and Losovskii (1968)
1.95	288 ± 30	**Kaftan-Kassim and Kellermann (1967)
1.95	350 ± 30	Morrison and Klein (1970)
2.82	375 ± 40	Medd (1968)***
3.75	380 ± 20	Klein (1968)
6.00	385 ± 20	Morrison and Klein (1970)

* Data rejected on apparent calibration error

** Data rejected due to inconsistency with more recent observations using the same equipment.

*** Datum quoted by Morrison and Klein (1970) with wavelength or depth is incompatible with any lunar-like conception of the upper few centimeters of Mercury's subsurface and currently accepted values of its Albedo and infrared emissivity. The difficulty appears to have been resolved, however. Model fits of the data of Ulich et al. and of Epstein et al. , chosen to be at similar phase angles, are shown in figures 17 and 18. Although measurements at millimeter wavelengths are only slightly sensitive to the value of χ , it may be seen that the data of Ulich et al. are matched quite satisfactorily with the parameter set determined from the previously presented data. The data of Epstein et al. are seen to be consistent with a higher value of ϵ ($\epsilon \sim 3.5$). As the possibility of a higher dielectric constant closer to the surface than that found to be typical of material at the greater depths observed at 6.0 and 3.71 cm is not in accord with simple concepts of mixing of material or with the lunar analogy, we believe that the data of Ulich et al. are more consistent with likely conditions in the top few centimeters of the Mercurian subsurface ($\epsilon = 2.4$, $\tan\Delta = .0075$, and $0.4 < \chi < 1.0$). Needless to say, although the data of Ulich et al. are consistent with models characterized by $0.4 < \chi < 1.0$, their interpretation of the mean temperature on the basis of such limited phase coverage in the light of the highly non-sinusoidal nature of the 3 mm phase curve must be regarded as premature. The interpretation of Ulich et al. of the fitted mean of their measurements as a true planetary mean temperature was also biased by the fact that their observations happened to fall mainly on "hot" longitudes.

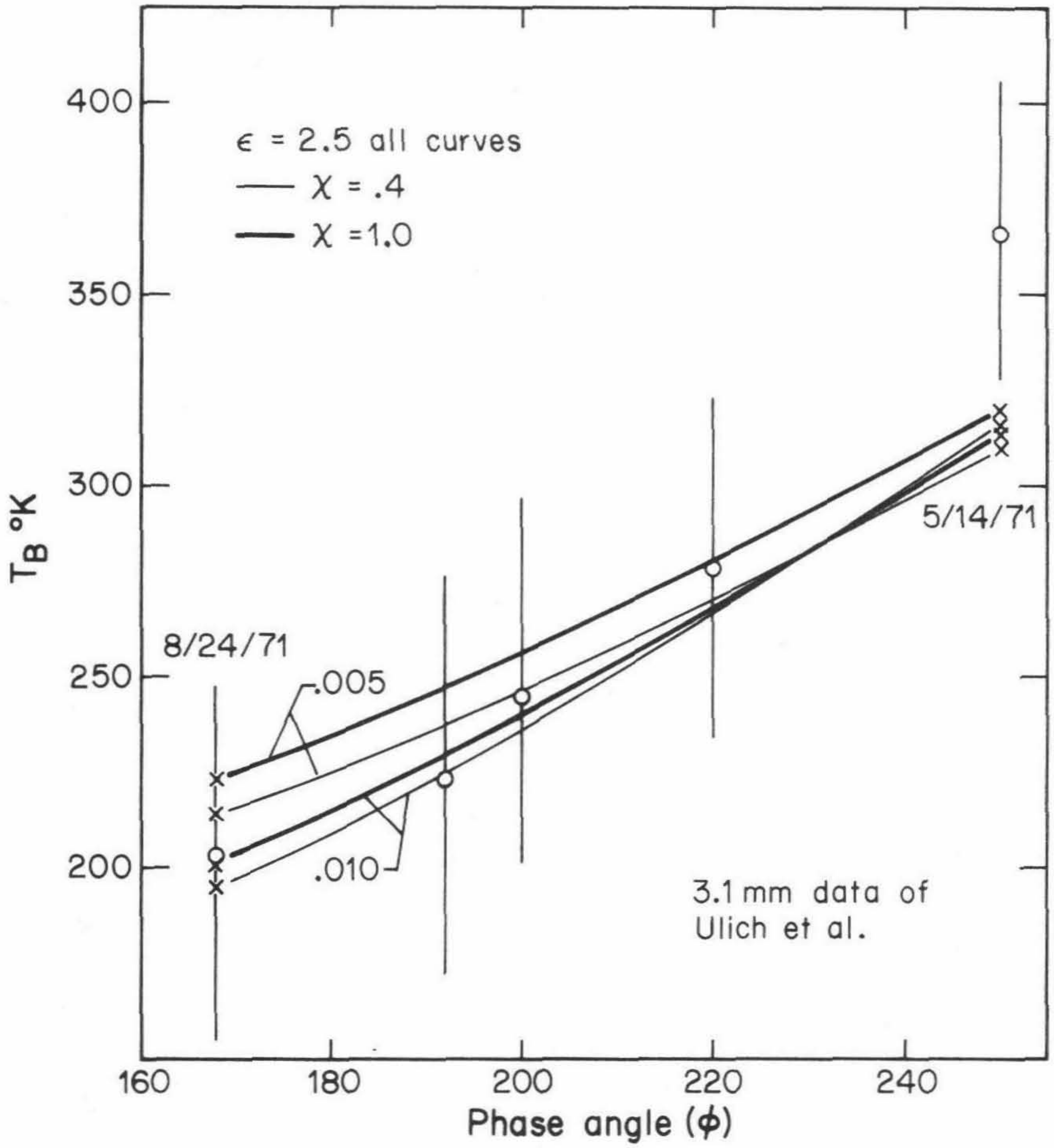

Fig. 17: Disk-average brightness temperature of Mercury at $\lambda = .31$ cm. Model predicted values are shown as smooth curves for various values of χ, ε, and $\tan\Delta$. The data, which do not represent a sequence in time, are shown as a function of phase angle

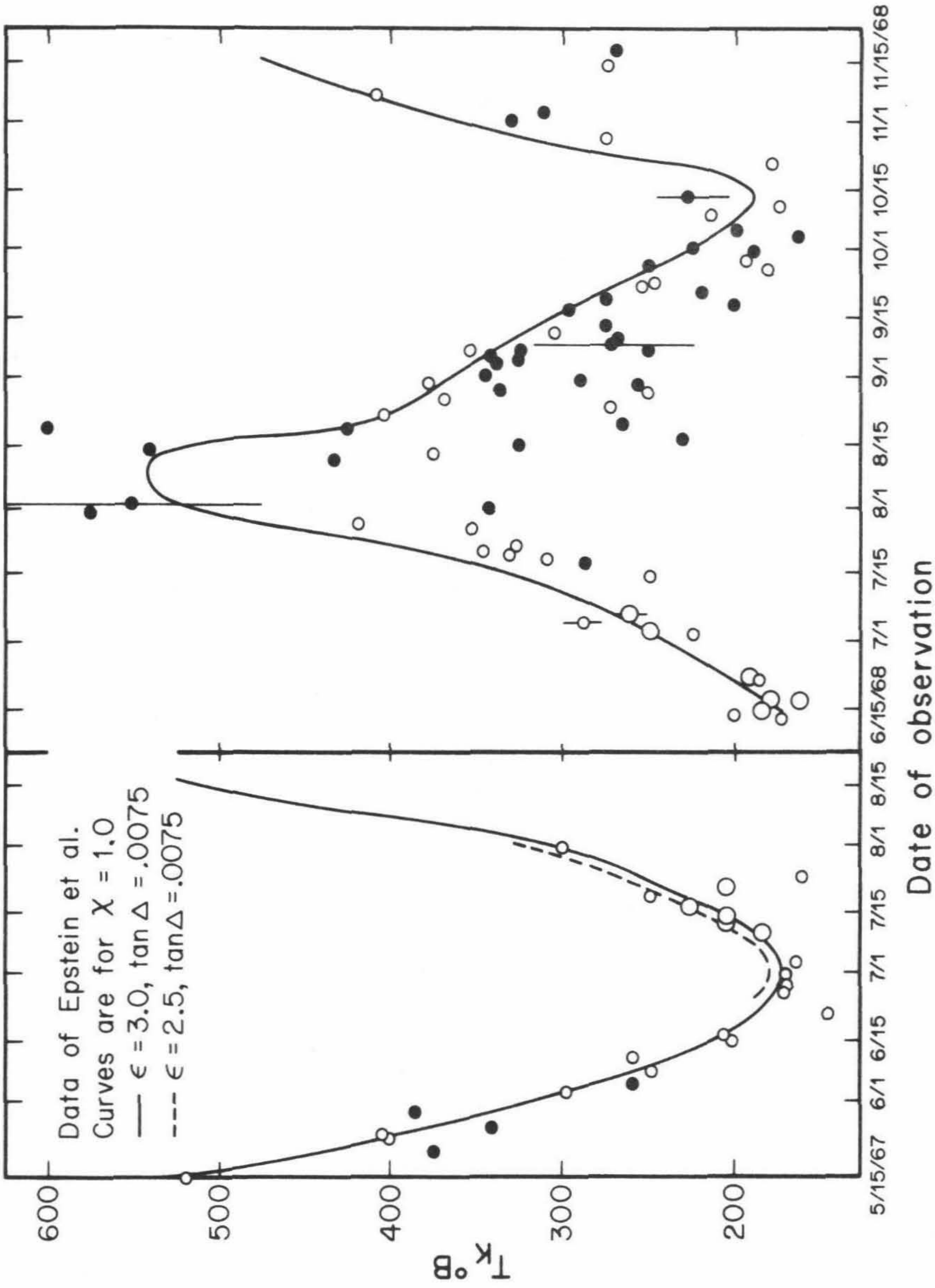

Fig. 18: Comparison of model-predicted observed brightness temperatures at $\lambda = .33$ cm with the data of Epstein et al. (1970). Errors typical of the various symbols (small open circles, large open circles, solid circles) are shown.

5.5: Data at 3.75 cm and a discussion of absolute calibration

The previously mentioned parameter determinations are primarily based on disk-average data at 3.1 mm, 6 cm, and 18 cm using a value of the surface dielectric constant that is well determined by the method of differencing the polarized visibility function data, and are weakly supported by the fitting of the detailed visibility functions. This weakness, and the strength of the dielectric constant determination, will be discussed in the next section. The strength attached to the measurements at .31, 6, and 18 cm is due to the relatively high confidence one may place on the validity of the flux density scale at these wavelengths.

In particular, investigations at 21 cm comprise the bulk of radio-astronomical work up to the present time. It is felt that the great amount of work spent in determining the flux scale at this wavelength and the relative abundance of celestial sources suitable for calibration purposes argue for a rather high level of accuracy in calibration. As little error is accrued in interpolation of normal source spectra to the nearby wavelength of 18 cm, it is felt that the flux density calibration scale that was used at 18 cm shares in this validity.

Investigations at 6 cm have been another extensive set. Two major surveys at 6 cm (Shimmins and Bolton, 1972; Pauliny-Toth and Kellerman, 1968) have been undertaken at this wavelength in the last several years. Although the calibration schemes used by these two groups differ slightly due to slightly different corrections for the finite size of the primary calibrator used by both groups (Hydra A), agreement within 3% in the flux scale is seen. The effect of this slight uncertainty on the 6 cm data presented here is shown in fig. 19. The total discrepancy between this flux density scale and absolute is thought to be less than 5% (Shimmins and Bolton, 1972). It is seen that the difference does not produce a significant change with respect to modeled observables, and that this uncertainty does not affect our conclusions.

The measurements at 3.1 mm of Ulich et al. are calibrated in an absolute fashion and are thought to avoid the serious systematic errors which result from the use of relative calibration schemes which have included assumptions of poorly known parameters such as the millimeter brightness temperature of Jupiter, or extrapolation of the radio spectra of what are known to be abnormally behaving nonthermal sources. The spectral shapes of sources that are even visible, not to mention suitable for calibration, at millimeter wavelengths differ widely and are not in general flat or even predictable. Although it is perhaps premature to accept this new flux scale on these arguments alone, the excellent agreement with planetary model calculations described in this part is perhaps less reasonably ascribed to coincidence than to a carefully done calibration. In addition, this work is completely independent of flux measurements at other wavelengths.

Such good agreement over this rather large range of wavelengths appears to put rather good limits on model parameters when combined with

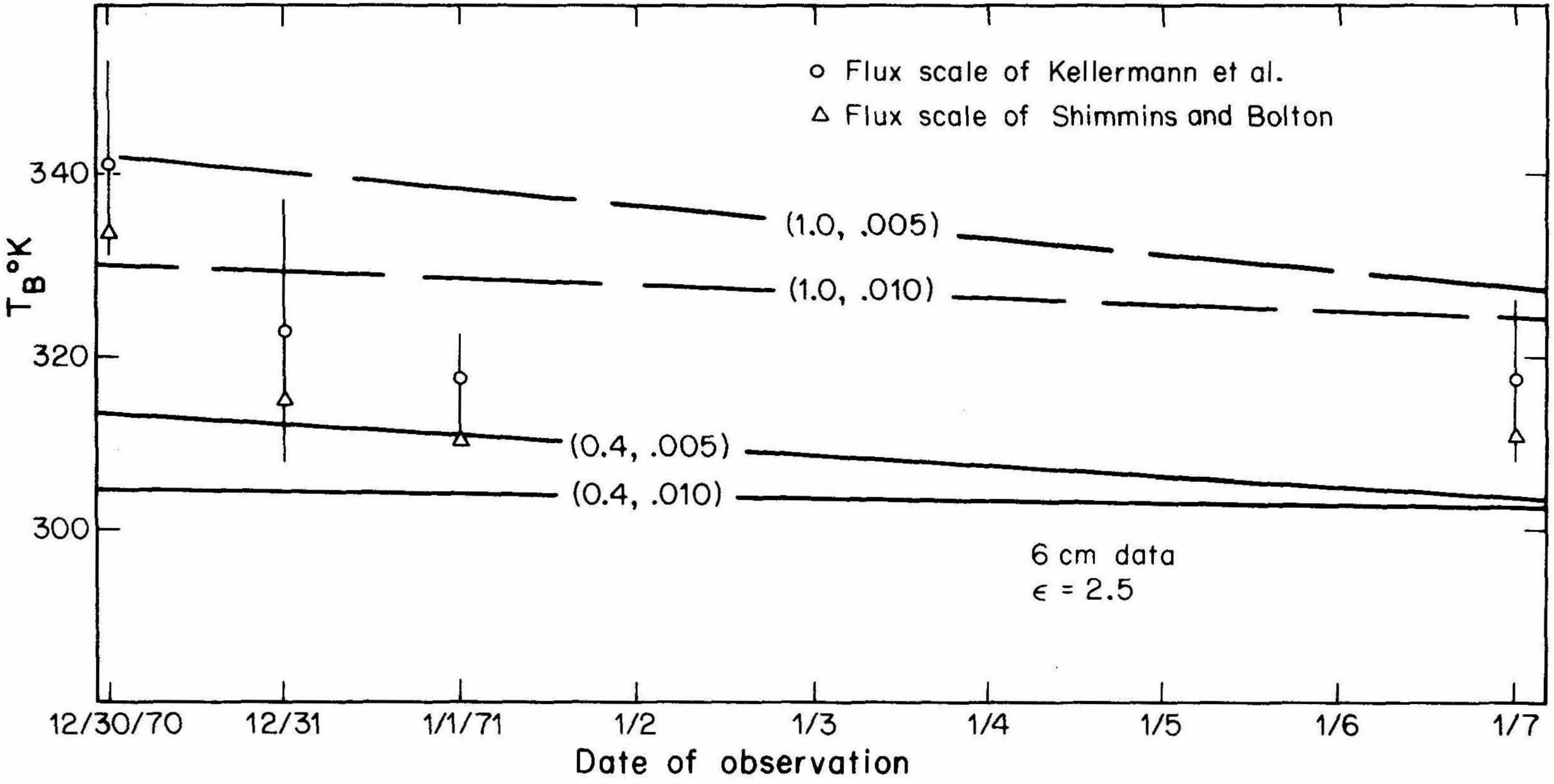

Fig. 19: Variation in the results at 6 cm due to use of alternate flux density scales. This difference is ~ 3%. Model predictions shown by the curves are for $\chi = 1.0$ and $\chi = 0.4$, and are the same as in fig. 12.

interferometric determination of the surface dielectric constant and simple treatment to account for surface roughness. This latter result is, of course, independent of uncertainties in absolute calibration. The final ambiguity in the results may be removed using the phase data of Klein (1968) at 3.75 cm. Utilizing all of his data covering the entire 350 day period of possible variation of disk temperature, Klein has fit a curve of the form

$$T(\varphi) = T_0 + T_1 \cos(\varphi + \psi) + T_2 \cos(2l + \xi)$$

where φ = phase angle

l = planetocentric longitude

and T_0, T_1, ψ, T_2, and ξ are to be determined. The rather large scatter in this early data prevents a more detailed fit than this series expansion, as will be discussed. Using the analytical theory discussed in Part III, Klein obtains a value of $T_0/T_1 = 1.28$, and consequently a value of $\delta = L_e/L_t = 2.6$. Using the relations (derived in Part III and in Appendix IV)

$$L_e = \lambda / 2\pi\sqrt{\epsilon}\tan\Delta$$

$$L_T = \left[\frac{2K_T}{C\rho\Omega}\right]^{\frac{1}{2}}$$

where Ω is the diurnal angular frequency, with the value for $\epsilon = 2.4$ determined earlier and a value for the thermal inertia of

$$\gamma_t = .0014^{+.0021}_{-.0008} ,$$

we obtain for the electrical loss tangent

$$\tan\Delta = .0088^{-.0053}_{+.0066} .$$

These values are independent of calibration error (by ratioing results) and may be used to discard the possible ambiguity of the surface being characterized by a large value of χ (≥ 1.5) combined with a large value of $\tan\Delta$ ($\geq .02$). This ambiguity was permitted due to the fact that all of the previously discussed data were obtained near inferior conjunction. The results are believed to be unambiguous and depend only on the assumption of surface roughness similar to that of the Moon. This is well borne out by radar results at 3.6 and 12.5 cm (Goldstein, 1971; Pettengill, Dyce, and Campbell, 1967; Haystack Observatory Staff, 1971; Hagfors and Evans, 1968). The data are well represented by a subsurface parameterized by

$$\epsilon = 2.4 \pm .3$$

$$\tan\Delta = .0075 \pm .002$$

$$0.4 < \chi < 1.0$$

and are consistent with

$$\rho = 1.0\text{-}1.5 \text{ gm cm}^{-3}$$

$$\gamma = .0014 \text{ cal/cm}^2 \text{deg sec}^{\frac{1}{2}} .$$

The above parameters would be similar to those for the Moon were it placed in the orbit of Mercury. However, when model predictions employing these parameters are compared with the 3.75 cm data of Klein (1968) and the 3.71 cm disk temperature obtained as part of this work, a discrepancy is seen. This is possibly due to uncertainty in the flux density scale at this wavelength and consists of observed brightness temperatures being systematically higher than predicted values.

The original work establishing the calibration scale with a large number of sources at 3.75 cm was that of Dent and Haddock (1966). These data relied on earlier measurements at 9400 MHz (3.2 cm) of Cas A, Tau A, and Cyg A (Stankevitch, 1962; Lazarevskii, Stankevitch, and Troitskii, 1963; Lastochkin, Sorin, and Stankevitch, 1964). Conflicting determinations of the flux density of CasA at 9360 MHz (Allen and Barrett, 1967) were adopted by Scheuer and Williams (1968) and Kellermann, Pauliny-Toth, and Williams (1969). This choice was apparently based on preference of the absolute calibration scheme of Allen and Barrett over the "artificial moon" method (also an absolute calibration method) used by the Russian workers. Subsequent absolute measurements of the flux density of Cas A at frequencies up to 20 GHz (see, e.g., Medd, 1972; Dent, 1972) appear to give a flat spectrum for this source and substantiate the results of Allen and Barrett. The spectrum of Cas A thus seems to be flat at least to 20 GHz. The flux density of Cas A at 8000MHz being thus established, the following correction was typically applied to the original Dent and Haddock results for the flux densities of several compact, non-variable sources unresolved at the long spacings characteristic of interferometric work ($s \sim 1000\lambda - 30{,}000\lambda$). The ratio of the flux density obtained by Allen and Barrett (S_{8000}=629.6 f.u., epoch 1964.4) to the flux density assumed by Dent and Haddock (S_{8000}=587.4 f.u., epoch 1964.4) for Cas A is 1.072. Original flux densities given by Dent and Haddock were multiplied by this factor. These values have been used to calibrate all planetary observations, and several of these values are given in Section 4.3.

More recent results (Aller, 1970) obtained on the same instrument but with higher sensitivity indicate that this correction is systematically high. These results employed the value of Allen and Barrett for Cas A ($S_{8000}=$ 629.6 f.u.; epoch 1964.4). Over all sources included in both of these studies it is found that the original (uncorrected) Dent and Haddock flux densities are 3-4% lower on the average than those of Aller, and not 7% as was expected from the ratio of the primary flux densities used. This is an average, and the real discrepancies vary from source to source from 0-14%. The particular subset of sources which constitutes the flux density scale of the 8085 MHz work presented here is not found to differ significantly between the original Dent and Haddock results and the more recent results of Aller. In other words, the 7% increase which has been applied to the original values of Dent and Haddock appears to give values for the flux densities of these sources which are about 7% too high relative to the more recent results. This systematic difference is not understood at present. Planetary brightness temperatures of Mars and Mercury obtained using the original Dent and Haddock values, corrected upwards by 7%, are shown in Table V.

TABLE V.

Planet	λ_{cm}	T^{obs}	T^{model}	$R = \frac{T^{obs}}{T^{model}}$	Comments
Mars	3.71	211 ± 20°K	197°K	1.07	8/15/71 from V(β) fit.
	3.75	199 ± 4	189	1.05	Avg. over 1965 & 1967 oppositions
Mercury	3.71	345 ± 21	299	1.15	8/15/71 from V(β) fit
	3.75	348 ± 40	299	1.16	Interpolated to correspond to 8/15/71
	3.75	356 ± 25	332	1.05*	Averages over 1/17-4/16/68 (Fig. 20).

3.71 cm data is that reported in this work
3.75 cm data from Klein (1968) and (1971)

All fluxes refer to flux scales of Kellermann, Pauliny-Toth, and Williams (1969) and Dent and Haddock (1966) as corrected upwards by 7%, except where noted.

*5% correction (Klein, 1972)

Also shown for comparison are model-predicted brightness temperatures which employ what is felt to be the best-fitting parameter sets for the two planets as determined from other data with more well-known calibration.

More recent, unpublished measurements by Aller and Olsen (Olsen, 1972) differ from the results of Aller (1970) by up to 10%, although not systematically. The most relevant of these values for the present work is the flux density of P1055 + 01. This source, a variable, was used as calibrator for the Mercury observations reported here. Its flux density was determined to be 3.28 ± .20 f.u. using the calibrator flux densities given in Sec. 4.3

which are the results of Dent and Haddock corrected upwards by 7%. This source was being observed simultaneously by Aller and Olsen in August 1971, and their result was 3.05 ± .21 f.u., with an internal error of ~ $2\frac{1}{2}$% for a two-hour integration. The ratio of the calibrator flux density determined for the resent work (3.28 f.u.) to the flux density measured independently (3.05 f.u.) is 1.07.

The rather large scatter (up to 10%) from source to source between the recent (Olsen, 1972) and previously published (Aller, 1970) results at 8000 MHz, all of which employ the same primary calibrator flux density (S_{8000}(Cas A) = 629.6 f.u. (1964.4)) indicate that a simple correction factor applied to all sources will not yield a satisfactory flux scale. It is believed that the flux density calibration used for the Mercury and Mars observations reported here at 3.71 cm is uncertain to at least 7% and probably high by at least 5%. This appears to be borne out by discrepancies with predicted model results (Table V) and a similar discrepancy with Venus models (Muhleman, 1972b). The large scatter (~10%) from source to source that is seen between the previous, correctly calibrated (Aller, 1970) and more recent, correctly calibrated (Olsen, 1972) results suggests that careful attention will have to be paid to this calibration problem before measurements of the planets near 8000 MHz may be used to improve our knowledge of the properties of these planets to a higher accuracy than has been presented here. Extensive observations at 6 cm would be an important step in our understanding. Klein (1972) has indicated that his Mercury data at 8000 MHz, calibrated mainly against Virgo A (3C274) should be corrected upwards by 5%. His data, including this correction, are shown in Fig. 20 along with model-predicted phase curves.

5.6 Detailed Interferometric Data and Associated Difficulties

The fitting scheme attempted will be described, and difficulties encountered which led to biased and ambiguous results will be discussed. In order to obtain more precise information relative to the details of variations in physical temperature and/or dielectric properties across the face of the planet, it was desired to be able to fit the observed visibility functions to model-predicted functions. It was hoped that the careful modeling of the apparent brightness distribution would allow this. Observable visibility functions were numerically generated by taking the Fourier Transform of computed maps of brightness temperature distribution in two orthogonal polarizations for a given date (8/15/71) shown in Figs. 21 and 22. The collected interferometric data were normalized point by point to this date using the ratio of disk-average temperature computed for the date of observation relative to the trial date (8/15). This is important in order to remove systematic variation of resolved-disk observations due to variation of total flux from day to day. The normalization correction never exceeded 4%. Sums of squares of residuals for the data relative to computed visibility functions were calculated for models employing a large range

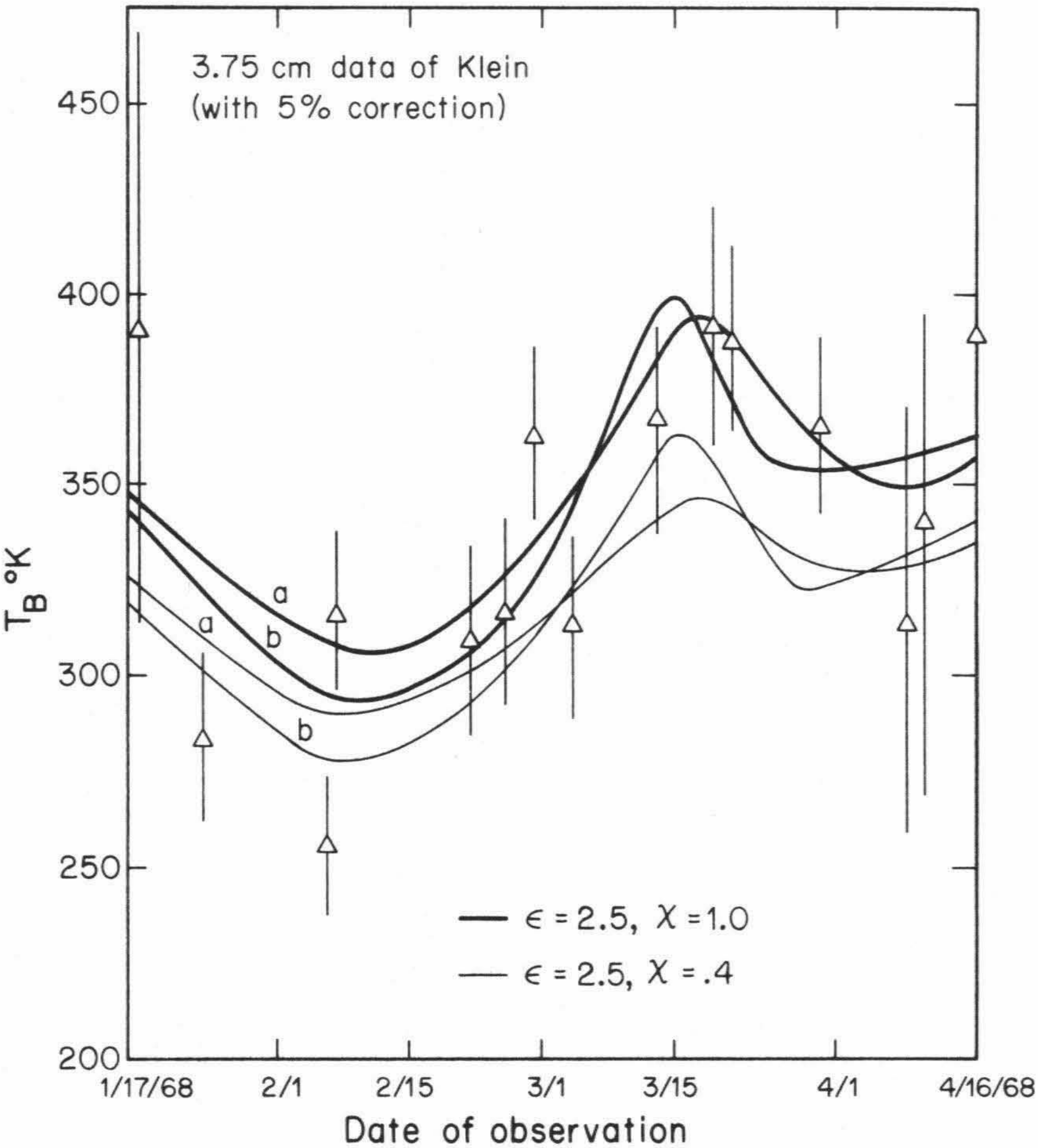

Fig. 20: Comparison of model-predicted observed brightness temperatures as a function of date of observation at a wavelength of $\lambda = 3.75$ cm with the 3.75cm data of Klein (1968) . The data have been corrected upward by 5% to conform to what Klein (1972) feels to be a more accurate calibration. Two sets of curves were generated for two values of χ (0.4 and 1.0). The curves labeled (a) employ $\tan\Delta = .005$ and the curves labeled (b) employ $\tan\Delta = .0075$.

```
THE MATRIX OF SURFACE KINETIC TEMPERATURES

   0.   0.   0.   0.   0.   0.   0.   0.   0.   0.   0.   0. 453.   0.   0.   0.   0.   0.   0.   0.   0.   0.   0.   0.   0.
   0.   0.   0.   0.   0.   0.   0.   0. 321. 269. 273. 310. 364. 370. 392. 442. 476.   0.   0.   0.   0.   0.   0.   0.   0.
   0.   0.   0.   0.   0.   0. 191. 121.  75.  77.  78. 136. 253. 283. 288. 399. 411. 451. 481.   0.   0.   0.   0.   0.   0.
   0.   0.   0.   0.   0.  93.  85.  84.  79.  79.  81.  82.  82.  82.  82. 213. 364. 424. 433. 474.   0.   0.   0.   0.   0.
   0.   0.   0.   0.  97.  90.  89.  84.  79.  80.  82.  82.  83.  83.  84. 218. 352. 362. 386. 420. 486.   0.   0.   0.   0.
   0.   0.   0.  98.  95.  92.  88.  85.  84.  82.  83.  83.  84.  84.  85. 135. 152. 220. 289. 380. 448. 486.   0.   0.   0.
   0.   0. 104.  98.  95.  91.  90.  90.  86.  83.  83.  83.  84.  85.  85.  86.  86.  86. 224. 362. 406. 463. 503.   0.   0.
   0.   0. 101.  99.  96.  92.  91.  90.  87.  83.  83.  84.  84.  85.  86.  86.  86.  86. 225. 364. 407. 451. 470.   0.   0.
   0. 116. 101.  98.  93.  93.  92.  91.  87.  83.  84.  84.  85.  86.  86.  87.  86.  86. 226. 243. 366. 430. 452. 477.   0.
   0. 110. 101.  97.  94.  93.  92.  92.  88.  84.  84.  84.  85.  86.  86.  87.  86.  86. 104. 156. 226. 317. 419. 464.   0.
   0. 103. 101.  93.  95.  94.  92.  91.  88.  84.  86.  85.  85.  86.  86.  87.  87.  86.  86.  86.  86. 226. 366. 429.   0.
   0. 104. 102.  99.  97.  96.  94.  94.  91.  88.  89.  87.  85.  86.  86.  86.  87.  87.  87.  86.  86. 225. 364. 427.   0.
 124. 104. 102. 101.  99.  98.  97.  96.  95.  93.  91.  89.  85.  86.  86.  86.  87.  87.  87.  87.  86. 224. 362. 424. 483.
   0. 105. 103. 101. 100.  98.  97.  96.  95.  93.  91.  89.  85.  86.  86.  86.  87.  87.  87.  86.  86. 224. 362. 421.   0.
   0. 105. 103. 101. 100.  98.  97.  96.  95.  93.  91.  89.  85.  86.  86.  86.  86.  87.  87.  86.  86. 224. 362. 418.   0.
   0. 112. 104. 102. 100.  99.  98.  97.  95.  93.  91.  89.  85.  86.  86.  86.  86.  87.  87.  86.  86. 155. 265. 412.   0.
   0. 119. 105. 102. 100.  99.  99.  97.  95.  93.  91.  89.  85.  86.  86.  86.  86.  87.  86.  86.  86.  85. 214. 408.   0.
   0.   0. 106. 103. 102. 100.  99.  97.  95.  93.  91.  89.  85.  85.  85.  85.  86.  86.  85.  85.  85.  84. 274.   0.   0.
   0.   0. 119. 104. 102. 100.  99.  97.  95.  93.  92.  89.  85.  85.  85.  85.  85.  85.  85.  85.  84. 145. 369.   0.   0.
   0.   0.   0. 106. 103. 101.  99.  97.  96.  95.  95.  92.  89.  87.  84.  84.  84.  84.  85.  84.  84. 260.   0.   0.   0.
   0.   0.   0.   0. 105. 102. 101.  98.  96.  96.  96.  95.  93.  88.  84.  84.  84.  84.  84.  83. 201.   0.   0.   0.   0.
   0.   0.   0.   0.   0. 105. 102. 100.  97.  96.  96.  94.  92.  88.  83.  83.  83.  82.  81.  80.   0.   0.   0.   0.   0.
   0.   0.   0.   0.   0.   0. 103. 101.  99.  98.  96.  95.  94.  91.  85.  82.  81.  80.  77.   0.   0.   0.   0.   0.   0.
   0.   0.   0.   0.   0.   0.   0.   0. 102.  99.  98.  96.  94.  92.  87.  85.  82.   0.   0.   0.   0.   0.   0.   0.   0.
   0.   0.   0.   0.   0.   0.   0.   0.   0.   0.   0.   0.  97.   0.   0.   0.   0.   0.   0.   0.   0.   0.   0.   0.   0.

  0.0   3.8  11.3  18.8  26.3  33.8  41.3  48.8  56.3  63.8  71.3  90.0 120.0 150.0 180.0 210.0 240.0 270.0 300.0 330.0
133.1 175.2 259.3 312.1 346.1 366.5 377.9 383.3 385.2 385.1 384.1 381.6 381.2 381.3 381.5 381.6 381.7 381.7 381.8 381.8
 9.6 MICRCN FLUX=0.1213E-05 MICRCWATTS/(SQ CM  MICRCN)
11.8 MICRCN FLUX=0.7681E-06 MICRCWATTS/(SQ CM  MICRCN)
  DISK TEMP AT 20.0 MICRCNS=196.79   FLUX=0.1380E-11
```

Fig. 21: Computed map of surface physical temperature of Mercury as seen from the Earth on 8/15/71. Celestial north is at the top of the map.

```
POLARIZED TEMPERATURE DISTRIBUTION

   0.   0.   0.   0.   0.   0.   0.   0. 102. 143. 195. 216. 234. 227. 220. 214. 148.   0.   0.   0.   0.   0.   0.   0.   0.
   0.   0.   0.   0.   0.   0. 124.  53. 141. 172. 206. 228. 253. 255. 255. 254. 227. 271. 155.   0.   0.   0.   0.   0.   0.
   0.   0.   0.   0.   0. 151. 164. 155. 180. 201. 221. 240. 272. 283. 250. 304. 306. 300. 281. 274.   0.   0.   0.   0.   0.
   0.   0.   0.   0. 211. 199. 204. 217. 211. 229. 249. 266. 282. 281. 281. 300. 322. 329. 327. 309. 307.   0.   0.   0.   0.
   0.   0.   0. 230. 247. 247. 255. 242. 221. 241. 260. 270. 280. 290. 301. 320. 339. 335. 340. 344. 335. 311.   0.   0.   0.
   0.   0. 247. 271. 283. 282. 267. 254. 258. 256. 261. 271. 281. 295. 309. 316. 324. 328. 344. 354. 363. 342. 280.   0.   0.
   0.   0. 286. 317. 303. 285. 285. 284. 272. 260. 267. 272. 284. 297. 306. 312. 322. 333. 347. 360. 368. 373. 325.   0.   0.
   0. 267. 325. 333. 318. 300. 297. 294. 278. 262. 269. 276. 291. 304. 311. 318. 327. 336. 351. 367. 377. 384. 370. 285.   0.
   0. 310. 350. 342. 314. 315. 308. 303. 283. 263. 274. 280. 298. 311. 319. 324. 331. 338. 355. 359. 373. 388. 383. 326.   0.
   0. 353. 364. 345. 325. 318. 317. 310. 289. 269. 280. 286. 303. 315. 323. 326. 335. 342. 346. 352. 361. 372. 384. 367.   0.
   0. 365. 375. 355. 335. 326. 317. 316. 295. 275. 290. 291. 306. 315. 320. 331. 338. 335. 347. 347. 346. 363. 375. 374.   0.
   0. 362. 383. 369. 352. 345. 335. 336. 317. 259. 306. 256. 257. 309. 311. 323. 331. 332. 341. 344. 346. 362. 375. 378.   0.
   2. 391. 351. 352. 372. 363. 355. 347. 339. 324. 314. 304. 285. 295. 307. 314. 323. 329. 334. 341. 348. 361. 373. 377.   2.
   0. 394. 355. 388. 376. 366. 357. 349. 341. 326. 315. 306. 286. 299. 306. 314. 325. 326. 333. 339. 345. 355. 372. 372.   0.
   0. 392. 358. 350. 380. 370. 355. 350. 343. 329. 316. 307. 286. 259. 306. 313. 322. 327. 332. 337. 342. 357. 370. 362.   0.
   0. 364. 400. 391. 381. 370. 363. 358. 343. 329. 317. 306. 285. 298. 305. 312. 319. 327. 330. 324. 325. 335. 350. 340.   0.
   0. 343. 358. 395. 382. 374. 365. 357. 342. 327. 316. 305. 283. 298. 303. 310. 317. 324. 315. 322. 316. 322. 326. 295.   0.
   0. 302. 384. 353. 387. 379. 367. 354. 340. 325. 313. 302. 280. 266. 289. 293. 301. 305. 308. 307. 312. 315. 310. 250.   0.
   0.   0. 337. 364. 382. 375. 363. 351. 336. 322. 315. 299. 276. 275. 280. 276. 284. 293. 295. 297. 301. 301. 270.   0.   0.
   0.   0. 290. 353. 376. 371. 356. 344. 337. 324. 330. 312. 294. 261. 265. 273. 277. 284. 288. 290. 282. 268. 230.   0.   0.
   0.   0.   0. 322. 346. 351. 358. 345. 333. 334. 335. 321. 307. 283. 259. 264. 268. 273. 272. 261. 246. 235.   0.   0.   0.
   0.   0.   0.   0. 316. 324. 343. 341. 323. 318. 320. 307. 254. 270. 246. 244. 244. 246. 234. 215. 210.   0.   0.   0.   0.
   0.   0.   0.   0.   0. 287. 267. 307. 310. 310. 302. 255. 242. 267. 240. 216. 208. 200. 158. 177.   0.   0.   0.   0.   0.
   0.   0.   0.   0.   0.   0. 191. 273. 232. 263. 272. 264. 254. 243. 268. 165. 143. 154.  82.   0.   0.   0.   0.   0.   0.
   0.   0.   0.   0.   0.   0.   0.   0. 154. 216. 242. 233. 216. 219. 176. 152.  78.   0.   0.   0.   0.   0.   0.   0.   0.
AS= 254.53438     AE= 122.26512     DE=  11.56768
SUBSOLAR LONGIT= 131.66DEGREES
SOIL                CONDUCTIVITY=0.002000JOULES/SEC-CM-DEG K
SPECIFIC HEAT=0.83700JOULES/GM-DEG K
DENSITY=1.50GM/CC
DIELECTRIC CONSTANT=2.0000
LOSS TANGENT=0.007
WAVELENGTH=  3.71CM
```

```
POLARIZED TEMPERATURE DISTRIBUTION

   0.   0.   0.   0.   0.   0.   0.   0. 167. 209. 265. 253. 317. 310. 310. 313. 251.   0.   0.   0.   0.   0.   0.   0.   0.
   0.   0.   0.   0.   0.   0. 168. 121. 187. 219. 260. 263. 313. 316. 320. 336. 301. 336. 261.   0.   0.   0.   0.   0.   0.
   0.   0.   0.   0.   0. 174. 154. 178. 207. 229. 251. 275. 309. 322. 330. 347. 351. 346. 307. 310.   0.   0.   0.   0.   0.
   0.   0.   0.   0. 217. 213. 220. 235. 229. 249. 271. 289. 307. 306. 305. 326. 349. 356. 352. 331. 315.   0.   0.   0.   0.
   0.   0.   0. 216. 247. 252. 264. 253. 233. 254. 275. 286. 297. 308. 318. 337. 356. 354. 353. 352. 335. 292.   0.   0.   0.
   0.   0. 204. 253. 277. 282. 271. 260. 265. 267. 271. 282. 292. 307. 321. 329. 334. 346. 345. 354. 355. 315. 231.   0.   0.
   0.   0. 243. 250. 290. 281. 285. 286. 276. 265. 274. 279. 291. 305. 314. 318. 328. 336. 347. 355. 355. 346. 276.   0.   0.
   0. 190. 262. 303. 304. 293. 294. 294. 280. 265. 273. 281. 256. 309. 316. 322. 329. 336. 348. 358. 360. 355. 321. 206.   0.
   0. 234. 306. 315. 299. 306. 303. 301. 283. 265. 276. 283. 301. 314. 321. 326. 331. 336. 345. 349. 355. 356. 335. 247.   0.
   0. 278. 319. 317. 308. 307. 310. 306. 288. 269. 281. 287. 305. 316. 324. 328. 335. 338. 335. 340. 342. 344. 336. 288.   0.
   0. 295. 329. 327. 316. 314. 310. 311. 293. 274. 290. 291. 308. 319. 320. 330. 335. 334. 335. 335. 329. 333. 330. 299.   0.
   0. 308. 337. 339. 334. 331. 328. 331. 314. 258. 306. 258. 297. 309. 311. 321. 328. 327. 332. 331. 329. 333. 324. 304.   0.
   1. 315. 344. 351. 351. 349. 346. 341. 335. 322. 313. 304. 285. 295. 306. 312. 320. 323. 325. 328. 328. 331. 328. 304.   1.
   0. 317. 348. 355. 355. 352. 348. 342. 337. 324. 314. 306. 286. 299. 306. 312. 320. 323. 325. 326. 326. 330. 327. 295.   0.
   0. 313. 350. 359. 357. 356. 351. 344. 340. 327. 316. 307. 287. 300. 306. 312. 319. 322. 324. 324. 323. 328. 325. 290.   0.
   0. 302. 351. 350. 362. 358. 356. 354. 341. 328. 316. 307. 268. 295. 308. 312. 316. 323. 323. 318. 312. 313. 308. 267.   0.
   0. 259. 347. 364. 363. 363. 363. 355. 342. 329. 319. 308. 286. 299. 306. 311. 317. 321. 314. 313. 300. 258. 267. 223.   0.
   0. 216. 333. 364. 371. 373. 363. 354. 342. 329. 318. 307. 284. 291. 254. 256. 303. 305. 305. 300. 258. 251. 269. 179.   0.
   0.   0. 286. 358. 368. 370. 363. 354. 342. 329. 323. 306. 283. 283. 287. 282. 289. 256. 255. 293. 250. 260. 229.   0.   0.
   0.   0. 239. 330. 367. 371. 361. 352. 347. 345. 343. 324. 305. 253. 279. 283. 285. 291. 292. 290. 275. 250. 189.   0.   0.
   0.   0.   0. 304. 346. 359. 372. 361. 350. 352. 354. 340. 326. 300. 274. 276. 281. 285. 282. 267. 246. 220.   0.   0.   0.
   0.   0.   0.   0. 325. 347. 365. 368. 350. 346. 348. 334. 320. 294. 267. 265. 264. 266. 252. 234. 217.   0.   0.   0.   0.
   0.   0.   0.   0.   0. 325. 315. 355. 355. 353. 344. 335. 332. 303. 273. 249. 239. 231. 166. 201.   0.   0.   0.   0.   0.
   0.   0.   0.   0.   0.   0. 261. 342. 307. 335. 340. 328. 315. 302. 260. 235. 150. 156. 120.   0.   0.   0.   0.   0.   0.
   0.   0.   0.   0.   0.   0.   0.   0. 259. 317. 336. 321. 258. 301. 247. 221. 141.   0.   0.   0.   0.   0.   0.   0.   0.
AS= 254.53438     AE= 122.26512     DE=  11.56768
SUBSOLAR LONGIT= 131.66DEGREES
SOIL                CONDUCTIVITY=0.002000JOULES/SEC-CM-DEG K
SPECIFIC HEAT=0.83700JOULES/GM-DEG K
DENSITY=1.50GM/CC
DIELECTRIC CONSTANT=2.0000
LOSS TANGENT=0.007
WAVELENGTH=  3.71CM
```

Fig. 22: Computed brightness temperature maps of Mercury for $\varepsilon=2.0$ giving the appearance of the planet as seen from Earth on 8/15/71 at a wavelength of 3.71 cm. Above, parallel polarization; below, perpendicular polarization.

of parameters. It was expected that a least-squares fit would separately yield best values for the different parameters to the extent that they are uncorrelated. This assumption was found to be generally valid by inspection of the results. Surprisingly, however, it was noticed that the parameters yielding the lowest residuals did not in general agree with what are considered firm results of the disk-average analyses. The discrepancies were found to be systematically similar when this technique was checked using the Mars model and interferometric data taken on Mars during the same observing run (8/12/71 - 8/19/71).

A likely explanation for this effect is due to the noise impressed on the data by gain variations. This effect would, of course, be the same for any object observed and would produce similar systematic errors for both Mars and Mercury. A simple method was devised to qualitatively investigate the effects of gain variations, as follows.

The statistical noise associated with a given data point is considered to obey a Gaussian distribution with mean = 0 and standard deviation σ^*, where

$$\sigma^* = (\sigma_n^{\,2} + [(\Delta G/G)S]^2)^{\frac{1}{2}}$$

σ_n = standard deviation of random noise = constant

$\Delta G/G$ = relative gain variation error

S = signal or visibility amplitude, a function of resolution

(See e.g.; Christiansen and Högbom, 1969)

This is mentioned in Appendix V where it is stated that the error due to gain variations is proportional to the flux observed, and vanishes near the zero of the visibility function. In addition, the measurement of signal S from the planet is subject to uncertainty in knowlege of the real system gain obtaining during the measurement. Consequently, it was assumed that the result of an attempted measurement of a signal S was "data point" D given by

$$D = (S+\sigma^*)G'$$

where S="real" signal amplitude

σ^* = associated error

G' = real gain

G' was taken from a random gaussian population with mean 1 and standard deviation of 5% (.05).

A single model result consisting of visibility functions in orthogonal polarizations was used as signal, and a sample "data set" was computed by operating on these values of S in accordance with the above "transfer function". The gain was assumed to vary for every other point; that is, each pair of "measurements" in orthogonal polarizations was subject to the same value of G'. This was allowed since data points are obtained alternately in orthogonal polarizations and the effective gain for each point of a pair is not independent of the gain applying to the other point. Clearly, as the gain is a continuous function of time, this assumption is not entirely satisfactory but was felt to be justified for this simple test. Residuals were then computed using a range of model-generated test functions including the one originally used as signal. Results are shown in fig. 23. Curve (a) shows convergence at the proper value of ϵ initially used, for the case of no gain variations. This was observed to be true for both polarizations as of course would be expected. Curves (b) and (c) show convergence at anomalously low values of ϵ obtained when 5%

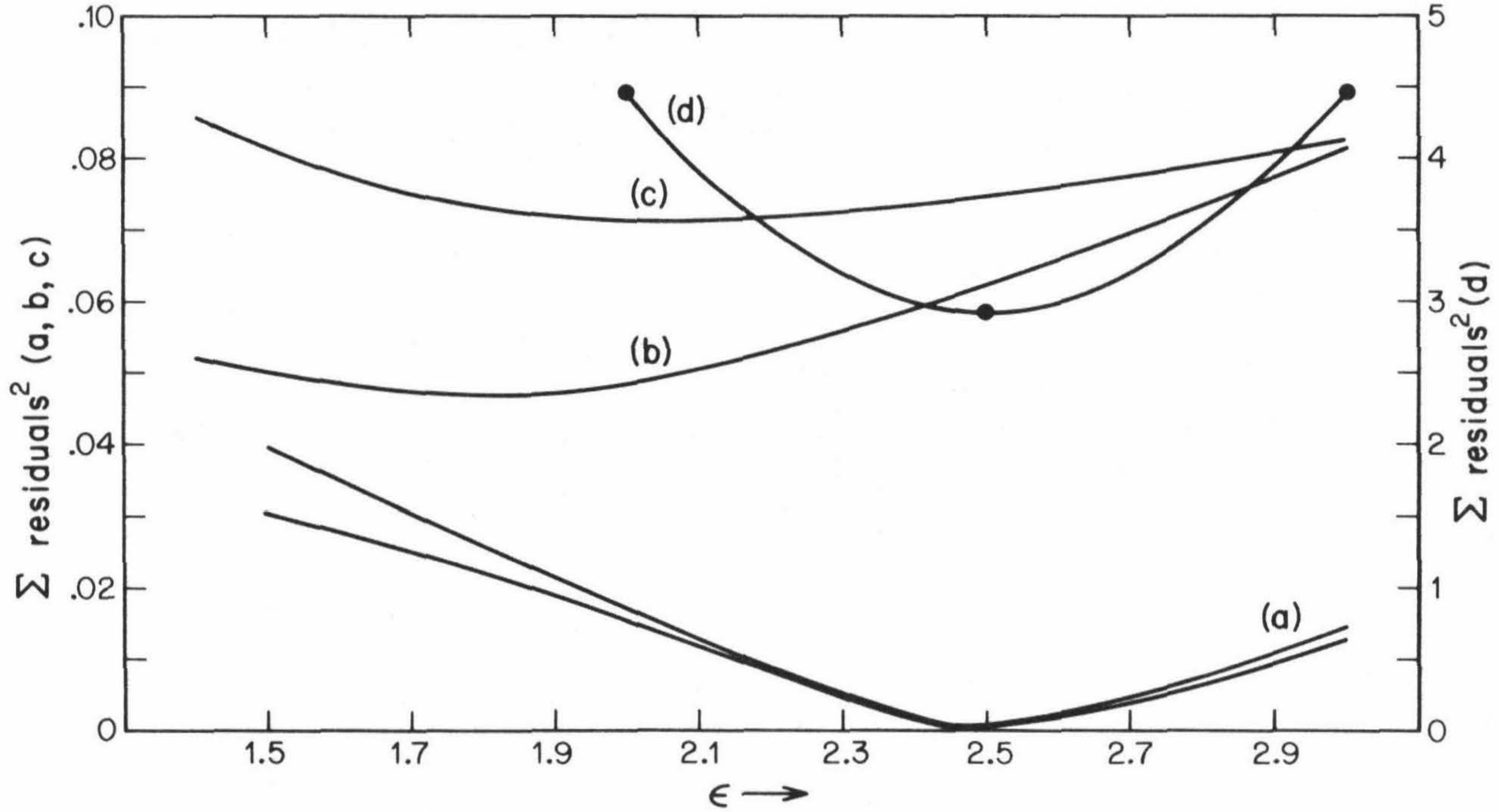

Fig. 23: Residuals of model-generated visibility functions from simulated data set. (a) No gain variations (b) and (c), Gain variations of 5%, $\parallel$ and $\perp$ polarizations respectively (d) Residuals of model-generated polarization difference functions from simulated data set, Gain variations of 5%. Residuals are shown as functions of dielectric constant (ϵ).

gain variations were allowed. In addition, the model curves that best fit the data yielded different values of ϵ in the two orthogonal polarizations. (Different locations of the minima in curves (b) and (c).)

We conclude that the use of detailed full visibility functions to determine ϵ gives a biased estimate. For the simulated "data" test, polarization differences were also computed for adjacent points. The results of a residual calculation relative to model results are shown as curve (d) in fig. 23 and the difference "data" are shown in fig. 24. It is apparent that the result obtained by the polarization difference technique is not biased and indeed yields the correct value of ϵ. This independence of gain variation error coupled with the independence of temperature distribution mentioned in Appendix V makes the polarization difference estimator a very useful tool and justifies the confidence placed in its use. Similar bias effects are noted in fitting the simulated data set for the parameter χ (see fig. 25). These results indicate that a straight-forward use of this model-fitting technique may be subject to significant bias when applied to real data with non-zero scatter of systematic origin in an attempt to look for small differences in the parameters.

The precise nature of the noise in the interferometer gain is probably different from that assumed for this simulation, and produces somewhat different, but still similarly biased, results for ϵ. Results obtained from the real data are shown in fig. 26, in which residuals obtained from both the Mercury and Mars data are plotted against both ϵ (on a sliding scale) and r, a dimensionless parameter:

$$r = \epsilon/\epsilon^*$$

ϵ^* = dielectric constant determined by polarization difference technique.

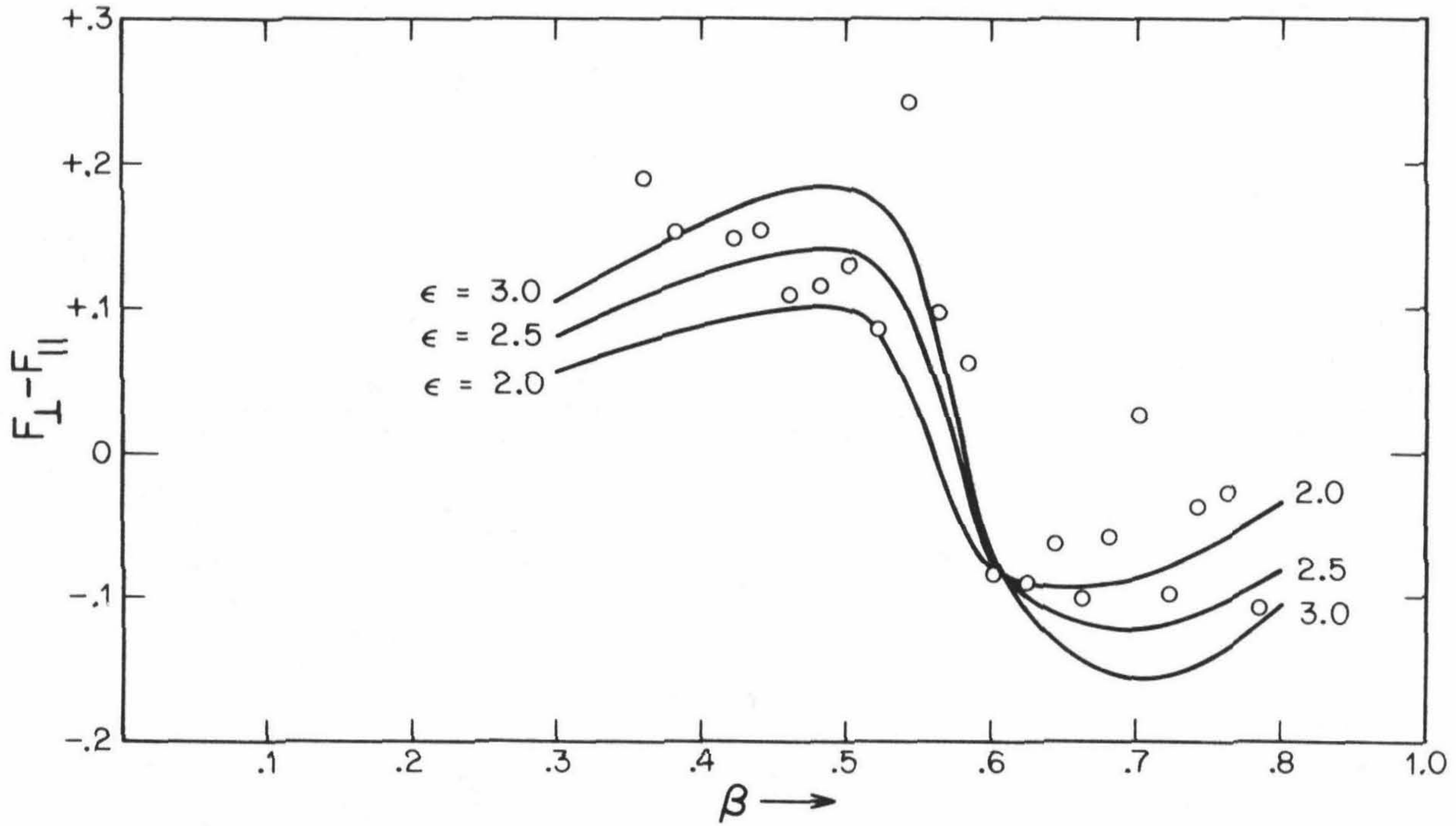

Fig. 24: Polarization difference "data" used in calculation of curve (d) of fig. 23. Curves are model-generated polarization difference functions for various values of dielectric constant employed.

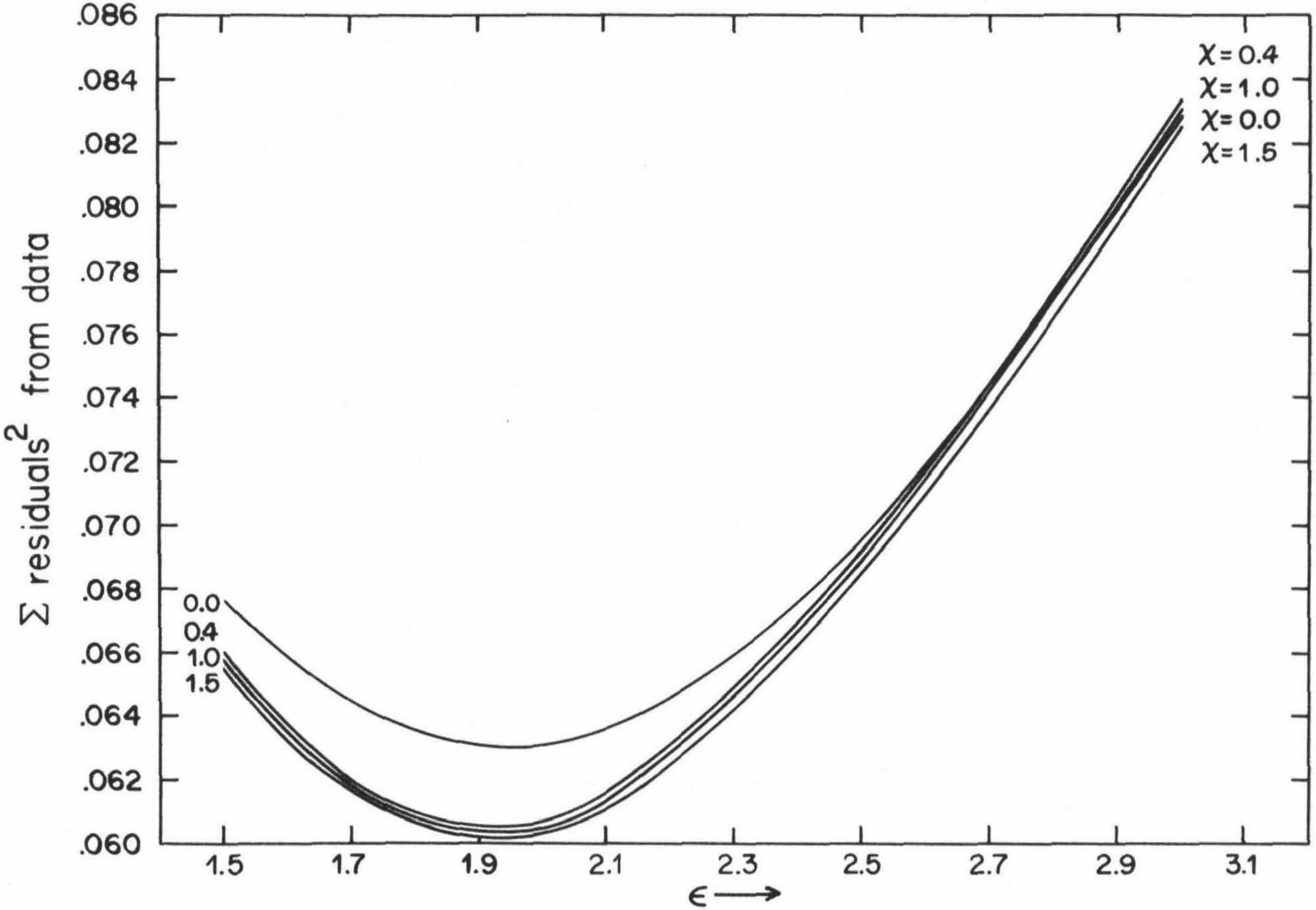

Fig. 25: Residual calculations as functions of ϵ and χ. The simulated data employed a value for χ of 0.4, and it is clear that this value does not minimize the residuals when used in a model to fit the "data". Residuals are averaged over both polarizations.

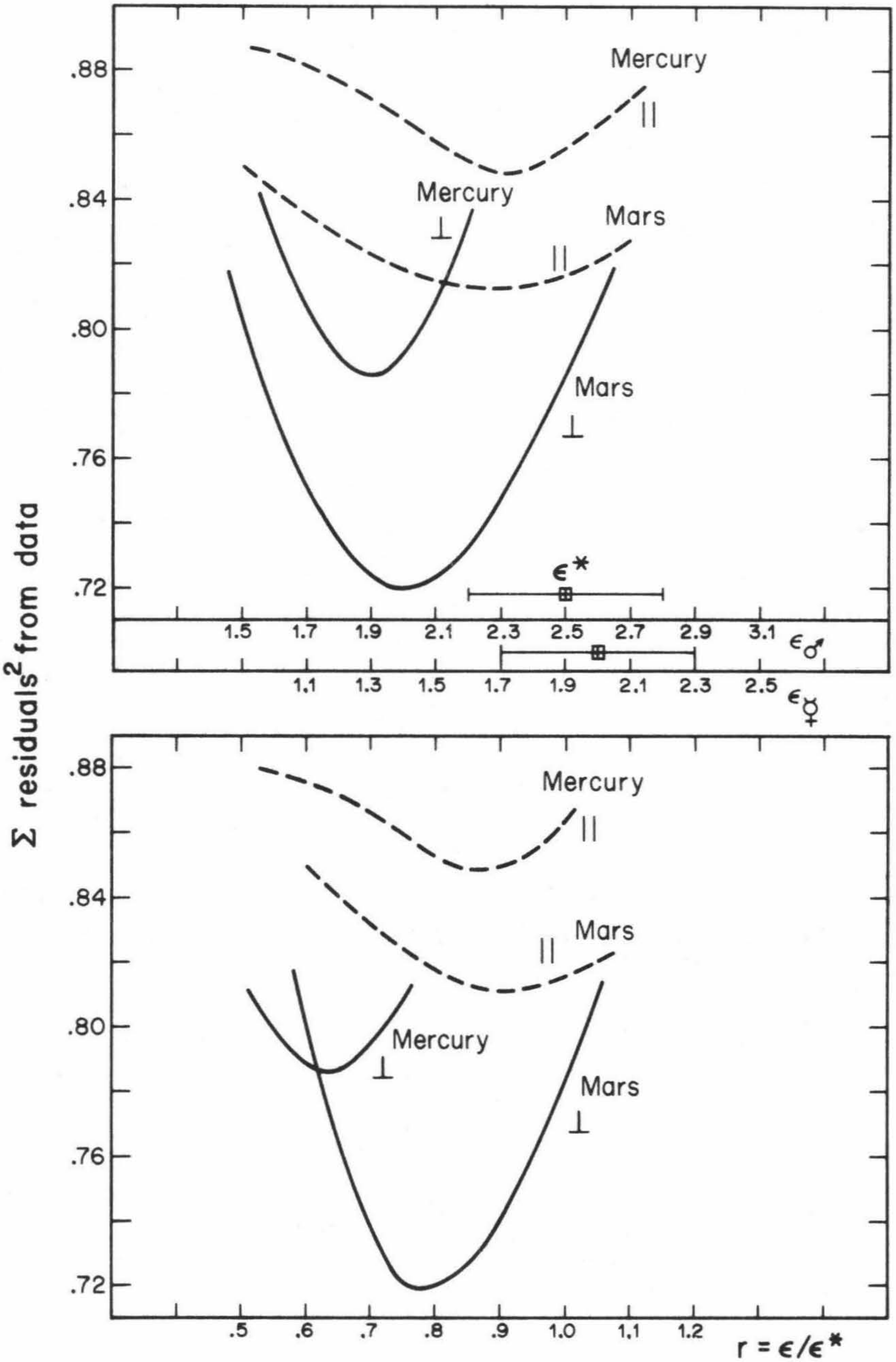

Fig. 26: Curves of residuals from the 3.71 cm visibility function data showing systematic bias in determination of the dielectric constant that best fits these data. ε* is the dielectric constant determined from polarization difference data.

Again, systematic bias was observed. The details of the curves in the orthogonal polarizations are somewhat different, perhaps reflecting deviation of the real transfer function from the simple one assumed. The striking feature is the great similarity in the discrepancies. The curves of residuals bear an almost identical relationship with each other and with the well-determined dielectric constant, ϵ^*, or $r=1$, for each planet. This similarity produced by two planets having such different brightness maps and visibility functions argues strongly for an error of the type described above. Residuals in χ averaged over the two polarizations for the real data set obtained on Mercury are shown in fig. 27 for a variety of model dielectric parameters. Three facts are evident:

a. The best-fitting value of χ is not discrepant with our previous conclusions.

b. The best-fitting value of χ is independent of choice of dielectric parameters.

c. The lowest residuals (supposedly best-fitting model) are not seen to occur at the true value of $\epsilon=\epsilon^*=2.0$.

As (c) is merely a reflection of the bias in the dielectric constant fit, this leads us to suspect that the real world is not as unkind as expected from our simulation . The technique does, in this case, show some promise, and will surely be used with future data of, perhaps, higher quality. Still, these fits may not be considered an independent determination of χ.

Finally, the attempted determination of the position of the rotation pole was inconclusive primarily because of the bias effects described above which render any conclusion of this type dubious . An attempt was made to see whether the data would enable us to discriminate between the two likely pole positions through changes in the residuals. Models were generated and trial visibility functions computed using the alternate pole positions suggested by

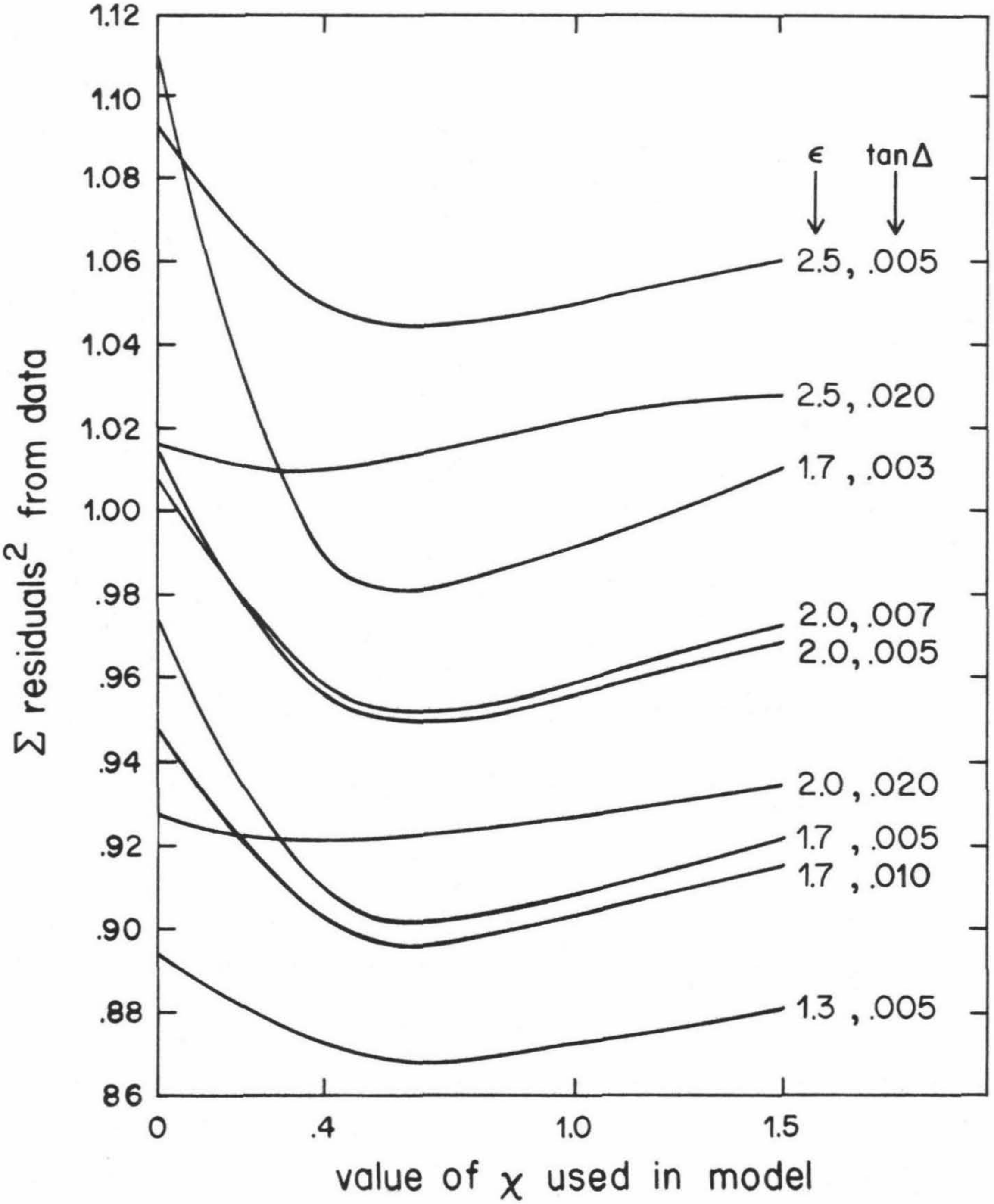

Fig. 27: Residuals of models employing various values of χ, ε, and tanΔ from 3.71 cm data, shown as functions of the value of χ employed in the models.

Peale (1969) in the aspect geometry. The results showed no significant difference in residuals using the set of parameters regarded as best, and no systematic difference over the entire range of parameters. Consequently, no discrimination may be made on the basis of this single data set. The differences that were seen (fig. 28) indicate that this may be a useful avenue of approach once the nature of the biasing of the data is understood and accounted for fully.

6. Conclusions from the study of Mercury

On the basis of the interferometric determination of the effective dielectric constant, and the assumption of lunar-like surface roughness which is regarded as quite likely from results of radar investigations at several wavelengths, disk-average data at .31, 6, and 18 cm are seen to be readily understandable in the light of a homogeneous, lunar-like model . No discrepancies are found with the concept that the subsurface of Mercury is similar to that of the Moon in dielectric properties and physical state. Observations are in accord with epilith temperatures characterizing a porous regolith which exhibits the effects of radiative thermal conductivity. Apparent discrepancies with this concept (Epstein et al., 1970; Ulich et al., 1972) are shown to vanish when interpreted using a detailed modeling approach. The subsurface appears to be well represented by homogeneous dielectric and physical properties to a depth of several meters, and the importance of the radiative term in the thermal conductivity is inconsistent with the presence of an atmosphere having surface pressure greater than a few tenths of a millibar.

The use of interferometric visibility functions, although not of their difference, in detailed analysis of surface brightness distributions has been

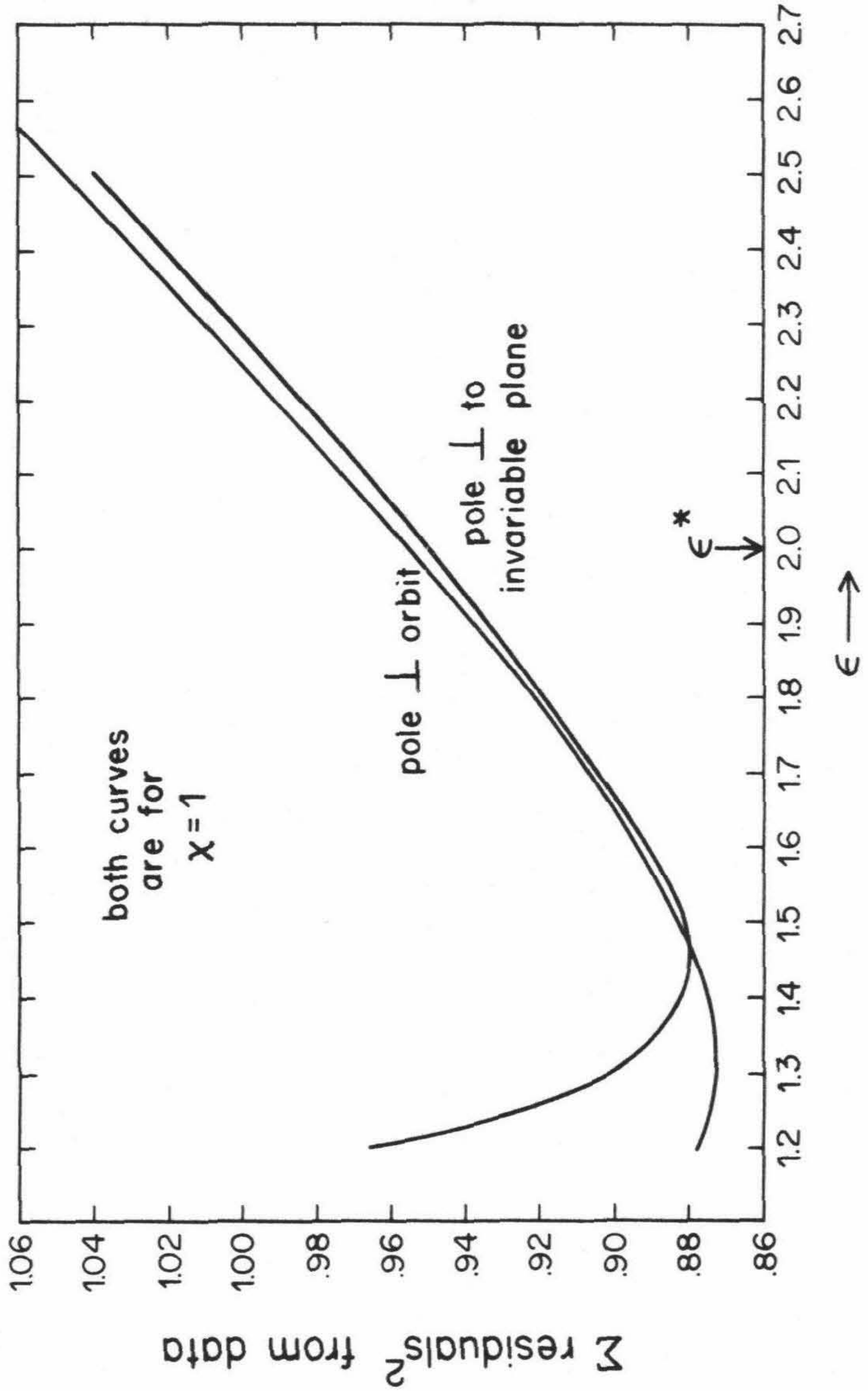

Fig. 28: Residuals from 3.71 cm data of models employing various values of ϵ and $\chi = 1.0$. Residuals obtained using alternate probable positions of the rotation axis of Mercury in the aspect geometry are shown in the two curves.

shown to be subject to rather significant bias. One possible source of this is instrumental gain variations which are correlated between data points taken sequentially. It is believed that this problem is the limiting factor on further detailed analyses of this type dealing with the surface properties of the terrestrial planets by interferometric techniques.

Part III

7. The following work has been published practically verbatim (Cuzzi and Muhleman, 1972) under the title:

"The Microwave Spectrum and Nature of the Subsurface of Mars"

7.1 Introduction and Summary of Results

Observations of the emission from Mars at many radio wavelengths have been made during the last four oppositions of the planet. Suprisingly, the microwave spectra appear to be significantly different from the radio spectrum of the moon. The lunar spectrum has been adequately interpreted using the analytical theory of Piddington and Minnet (1949), e.g. see Troitskii (1970). Several authors have pointed out the discrepancy between the data and predictions of the analytical theory, e.g. Epstein, (1971). Sagan and Veverka (1971) have suggested a model with non-homogeneous dielectric properties which produces an inverted spectrum to match a least-squares fit of the data.

We feel that the data set appears to rule out the analytical theory for reasonable (i.e., lunar-type) conditions in the subsurface and, furthermore, it cannot be used to infer the short-wavelength behavior of the spectrum to an accuracy of better than 10-15° K. Any upturn or downturn of the spectrum toward short wavelengths would be undetectable if it were of a smaller magnitude. A fairly "flat" spectrum approaching this criterion is obtained from the analytical theory only at the expense of radical, ad hoc changes in the physical parameters of the surface from those found to be typical of the Moon or Mercury. We intend to show that an essentially flat spectrum which matches the data in shape and absolute value is the result of a completely proper treatment of a simple, but non-analytical, model which includes the thermodynamics of the CO_2 ice caps and atmosphere, but assumes only simple dielectric properties.

8. The Data

Meaningful radio spectra of Mars are more difficult to obtain than for the Moon or Mercury due to the rapid rotation of Mars which causes the diurnal temperature variations to occur over a small depth into the surface, i.e. the thermal skin depth, L_T, is small relative to that for the moon. Furthermore, radio observations of Mars are only available over a small range of phase angles near opposition. Consequently, meaningful data must be taken at millimeter and centimeter wavelengths. Difficulties of millimeter and centimeter work have been discussed by Epstein (1971). Typical mean errors, including calibration, are near 10 - 15° at best, and for these best data most of the error comes from uncertainties in absolute calibration. The nature of the spectrum of Jupiter, which is often used as a calibration source, is largely unknown from .1 -2.0 cm, and it is generally assumed to be flat. Errors in this assumption will carry over into the shape of the spectrum of Mars. Measurements published by Wrixon et al. (1971) indicate that the spectrum of Jupiter (Fig. 29) may turn up toward shorter wavelengths from its value of ~ 140° at 1 cm. This increase would be mapped into a decrease in any data taken which utilized a constant Jovian temperature of 140° for calibration. The present state of the art at these wavelengths is such that random errors, and, in particular, uncertainties in absolute calibration are on the order of the expected thermal structure. Nevertheless, the recent data are good enough to show that the analytically predicted spectra for lunar-type surface parameters possess a larger upturn at short wavelengths than can be reasonably inferred from the accumulated data. (see Fig. 30).

9.1 The Analytical Theory

In the analytical theory the surface temperature is expressed as a Fourier series

$$T(0,t) = T_0 + \sum_n T_n \cos n\Omega t \qquad (9.1.1)$$

The temperature in the subsurface as a function of depth, z, and time, t, can then be written rigorously as

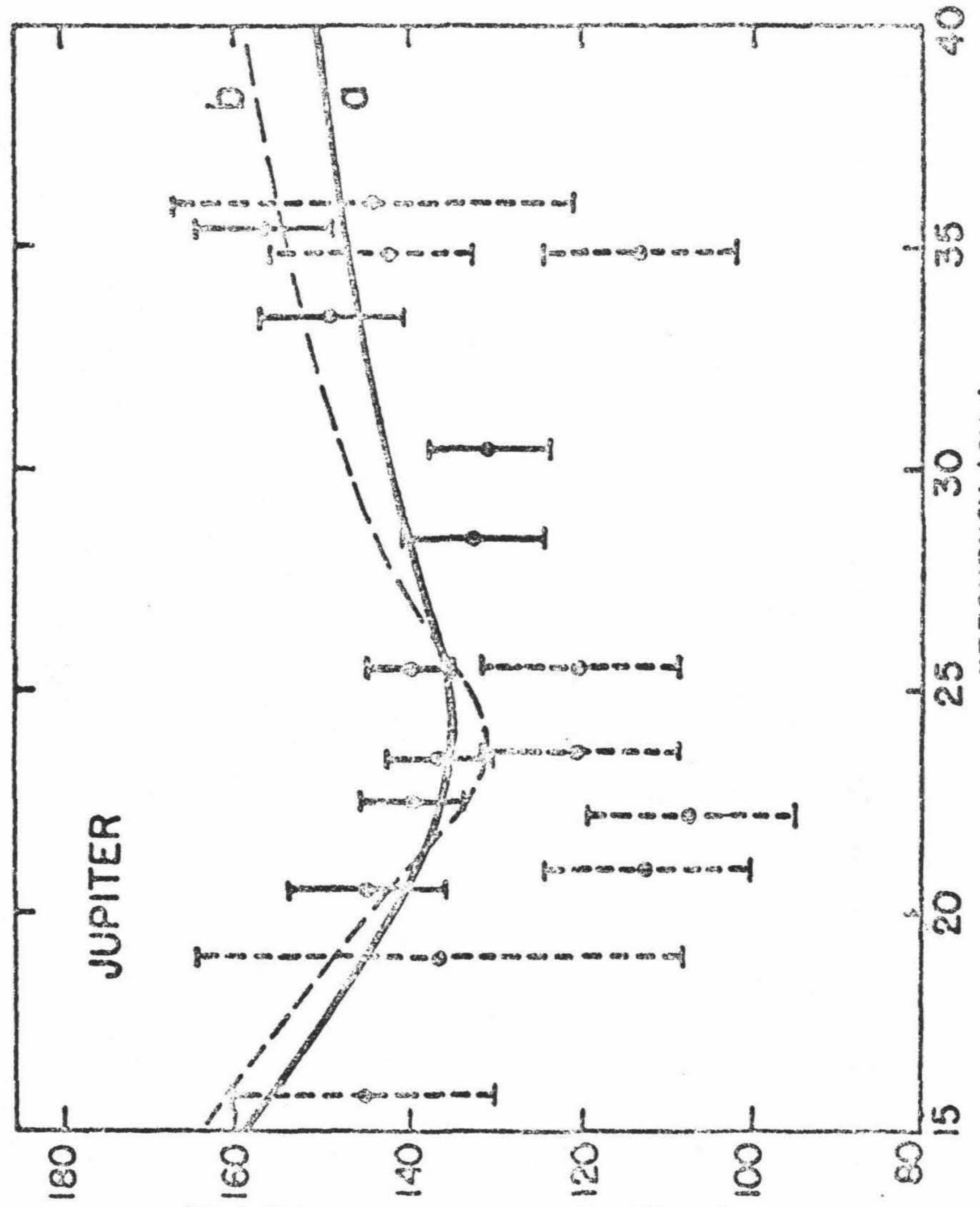

Fig. 29: Millimeter-range spectrum of Jupiter, from Wrixon et al., 1971. Model calculations of these authors are shown by the two curves, and the solid error bars are 2σ formal errors. Dashed points are earlier data.

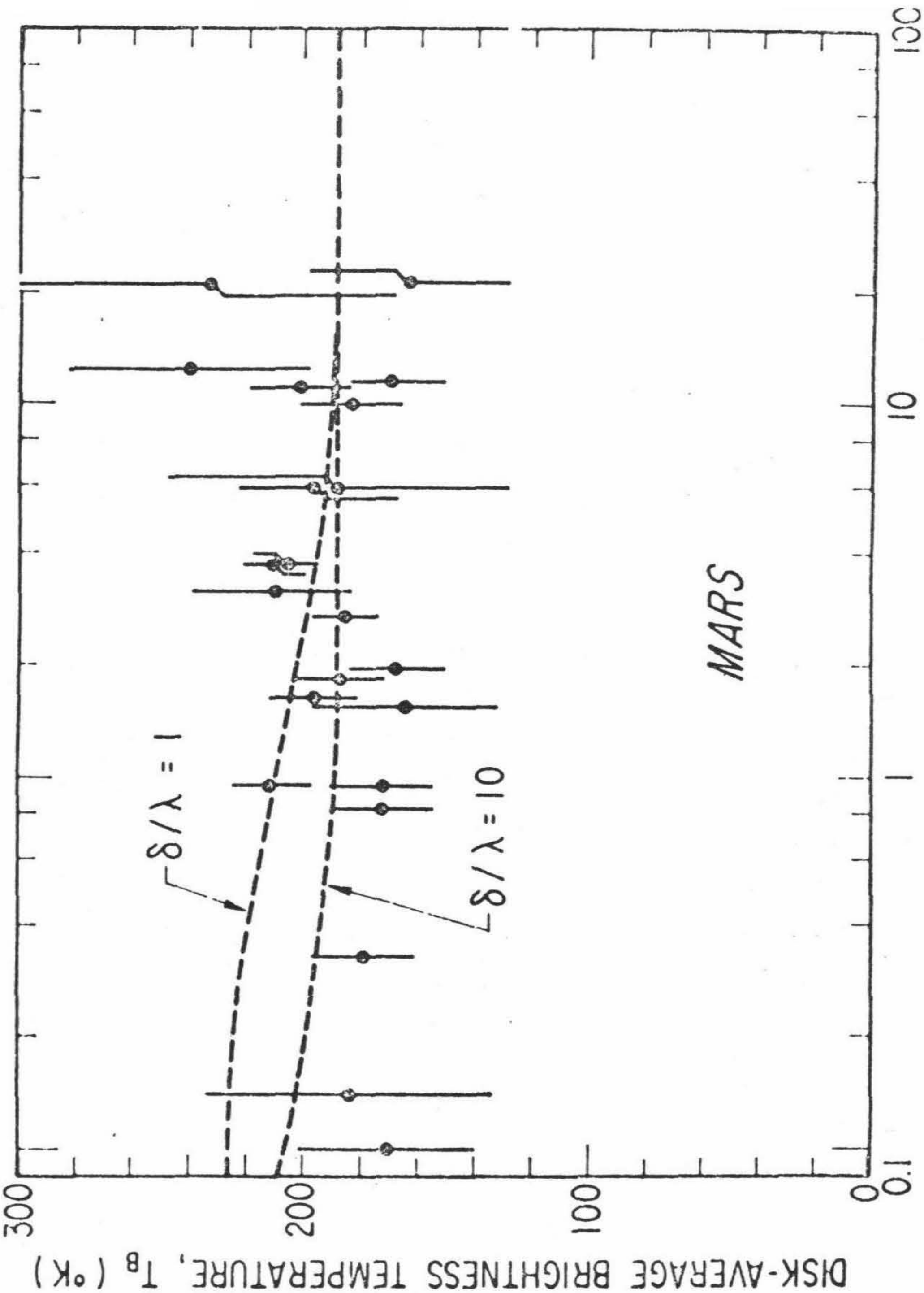

Fig. 30: The microwave spectrum of Mars as compiled by Epstein (1971) and the predictions based on the analytical theory with (a) lunar-like parameters ($\delta = \lambda$). (b) An extreme case of $\delta = 10\lambda$. ($\delta = L_e/L_T$).

$$T(z,t) = T_0 + T_1 e^{-z/L_T} \cos(\Omega t - z/L_T + \psi) + \ldots\ldots \quad (9.1.2)$$

$$L_T = (2K_T/C\rho\Omega)^{\frac{1}{2}} \quad (9.1.3)$$

where L_T is the thermal skin depth or the depth of attenuation of the amplitude of the temperature wave to l/e of its surface value. (K_T is thermal conductivity, C is the specific heat, and ρ is the material density). Using reasonable estimates of the parameters for Mars, we find that $L_T \sim$ 3cm. (This figure for the moon is about 6 cm). Thus, the diurnal thermal structure occurs only over relatively shallow depths in the subsurface of Mars. The electrical skin depth for radiation at vacuum wavelength λ_0 , L_e , can be written (making the reasonable assumption that the material loss tangent is small)

$$L_e = \frac{\lambda_0}{2\pi\sqrt{\varepsilon}\,\tan\Delta} \quad (9.1.4)$$

where ε is the dielectric constant relative to free space and $\tan\Delta$ is the material loss tangent or the ratio of the imaginary to the real parts of the complex dielectric constant. Equation 9.1.4 can be roughly interpreted as an estimate of the depth of the effective emitting layer for radiation at wavelength λ_0 . Thus, if the dielectric properties of the Martian surface are approximately the same as those for the moon, the observable microwave effective temperature structure will be shifted to much shorter wavelengths for Mars, e.g. to the l-l0mm range.

It should be mentioned that the radio spectra discussed in this paper crudely represent, in the analytical theory at least, scaled measurements of the temperature with depth in the subsurface through the relation shown in Eq. 9.l.l. Consequently, the prediction of an upturn of the spectrum at short wavelengths reflects nothing more than the fact that the temperature on the day side of a planet decreases away from the surface and that Mars is generally observed near opposition at phase angles near 0° and is always seen as a daylit planet. The resulting microwave spectrum and the temperature structure with depth will be referred to as normal. Temperature structures that decrease toward the surface which result in microwave spectra that decrease toward shorter wavelengths, although quite "normal" for the night side of a planet, will be referred to as "inverted" for the case at hand.

9.2: The thermophysical model

The thermophysical model used in this work was developed from that used by Leighton and Murray (1966) into which several refinements were incorporated. Basically, the heat equation

$$C\rho \frac{\partial T(z,t)}{\partial t} = \frac{\partial}{\partial z}\left(K_T \frac{\partial T}{\partial z}\right)$$

is numerically solved in a semi-infinite subsurface composed of plane-parallel slabs, 10 of 1.5 cm thickness and 10 of 30 cm thickness. Below the last layer, the temperature is assumed constant at the lowest layer temperature at the corresponding latitude. Since the lowest layer is at a depth of $\sim 100L_T$ the diurnal temperature fluctuation by eq. 9.1.2 is less than e^{-100} of its value at the surface. The effective skin depth for seasonal variations is about 80 cm and temperature variation at the lowest layer is less than 2% of the surface temperature variation. Thus, the resulting error from holding the lowest layer at constant temperature is negligible. An improved "implicit" algorithm is used for the numerical iteration.

$$\frac{T_i^{n+1} - T_i^{n}}{\Delta t} = \frac{K_T}{C\rho}\left\{\frac{(\delta^2 T)_i^{n} + (\delta^2 T)_i^{n+1}}{2\,\Delta z^2}\right\}$$

where

$$(\delta^2 T)_i = T_{i-1} - 2T_i + T_{i+1}$$

and the indices j and n refer to the depth step and time step under consideration. This algorithm provides increased accuracy and computing efficiency (Crank and Nicholson, 1947). The iteration is carried out, for each set of parameters, over the orbit for three Martian years. Convergence is obtained in the second year and verified in the third. The boundary condition in the top layer is solved by iteration of the equation

$$E\sigma T_s^4 = H_s(\theta\, ,\ \varphi\, ,\ R,\ D_s,\ t) + K_T \left.\frac{\partial T}{\partial z}\right|_s \qquad (9.2.1)$$

where E is the infrared emissivity, σ is the Stephan-Bolzmann constant, and depth increases downward. The solar flux is absorbed in the first layer of thickness 1.5 cm and effective depth .75 cm and the surface temperature T_s is obtained by linear extrapolation to the top (zero depth) layer;

$$T_s = 1.5\,(T_1) - .5\,(T_2) \quad .$$

The insolation function, H_s, varies with the position of Mars in its true orbit through the radius from the Sun, R, the solar declination or season, D_s, and the position on the sub-solar disk, (θ, φ). The latitude grid spacing is 10° and the longitude or solar hour angle grid spacing is one hour (local time).

The insolation function and orbit geometry scheme as devised by Leighton and Murray was inaccurate by some 10% at times in the Martian year, as the orbit was taken to be symmetrical and perihelion occurred at the south Summer Solstice. The insolation now depends on the true orbit parameters.

The thermal properties of the surface (K_T, the thermal conductivity, and C, the specific heat) are assumed temperature-independent at typical Martian temperature and pressure regimes (Fountain and West, 1970). Values are adopted of

$$\rho = \text{subsurface density} = 1.6 \text{ gm cm}^{-3}$$

$$C = \text{specific heat} = 0.2 \text{ cal gm}^{-1} \text{ deg}^{-1}$$

$$\gamma = \text{thermal inertia} = \sqrt{K_T \rho C}$$

$$= .006 \text{ cal cm}^{-2} \text{ sec}^{-\frac{1}{2}} \text{ deg}^{-1}$$

yielding $K_T = 1.1 \times 10^{-4} \text{ cal cm}^{-1} \text{ sec}^{-1} \text{ deg}^{-1}$.

An infrared emissivity of 0.90 was chosen, and the infrared effect of the atmosphere was treated as a greenhouse backradiation of 1% of the noon solar flux. All values are consistent with the mean surface parameters determined by Neugebauer et al. (1971) as results of the Mariner 1969 infrared photometry flyby experiment. The main improvement in the thermophysical model originally introduced by Leighton and Murray is the numerical incorporation of the thermodynamics of CO_2 phase changes into the heat budget at the surface. When, for instance, the temperature at a given surface element decreases to the condensation temperature of CO_2 at the ambient vapor pressure, the temperature remains constant while CO_2 frost is built up, releasing latent heat. Similarly, when that surface element begins to heat up beyond the condensation temperature all CO_2 present must sublimate away, absorbing latent heat, before the actual surface temperature can increase further. These processes obviously have a profound effect on the temperature distribution, at least on and near the polar caps. Surface Bolometric Bond Albedos are continuously adjusted such that

$A = 0.25$ if no frost present

$A = 0.30$ if only H_2O frost present (small amounts only)

$A = 0.65$ if CO_2 frost present .

The value of .25 for the mean Bolometric Albedo is given by de Vaucouleurs

(1964).

A check of model-generated temperatures in the subsurface was made near the equator where CO_2 effects are negligible. Thermal skin depths and absolute temperatures agree with theoretical analytic values to within 2%. The behavior of the polar caps in extent as a function of time is very important to the thermal behavior and microwave appearance of the planet. The claim has been made (Cross, 1971) that surface microroughness and embedded dirt control the behavior of the advancing and receding caps, and that a purely thermal model such as that of Leighton and Murray does not predict their behavior correctly. This claim was checked against data taken by Capen and Capen (1970) and the results are shown in fig. 31. It may be seen that the polar cap extent and date of disappearance at several latitudes predicted by the present model, neglecting surface roughness, provide quite a satisfactory fit to the observed data. Therefore we feel justified in neglecting the role of roughness in controlling the behavior of the polar caps, and in assuming that seasonal change in insolation is the dominant factor.

9.3: The geometrical treatment and radiative transfer problem

The thermal model as it is set up computes thermometric temperatures at the surface and with depth in the sub-surface as a function of latitude on the planet and longitude from noon or zero solar hour angle. In order to relate these temperatures to those as seen from the Earth and to compute observable quantities, it was necessary to create a coordinate transformation program . This (computer) program takes the coordinates of a surface element on the disk of Mars as seen from Earth (related to the projected celestial

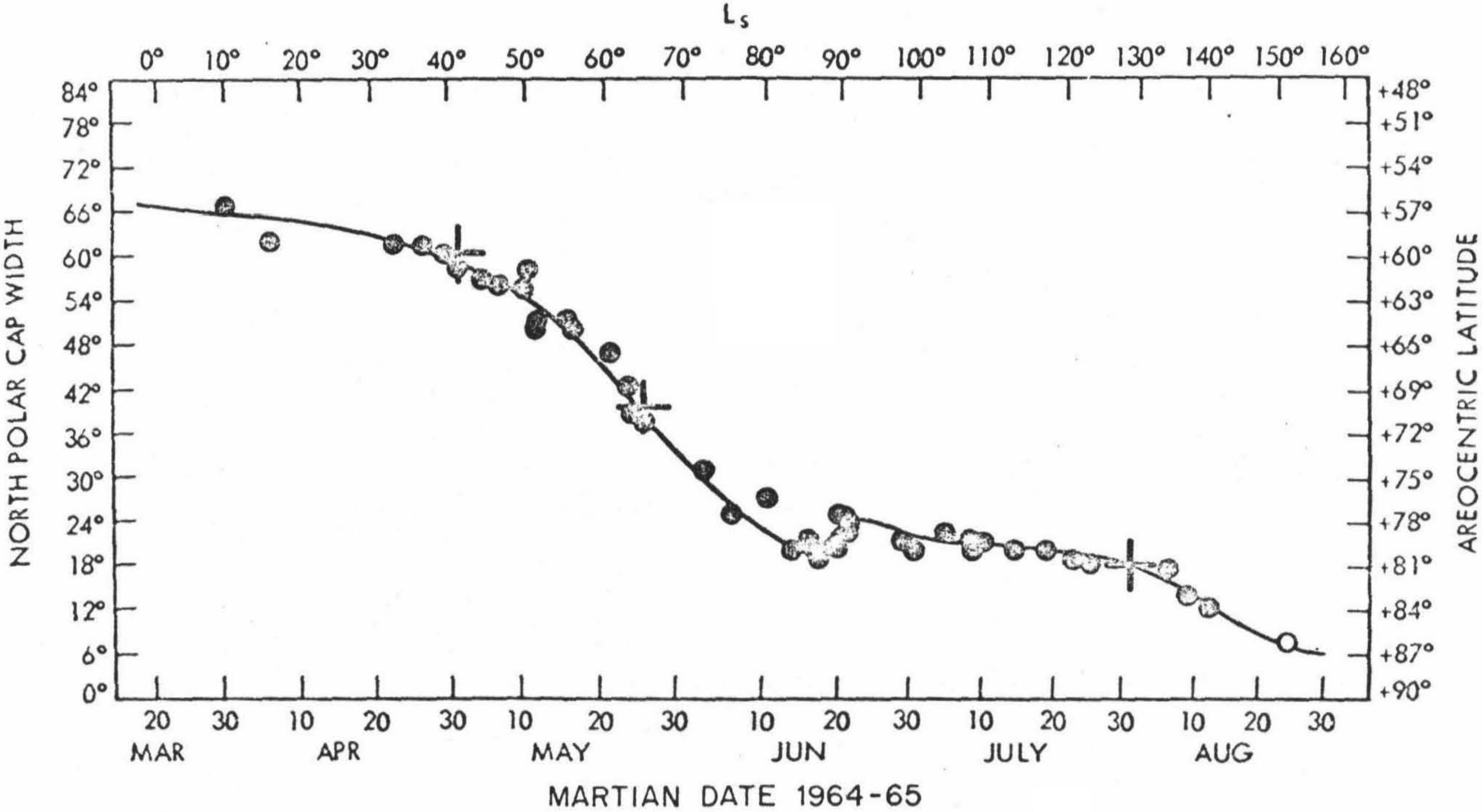

Fig. 31: Data from Capen and Capen (1970) on regression of the North polar cap of Mars. Crosses represent dates of disappearance of CO_2 frost at the indicated latitudes as predicted from the present model. Data from 1964-1965.

equator and projected celestial North) and calculates the Areocentric inertial coordinates as related to local noon on Mars and the planetary equator. These coordinates determine the temperature structure at that point on the apparent disk. This transformation is basically a combination of solid body rotations and may be written as

$$\begin{matrix}\text{Mars-centered}\\ \text{coordinates}\end{matrix} = [M] \begin{matrix}\text{Earth-based}\\ \text{coordinates}\end{matrix}$$

where [M] is a rank 3 matrix whose elements are functions of the orbital elements of Mars, the celestial coordinates of its pole of rotation, and published physical ephemerides of Mars for the date desired (see Appendix I). In this way the geocentric aspect of the disk may be reproduced for any date for which the ephemerides exist. The validity of the results has been ascertained by the two-dimensional fix provided by the published position angle of the axis and planetocentric declination of the Earth, or sub-Earth latitude, for all dates. By this method the conditions on , and geocentric aspect of Mars have been reproduced for the favorable oppositions of 1965, 1967, 1969, and 1971. Computed surface temperature maps and microwave brightness maps for these dates and several wavelengths of observation are shown in figs. 38-49. The expected microwave spectra, consisting of disk-average brightness temperatures for a range of wavelengths, were calculated for each opposition. The favorable opposition of 1954 was also reproduced for comparison with the infrared data of Sinton and Strong (1960) as reduced and presented by Morrison, Sagan, and Pollack (1969). These data will be described in the next section.

In order to compute microwave spectra, the radiative transfer equation

$$I_-(\theta_1) = \left[\frac{n_1{}^2 K_\nu}{\cos\theta_1}\right]\left[\frac{2k}{\lambda_0{}^2}\right]\int_0^\infty T(z)e^{-K_\nu \sec\theta_1 z}\, dz \qquad (9.3.1)$$

was solved numerically in the subsurface to determine the net microwave flux outward in the direction of the Earth and thus the equivalent blackbody temperature at several wavelengths λ_0. In eq. 9.3.1, $I_-(\theta_1)$ is the intensity reaching the surface from below at an angle θ_1 from the surface normal, and

K_ν = intensity absorbtion coefficient per unit length at frequency ν

$= 1/L_e = 2\pi\sqrt{\epsilon}\tan\Delta/\lambda_0$

k = Bolzmann constant

n_1 = refractive index $= \sqrt{\epsilon}$, ϵ = effective dielectric constant

The angle θ_1 is defined by the angle from the surface normal direction to the direction of the Earth, θ_0, through the refraction law:

$$\sin\theta_0/\sin\theta_1 = n_1/n_0 = n_1 = \sqrt{\epsilon_1}$$

as shown in fig. 32 . At the surface the upward-traveling ray is partially reflected back down and partially transmitted toward the Earth as determined by the Fresnel coefficients at a dielectric boundary (see Appendix IV). In general, the radio emission is polarized by this mechanism. The outcoming flux density at a given surface element is transformed to an equivalent brightness temperature at the corresponding point on the brightness map of Mars as seen from the Earth. In this part of the calculation, several more physical assumptions were made. (1) The planet is assumed to be a smooth, homogeneous dielectric sphere. (2) Neither H_2O nor CO_2 frosts, if present, were treated as distinct in their dielectric properties. This will be discussed in

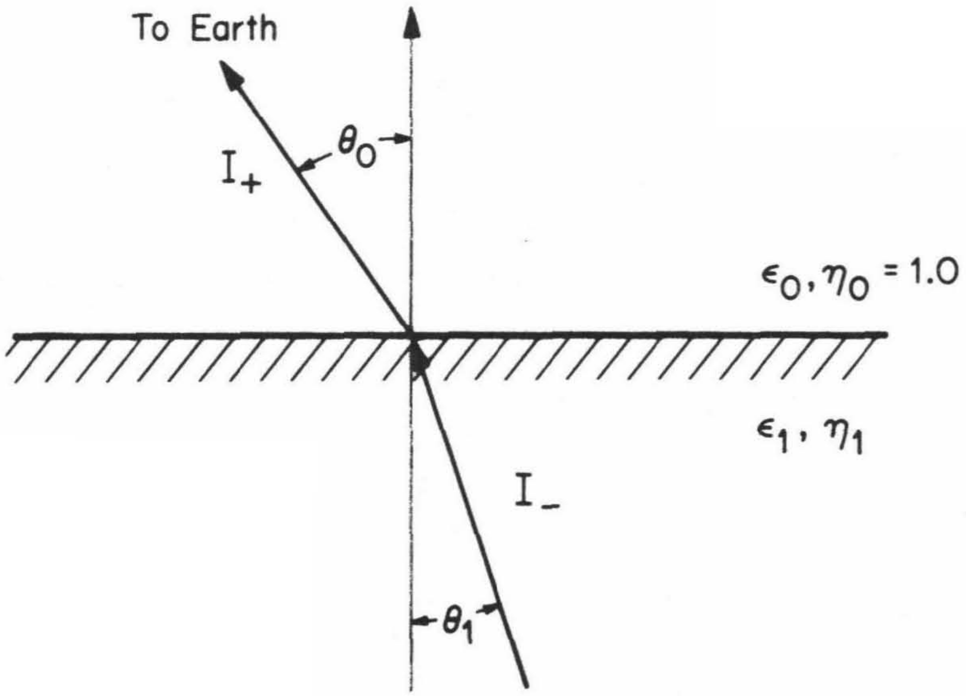

Fig. 32: Geometry of refraction and partial reflection at a dielectric boundary.

section 11. (3) Atmospheric microwave emission and absorbtion were assumed negligible.

Spectra were computed for two values of the effective dielectric constant, $\epsilon = 1.5$ and 2.5. The most likely value of $\epsilon = 2.5 \pm .3$ (est.) was obtained by interferometric observations of Mars at a wavelength of 6 cm in 1969 (Muhleman et al. ,1971) . This value is based on the same theory as used here, and is not expected to be seriously affected by roughness effects as small-scale roughness (on the scale of a wavelength) on Mars appears to be less than on the Moon due to erosional processes.

The final unknown parameter, the electrical loss tangent, was varied over the range of values measured for particulate geological materials by Campbell and Ulrichs (1969). For a material density of 1.6 g/cm^3 ' this range is

$$.003 < \tan \Delta < .015$$

These two values, representing the extreme limits on reasonable values for $\tan \Delta$, were used in the model calculations. As these are rather extreme limits, we also compute spectra using a lunar loss tangent of $\tan \Delta = .0075$. The parameter $\delta = Le/L_T$ may be computed from the parameters used for the purpose of comparison with previous models. A range of $\tan \Delta$ of .003 - .015 and other parameters as previously mentioned yields a range for δ of $1.2\lambda - 6.5\lambda$. For $\tan\Delta = .0075$, $\delta = 2.9\lambda$. If the Moon and Mercury had Mars' diurnal period and the thermal conductivity derived from infrared observations of Mars, they would each have an observed value of $\delta \sim 3\lambda$ where λ is the wavelength of observation (Epstein, 1971).

10.1 Results and Comparisons With Thermal Infrared Data

The model has been tested in several ways. Besides reproducing the polar cap behavior observed by Capen and Capen, it has been utilized to reproduce the infrared data. The objection to all simple dry models has been raised by Sagan and Veverka (1971) that the latitude scans made by Sinton and Strong (1960) in 1954 do not fit the cosine dependence of the analytical theory, $(T(\theta) \sim \mathrm{Cos}^{\frac{1}{4}}\theta)$. They propose this as possible evidence for latent heat exchange of water vapor to liquid water in mid-latitudes. The observable disk of Mars was reproduced for July 2, 1954 and surface thermometric temperatures were computed over it. The disk was then scanned in latitude in a manner designed to duplicate the experimental scans of Sinton and Strong. The resultant curve of temperature vs. latitude fits the data as reduced and presented by Morrison, Sagan and Pollack (1969) to well within the accuracy of the data, as shown in Fig. 33. We find no indication of the excess flux at temperate latitudes which Sagan and Veverka (1971) ascribe to latent heat release of condensing water vapor.

10.2 Results and Comparison With Microwave Data

Computed results consisting of "expected" spectra of Mars from $\lambda =$ 1mm to $\lambda = 21$cm were obtained for the favorable oppositions of 1965, 1967, 1969, and 1971. These spectra are plotted along with a sketch of the planet's appearance at each opposition in Fig. 34. Also plotted in Fig. 34 are analytically predicted spectra for $\delta = 2\lambda$ and $\delta = 10\lambda$. (Sagan and Veverka, 1971). The magnitude of the upturn predicted at short wavelengths for the $\delta = 2\lambda$ case is several times as large as a typical observational error. An upturn of this magnitude would be seen in the data if the analytical model accurately represented reality. The curve for $\delta = 10\lambda$ represents a significantly different surface nature than is observed for either the Moon

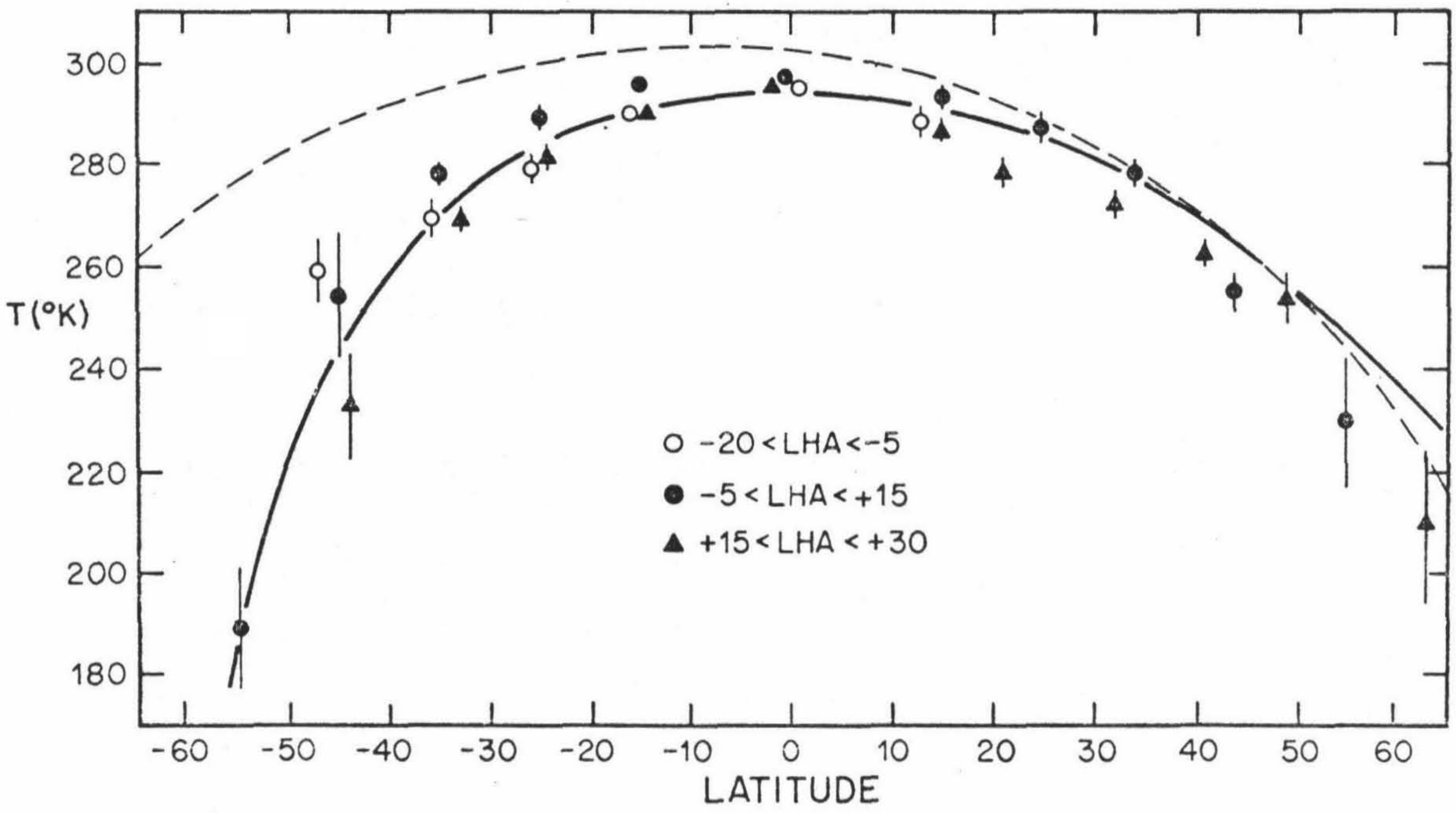

Fig. 33: Model prediction of a latitude scan at the favorable opposition of 1954 is shown by the solid curve. Points are data from Sinton and Strong (1960) as compiled by Morrison, Sagan, and Pollack (1969). The dashed curve is the prediction of the analytical theory for $\gamma = .004$ from the same paper, neglecting seasonal effects. The local hour angle (LHA) of the Sun is in degrees.

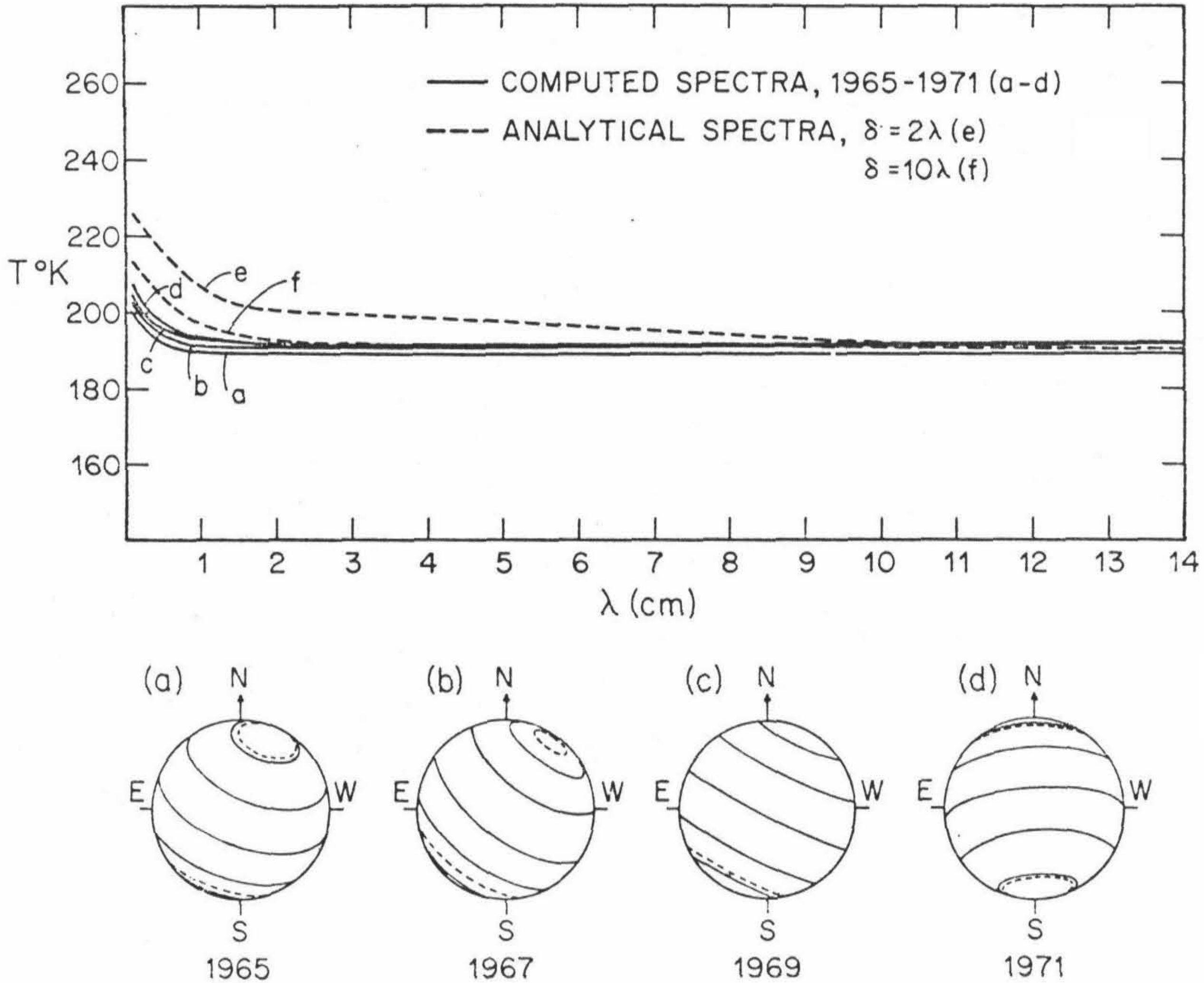

Fig. 34: Predicted microwave spectra and apparent disks of Mars as seen from the Earth, reproduced for the oppositions of 1965, 1967, 1969, and 1971. (a-d): model-generated spectra for a lunar-like loss tangent of .0075; (e) analytically predicted spectrum, $\delta = 2\lambda$; (f) analytically predicted spectrum, $\delta = 10\lambda$.

or Mercury, when differences in rotation rates are removed.

The parameters used were fixed by previous observations with the exception of the loss tangent, which was varied over a range of experimentally determined values. It is shown in Fig. 35 that spectra computed using these parameters are still rigorously "normal" in shape, but that the amplitudes of the temperature differences from .1 to 21 cm are smaller than the error of a typical measurement. For comparison with these spectra, the data as published has to be corrected from their quoted values "at mean distance from the sun" to the value at the time of observation.

On the assumption that the data really represent flat spectra, the measurements for each year were averaged as weighted by the inverse square of the quoted errors. Those averages are shown on each graph. We emphasize that no "model-fitting" went on here. The physical parameters are all taken straight from various other data. It is interesting to note that the 1971 opposition afforded the best opportunity to see any deviation of the spectrum from constancy. Recent observations at 3.1mm by Ulich et al. for this opposition yield a value of $T_B = 227 \pm 16^\circ$ K, when de-corrected from mean solar distance to the value at the date of observation. This value is shown in Fig. 35. Also shown in Fig. 35 for 1971 is the result of a week's interferometric observations at 3.71cm. This result and associated uncertainties in absolute calibration have been discussed in Part II, Section 5.5.

The general cause of the flattening of the microwave spectrum is the averaging together of usual "normal" daylight side spectra with previously ignored "inverted" spectra which occur on and near the edge of the polar caps. It is the case that, even in this simple thermophysical model, there are regions on the daylight side of the planet at which the temperature

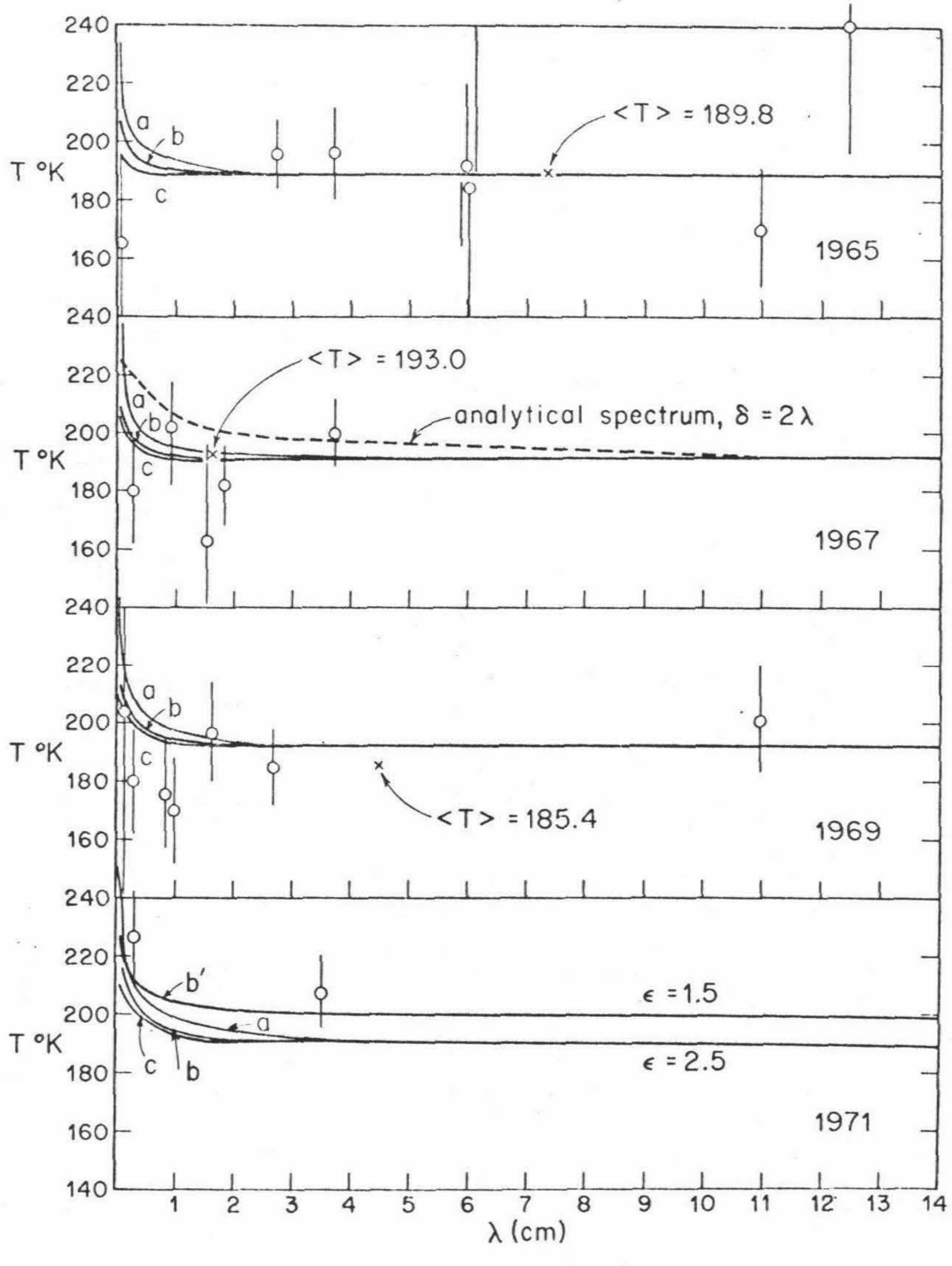

Fig. 35: Microwave spectra of Mars for the four most recent oppositions. Model generated spectra (smooth curves) employ (a) loss tangent = .015 (b) loss tangent =.0075 (c) loss tangent= .003. All spectra refer to a dielectric constant of 2.5, except one which employs a value of 1.5 (labeled b' in the bottom panel). The mean observed brightness temperature for each opposition is shown by a cross.

increases with depth. For instance, Fig. 36 shows temperature as a function of depth at the edge of the growing south polar cap (autumn in the south) at noon. Since the radio emission is in the Rayleigh-Jeans part of the spectrum, temperatures average linearly with flux at microwave frequencies and areas of low temperature are weighted in the effective average equally with high temperature areas. This is of course not the case at infrared wavelengths, where high temperatures receive a much larger weight in the average. This is the reason why the distribution of low temperature areas is so important to microwave models.

11. Weaknesses of the Model and Implications for Future Observations

The fact that meaningful information is mainly found on Mars very close to the surface requires we mention some relevant weaknesses in the model:

(1) A finite step size in depth is used, i.e. a step size or layer depth of 1.5 cm close to the surface. If $L_e \sim 10\lambda$ this means that radiation at wavelength of .1cm or shorter begins to see the "grid size" of the depth layering. It is also means that subsurface temperature variation is lost if it is on a smaller scale than 1.5 cm, i.e., a very thin layer of frost, like hoarfrost, may be "seen" by .1 cm radiation and not seen by 1 cm radiation causing an even greater flattening of the measured spectra relative to the computed ones. It is imaginable that large areas covered very thinly by frost might even cause the entire spectrum to invert. Our model does not have the depth resolution to show this, if it indeed exists.

(2) Roughness and shadowing enter in several ways. In the presence of roughness there is some shadowing. Unless the earth is at precisely

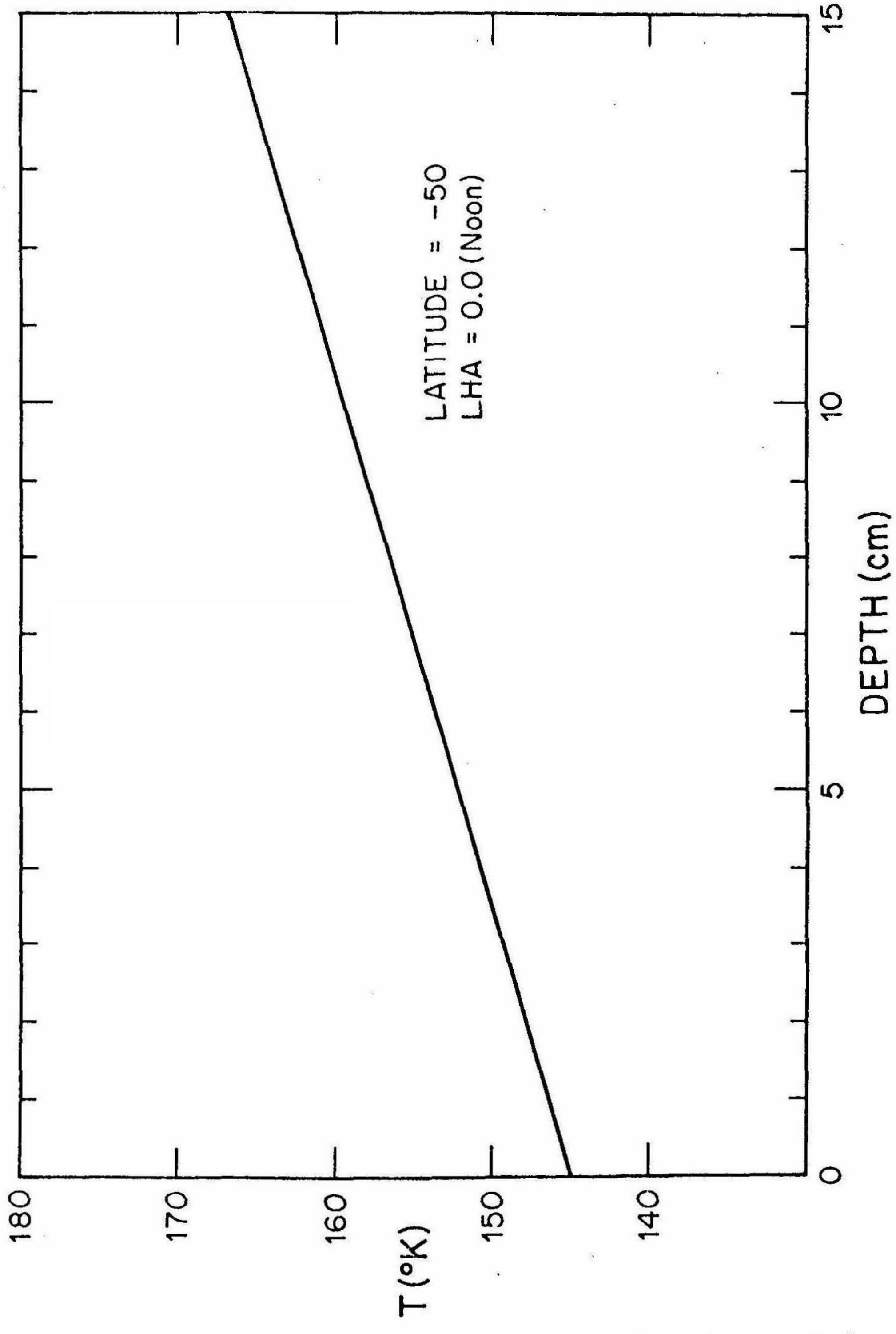

Fig. 36: Inverted temperature structure occurring at noon at the edge of the growing South polar cap.

the solar declination, shadows will be seen that are not accounted for in the model. The effect of a shadow on the surface is primarily to decrease the temperature at shallow depths and, because of its transience, not to affect greatly the temperature of deeper material. This would also tend to preferentially decrease effective temperatures at short radio wavelengths. The effective IR disk temperature is less dependent on low temperatures and would be less affected by their inclusion in the average. These effects have not yet been treated in our model.

(3) Dielectric variations of frost were not treated. On the basis of extrapolation of presently available laboratory data, it appears that there is little significant difference between the dielectric constants of CO_2 or H_2O frost and that of "dry soil" at these frequencies.

(4) A weakness common to both model and data is neglect of areal variations in surface topograghy and/or dielectric parameters. The quality of present microwave data does not justify a more complex treatment than presented here although topographical variations of the thermal inertia certainly do exist (Neugebauer, et al., 1971), and similar variations in dielectric constant are also to be expected. It is very likely that variation of the nature of sub-earth topography will affect the important millimeter temperatures and we suggest, as did Sagan and Veverka, that any extensive observing program at these short wavelengths correlate observed temperatures with the central meridian longitude of the apparent disk.

Suggestions for future experimental work

Naturally it is important to test this theory with more precise data, particularly as the current version of the model begins to lose credibility at wavelengths less than about .1 cm.

The spectrum of Jupiter or another source suitable for calibration should be carefully determined. These considerations would be less critical if the Martian spectrum turned up by 30-40° at short wavelengths, but we have shown in this paper that the magnitude of the entire upturn in this range is $\sim$ 10-15°K.

If one wishes to do analytical work on the nature of the subsurface of Mars, however, more than this is needed. The spectrum must be measured at several points along the effective "skin depth" of the upturn. It is evident from Fig. 34 that not only are the amplitudes of the upturns of the computed spectra less than had been previously expected, but the range of wavelengths over which this change occurs is also greatly limited. Whereas the analytical theory predicted microwave temperature structure over a range of .1 -4 or 5 cm observed wavelength, corresponding to the theoretical thermal skin depth of $L \cong 3.0$ cm, the present model indicates observable microwave temperature structure over a range of only about .1 - 1 cm, indicating a much smaller thermal skin depth, or giving the effect of greater apparent isothermality of the subsurface. This effect in the data has been mentioned by several observers. [Hobbs and Knapp, (1971), Epstein, (1971)].

The computed flattening of the spectrum is largely dependent on frost effects. If the dielectric constant of frosts at these frequencies is greatly different from our assumed value for dry soil, the microwave emissivities of these areas and their effective brightness temperatures will then be different. The spectrum will be significantly affected, particularly if thin frosts cover a large proportion of the surface. Consequently, laboratory measurements of the dielectric constants of various frosts at microwave frequencies will be a very important factor in understanding the observations.

12. Conclusion

It is our finding that a numerical thermophysical model of the Martian subsurface (uniform, homogeneous, lunar-type material) as supplemented by first-order treatment of CO_2 and H_2O vapor-solid thermodynamics provides a satisfactory fit to presently existing microwave spectral data when proper attention is paid to seasonal and geometric factors in their roles in determining the extent of polar areas on the apparent disk. That match is seen to be an essentially flat spectrum turning up slightly toward 1 mm by an amount that is comparable to the uncertainties in current data. We have used a single set of surface parameters in the results presented here. The mean brightness temperatures averaged over the longer wavelengths are in good agreement with calculations for $\epsilon = 2.5$ although a value as low as 1.5 is possible as can be seen in the bottom panel of Fig. 35. Although the surface density, ρ, is difficult to determine from remote observations, our adopted value of $\rho = 1.6$ gm/cm^3 is consistent with a surface dielectric constant in the range of 2.5 - 3.0, based on laboratory measurements of likely surface materials. See, e.g., Troitskii et al., (1970) for discussion. These results are in good agreement with the value of $\epsilon = 2.5 \pm .3$ (not corrected for the effects of roughness) obtained from independent interferometric observations.

An alternative model has been proposed by Sagan and Veverka (1971) which produces an inverted spectrum designed to approach a least-squares fit of the published data. The model involves an ad hoc assumption of a thin layer of liquid water near the surface. This hypothesis is difficult to reconcile with the liquid/vapor equilibrium of water at the Martian surface as discussed by Ingersoll (1970). We agree with Sagan and Veverka that the data do not fit the predictions of the conventional analytical theory. However, an accurate utilization of lunar-type surface properties in numerical calculations of the thermophysics including the thermodynamics of CO_2 and H_2O adequately explains the microwave spectral observations without the use of further assumptions. The average-disk microwave observations at millimeter wavelengths are simply not sufficiently sensitive to yield information on the existence of subsurface water and/or permafrost. It is unlikely that the accuracy of these measurements can be improved sufficiently to resolve these questions. Significant progress will require high-resolution interferometric measurements at short wavelengths. Clearly, high resolution spacecraft measurements utilizing an accurate flux calibration technique will be very important.

APPENDIX I

Given the temperature structure at and beneath the surface of a planet as a function of planetary latitude and solar hour angle, we wish to compute the brightness map over the disk of the planet as seen from earth at any given time.

We take (x,y,z) to be the co-ordinates of a surface element as related to basis (i,j,k) where k lies along the north pole of rotation, and i is oriented toward zero solar h.a. We wish to transform the co-ordinates (x',y',z') with basis (i',j',k') to this unprimed system. $\hat{i}'$ lies along the planet-earth line and k' lies along projected celestial north, or at position angle 0° in the plane of the sky.

A linear transformation $\underline{\underline{M}}$ is devised to transform the primed basis vectors into the unprimed basis vectors by combinations of rotations.

$$\begin{pmatrix} i \\ j \\ k \end{pmatrix} = \underline{\underline{M}} \begin{pmatrix} i' \\ j' \\ k' \end{pmatrix}$$

then since $\bar{V} = (xyz)\begin{pmatrix} i \\ j \\ k \end{pmatrix} = (x'y'z')\begin{pmatrix} i' \\ j' \\ k' \end{pmatrix}$

$$(xyz)\ \underline{\underline{M}} \begin{pmatrix} i' \\ j' \\ k' \end{pmatrix} = (x'y'z')\begin{pmatrix} i' \\ j' \\ k' \end{pmatrix}$$

$$(xyz)\ \underline{\underline{M}} = (x'y'z') \quad , \quad (xyz) = (x'y'z')\ \underline{\underline{M}}^{-1}$$

and $\underline{\underline{M}} = \underline{\underline{M}}^{T}$ (unitary) $\begin{pmatrix} x \\ y \\ z \end{pmatrix} = \underline{\underline{M}} \begin{pmatrix} x' \\ y' \\ z' \end{pmatrix}$

The actual transformation is composed of four steps. In each step, a rotation is performed about one of the current basis vectors. In other words, $\underline{\underline{M}}$ is the product of four simple rotation transformations.

$$\underline{\underline{M}} = [As]_z[-I]_{x'''}[-\gamma]_{z''}[-P]_{x'}$$

In this equation, positive rotation is in a right-hand sense, i.e. counter-clockwise, and the subscript denotes the axis of rotation. This gives

$$M = \begin{bmatrix} \text{Cos}A_s & \text{Sin}A_s & 0 \\ -\text{Sin}A_s & \text{Cos}A_s & 0 \\ 0 & 0 & 1 \end{bmatrix} \begin{bmatrix} 1 & 0 & 0 \\ 0 & \text{Cos}I & -\text{Sin}I \\ 0 & \text{Sin}I & \text{Cos}I \end{bmatrix} \begin{bmatrix} \text{Cos}\gamma & -\text{Sin}\gamma & 0 \\ \text{Sin}\gamma & \text{Cos}\gamma & 0 \\ 0 & 0 & 1 \end{bmatrix} \begin{bmatrix} 1 & 0 & 0 \\ 0 & \text{Cos}P & -\text{Sin}P \\ 0 & \text{Sin}P & \text{Cos}P \end{bmatrix}$$

where A_s = planetocentric right ascension of the sun (measured east from the planet's vernal equinox)

I = inclination of the planet's equator to its orbit

P = position angle of the pole of the planet's orbit

$\gamma = \text{Cos}^{-1}$ [CosAe CosDe]

(Ae, De) = planetocentric right ascension and declination of the earth.

(See Fig. 37 for definition of angles and geometry.)

Ae, De, and As are tabulated in the Nautical Ephemeris for a given date.

Given the co-ordinates of a surface element on the sub-earth disk of the planet (x', y', z'), we may then compute the co-ordinates of that point as related to planetary latitude and solar hour angle (J1, J2), by the complete transformation:

$$x = M_{11}x' + M_{12}y' + M_{13}z' \qquad J1 = \sin^{-1}(z)$$

$$y = M_{21}x' + M_{22}y' + M_{23}z' \qquad J2 = \tan^{-1}(y/x)$$

$$z = M_{31}x' + M_{32}y' + M_{33}z'$$

Where M_{11} = CosAs Cosγ + SinAs Sinγ CosI

M_{12} = SinAs CosI Cosγ CosP - SinI SinAs SinP - CosAs Sinγ CosP

M_{13} = CosAs SinP Sinγ - SinAs CosI SinP Cosγ - SinI SinAs CosP

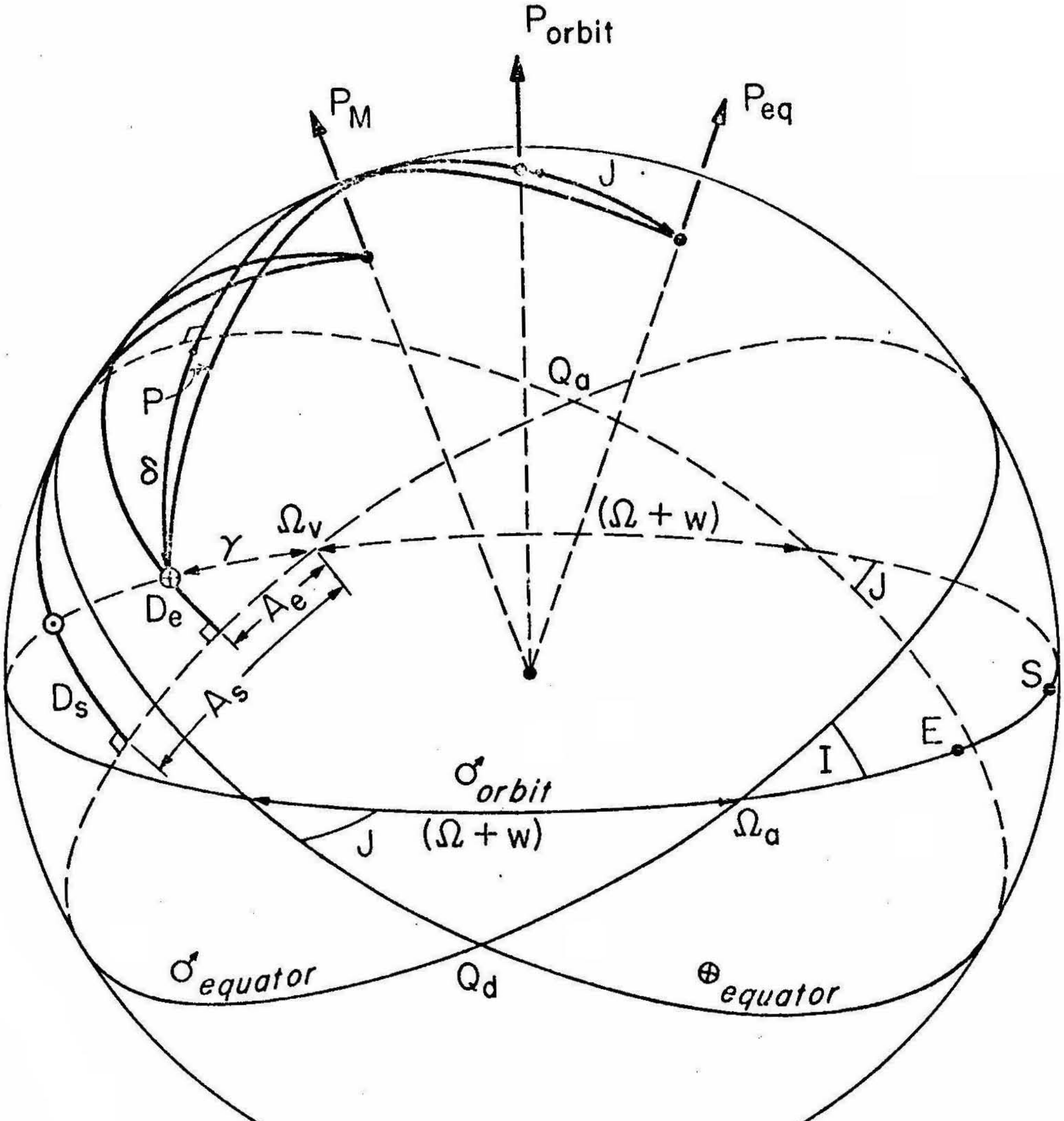

Fig. 37: Areocentric celestial sphere: (E, S) = geocentric and heliocentric positions of Mars, (⊕, ⊙) = areocentric positions of Earth and Sun, P = position angle of the normal to the orbit of Mars. P_M is the north pole of the axis of rotation of Mars, P_{eq} is the celestial north pole, and P_{orbit} is the north pole of the orbit of Mars. D_e and D_s are the Areocentric declinations of Earth and Sun, and A_e and A_s are the Areocentric right ascensions of Earth and Sun. Ω_v is the vernal equinox of Mars.

M_{21} = CosAs CosI Sinγ - SinAs Cosγ

M_{22} = SinAs Sinγ CosP + CosAs CosI Cosγ CosP - SinI SinP CosAs

M_{23} = -SinAs SinP Sinγ - CosAs CosI SinP Cosγ - SinI CosAs CosP

M_{31} = SinI Sinγ

M_{32} = SinI Cosγ CosP + CosI SinP

M_{33} = CosI CosP - SinI SinP Sinγ

In this case (Mars) the planetary orbit may for purposes of this calculation be assured parallel to the ecliptic and the Earth-Mars vector to lie in it. (Actually Mars' orbit is inclined by 1° 51' to the ecliptic.) The error due to this assumption depends on the orbital position of Mars at opposition but, is ~ 3° at its largest. This is small with respect to the width of a temperature band of latitude 10°. It is easily corrected by a further rotation, performed for desired dates near opposition. In the use of this technique for Mercury, having an orbit inclination of 7°, such a correction is obviously necessary.

Figures 38-49: Surface physical temperature maps and polarized brightness distributions for the last four oppositions. In each case, one surface temperature map and two pairs of polarized brightness maps will be shown. The brightness temperature maps are for wavelengths of λ = 0.9 cm. and λ = 21.0 cm. In the polarized brightness maps, the top map is in the polarization perpendicular to the baseline (for an east-west baseline) and the bottom map is in the polarization parallel to the baseline. NOTE: In all maps, celestial east is to the left and celestial north at the top of the page. The South polar cap is clearly visible as an isothermal region in figure 47, at a temperature of 147°K.

```
THE MATRIX OF SURFACE KINETIC TEMPERATURES

    0.    0.    0.    0.    0.    0.    0.    0.    0.    0.    0.    0.  209.    0.    0.    0.    0.    0.    0.    0.    0.    0.    0.    0.    0.
    0.    0.    0.    0.    0.    0.    0.    0.  223.  230.  239.  234.  230.  230.  230.  222.  219.    0.    0.    0.    0.    0.    0.    0.    0.
    0.    0.    0.    0.    0.    0.  216.  236.  243.  247.  252.  252.  242.  246.  240.  237.  234.  226.  204.    0.    0.    0.    0.    0.    0.
    0.    0.    0.    0.    0.  231.  242.  249.  253.  254.  257.  257.  257.  254.  251.  250.  244.  239.  231.  214.    0.    0.    0.    0.    0.
    0.    0.    0.    0.  222.  243.  252.  254.  261.  262.  262.  262.  251.  261.  261.  259.  257.  246.  244.  233.  205.    0.    0.    0.    0.
    0.    0.    0.  218.  241.  252.  259.  260.  263.  265.  255.  255.  265.  264.  264.  262.  259.  254.  251.  246.  227.  194.    0.    0.    0.
    0.    0.  214.  234.  247.  257.  262.  263.  265.  265.  265.  265.  253.  247.  256.  264.  240.  257.  254.  253.  246.  219.  196.    0.    0.
    0.    0.  227.  244.  250.  259.  265.  267.  268.  269.  269.  255.  269.  268.  267.  264.  262.  259.  256.  256.  252.  255.  194.    0.    0.
    0.  219.  234.  244.  250.  251.  265.  267.  269.  269.  270.  270.  270.  269.  259.  266.  265.  262.  260.  259.  253.  249.  205.  190.    0.
    0.  216.  239.  248.  254.  240.  265.  267.  269.  270.  271.  271.  271.  270.  269.  265.  268.  266.  263.  259.  253.  242.  216.  196.    0.
    0.  223.  242.  252.  259.  263.  266.  267.  269.  270.  271.  271.  271.  270.  269.  269.  267.  264.  262.  261.  254.  239.  224.  197.    0.
    0.  226.  243.  256.  257.  261.  264.  264.  265.  270.  271.  271.  271.  269.  265.  267.  265.  263.  250.  258.  252.  241.  220.  197.    0.
  200.  230.  245.  254.  256.  250.  263.  266.  268.  269.  270.  270.  270.  269.  266.  265.  264.  260.  256.  255.  251.  243.  223.  206.  190.
    0.  225.  234.  251.  254.  257.  259.  262.  265.  266.  266.  257.  264.  267.  256.  243.  261.  259.  257.  253.  245.  237.  219.  205.    0.
    0.  214.  233.  245.  253.  255.  258.  260.  264.  264.  255.  264.  264.  266.  266.  264.  240.  258.  255.  251.  241.  230.  217.  200.    0.
    0.  210.  225.  236.  244.  252.  255.  259.  262.  262.  262.  264.  265.  265.  265.  261.  257.  257.  257.  244.  235.  230.  211.  194.    0.
    0.  172.  215.  227.  239.  250.  252.  253.  255.  255.  254.  256.  259.  259.  259.  254.  250.  240.  251.  244.  229.  224.  202.  179.    0.
    0.    0.  203.  227.  239.  246.  248.  249.  248.  247.  251.  254.  255.  255.  256.  247.  242.  243.  244.  236.  224.  207.  194.    0.    0.
    0.    0.  160.  205.  219.  237.  243.  243.  243.  244.  246.  249.  252.  252.  252.  245.  231.  232.  234.  230.  215.  193.  181.    0.    0.
    0.    0.    0.  159.  204.  223.  237.  237.  240.  242.  242.  241.  241.  243.  245.  239.  229.  222.  224.  218.  205.  198.    0.    0.    0.
    0.    0.    0.    0.  176.  206.  222.  222.  237.  237.  237.  234.  233.  234.  233.  229.  219.  212.  210.  200.  198.    0.    0.    0.    0.
    0.    0.    0.    0.    0.  187.  199.  206.  214.  222.  222.  216.  215.  219.  223.  218.  211.  202.  194.  189.    0.    0.    0.    0.    0.
    0.    0.    0.    0.    0.    0.  160.  157.  181.  198.  206.  203.  195.  204.  208.  202.  198.  192.  180.    0.    0.    0.    0.    0.    0.
    0.    0.    0.    0.    0.    0.    0.    0.  164.  171.  183.  187.  191.  189.  184.  190.  179.    0.    0.    0.    0.    0.    0.    0.    0.
    0.    0.    0.    0.    0.    0.    0.    0.    0.    0.    0.    0.  169.    0.    0.    0.    0.    0.    0.    0.    0.    0.    0.    0.    0.
    0.0   1.5   2.3   3.8   5.3   6.3   8.3   9.8  11.3  12.8  14.3  22.5  37.5  52.5  67.5  82.5  97.5 112.5 127.5 142.5
  243.4 234.7 222.9 214.2 209.5 207.7 207.3 207.6 209.0 208.3 208.6 209.5 209.4 208.0 205.2 206.4 208.5 209.6 209.7 209.8
 DISK TEMP AT 5.0 MICRONS=241.56    FLUX=0.3507E-13
     DISK TEMP AT 10.5 MICRONS=247.42    FLUX=0.1381E-11
     DISK TEMP AT 20.0 MICRONS=244.11    FLUX=0.2804E-11
```

Fig. 38: Surface temperature map, 1965 opposition.

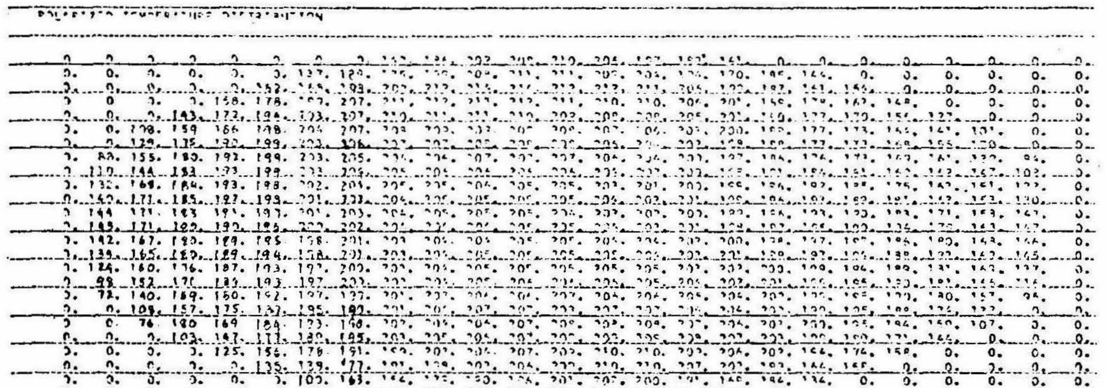

DIELECTRIC CONSTANT=2.5000
LOSS TANGENT=0.005
WAVELENGTH= 0.90CM

1965

Fig. 39: Polarized brightness distributions, 1965 opposition, λ = 0.9 cm.

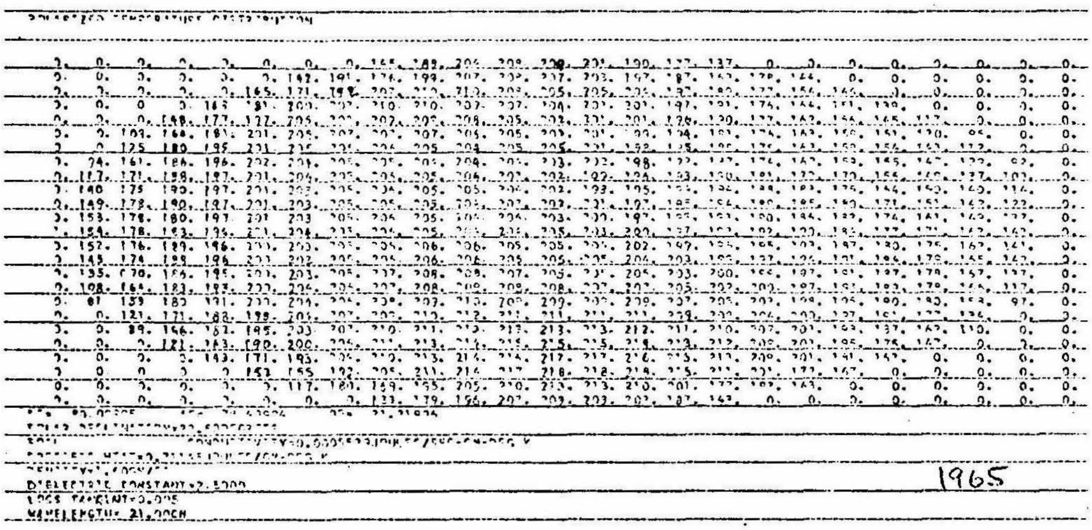

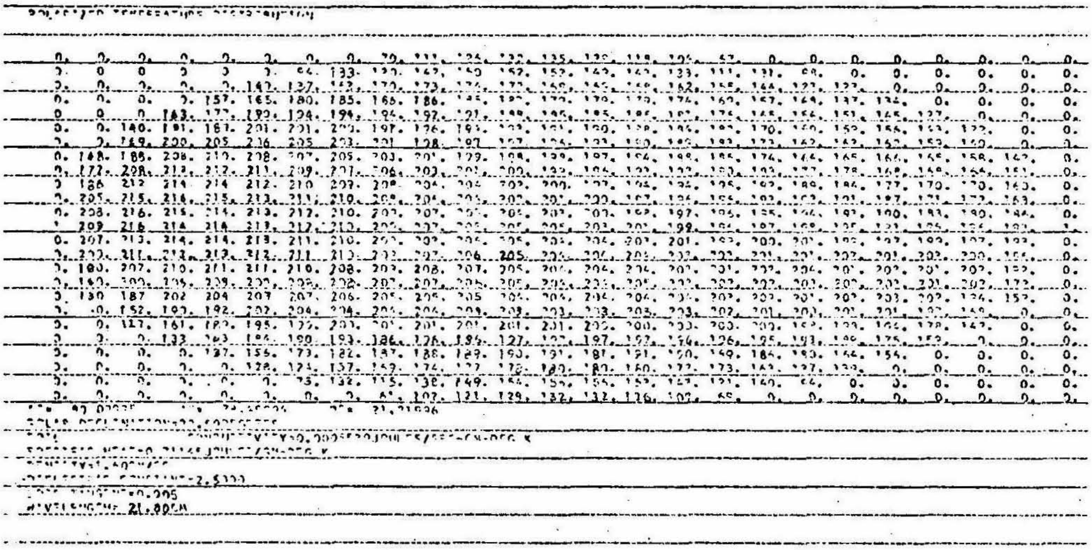

Fig. 40: Polarized brightness distributions, 1965 opposition, λ = 21.0 cm.

```
 THE MATRIX OF SURFACE KINETIC TEMPERATURES

   0.   0.   0.   0.   0.   0.   0.   0.   0.   0.   0.   0. 205.   0.   0.   0.   0.   0.   0.   0.   0.   0.   0.   0.   0.
   0.   0.   0.   0.   0.   0.   0.   0. 209. 210. 221. 224. 227. 227. 228. 218. 213.   0.   0.   0.   0.   0.   0.   0.   0.
   0.   0.   0.   0.   0.   0. 214. 222. 222. 230. 236. 239. 241. 243. 244. 240. 237. 225. 207.   0.   0.   0.   0.   0.   0.
   0.   0.   0.   0.   0. 227. 229. 233. 240. 245. 246. 247. 249. 250. 251. 251. 249. 239. 227. 219.   0.   0.   0.   0.   0.
   0.   0.   0.   0. 215. 233. 238. 241. 252. 254. 255. 256. 256. 257. 258. 258. 257. 248. 244. 232. 214.   0.   0.   0.   0.
   0.   0.   0. 213. 234. 232. 246. 249. 256. 260. 262. 262. 262. 263. 263. 263. 260. 257. 257. 246. 233. 207.   0.   0.   0.
   0.   0. 223. 229. 237. 249. 252. 255. 258. 263. 267. 269. 268. 268. 268. 265. 262. 261. 260. 257. 242. 226. 199.   0.   0.
   0.   0. 226. 239. 244. 254. 258. 261. 263. 265. 269. 269. 270. 270. 270. 268. 267. 265. 263. 263. 254. 245. 213.   0.   0.
   0. 205. 240. 247. 252. 259. 262. 265. 267. 269. 271. 271. 271. 271. 271. 271. 271. 270. 269. 269. 263. 259. 233. 191.   0.
   0. 223. 241. 248. 253. 253. 266. 269. 271. 273. 274. 274. 274. 274. 274. 275. 275. 275. 275. 269. 266. 266. 256. 195.   0.
   0. 228. 245. 246. 255. 262. 266. 269. 272. 273. 274. 275. 275. 275. 275. 275. 275. 275. 274. 273. 270. 269. 265. 230.   0.
   0. 233. 246. 245. 257. 264. 268. 270. 273. 273. 274. 275. 276. 275. 275. 275. 274. 274. 274. 271. 267. 267. 259. 198.   0.
 205. 235. 247. 249. 258. 265. 269. 272. 274. 274. 274. 276. 277. 277. 276. 275. 273. 273. 273. 269. 264. 264. 249. 206. 179.
   0. 231. 239. 249. 257. 264. 269. 270. 271. 272. 274. 275. 277. 275. 273. 273. 272. 272. 271. 266. 260. 254. 237. 201.   0.
   0. 216. 237. 249. 257. 264. 267. 269. 270. 272. 274. 276. 276. 275. 273. 272. 272. 271. 269. 264. 255. 244. 233. 231.   0.
   0. 210. 233. 248. 251. 258. 268. 269. 258. 271. 273. 275. 276. 273. 270. 271. 271. 270. 269. 259. 261. 245. 225. 188.   0.
   0. 195. 230. 235. 246. 256. 260. 262. 264. 267. 270. 270. 271. 269. 264. 265. 266. 265. 265. 259. 246. 241. 215. 178.   0.
   0.   0. 225. 217. 240. 249. 251. 254. 262. 263. 268. 265. 269. 267. 263. 259. 260. 260. 260. 253. 234. 225. 197.   0.   0.
   0.   0. 192. 217. 229. 247. 251. 250. 249. 260. 266. 266. 266. 262. 258. 253. 251. 252. 253. 244. 219. 206. 182.   0.   0.
   0.   0.   0. 189. 216. 237. 251. 245. 246. 253. 257. 259. 261. 253. 246. 249. 245. 244. 246. 229. 206. 185.   0.   0.   0.
   0.   0.   0.   0. 184. 212. 226. 231. 233. 243. 248. 252. 256. 245. 233. 238. 242. 229. 231. 209. 183.   0.   0.   0.   0.
   0.   0.   0.   0.   0. 192. 211. 217. 220. 229. 231. 236. 241. 231. 222. 224. 218. 213. 209. 195.   0.   0.   0.   0.   0.
   0.   0.   0.   0.   0.   0. 176. 191. 197. 207. 214. 220. 225. 218. 210. 206. 199. 194. 180.   0.   0.   0.   0.   0.   0.
   0.   0.   0.   0.   0.   0.   0.   0. 173. 180. 197. 193. 200. 202. 204. 189. 179.   0.   0.   0.   0.   0.   0.   0.   0.
   0.   0.   0.   0.   0.   0.   0.   0.   0.   0.   0.   0. 175.   0.   0.   0.   0.   0.   0.   0.   0.   0.   0.   0.   0.
   0.0   0.8   2.3   3.8   5.3   6.8   8.3   9.8  11.3  12.8  14.3  22.5  37.5  52.5  67.5  82.5  97.5 112.5 127.5 142.5
 249.4 241.1 224.6 214.9 210.2 208.9 209.1 209.6 210.2 210.4 210.4 209.9 209.5 209.4 209.4 209.5 209.6 209.7 209.8 209.8
 DISK TEMP AT 5.0 MICRONS=257.49   FLUX=0.4598E-13
    DISK TEMP AT 10.5 MICRONS=253.30   FLUX=0.1563E-11
    DISK TEMP AT 20.0 MICRONS=250.95   FLUX=0.3014E-11
```

Fig. 41: Surface temperature map, 1967 opposition.

```
POLARIZED TEMPERATURE DISTRIBUTION

   0.    0.    0.    0.    0.    0.    0.    0.  141.  185.  202.  209.  210.  209.  203.  188.  143.    0.    0.    0.    0.    0.    0.    0.    0.
   0.    0.    0.    0.    0.    0.  135.  163.  174.  199.  209.  213.  214.  213.  209.  200.  175.  150.  140.    0.    0.    0.    0.    0.    0.
   0.    0.    0.    0.    0.  160.  166.  197.  207.  213.  216.  217.  216.  217.  215.  212.  207.  197.  166.  163.    0.    0.    0.    0.    0.
   0.    0.    0.    0.  154.  176.  197.  206.  211.  214.  215.  216.  216.  216.  214.  212.  204.  204.  196.  177.  159.    0.    0.    0.    0.
   0.    0.    0.  139.  168.  192.  202.  207.  211.  212.  213.  214.  214.  213.  213.  210.  207.  205.  201.  191.  171.  141.    0.    0.    0.
   0.    0.   97.  154.  182.  195.  202.  206.  209.  211.  212.  212.  212.  211.  211.  208.  207.  204.  201.  194.  183.  157.  165.    0.    0.
   0.    0.  125.  167.  186.  196.  202.  205.  208.  209.  210.  210.  209.  204.  205.  206.  205.  202.  199.  194.  187.  173.  151.    0.    0.
   0.   85.  153.  175.  189.  197.  202.  205.  207.  208.  208.  208.  208.  208.  208.  206.  203.  200.  196.  193.  180.  179.  156.   99.    0.
   0.  108.  163.  181.  190.  196.  201.  204.  206.  207.  208.  206.  207.  207.  207.  205.  202.  200.  197.  193.  180.  181.  165.  115.    0.
   0.  131.  167.  181.  190.  195.  200.  203.  205.  206.  207.  207.  207.  206.  206.  204.  201.  200.  198.  193.  180.  182.  170.  136.    0.
   0.  139.  169.  179.  189.  196.  200.  202.  205.  205.  206.  206.  206.  206.  205.  204.  201.  200.  197.  194.  188.  182.  171.  145.    0.
   0.  143.  164.  179.  189.  195.  200.  202.  204.  205.  206.  206.  206.  205.  204.  203.  200.  199.  196.  193.  187.  182.  171.  146.    0.
   0.  144.  169.  177.  187.  195.  199.  202.  204.  205.  205.  206.  206.  205.  204.  202.  203.  199.  197.  193.  187.  181.  171.  149.    0.
   0.  142.  165.  179.  188.  195.  199.  201.  203.  204.  205.  205.  206.  205.  204.  202.  201.  199.  197.  193.  185.  181.  170.  147.    0.
   0.  132.  164.  174.  188.  195.  199.  201.  203.  204.  205.  205.  206.  206.  205.  204.  202.  200.  197.  194.  185.  180.  170.  144.    0.
   0.  123.  160.  175.  186.  193.  199.  201.  202.  204.  205.  205.  206.  206.  205.  204.  203.  200.  197.  194.  189.  181.  170.  137.    0.
   0.   99.  156.  174.  184.  193.  198.  200.  202.  204.  206.  206.  206.  206.  205.  204.  203.  201.  199.  195.  189.  182.  165.  115.    0.
   0.   75.  141.  180.  182.  191.  196.  200.  203.  205.  207.  207.  207.  207.  206.  205.  204.  202.  200.  195.  189.  175.  150.   93.    0.
   0.    0.  116.  161.  176.  190.  196.  199.  202.  206.  205.  208.  206.  206.  207.  206.  205.  203.  201.  195.  168.  174.  132.    0.    0.
   0.    0.   91.  140.  171.  187.  197.  199.  203.  205.  206.  209.  209.  209.  208.  207.  206.  203.  200.  195.  184.  159.  108.    0.    0.
   0.    0.    0.  119.  153.  170.  193.  196.  202.  205.  206.  209.  211.  210.  209.  208.  207.  204.  200.  191.  171.  144.    0.    0.    0.
   0.    0.    0.    0.  155.  161.  183.  195.  202.  205.  207.  209.  211.  211.  210.  209.  207.  203.  195.  175.  150.    0.    0.    0.    0.
   0.    0.    0.    0.    0.  144.  152.  162.  186.  202.  206.  209.  211.  211.  211.  205.  204.  194.  166.  159.    0.    0.    0.    0.    0.
   0.    0.    0.    0.    0.    0.  115.  169.  160.  180.  195.  203.  204.  205.  203.  194.  171.  185.  157.    0.    0.    0.    0.    0.    0.
   0.    0.    0.    0.    0.    0.    0.    0.  124.  173.  192.  197.  197.  199.  199.  180.  131.    0.    0.    0.    0.    0.    0.    0.    0.
AS= 121.73564     AE= 115.65960     DE= 20.80990
SOLAR DECLINATION=22.50DEGREES
SOIL          CONDUCTIVITY=0.0005539JOULES/SEC-CM-DEG K
SPECIFIC HEAT=0.71145JOULES/GM-DEG K
DENSITY=1.60GM/CC
DIELECTRIC CONSTANT=2.5000
LOSS TANGENT=0.005
WAVELENGTH= 0.90CM
```

1967

```
POLARIZED TEMPERATURE DISTRIBUTION

   0.    0.    0.    0.    0.    0.    0.    0.   65.  107.  124.  133.  134.  133.  126.  105.   66.    0.    0.    0.    0.    0.    0.    0.    0.
   0.    0.    0.    0.    0.    0.   85.  133.  118.  141.  151.  150.  157.  156.  152.  142.  119.  138.   92.    0.    0.    0.    0.    0.    0.
   0.    0.    0.    0.    0.  135.  153.  160.  173.  175.  178.  179.  180.  179.  178.  175.  170.  160.  134.  136.    0.    0.    0.    0.    0.
   0.    0.    0.    0.  147.  166.  177.  184.  187.  187.  190.  190.  190.  190.  184.  187.  185.  182.  176.  160.  153.    0.    0.    0.    0.
   0.    0.    0.  152.  164.  185.  191.  194.  195.  196.  196.  196.  196.  196.  195.  194.  192.  192.  190.  184.  171.  154.    0.    0.    0.
   0.    0.  127.  170.  185.  195.  196.  199.  200.  203.  200.  199.  193.  199.  199.  192.  197.  197.  197.  194.  189.  173.  130.    0.    0.
   0.    0.  157.  188.  196.  201.  202.  202.  203.  203.  202.  202.  201.  201.  201.  201.  200.  199.  199.  196.  197.  192.  164.    0.    0.
   0.  134.  167.  193.  202.  204.  205.  205.  205.  204.  204.  203.  203.  203.  203.  202.  201.  200.  199.  200.  201.  200.  192.  140.    0.
   0.  155.  198.  204.  205.  205.  206.  206.  206.  205.  205.  204.  204.  204.  204.  203.  202.  202.  202.  202.  203.  204.  201.  165.    0.
   0.  184.  203.  205.  206.  205.  207.  207.  207.  206.  206.  205.  205.  205.  205.  204.  203.  204.  205.  203.  204.  206.  206.  192.    0.
   0.  192.  204.  203.  206.  207.  207.  207.  207.  205.  206.  206.  206.  205.  205.  205.  204.  204.  205.  205.  204.  206.  207.  197.    0.
   0.  195.  205.  204.  206.  207.  208.  207.  207.  207.  206.  205.  205.  205.  205.  204.  203.  204.  206.  205.  204.  206.  207.  202.    0.
   1.  196.  205.  206.  206.  207.  206.  207.  207.  205.  205.  206.  206.  205.  205.  204.  203.  204.  206.  205.  204.  206.  207.  202.    1.
   0.  192.  203.  203.  206.  207.  207.  206.  205.  205.  206.  205.  205.  205.  205.  204.  204.  204.  205.  205.  205.  205.  206.  201.    0.
   0.  182.  198.  203.  205.  206.  206.  206.  205.  205.  205.  205.  205.  205.  205.  205.  205.  204.  205.  206.  206.  204.  206.  195.    0.
   0.  173.  194.  201.  203.  203.  206.  205.  204.  204.  205.  204.  204.  204.  204.  204.  204.  204.  204.  205.  205.  205.  206.  193.    0.
   0.  145.  169.  195.  196.  203.  203.  202.  202.  203.  203.  203.  203.  203.  203.  203.  203.  203.  204.  204.  204.  205.  201.  170.    0.
   0.  119.  174.  187.  194.  197.  199.  200.  201.  201.  202.  202.  202.  202.  202.  201.  201.  202.  203.  203.  202.  200.  192.  147.    0.
   0.    0.  145.  179.  187.  194.  195.  197.  197.  199.  200.  200.  200.  200.  199.  195.  199.  200.  200.  200.  196.  194.  165.    0.    0.
   0.    0.  116.  154.  177.  187.  193.  192.  193.  195.  196.  196.  197.  197.  196.  196.  197.  196.  196.  195.  191.  175.  156.    0.    0.
   0.    0.    0.  129.  153.  172.  183.  195.  177.  187.  191.  192.  193.  192.  192.  192.  192.  191.  185.  185.  171.  152.    0.    0.    0.
   0.    0.    0.    0.  124.  146.  165.  174.  177.  181.  183.  184.  185.  186.  185.  185.  185.  182.  175.  159.  151.    0.    0.    0.    0.
   0.    0.    0.    0.    0.  120.  121.  143.  161.  167.  170.  172.  174.  175.  174.  172.  167.  156.  132.  133.    0.    0.    0.    0.    0.
   0.    0.    0.    0.    0.    0.   77.  122.  103.  132.  144.  148.  150.  150.  147.  138.  110.  135.   69.    0.    0.    0.    0.    0.    0.
   0.    0.    0.    0.    0.    0.    0.    0.   55.   97.  116.  124.  126.  125.  120.  104.   65.    0.    0.    0.    0.    0.    0.    0.    0.
AS= 121.73564     AE= 115.65960     DE= 20.80990
SOLAR DECLINATION=22.50DEGREES
SOIL          CONDUCTIVITY=0.0005539JOULES/SEC-CM-DEG K
SPECIFIC HEAT=0.71145JOULES/GM-DEG K
DENSITY=1.60GM/CC
DIELECTRIC CONSTANT=2.5000
LOSS TANGENT=0.005
WAVELENGTH= 0.90CM
```

Fig. 42: Polarized brightness distributions, 1967 opposition, λ = 0.9 cm.

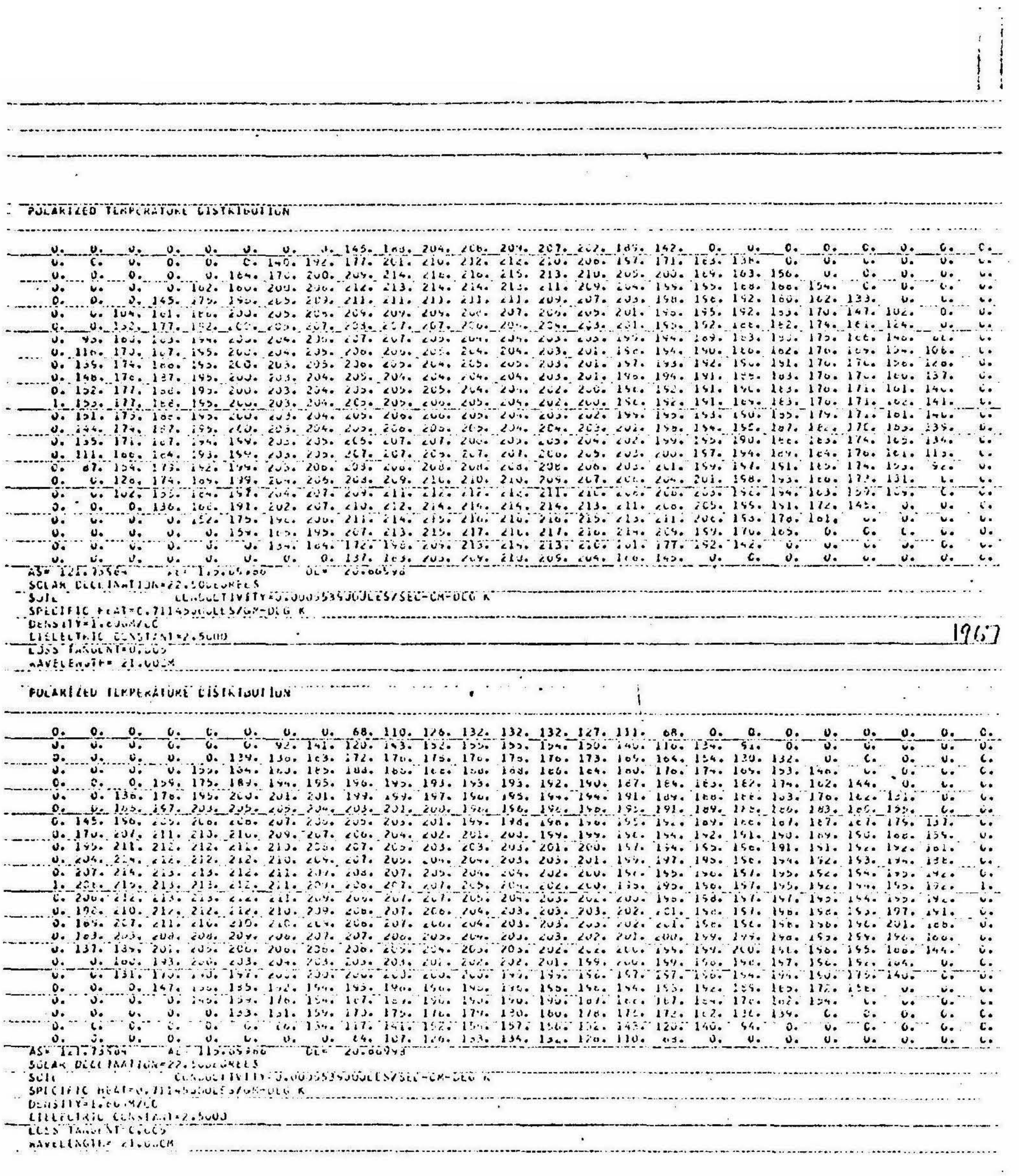

POLARIZED TEMPERATURE DISTRIBUTION

1967

POLARIZED TEMPERATURE DISTRIBUTION

Fig. 43: Polarized brightness distributions, 1967 opposition, $\lambda = 21.0$ cm.

```
     THE MATRIX OF SURFACE KINETIC TEMPERATURES

    0.   0.   0.   0.   0.   0.   0.   0.   0.   0.   0.   0. 221.   0.   0.   0.   0.   0.   0.   0.   0.   0.   0.   0.   0.
    0.   0.   0.   0.   0.   0.   0.   0. 219. 227. 241. 243. 245. 234. 222. 213. 210.   0.   0.   0.   0.   0.   0.   0.   0.
    0.   0.   0.   0.   0.   0. 212. 233. 240. 248. 256. 258. 260. 251. 241. 235. 230. 223. 210.   0.   0.   0.   0.   0.   0.
    0.   0.   0.   0.   0. 222. 243. 249. 254. 262. 265. 267. 269. 260. 252. 252. 247. 241. 234. 222.   0.   0.   0.   0.   0.
    0.   0.   0.   0. 210. 245. 256. 258. 270. 272. 274. 275. 276. 269. 262. 262. 262. 251. 250. 239. 219.   0.   0.   0.   0.
    0.   0.   0. 226. 242. 255. 263. 267. 274. 277. 280. 281. 282. 275. 269. 268. 265. 261. 260. 253. 241. 219.   0.   0.   0.
    0.   0. 145. 226. 247. 265. 268. 271. 275. 281. 285. 286. 287. 292. 276. 272. 268. 266. 264. 263. 251. 236. 211.   0.   0.
    0.   0. 167. 241. 260. 272. 272. 276. 280. 283. 286. 287. 287. 285. 281. 275. 273. 271. 269. 268. 259. 249. 221.   0.   0.
    0. 149. 244. 258. 270. 275. 278. 281. 284. 285. 287. 287. 287. 284. 292. 280. 279. 276. 273. 271. 263. 249. 232. 201.   0.
    0. 164. 246. 263. 271. 276. 283. 286. 288. 283. 288. 289. 287. 297. 297. 296. 284. 281. 278. 270. 266. 250. 238. 219.   0.
    0. 174. 245. 262. 272. 279. 283. 286. 288. 289. 288. 288. 288. 287. 297. 286. 285. 282. 278. 274. 266. 250. 247. 222.   0.
    0. 226. 249. 267. 272. 279. 283. 286. 289. 289. 290. 289. 289. 287. 287. 286. 285. 282. 290. 275. 266. 254. 248. 230.   0.
  147. 239. 256. 262. 272. 279. 283. 286. 289. 290. 291. 290. 289. 289. 286. 286. 286. 284. 281. 277. 263. 257. 244. 235. 187.
    0. 225. 256. 265. 269. 275. 279. 282. 285. 286. 287. 286. 290. 288. 287. 285. 284. 280. 276. 274. 263. 258. 243. 236.   0.
    0. 220. 254. 267. 257. 271. 277. 280. 283. 284. 286. 289. 291. 290. 288. 286. 283. 278. 275. 271. 268. 259. 246. 235.   0.
    0. 196. 233. 261. 264. 269. 275. 278. 280. 281. 282. 287. 291. 289. 287. 284. 281. 276. 271. 267. 259. 255. 237. 207.   0.
    0. 176. 226. 248. 251. 259. 272. 273. 275. 276. 277. 282. 287. 285. 283. 280. 277. 272. 267. 264. 250. 242. 224. 175.   0.
    0.   0. 205. 228. 249. 266. 269. 269. 269. 271. 277. 282. 284. 283. 282. 276. 273. 268. 263. 257. 242. 217. 205.   0.   0.
    0.   0. 191. 207. 230. 253. 256. 255. 257. 265. 272. 277. 262. 281. 279. 275. 268. 263. 258. 251. 223. 237. 177.   0.   0.
    0.   0.   0. 203. 215. 223. 242. 244. 251. 259. 255. 268. 277. 275. 274. 271. 266. 257. 252. 240. 220. 172.   0.   0.   0.
    0.   0.   0.   0. 200. 212. 228. 229. 245. 245. 246. 259. 272. 270. 269. 265. 262. 245. 241. 224. 196.   0.   0.   0.   0.
    0.   0.   0.   0.   0. 212. 214. 215. 223. 231. 231. 238. 245. 243. 242. 246. 243. 233. 217. 191.   0.   0.   0.   0.   0.
    0.   0.   0.   0.   0.   0. 199. 215. 216. 213. 217. 217. 217. 216. 215. 216. 211. 196. 177.   0.   0.   0.   0.   0.   0.
    0.   0.   0.   0.   0.   0.   0.   0. 200. 197. 195. 195. 195. 194. 194. 183. 179.   0.   0.   0.   0.   0.   0.   0.   0.
    0.   0.   0.   0.   0.   0.   0.   0.   0.   0.   0.   0. 178.   0.   0.   0.   0.   0.   0.   0.   0.   0.   0.   0.   0.
    0.0   0.8   2.3   3.8   5.3   6.8   8.3   9.8  11.3  12.8  14.3  22.5  37.5  52.5  67.5  82.5  97.5 112.5 127.5 142.5
  258.5 248.4 228.0 215.9 210.4 209.7 209.8 209.3 209.8 210.0 209.8 208.6 207.9 207.8 207.9 208.1 208.5 208.6 208.6 208.6
  DISK TEMP AT 5.0 MICRONS=258.28    FLUX=0.7197E-13
     DISK TEMP AT 10.5 MICRONS=263.38    FLUX=0.1923E-11
     DISK TEMP AT 20.0 MICRONS=260.52    FLUX=0.3370E-11
```

Fig. 44: Surface temperature map, 1969 opposition.

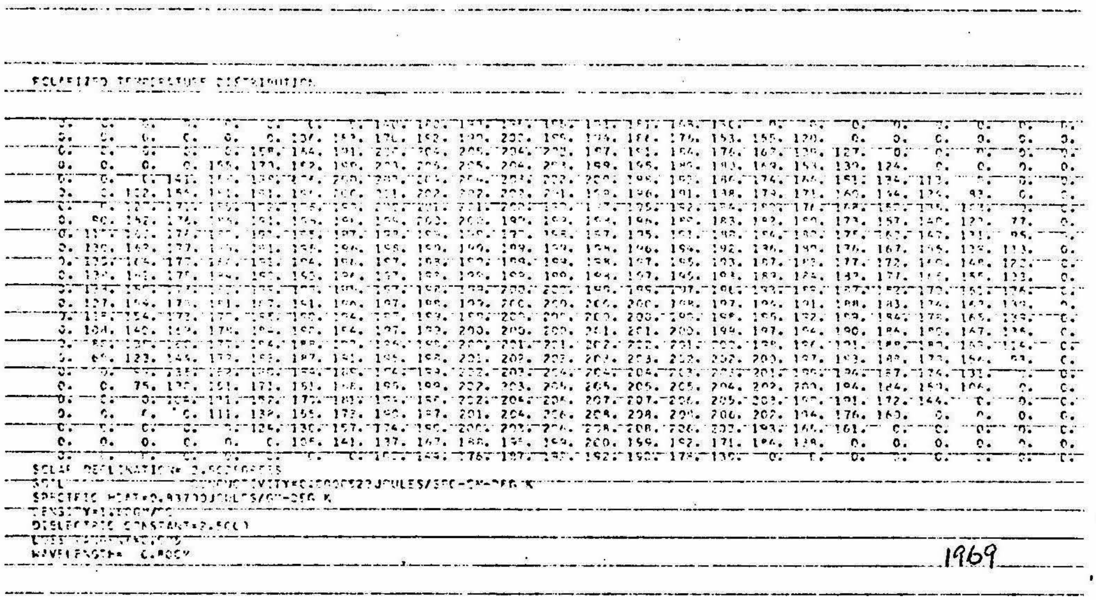

1969

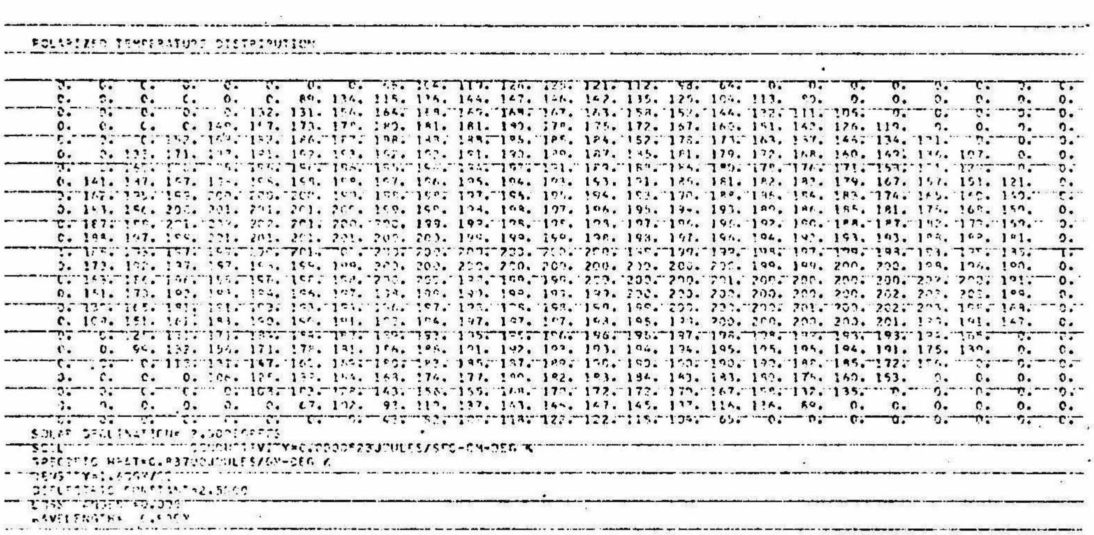

Fig. 45: Polarized brightness distributions, 1969 opposition , λ = 0.9 cm.

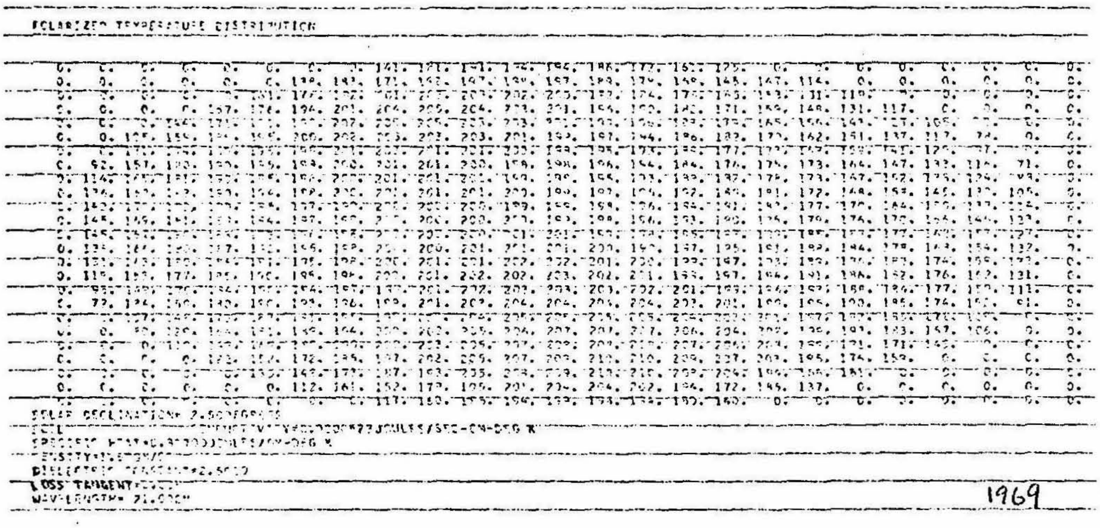

1969

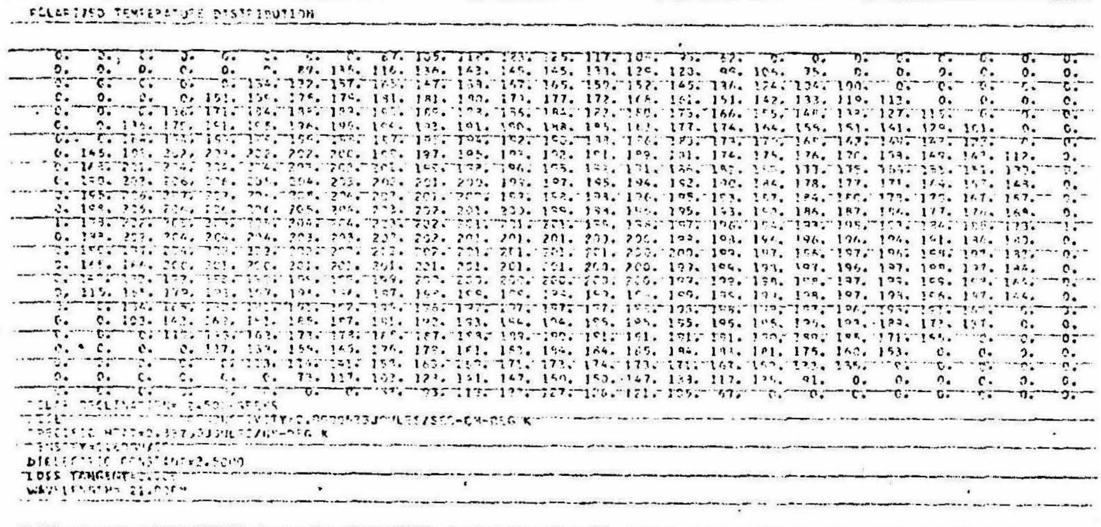

Fig. 46: Polarized brightness distributions, 1969 opposition, λ = 21.0 cm.

```
THE MATRIX OF SURFACE KINETIC TEMPERATURES
   0.   0.   0.   0.   0.   0.   0.   0.   0.   0.   0.   0 209.   0.   0.   0.   0.   0.   0.   0.   0.   0.   0.   0.   0.
   0.   0.   0.   0.   0.   0.   0.   0. 219. 223. 234. 230. 227. 223. 219. 214. 214.   0.   0.   0.   0.   0.   0.   0.   0.
   0.   0.   0.   0.   0.   0. 207. 226. 245. 250. 256. 254. 252. 249. 246. 244. 244. 229. 205.   0.   0.   0.   0.   0.   0.
   0.   0.   0.   0.   0. 219. 231. 249. 262. 265. 265. 263. 262. 259. 256. 258  260. 255. 240. 215.   0.   0.   0.   0.   0.
   0.   0.   0.   0. 222. 240. 249. 257. 274. 274. 273. 272. 271. 269. 266. 263. 260. 259. 257. 243. 205.   0.   0.   0.   0.
   0.   0.   0. 226. 244. 253. 258. 266. 277. 281. 281. 280. 279. 277. 274. 271. 265. 263. 265. 255. 236. 200.   0.   0.   0.
   0.   0. 213. 243. 252. 257. 272. 276. 281. 285. 289. 288. 287. 285. 282. 276. 267. 266. 265. 261. 243. 222. 169.   0.   0.
   0.   0. 207. 251. 261. 277. 285. 287. 289. 299. 290. 290. 290. 298. 286. 278. 274. 270. 265. 263. 252. 234. 206.   0.   0.
   0. 169. 174. 259. 267. 277. 286. 288. 290. 291. 292. 292  292. 290. 289. 285  283. 279. 274. 272. 257. 241. 217. 156.   0.
   0. 147. 166. 204. 253. 273. 286. 289. 292. 294. 295. 296. 297. 296. 295. 294. 292. 290. 286. 274. 265. 255. 219. 159.   0.
   0. 152. 157. 147. 229. 279. 285. 290. 294. 296. 297. 298. 299. 298. 297. 296. 294. 290. 286. 281. 273. 266. 243. 170.   0.
   0. 201. 147. 147. 242. 280. 288. 291. 295. 296. 298. 299. 300. 299. 298. 296. 295. 291. 288. 283. 275. 266. 249. 216.   0.
 159. 221. 147. 147. 245. 283. 289. 293. 297. 299. 301. 302. 303. 302. 301. 299. 297. 293. 289. 285. 277. 266. 251. 275. 149.
   0. 205. 147. 147. 244. 283. 289. 292. 296. 298. 300. 301. 302. 301. 301. 299. 297. 293. 290. 285. 276. 265. 247. 219.   0.
   0. 168. 147. 147. 244. 282. 287. 292. 297. 299. 300. 301. 302. 301. 301. 299. 297. 292. 289. 285. 275. 263. 247. 204.   0.
   0  149. 147. 147. 233. 276. 289. 292. 295. 297. 299. 300. 301. 301. 300. 299. 296. 293. 290. 280. 271. 260. 238. 165.   0.
   0. 147. 147. 147. 234. 275. 281. 287. 293. 295. 297. 298. 299. 298. 298. 296. 294. 290. 286. 280. 267. 251. 237. 155.   0.
   0.   0. 156. 147. 230. 269. 274. 283. 291. 293. 297. 298. 298. 298. 297. 293. 291. 286. 291. 276. 259. 235. 204.   0.   0.
   0.   0. 192. 127. 221. 262. 257. 273. 279. 290. 295. 296. 297. 296. 295. 291. 284. 280. 276. 269. 243. 212. 178.   0.   0.
   0.   0.   0. 201. 237. 251. 255. 267. 276. 284. 289. 290. 291. 290. 289. 286. 282. 274. 270. 252. 223. 197.   0.   0.   0.
   0.   0.   0.   0. 211. 240. 249. 250. 266. 275. 283. 284. 284. 283. 282. 280. 277. 254. 249. 219. 197.   0.   0.   0.   0.
   0.   0.   0.   0.   0. 220. 232. 237. 244. 263. 275. 274. 274. 271. 269. 264. 250. 234. 220. 208.   0.   0.   0.   0.   0.
   0.   0.   0.   0.   0.   0. 196. 217. 222. 244. 266. 265. 263. 260. 256. 240. 226. 212. 182.   0.   0.   0.   0.   0.   0.
   0.   0.   0.   0.   0.   0.   0.   0. 192. 213. 242. 240. 238. 234. 220. 206. 191.   0.   0.   0.   0.   0.   0.   0.   0.
   0.   0.   0.   0.   0.   0.   0.   0.   0.   0.   0.   0. 199.   0.   0.   0.   0.   0.   0.   0.   0.   0.   0.   0.   0.
   0.0   0.8   2.3   3.8   5.3   6.8   8.3   9.8  11.3  12.8  14.3  22.5  37.5  52.5  67.5  82.5  97.5 112.5 127.5 142.5
 261.0 251.5 232.2 219.9 213.3 210.8 210.2 210.2 210.2 210.0 209.5 206.0 204.1 203.3 203.5 203.8 204.4 204.6 205.0 205.1
 DISK TEMP AT 5.0 MICRONS=276.61    FLUX=0.9932E-13
   DISK TEMP AT 10.5 MICRONS=269.97    FLUX=0.2183E-11
   DISK TEMP AT 20.0 MICRONS=265.14    FLUX=0.3547E-11
```

Fig. 47: Surface temperature map, 1971 opposition.

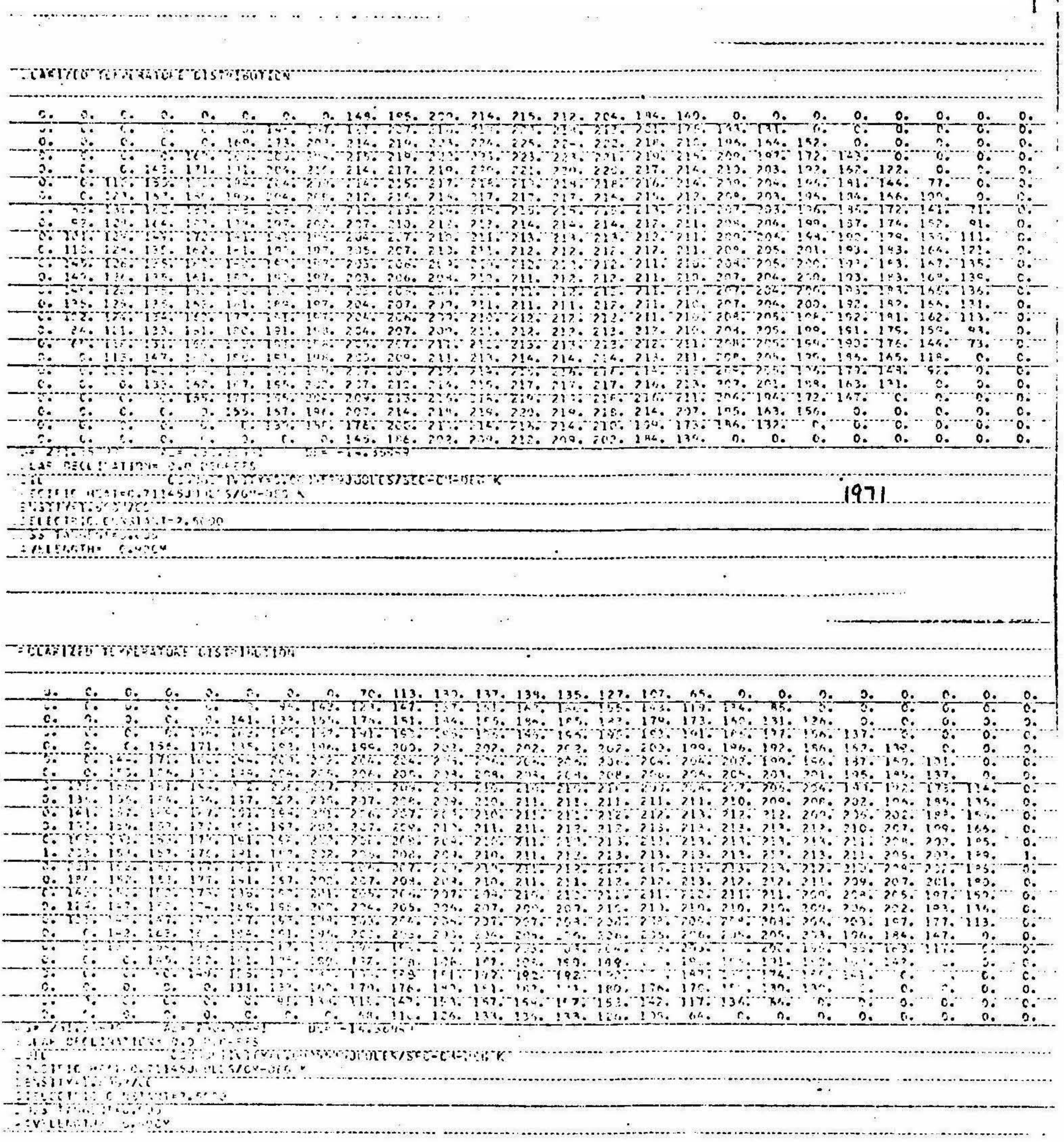

```
POLARIZED TEMPERATURE DISTRIBUTION

   0.   0.   0.   0.   0.   0.   0.   0. 149. 195. 200. 214. 215. 212. 204. 194. 140.   0.   0.   0.   0.   0.   0.   0.   0.
   0.   0.   0.   0.   0.   0. 141. 177. 181. 207. 210. 217. 221. 213. 212. 201. 175. 133. 131.   0.   0.   0.   0.   0.   0.
   0.   0.   0.   0.   0. 169. 173. 201. 214. 219. 223. 224. 225. 224. 222. 210. 210. 196. 164. 152.   0.   0.   0.   0.   0.
   0.   0.   0.   0. 167. 187. 200. 205. 215. 219. 222. 225. 223. 223. 221. 219. 215. 200. 197. 172. 143.   0.   0.   0.   0.
   0.   0.   0. 143. 171. 171. 204. 216. 214. 217. 219. 220. 221. 220. 220. 217. 214. 210. 203. 192. 162. 122.   0.   0.   0.
   0.   0. 115. 153. 177. 194. 204. 210. 214. 215. 217. 218. 219. 214. 218. 216. 214. 209. 204. 196. 191. 144.  77.   0.   0.
   0.   0. 123. 157. 157. 195. 204. 209. 212. 216. 216. 217. 217. 217. 216. 215. 212. 209. 203. 195. 184. 166. 100.   0.   0.
   0.  52. 131. 162. 171. 185. 207. 207. 210. 213. 214. 215. 215. 215. 215. 213. 211. 207. 203. 196. 186. 172. 141.  71.   0.
   0.  97. 120. 144. 157. 174. 197. 202. 207. 210. 212. 212. 214. 214. 214. 217. 211. 208. 206. 199. 187. 174. 152.  91.   0.
   0. 101. 124. 149. 172. 181. 187. 195. 204. 207. 210. 211. 213. 213. 213. 212. 211. 209. 204. 194. 190. 179. 155. 111.   0.
   0. 110. 124. 135. 162. 181. 187. 197. 205. 207. 210. 211. 212. 212. 212. 212. 211. 209. 205. 201. 193. 183. 164. 121.   0.
   0. 145. 126. 135. 157. 177. 187. 197. 203. 206. 210. 211. 212. 212. 212. 211. 210. 204. 205. 200. 193. 183. 167. 135.   0.
   0. 143. 134. 135. 141. 157. 190. 197. 203. 206. 208. 210. 211. 212. 212. 211. 210. 207. 204. 200. 193. 183. 169. 139.   0.
   0. 137. 126. 135. 150. 179. 187. 197. 202. 205. 208. 210. 211. 212. 212. 211. 210. 207. 204. 200. 193. 183. 165. 136.   0.
   0. 125. 125. 125. 153. 161. 189. 197. 204. 207. 209. 211. 211. 211. 212. 211. 210. 207. 206. 200. 192. 182. 155. 131.   0.
   0. 112. 124. 134. 150. 177. 181. 187. 204. 206. 209. 210. 212. 212. 212. 211. 210. 204. 205. 196. 192. 191. 162. 113.   0.
   0.  24. 111. 123. 151. 180. 191. 198. 204. 207. 209. 211. 212. 212. 213. 212. 210. 204. 205. 199. 191. 175. 159.  93.   0.
   0.  77. 117. 131. 160. 170. 187. 198. 205. 207. 211. 212. 213. 213. 213. 212. 211. 208. 205. 199. 190. 176. 144.  73.   0.
   0.   0. 113. 147. 170. 180. 181. 198. 205. 209. 211. 213. 214. 214. 214. 213. 211. 208. 205. 196. 185. 165. 118.   0.   0.
   0.   0. 122. 150. 172. 180. 190. 204. 207. 210. 212. 213. 215. 216. 217. 215. 213. 209. 205. 196. 179. 149.  92.   0.   0.
   0.   0.   0. 133. 167. 187. 195. 202. 207. 212. 214. 215. 217. 217. 217. 216. 213. 207. 201. 188. 163. 131.   0.   0.   0.
   0.   0.   0.   0. 135. 171. 195. 204. 209. 213. 216. 216. 219. 217. 216. 216. 211. 206. 194. 172. 147.   0.   0.   0.   0.
   0.   0.   0.   0.   0. 155. 157. 196. 207. 214. 219. 219. 220. 219. 218. 214. 207. 195. 163. 156.   0.   0.   0.   0.   0.
   0.   0.   0.   0.   0.   0. 137. 156. 178. 205. 211. 214. 215. 214. 210. 199. 173. 156. 132.   0.   0.   0.   0.   0.   0.
   0.   0.   0.   0.   0.   0.   0.   0. 145. 186. 202. 209. 212. 209. 202. 184. 139.   0.   0.   0.   0.   0.   0.   0.   0.
[illegible] 221.[illegible]        [illegible]          DE= -14.35659
POLAR DECLINATION= 0.0 DEGREES
[illegible]          CONDUCTIVITY=[illegible]JOULES/SEC-CM-DEG K
SPECIFIC HEAT=0.711450 JOULES/GM-DEG K
DENSITY=1.[illegible] G/CC
DIELECTRIC CONSTANT=2.5000
LOSS TANGENT=0.0[illegible]
WAVELENGTH= 0.90CM
```

1971

```
POLARIZED TEMPERATURE DISTRIBUTION

   0.   0.   0.   0.   0.   0.   0.   0.  70. 113. 130. 137. 134. 135. 127. 107.  65.   0.   0.   0.   0.   0.   0.   0.   0.
   0.   0.   0.   0.   0.   0.  94. 142. 121. 147. 137. 151. 147. 152. 155. 143. 119. 134.  85.   0.   0.   0.   0.   0.   0.
   0.   0.   0.   0.   0. 141. 133. 155. 174. 151. 134. 165. 194. 165. 127. 179. 173. 150. 131. 126.   0.   0.   0.   0.   0.
   0.   0.   0.   0. 176. 163. 185. 187. 191. 192. 185. 175. 195. 195. 195. 192. 191. 164. 177. 156. 137.   0.   0.   0.   0.
   0.   0.   0. 156. 171. 175. 183. 196. 199. 200. 202. 202. 202. 202. 202. 202. 199. 196. 192. 156. 157. 139.   0.   0.   0.
   0.   0. 144. 171. 180. 194. 203. 207. 204. 204. 204. 204. 204. 206. 206. 204. 204. 202. 199. 196. 187. 157. 131.   0.   0.
   0.   0. 175. 176. 177. 189. 204. 205. 206. 205. 203. 209. 203. 204. 208. 206. 206. 205. 203. 201. 195. 195. 137.   0.   0.
   0. 131. 165. 181. 184. 202. 207. 207. 208. 209. 209. 210. 210. 210. 210. 207. 208. 207. 206. 204. 191. 192. 173. 134.   0.
   0. 134. 136. 136. 136. 157. 202. 205. 207. 208. 209. 210. 211. 211. 211. 211. 211. 210. 209. 208. 202. 196. 185. 135.   0.
   0. 141. 137. 159. 177. 193. 194. 201. 206. 207. 209. 210. 211. 212. 212. 212. 213. 212. 212. 209. 206. 202. 193. 155.   0.
   0. 151. 154. 157. 173. 181. 187. 202. 207. 209. 210. 211. 211. 212. 212. 213. 213. 213. 213. 212. 210. 207. 199. 166.   0.
   0. 165. 152. 153. 175. 191. 194. 203. 207. 208. 204. 210. 211. 212. 213. 212. 213. 213. 213. 213. 211. 208. 202. 185.   0.
   1. 213. 154. 157. 176. 191. 197. 202. 205. 208. 209. 210. 211. 212. 213. 213. 213. 213. 213. 213. 211. 205. 203. 189.   1.
   0. 161. 152. 157. 177. 191. 197. 203. 206. 207. 209. 210. 211. 212. 212. 213. 213. 213. 213. 212. 210. 209. 207. 195.   0.
   0. 187. 182. 153. 177. 181. 197. 202. 207. 208. 209. 210. 211. 211. 212. 212. 213. 212. 212. 211. 209. 207. 201. 190.   0.
   0. 145. 156. 150. 173. 195. 187. 201. 205. 206. 207. 209. 210. 212. 212. 211. 212. 211. 211. 209. 208. 205. 197. 152.   0.
   0. 114. 147. 170. 174. 169. 195. 207. 204. 205. 206. 207. 209. 207. 210. 210. 210. 210. 210. 209. 206. 202. 193. 136.   0.
   0. 137. 147. 147. 177. 177. 187. 198. 203. 204. 204. 207. 207. 203. 204. 203. 205. 204. 204. 206. 203. 197. 177. 113.   0.
   0.   0. 142. 143. 170. 184. 161. 196. 201. 203. 203. 204. 205. 206. 206. 205. 206. 205. 205. 203. 196. 184. 147.   0.   0.
   0.   0. [illegible] 155. 170. 180. 217. [illegible] [illegible] [illegible] [illegible] [illegible] 205. 205. 204. [illegible] 205. [illegible] 205. 195. 186. 163. 117.   0.   0.
   0.   0.   0. 145. 147. 152. 177. 180. 137. 178. 136. 147. 195. 150. 149. [illegible] 190. [illegible] 131. 152. [illegible] 142. [illegible]   0.   0.
   0.   0.   0.  90. 149. 175. 177. [illegible] 175. 179. 181. 177. 192. 192. [illegible] [illegible] [illegible] 147. [illegible] 174. [illegible] 141.   0.   0.   0.
   0.   0.   0.   0.   0. 131. 137. 160. 170. 176. 180. 181. 162. [illegible] 180. 176. 170. [illegible] 139. 130.   0.   0.   0.   0.   0.
   0.   0.   0.   0.   0.   0.  95. 134. 115. 147. 153. 157. 154. 147. 153. 142. 117. 134.  96.   0.   0.   0.   0.   0.   0.
   0.   0.   0.   0.   0.   0.   0.   0.  68. 116. 126. 133. 135. 133. 126. 105.  64.   0.   0.   0.   0.   0.   0.   0.   0.
[illegible] 221.[illegible]        [illegible]          DE= -14.3[illegible]
POLAR DECLINATION= 0.0 DEGREES
[illegible]          CONDUCTIVITY=[illegible]JOULES/SEC-CM-DEG K
SPECIFIC HEAT=0.711450 JOULES/GM-DEG K
DENSITY=1.[illegible] G/CC
DIELECTRIC CONSTANT=2.5000
LOSS TANGENT=0.0[illegible]
WAVELENGTH= 0.90CM
```

Fig. 48: Polarized brightness distributions, 1971 opposition, λ = 0.9 cm.

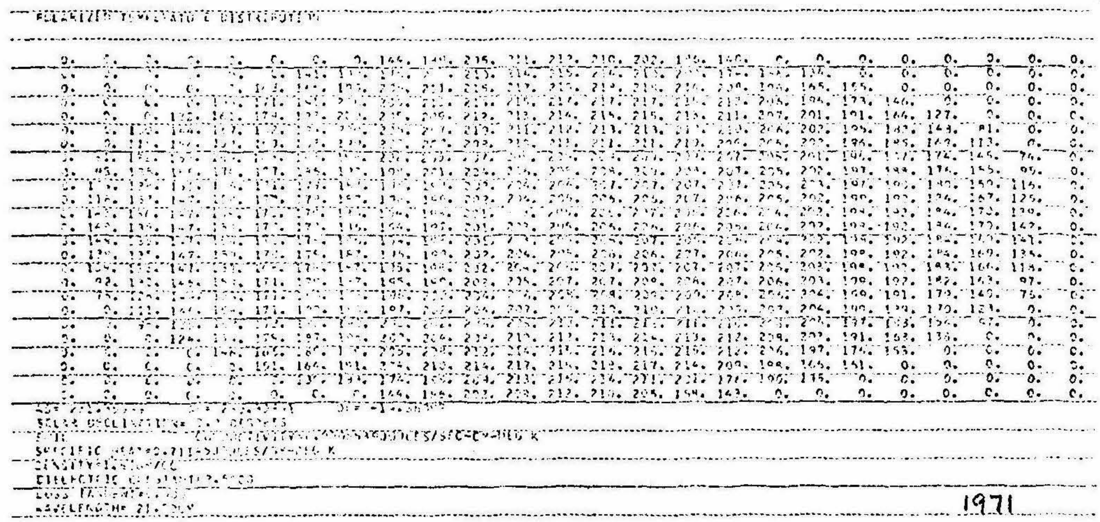

1971

POLARIZED TEMPERATURE DISTRIBUTION

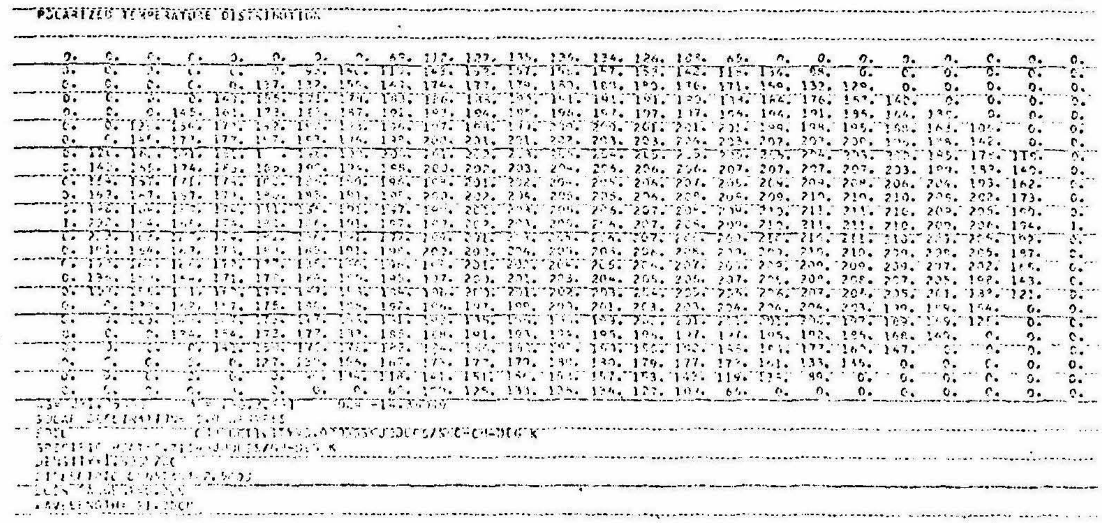

Fig. 49: Polarized brightness distributions, 1971 opposition, λ = 21.0 cm.

APPENDIX II

Co-ordinate Transformation Used for Mercury

It is desired to transform the co-ordinates of a surface element on the sub-earth disk to the corresponding co-ordinates relating the surface element to the planetary co-ordinate system in which the temperature structure is generated and defined (planetocentric latitude and longitude, IAU system (1970)). The method used is different from the one used for Mars, due to the lack of validity of the assumption used for Mars that the planet-earth vector lies in the ecliptic. It is also conceptually simpler and is indeed valid for both planets. Basically, the three transformation rotations are:

a) Rotation about the pole of the planet by $(A_s - A_e + \lambda_{ss})$ bringing the origins of longitude together.

A_s = planetocentric right ascension of Sun

A_e = planetocentric right ascension of Earth

λ_{ss} = subsolar longitude for date

(A_s, A_e) = measured eastward along the plane of the equator of the planet.

b) Rotation about the axis perpendicular to the pole of the planet and the above determined origin of longitude by (-De), where De is the planetocentric declination of the earth. This transforms the origin of longitude to the planet-earth vector.

c) Rotation about the planet-earth vector by (P_a). This aligns the temperature map with the orientation of the planet as seen from Earth.

These quantities are shown in Fig. 37.

This method is quite simple, and due to the fact that the quantities (A_s, A_e, D_e, P_a) are standard physical ephemerides and published for most of the planets, quite general. The lack of good knowledge on the position of the rotation pole of Mercury has prevented the precise determination of these values for Mercury. (Venus is similarly not treated in the published ephemerides). The derivation of these quantities is, however, quite straight-forward. (See, e.g., Supplement to American Ephemeris and Nautical Almanac). The derivation will be briefly outlined.

We begin with the pole position derived in Appendix III where (α_o, δ_o) are the geocentric right ascension and declination of the pole of rotation.

Let $x = \tan^{-1} [\sin\epsilon \cos\alpha_o/(-\cos\epsilon \cos\Omega \cos\alpha_o - \sin\Omega \sin\alpha_o)]$

$y = \tan^{-1} [\sin\epsilon \sin\Omega/(\cos\epsilon \sin\Omega \sin\alpha_o + \cos\Omega \cos\alpha_o)]$

$z = \cos^{-1} [\cos\epsilon \sin\Omega \cos\alpha_o - \cos\Omega \sin\alpha_o]$

Then

$$\boldsymbol{\Omega} = \tan^{-1} \frac{\sin z \cos(y-\delta_o)}{\sin(x-i_M) \sin(y-\delta_o) - \cos(x-i_M) \cos(y-\delta_o) \cos z}$$

$$\Delta = \tan^{-1} \frac{\sin z \sin(x-i_M)}{\sin(x-i_M) \sin(y-\delta_o) \cos z - \cos(x-i_M) \cos(y-\delta_o)}$$

and

$$L_s = \tan^{-1} [\tan(L_h-\Omega) \sec i_M] - \boldsymbol{\Omega}$$

$$A_s = \tan^{-1} [\tan L_s \cos\theta]$$

$$A_e = \left[\tan^{-1}\left(\frac{\cos\delta_o \sin\delta - \sin\delta_o \cos\delta \cos(\alpha_o - \alpha)}{-\cos\delta \sin(\alpha_o - \alpha)}\right)\right] - \Delta$$

$$D_e = \sin^{-1}(-\sin\delta \sin\delta_o - \cos\delta_o \cos\delta \cos(\alpha_o - \alpha))$$

$$P_a = \tan^{-1} \frac{\cos\delta_o \sin(\alpha_o - \alpha)}{\sin\delta_o \cos\delta - \cos\delta_o \sin\delta \cos(\alpha_o - \alpha)}$$

where A_s, A_e, D_e, and P_a are the desired physical ephemerides and

ε = true obliquity

Ω = longitude of the ascending node of the orbit on the ecliptic

i_M = inclination of the orbit to the ecliptic

θ = small angular separation of the spin axis from either $\hat{K}$ or $\hat{\mu}$, $\sim\frac{1}{2}^\circ$ for either case.

L_h = heliocentric longitude of the planet in its orbit (tabulated for a given date)

(α, δ) = geocentric right ascension and declination of the planet for a given date

All quantities are thus known with the exception of θ, which may be assumed small, and (α_o, δ_o) which may be calculated using the method described in Appendix III. Ambiguities arising in using the inverse trigonometric functions must be anticipated and accounted for. It was found that varying θ from 0° to 1° did not change the ephemerides by more than 0.6°. The full coordinate transformation matrix may then be written

$$\begin{vmatrix} P_1 \\ P_2 \\ P_3 \end{vmatrix} = \begin{vmatrix} M_{11} & M_{12} & M_{13} \\ M_{21} & M_{22} & M_{23} \\ M_{31} & M_{32} & M_{33} \end{vmatrix} \begin{vmatrix} E_1 \\ E_2 \\ E_3 \end{vmatrix}$$

where E_i and P_i are cartesian coordinates of any given point on the planet in the earth-centered and planet-centered coordinate systems respectively. The earth-centered system is defined by the planet-earth vector and projected celestial north. The planet-centered system is defined by the planet-sun vector (taken to lie in the orbital plane of the planet) and the pole of rotation of the planet. The matrix elements are:

$$M_{11} = \cos L \cos D_e$$

$$M_{12} = \cos L \sin D_e \sin P_a - \sin L \cos P_a$$

$$M_{13} = -\cos L \sin D_e \cos P_a - \sin L \sin P_a$$

$$M_{21} = \sin L \cos D_e$$

$$M_{22} = \sin L \sin D_e \sin P_a + \cos L \cos P_a$$

$$M_{23} = -\sin L \sin D_e \cos P_a + \cos L \sin P_a$$

$$M_{31} = \sin D_e$$

$$M_{32} = -\cos D_e \sin P_a$$

$$M_{33} = \cos D_e \cos P_a$$

where

$$L = A_s - A_e + \lambda_{ss}$$

and planetocentric latitude and longitude are then

$$\mathrm{lat} = \sin^{-1} (P_3)$$

$$\mathrm{long} = -\tan^{-1} (P_2/P_1)$$

The minus sign is required as the planetocentric system (IAU, 1970) is left-handed and the earth-centered system is defined in a right-handed sense.

APPENDIX III

Determination of the Position of the Spin Axis

A precise determination of the celestial co-ordinates of the spin axis of Mercury is required in the geometrical method that was described in Appendix II. Use is made of the claim of Peale (1969) that, for the case of a planet having spin period commensurate with its orbital period, energy and stability considerations limit possible orientations for the spin axis. Cassini's laws for the moon state that the inclination of the spin pole to the orbital pole is constant, and the spin axis, orbital axis and normal to the ecliptic are co-planar. Generalizing Cassini's laws to the case of Mercury, Peale finds the following similar considerations assuming Mercury's total angular momentum has achieved stability.

a) The spin axis and orbital axis of Mercury, and the pole of the invariable plane of the solar system are co-planar. (The invariable plane is the precession axis for Mercury's orbit.)

b) The spin axis shares the precession of the orbital pole.

c) For spin-orbit commensurability to be maintained, the spin axis must not lie between the orbital pole and the pole of the invariable plane.

d) Potential positions of stability are found to be separated by less than 1° from either the orbital pole or the pole of the invariable plane.

As the orbital pole and the pole of the invariable plane are separated by approximately 7°, there are two similar but perhaps distinguishable possible positions for a stable configuration. The position near the orbital pole is more stable for a lunar-like value of planetary oblateness ($\frac{C-A}{C}$ of $\geq 10^{-8}$). For a smaller oblateness ($\leq 10^{-8}$), the position near the pole of the invariable plane is the more likely. As this parameter for Mercury is not known, geometry for both possible positions of the pole was worked out.

We define the following parameters:

$\hat{k}$ = unit vector along the spin axis of Mercury

$\hat{\mu}$ = unit vector along pole of invariable plane

$\hat{K}$ = unit vector normal to Mercury's orbit

θ = displacement of $\hat{k}$ from $\hat{K}$

(λ_μ, β_μ) = ecliptic longitude and latitude of $\hat{\mu}$

(λ_M, β_M) = ecliptic longitude and latitude of $\hat{K}$

These parameters are known (see eg. Allen, 1964). θ will be assumed to be $\approx 0.5°$. The geometry shown in Fig. 50 and derived below will be used to derive (λ_s, β_s), which are the ecliptic longitude and latitude of $\hat{k}$. From these, the right ascension and declination are readily determined. (α_o, δ_o).

We will be using the parameters

$$i_\mu = \frac{\pi}{2} - \beta_\mu$$

$$i_M = \frac{\pi}{2} - \beta_M$$

$$i_s = \frac{\pi}{2} - \beta_s$$

and $(I, \gamma_2, \lambda_k, \theta)$, defined in Fig. 50.

Case 1: spin pole near to orbital pole.

1. $\cos I = \cos i_\mu \cos i_M + \sin i_\mu \sin i_M \cos(\lambda_m - \lambda_\mu)$

2. $\sin\gamma_2 = \dfrac{\sin i_M \sin(\lambda_\mu - \lambda_M)}{\sin I}$; $\cos\gamma_2 = \dfrac{\cos i_M - \cos I \cos i_\mu}{\sin i_\mu \sin I}$

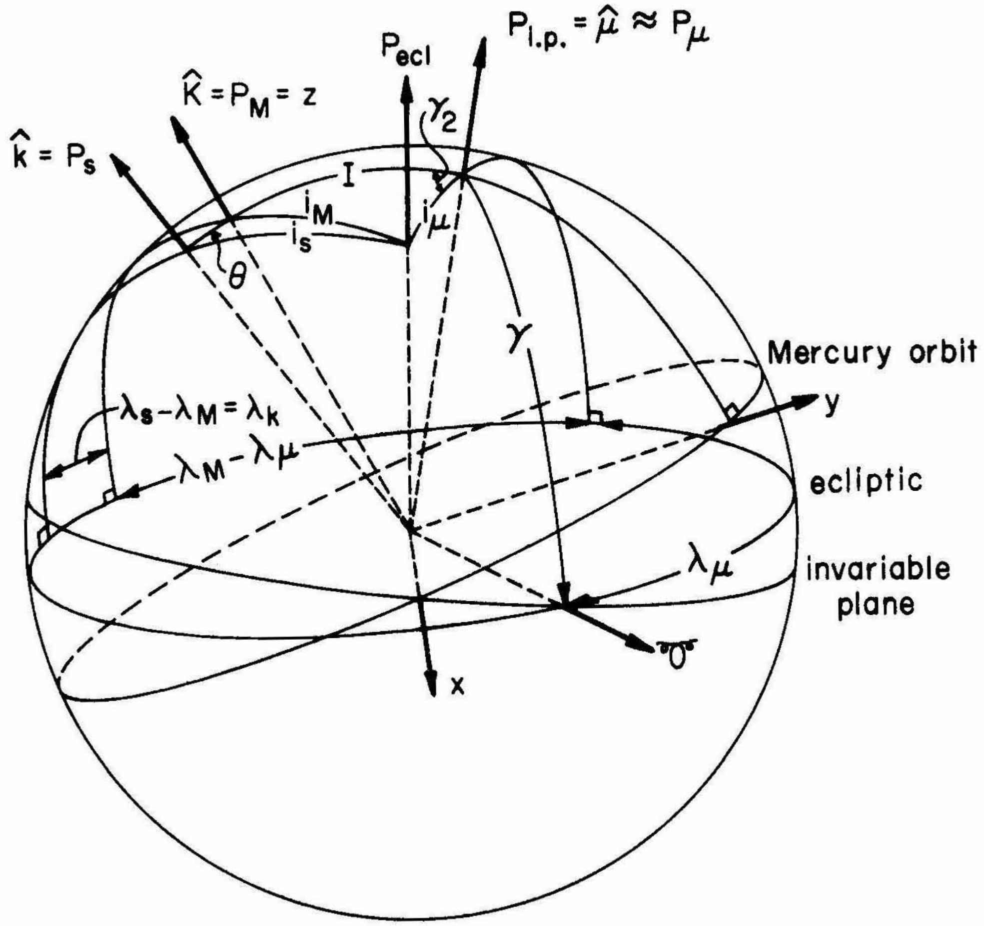

Determination of the Co-ordinates of the Spin Axis of Mercury ($P_s = \hat{k}$)

P_M is the pole of the orbit of Mercury

P_{μ} is the pole of the invariable plane

$(\lambda_{\alpha}, \frac{\pi}{2} - i_{\alpha})$ = celestial longitude and latitude of P_{α} (α = s, M, μ)

Fig. 50: The celestial sphere. Pecl is the pole of the ecliptic, $\hat{k} = P_s$ is the (unknown) pole of the rotation axis of Mercury, and θ is the small(also unknown) separation of the axial pole from the orbital pole.

3. $\cos i_s = \cos(I+\theta)\cos i_\mu + \sin(I+\theta)\sin i_\mu \cos\gamma_2$

4. $\cos\lambda_k = \dfrac{\cos\theta = \cos i_s \cos i_M}{\sin i_s \sin i_M}$

then:

$$\lambda_s = \lambda_M - \lambda_k$$

$$\beta_s = \frac{\pi}{2} - i_s \quad .$$

Case 2: If $\hat{k}$ is closer to $\hat{\mu}$ (on the other side of $\hat{\mu}$ from $\hat{K}$), the geometry is slightly different, and is outlined below. Here, θ is the small separation of $\hat{k}$ from $\hat{\mu}$.

1. $\cos I = \cos i_\mu \cos i_M + \sin i_\mu \sin i_M \cos(\lambda_M - \lambda_\mu)$

2. $\sin\gamma_2 = \dfrac{\sin i_M \sin(\lambda_M - \lambda_\mu)}{\sin I}$

$$\cos\gamma_2 = \frac{\cos i_M - \cos i_\mu \cos I}{\sin i_\mu \sin I}$$

3. $\cos i_s = \cos\theta \cos i_\mu - \sin\theta \sin i_\mu \cos\gamma_2$

4. $\cos\lambda_k = \dfrac{\cos\theta - \cos i_s \cos i_\mu}{\sin i_s \sin i_\mu}$

then:

$$\lambda_s = \lambda_\mu + \lambda_k$$

$$\beta_s = \frac{\pi}{2} - i_s \quad .$$

Given (λ_s, β_s) for either of these two cases, the simple transformations giving (α_o, δ_o), the corresponding right ascension and declination of the spin pole, are:

$$\sin\delta_o = \cos\beta_s \sin\lambda_s \sin\epsilon + \sin\beta_s \cos\epsilon$$

$$\cos\alpha_o \cos\delta_o = \cos\beta_s \cos\lambda_s$$

$$\sin\alpha_o \cos\delta_o = \cos\beta_s \sin\lambda_s \cos\epsilon - \sin\beta \sin\epsilon$$

where ϵ is the true obliquity (see e.g. Supplement to American Ephemeris, p. 110).

APPENDIX IV

Microwave Thermal Emission and the Radiative Transfer Problem in a Planetary Surface

A brief sketch will be given of the theory of thermal microwave emission. We will immediately make use of the Rayleigh-Jeans approximation to the Planck radiation law.

$$F_\lambda(T) = \frac{2k\ T}{\lambda_o{}^2}\ d\Omega = B_\lambda(T)\ d\Omega(\omega\ cm^{-2}\ Hz^{-1}) \quad (1)$$

where B_λ = Specific Intensity (ω cm^{-2} Hz^{-1} str^{-1})

k = Bolzmann's constant

T = Blackbody temperature

λ_o = Vacuum wavelength of radiated energy

The emitted intensity from an element of volume dV is given by

$$dI_\lambda = j_\lambda dV \qquad (\omega\ str^{-1}\ Hz^{-1})$$

Using Kirchoff's law for the case of local thermodynamic equilibrium,

$$dI_\lambda = 4\pi n_i^2\ k_\lambda\ B_\lambda(T)\ dV$$

where n_i = Material index of refraction

and k_λ = Microwave absorbtion coefficient (cm^{-1})

$$\frac{dI_\lambda}{ds} = -k_\lambda I_\lambda$$

The spectral energy reaching the surface at a distance s = z sec (θ_i) from this element defined to lie within $d\Omega_i$ is then (see fig. 51)

$$dE_\lambda = dI_\lambda e^{-k_\lambda s}\ d\Omega_s$$

$$dE_\lambda = \frac{4\pi n_i^2 \; k_\lambda \; B_\lambda(T)\, e^{-k_\lambda z \sec\theta_i}}{4\pi(z \sec\theta_i)^2} \; dV \; dA \; \cos\theta_i \left(\text{watts Hz}^{-1}\right)$$

where $d\Omega_s$ = solid angle subtended by surface element dA.

Using the fact that, in a cone of solid angle $d\Omega_i$,

$$dV = s^2 ds \; d\Omega_i$$

$$dE\lambda = \frac{n_i^2 \; k_\lambda B_\lambda(T) e^{-k_\lambda z \sec\theta_i} (z \sec\theta_i)^2 \; d(z \sec\theta_i) \; dA \; \cos\theta_i \; d\Omega_i}{(z \sec\theta_i)^2}$$

or,

$$dE_\lambda = n_i^2 \; k_\lambda \; B_\lambda \; (T) \; e^{-k_\lambda z \sec\theta_i} \; d(z \sec\theta_i) \;\; dA \; \cos\theta_i \; d\Omega_i$$

since θ_i is constant,

$$dE_\lambda = n_i^2 \; k_\lambda \; \sec\theta_i \; B_\lambda(T) e^{-k_\lambda z \sec\theta_i} \; dz \; dA \; \cos\theta_i \; d\Omega_i$$

the net spectral energy impinging the surface element dA is thus

$$E_\lambda(\theta_i) = n_i^2 \; k_\lambda \; \sec\theta_i \int_0^\infty B_\lambda \; (T) e^{-k_\lambda z \sec\theta_i} \; dz \; dA \; \cos\theta_i \; d\Omega_i$$

or, using (1),

$$E_\lambda(\theta_i) = \frac{n_i^2 \; k_\lambda \; 2k \sec\theta_i}{\lambda_0{}^2} \int_0^\infty T(z) e^{-k_\lambda z \sec\theta_i} \; dz \; dA \; \cos\theta_i \; d\Omega_i$$

From the traveling wave equation in the medium,

$$\overline{E(z,t)} = E_0 e^{i(\kappa z - \omega t)}$$

$$\kappa = \alpha + i\beta \qquad .$$

The power absorbtion coefficient, $k_\lambda = 2\beta$. Solving Maxwell's equations using this form for $\overline{E}$ yields the form of k_λ:

$$k_\lambda = \frac{2\pi\sqrt{\epsilon} \; \tan\Delta}{\lambda_0} \tag{2}$$

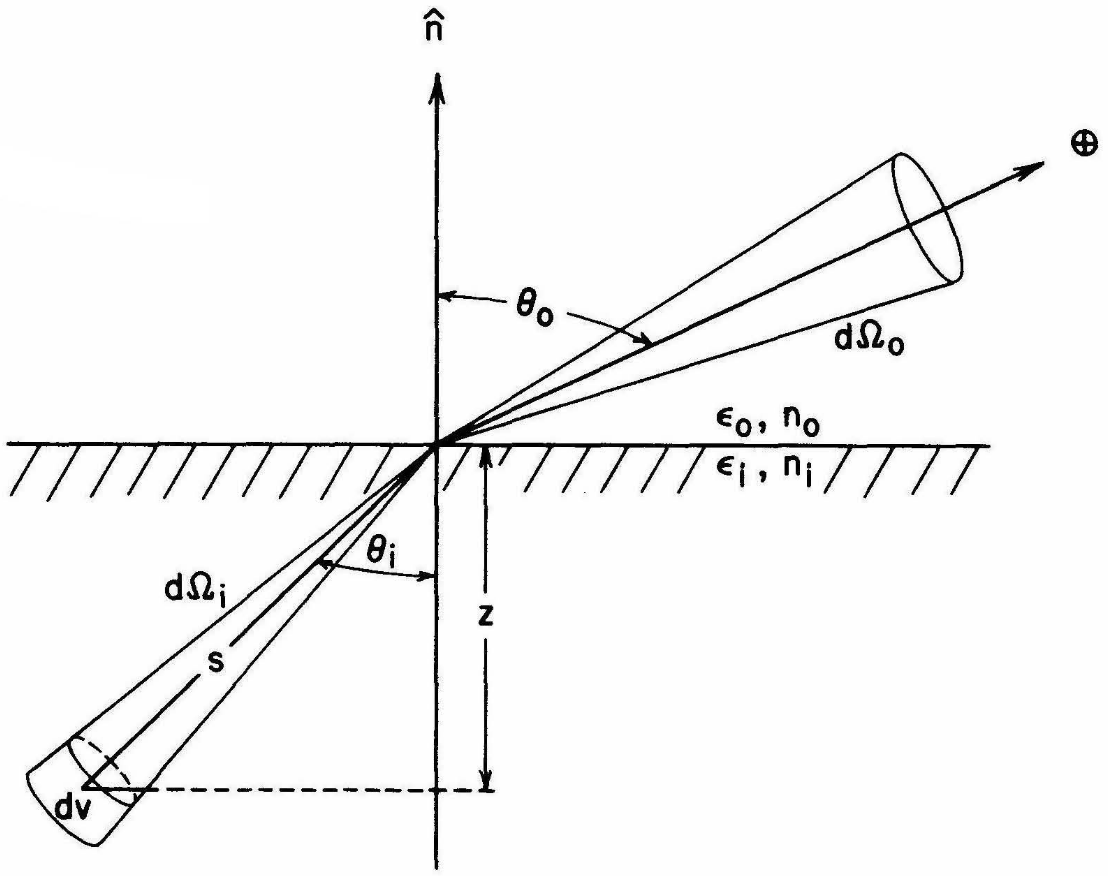

Fig. 51: Illustration of the refraction of radiated energy in a cone of solid angle $d\Omega_i$ from beneath the surface into a cone of solid angle $d\Omega_o$ in the direction of the Earth. The index of refraction in the material is $n_i = \sqrt{\epsilon_i}$.

where ϵ = material dielectric constant relative to free space

$(\epsilon = n_i^2)$

$\tan\Delta$ = material loss tangent $(\tan\Delta = \sigma/\epsilon\omega)$

σ = material conductivity, mhos/m^2

ω = angular frequency of emitted radiation

thus

$$\frac{E_\lambda(\theta_i)}{d\Omega_i dA \cos\theta_i} = \frac{2\pi\sqrt{\epsilon}\,\tan\Delta}{\lambda_o}\left[\frac{2k}{\lambda_o^2}\right] n_i^2 \sec\theta_i \int_0^\infty T(z)\, e^{-k_\lambda z \sec\theta_i}\, dz \quad .$$

In passing across the surface, the upward moving radiation is partially reflected back down and partially refracted toward the observer. The coefficients for transmission and reflection are the well-known Fresnel coefficients, which are readily derived from vector conservation boundary conditions at the surface (see e.g., Stratton, 1941; p. 492), and are dependent on the plane of polarization of the $\overline{E}$ vector. The direction of the refracted wave normal relative to the surface normal is given by Snell's laws of refraction.

$$n_o \sin\theta_o = n_i \sin\theta_i \tag{3}$$

In addition, the specific intensity is decreased by the ratio of the bounding solid angles and apparent areas. By energy conservation,

$$E_{\lambda_i} = B_{\lambda_i} dA_s \cos\theta_i \, d\Omega_i = B_{\lambda_o} dA_s \cos\theta_o \, d\Omega_o$$

using (3) to get

$$n_o \cos\theta_o \, d\theta_o = n_i \cos\theta_i \, d\theta_i \quad ,$$

and the fact that

$$d\varphi_o = d\varphi_i \quad ,$$

we get

$$\frac{B_\lambda^{o}}{B_\lambda^{i}} = \frac{n_o^{2}}{n_i^{2}} = \frac{1}{n_i^{2}} \; ; \; B_\lambda^{o} = \frac{E_\lambda^{i}}{n_i^{2}\, d\Omega_i\, dA \, \cos\theta_i} \; .$$

We may then write the final intensity in polarizations respectively parallel and perpendicular to the local surface as

$$B_\lambda^{p}(\theta_i) = T^{p} \, \frac{2\pi\sqrt{\epsilon}\, \tan\Delta}{\lambda_o} \left[\frac{2k}{\lambda_o^{2}} \right] \sec\theta_i \int_0^{\infty} T(z)\, e^{-k_\lambda z \sec\theta_i} \, dz \qquad (4)$$

$$(\omega \; m^{-2}\, Hz^{-1}\, str^{-1})$$

where T^p is the power transmission coefficient in polarization p ($p = \perp, \parallel$) and

$$T^{\perp} = 1 - \left[\frac{\epsilon \cos\theta_i - \sqrt{\epsilon - \sin^2\theta_i}}{\epsilon \cos\theta_i + \sqrt{\epsilon - \sin^2\theta_i}} \right]^2 \qquad (5)$$

$T^{\perp} = E^{\perp}$ = Emissivity of the surface in $\perp$ polarization

$$T^{\parallel} = 1 - \left[\frac{\cos\theta_i - \sqrt{\epsilon - \sin^2\theta_i}}{\cos\theta_i + \sqrt{\epsilon - \sin^2\theta_i}} \right]^2 = E^{\parallel} \text{ (Emissivity in } \parallel \text{ polarization.)} \qquad (6)$$

The angle θ_i is determined from the viewing angle to the observer, θ_o, by the refraction law (3). Thus, for every spot (θ_o, φ) on the surface overlying temperature structure $T(z, \theta_o, \varphi)$ and being observed in polarization p at viewing angle θ_o to the local normal, we may define a brightness temperature, given by

$$T_B^{p}(\theta_o, \varphi) = \frac{\lambda_o^{2}}{2k} \left[B_\lambda^{p}\big(\theta_o; T(z, \theta_o, \varphi)\big) \right] \qquad (7)$$

where B_λ is the specific intensity. The distribution of $T_B^{\,p}$ across the visible disk of the planet will be referred to as a "brightness map". In general, observations are made with the polarization of accepted radiation respectively parallel and perpendicular to the interferometer baseline as projected on the planet. Denoting $T_B^s(\theta,\varphi)$ = surface brightness temperature [defined by (7)], the resultant maps have the form

$$T_{B_\perp}^{obs}(\theta,\varphi) = T_B^s(\theta,\varphi)\ [E^{\parallel} \sin^2\varphi + E^{\perp} \cos^2\varphi]$$

$$T_{B_\parallel}^{obs}(\theta,\varphi) = T_B^s(\theta,\varphi)\ [E^{\perp} \sin^2\varphi + E^{\parallel} \cos^2\varphi]$$

where φ is azimuthal angle measured from the baseline direction. For the situation in which $T_B^s(\theta,\varphi)$ = constant = T_o, the resultant brightness maps are shown schematically in Fig. 52.

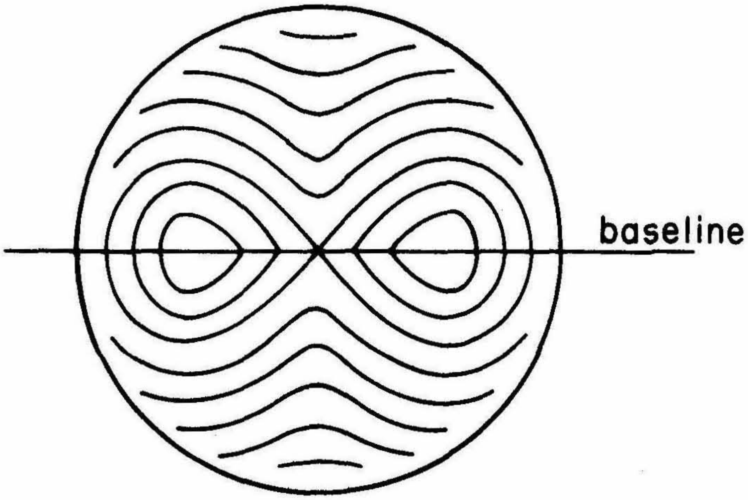

Parallel polarization

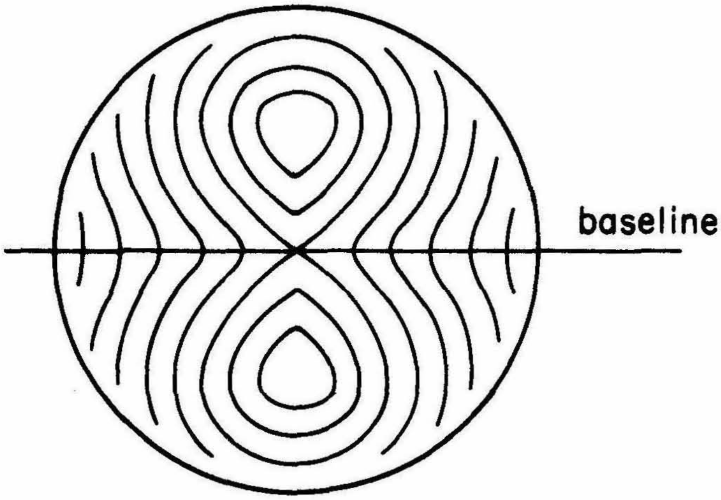

Perpendicular polarization

Fig. 52: Schematic representation of contours of equal brightness temperature in orthogonal polarizations as distributed over a sphere of uniform physical temperature and dielectric constant.

APPENDIX V

Interferometer Theory

Theory behind practical interferometry has been competently and thoroughly discussed elsewhere. (See, e.g., Moffet, 1962; Read, 1963; Kraus, 1966). Before treating the observation process in some detail, it seems proper to give only a brief sketch of interferometer fundamentals. Consider a pair of antennas separated by distance D, as shown in Fig. 53. In typical interferometers the celestial signal at some frequency is mixed with generated signals at slightly different frequencies to produce a lower frequency (IF) resultant. The low frequency signals from the two antennas in which initial phase relationships are conserved by the superheterodyne process, are then brought together and multiplied. The incoming signal from the celestial source, S(t), although of stochastic nature in time, is constant across a given wave front and in this sense the signals from the two antennas may be regarded as instantaneously coherent with a phase difference proportional to the difference in arrival time of the wavefront at the two antennas. Choosing the zero point of phase to lie at antenna #1, the situation is as depicted in Fig. 53.

If E_o is the amplitude of the monochromatic signal from the source, then the output power of the instrument is given by the time average of the product of the IF voltages accepted from the two antennas, or, $P = \overline{E1 \times E2}$.

$$P = \overline{(E_o e^{i\omega t} + n_1)(E_o e^{i(\omega t + \psi)} + n_2)}$$

$$P = \overline{E_o^2 e^{2i\omega t + i\psi}} + \overline{n_1 n_2} + \overline{n_1 E_o e^{i(\omega t + \psi)}} + \overline{n_2 E_o e^{i\omega t}}$$

$P = E_o^2 \cos^2\psi$ (last 3 terms are uncorrelated and average to 0.)

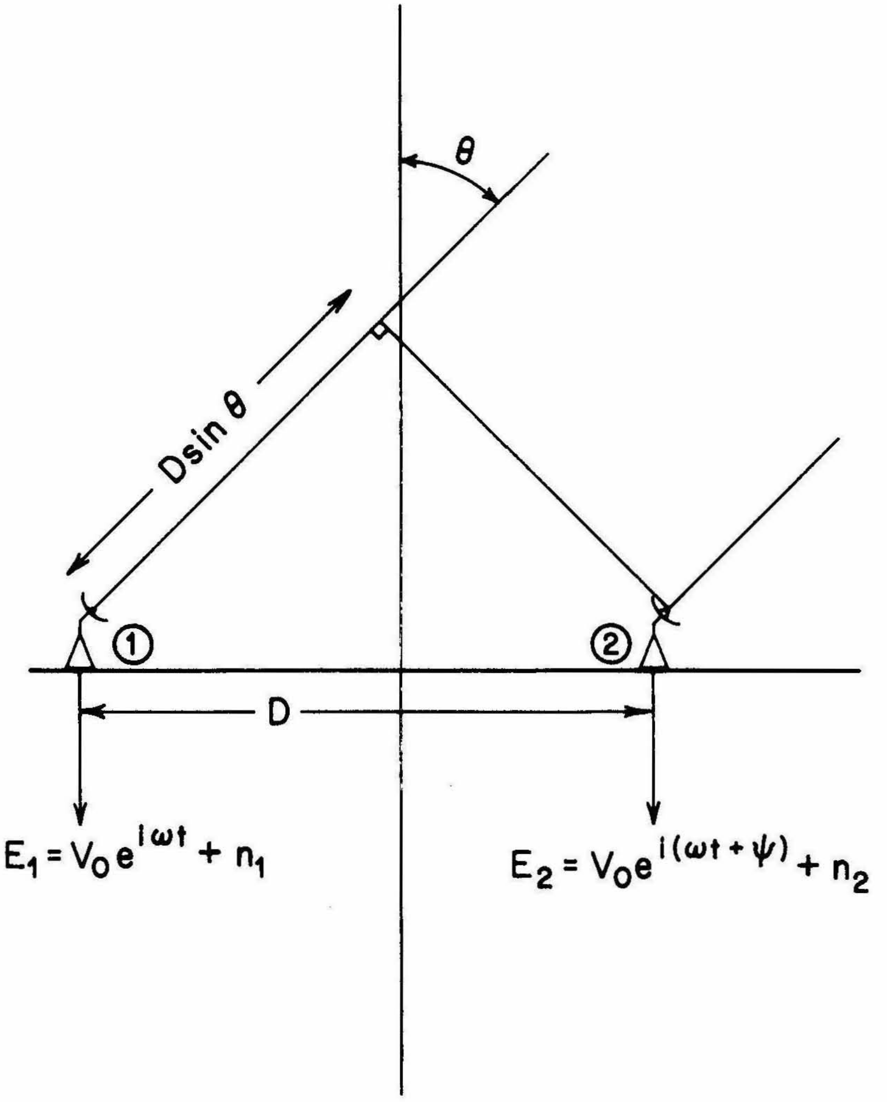

Fig. 53: Geometry of the interferometer baseline as seen observing a source at an angle θ from the median plane of the interferometer.

or

$$P_{out} = E_o^2 \cos \frac{2\pi\ D \sin\theta}{\lambda} \quad .$$

Allowing for an undetermined instrumental phase, Ψ, and letting

$S = D/\lambda$ = baseline length measured in wavelengths

$$P_{out} = E_o^2 \cos(2\pi\, S \sin\theta + \Psi) \qquad (1)$$

This expression is strictly true only for unit gain, isotropic response antennas. The net response pattern is actually the product of (1) and the angular response pattern of an individual component antenna . If the antennas are identical with normalized power response pattern $P = A(\theta,\varphi)$ and system gain G,

$$P_{out} = G\, E_o^2 A(\theta,\varphi) \cos(2\pi S \sin\theta + \Psi) \qquad (2)$$

If a point source of monochromatic radiation were to be observed over a range of θ, the response would be seen to describe a set of interference fringes as the contribution from one antenna went in and out of phase with the contribution from the other at a rate determined by the separation of the antennas and the celestial position of the source.

The following outline of the Fourier Transform measurement process follows closely that of Moffet (1962) but is specially adapted to the problem of planetary radio interferometry. We wish to write the response of the interferometer to a source of some extended brightness distribution. The far-field response pattern (monochromatic) of an interferometer composed of two identical antennas is given by (2), where θ is the angle between the source direction and the median plane of the interferometer, $G = G(t)$ allows for receiver gain changes, and Ψ is an initially undetermined instrumental phase. In practical use this monochromatic response is averaged over the finite passband width of the receiver. This effectively degrades the source fringe amplitude in directions away from the electrical median plane of the interferometer. Our wide hour angle coverage is made possible by insertion of a variable delay $\tau(t)$ into the IF cable of one antenna equal to the difference in travel time of radiation reaching the two antennas. From Fig. 3,

$$\tau(t) = \frac{D}{c} \sin\theta(t) \quad .$$

Tracking delay makes it possible to maintain the electrical median plane on the source being observed. The orientation of the interference fringes with respect to the source may be obtained from (2). As the fringes lie along lines of constant $\sin\theta$, their gradient, or the orientation of the effective baseline projected on the sky at the source, is parallel to grad $(\sin\theta)$. Denoting the position angle of this gradient by p, and establishing in a small area of the sky near the source a grid defined by local declination and hour circles, we locate the fringe pattern as shown in Fig. 54.

Assuming a source of extended brightness distribution $B(\alpha, \delta)$ with centroid at (α_o, δ_o), we define a cartesian grid (x,y) using the assumption that the source is small enough to be contained entirely in the region of validity of our local cartesian approximation to the (α, δ) system. Thus, if x and y are in radians and $|x|$, $|y| \ll 1$, the following relations are valid.

$$x = (\alpha - \alpha_o) \cos\delta_o \text{ (increases to the east)}$$

$$y = \delta - \delta_o \text{ (increases north)}$$

also, we will use the relation

$$\alpha = \Omega t - h$$

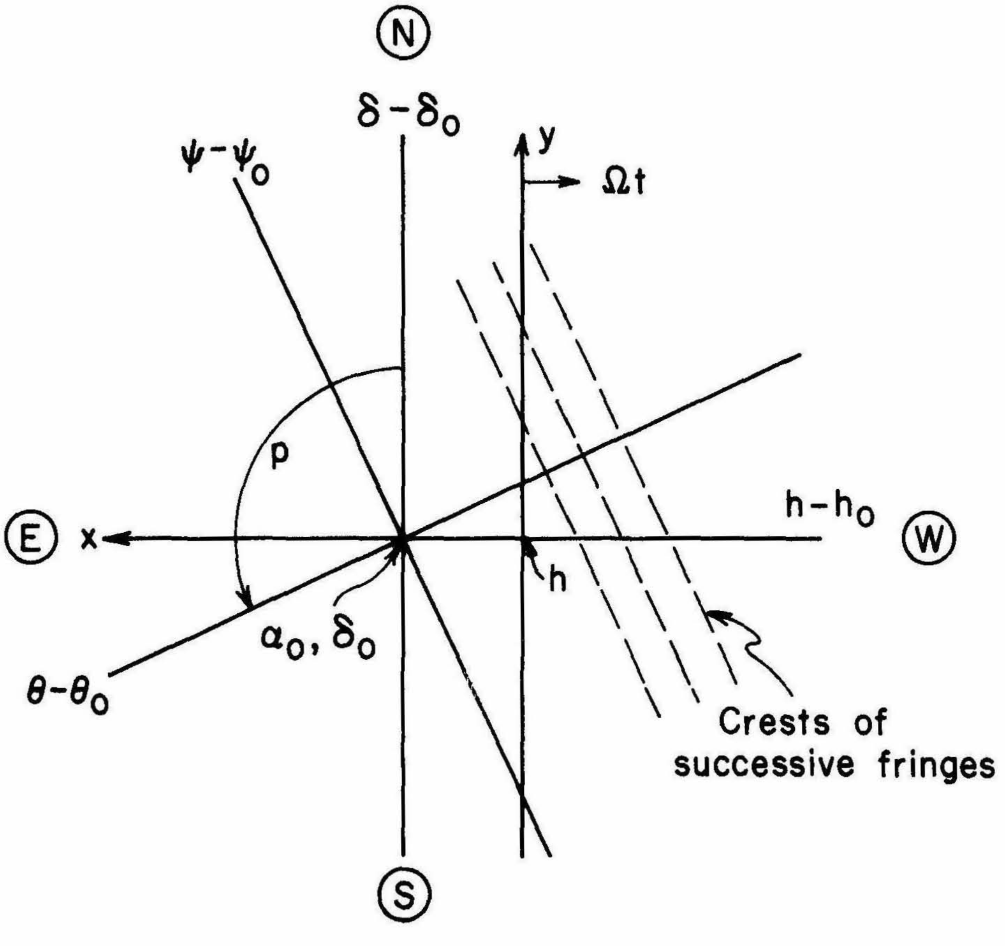

Fig. 54: Baseline and fringe pattern geometry as projected on the sky in the region of a source at (α_0, δ_0). The projected baseline is parallel to the $(\theta - \theta_0)$ axis.

where Ω is the sidereal rate , h is hour angle, and t is the sidereal time. The coordinates in which we have described the interferometer fringes (θ, φ) represent a system rotated with respect to the (x,y) system by $(p-\frac{\pi}{2})$. We define

$$\varphi' = \varphi - \varphi_o$$

$$\theta' = \theta - \theta_o$$

then from (1),

$$R(\theta') = GA(\theta', \varphi')\cos(2\pi s \sin(\theta' + \theta_o) + \Psi)$$

for $\theta' << 1$,

$$R(\theta') = GA(\theta', \varphi')\cos(2\pi s \sin(\theta' \cos\theta_o + \sin\theta_o) + \Psi) \quad (3)$$

However, θ' may be written in terms of the x and y coordinates as

$$\theta' = x' \sin p + y \cos p$$

where x' is the x-component of θ' measured from the instantaneous y-axis, or, measured from (α_o, δ_o),

$$x' = x - \Omega t$$

$$\theta' = (x - \Omega t)\sin p + y \cos p \quad .$$

Substituting in (2) and rearranging terms we have

$$R(x,y,t) = G A(x,y) \cos(2\pi(s_x(x-\Omega t) + s_y y) + \Psi(t))$$

$$s_x = s \cos\theta \sin p$$

$$s_y = s \cos\theta \cos p \quad .$$

Since θ and $p(=\text{grad} \sin\theta)$ are both functions of time, the orientation of the baseline relative to the (x,y) system describing the source, as given by its projected coordinates (s_x, s_y), will change with time. The implications of this baseline rotation effect will be discussed in more detail further in this section. The instrumental phase $\Psi(t)$ has absorbed factors constant over the small region (x,y) but does vary with θ. The resulting periodic response is the so-called natural fringe rate. An additional phase rotation is introduced to facilitate data reduction, which varies with the celestial position of the source and is designed to offset the natural fringe rate and produce an artificial constant fringe rate of one fringe per minute. These various phase variations are not critical to the following discussion and will be carried together in $\Psi(t)$.

The response of the system to the extended source $B(\alpha,\delta)$, or equivalently $B(x,y)$, is given by

$$R(t) = \frac{2k}{\lambda_o^2} \iint T(x,y)\ R(x,y)\, dx\, dy \quad . \tag{4}$$

Using the Rayleigh-Jeans approximation,

$$B(x,y) = \frac{2k\,T(x,y)}{\lambda_o^2} \quad .$$

Further, substituting equation (3),

$$R(t) = \frac{2k\,G}{\lambda^2} \iint A(x,y)\ T(x,y)\ \cos\left(2\pi[s_y y + s_x(x-\Omega t)] + \Psi\right) dx\, dy \ .$$

If the antennas are centered on the source and are made to track it then we may simplify further,

$$A(x,y)\ T(x,y) = A'\,T'(x,y)$$

$$A' = \text{Constant} = A(0,0)$$

then,

$$R(t) = \frac{2k\,GA'}{\lambda^2} \iint T'(x,y)\ \cos\left(2\pi\left[s_y y + s_x(x-\Omega t)\right] + \Psi\right) dx\, dy$$

$$= \frac{2k\,GA'}{\lambda^2}\ \mathrm{Re}\left[e^{2\pi i(\Psi - s_x \Omega t)} \iint T'(x,y)\ e^{2\pi i(s_y y + s_x x)}\ dx\, dy \right]$$

or,

$$R(t) = GA'S' \; V(s_x, s_y) \; \cos(\Phi(s_x, s_y) - 2\pi \; s_x \Omega t + \Psi) \tag{5}$$

where the functions V and Φ now define the complex visibility function of the source, $C(s_x, s_y)$:

$$C(s_x, s_y) = Ve^{i\Phi} = \frac{\iint T'(x,y) \; e^{2\pi i(s_x x + s_y y)} dx\,dy}{\iint T'(x,y) \; dx\,dy} \tag{6}$$

and

$$S' = \frac{2k}{\lambda^2} \iint T'(x,y) \; dx\,dy \tag{7}$$

The complex visibility function is the complex, two-dimensional Fourier Transform of the apparent source brightness distribution, normalized by the net integrated flux. It is possible in theory to recover the source distribution, given sufficient spatial frequency coverage ($s_x, s_y \rightarrow \infty$) and knowing A(x,y) to derive T(x,y) from T'(x,y). In practice, however, this is not possible because s_x and s_y are bounded and generally assume quite limited values due to use of only one or two baselines. In the case of an east-west baseline used to observe a source near the celestial equator, as was the case in the Mercury observations which will be discussed later, $s_y \rightarrow 0$. The visibility function may then be written as

$$Ve^{i\Phi} = \frac{\iint T'(x,y) \; e^{i2\pi s_x x} \; dx\,dy}{\iint T'(x,y) \; dx\,dy}$$

or

$$V(s)e^{i\Phi(s)} = \frac{\int T'(x)e^{2\pi i sx}\,dx}{\int T'(x)\,dx} \tag{8}$$

where

$$T'(x) \equiv \int T'(x,y)\,dy$$

or effectively a one-dimensional transform. In this case T′(x) is in theory recoverable but the normal use of only one or two values of s renders this unfeasible. The lack of high spatial-frequencies ($s_{max} \ll \infty$) causes loss of detailed information on the brightness distribution. We choose rather to use our *a priori* knowledge of the general nature of planetary brightness distributions and to compute models for comparison with observed data. For planetary applications, and for convenience in modeling, the transforming co-ordinates (x,y) are normalized by the planetary radius (r) in radians. We let

$$x' = x/r$$

$$y' = y/r$$

then

$$T'(x') = \int T'(x',y')\,dy' = \frac{1}{r}\int T'(x',y')\,dy = \frac{T'(x)}{r}$$

or

$$T'(x) = rT'(x') \quad .$$

Substituting in (8)

$$V(s)e^{i\Phi(s)} = \frac{\int rT'(x')e^{2\pi i s rx'}\,rdx'}{r\int T'(x')rdx'}$$

defining the parameter $\beta \equiv rs$

$$V(\beta)e^{i\Phi(\beta)} = \frac{\int T'(x')e^{2\pi i \beta x'}\,dx'}{\int T'(x')\,dx} \tag{9}$$

The usefulness of this transformation is evidenced as follows. It is simple to calculate the approximate form of the response in general due to the basic similarity of planetary distributions which we may approximate to first order by

$$T'(x',y') = T_o \quad , \quad \sqrt{x^2 + y^2} \le 1$$

$$= 0 \quad , \quad \text{else}$$

It is also convenient to convert (9) to polar cylindrical coordinates centered on (0,0). This gives us

$$V(\beta)e^{i\Phi(\beta)} = \frac{\int_0^{2\pi}\int_0^1 T'(\rho,\theta)e^{2\pi_i\beta\rho\cos\theta}\rho d\rho d\theta}{S_{tot}}$$

this yields

$$\Phi(\beta) = (0,\pi) \quad \text{depending on range of } \beta. \tag{10}$$

$$V(\beta) = \frac{J_1(2\pi\beta)}{\pi\beta}$$

which represents a useful first approximation to most planetary visibility functions. Further information is obtained from second order variations; in particular, surface polarization produces a significant effect. The effects of reflection and transmission at the surface boundary have been discussed. The somewhat different brightness distributions observed when the feed horn of each antenna is oriented alternately to accept $\bar{E}$-vector polarizations respectively parallel and perpendicular to the projected baseline exhibit a characteristic "splitting" effect shown schematically in Fig. 55. The magnitude of the difference between these curves is nearly entirely dependent on the value of the effective surface dielectric constant. This is

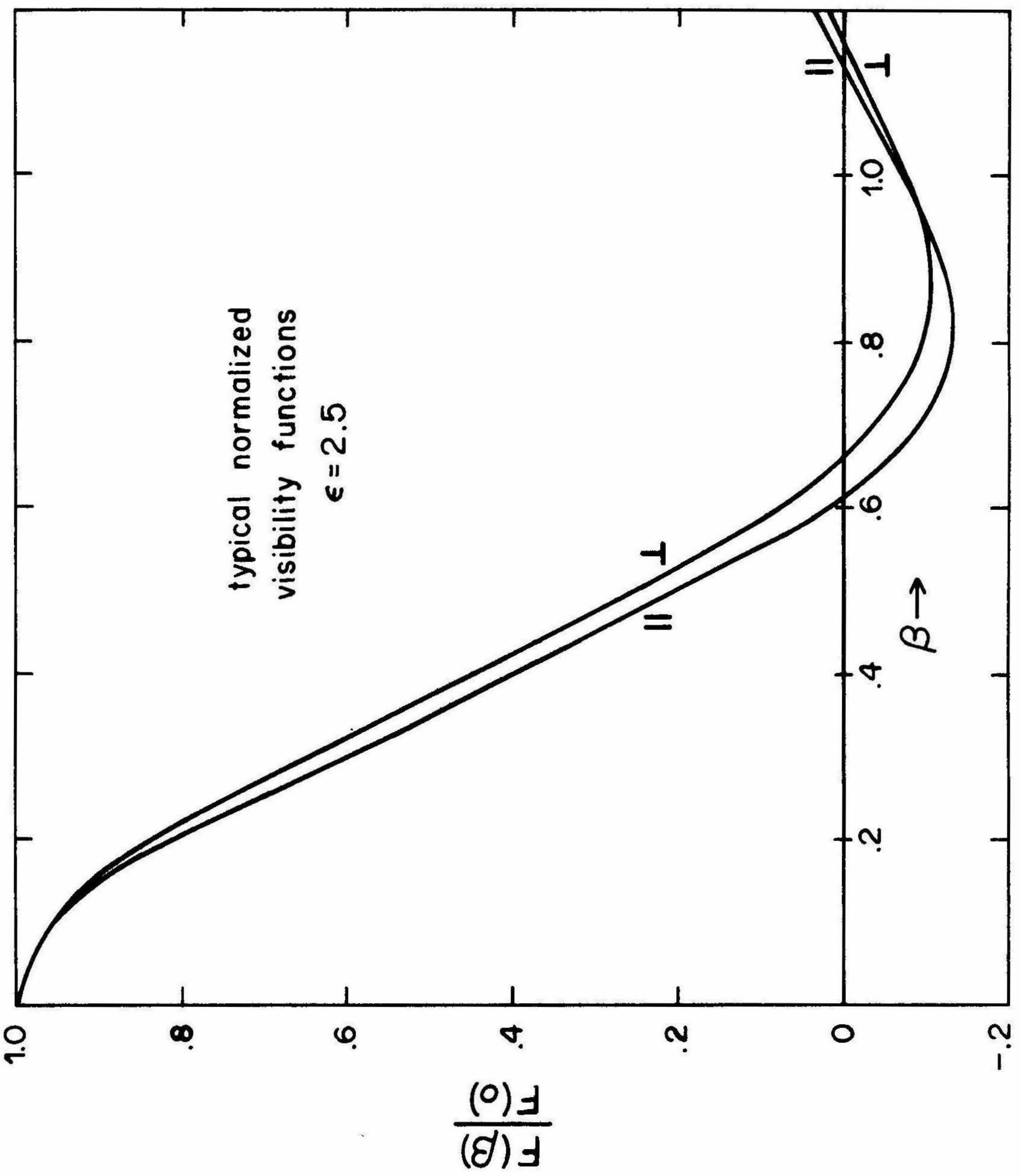

Fig. 55: Typical polarized visibility functions. (for a dielectric constant of 2.5)

demonstrated in Fig. 56 in which values of this difference are plotted as a function of beta for quite different distributions of brightness temperature over surfaces of the same dielectric constant. The higher order variations in these differences are small with respect to those produced by small changes in dielectric constant.

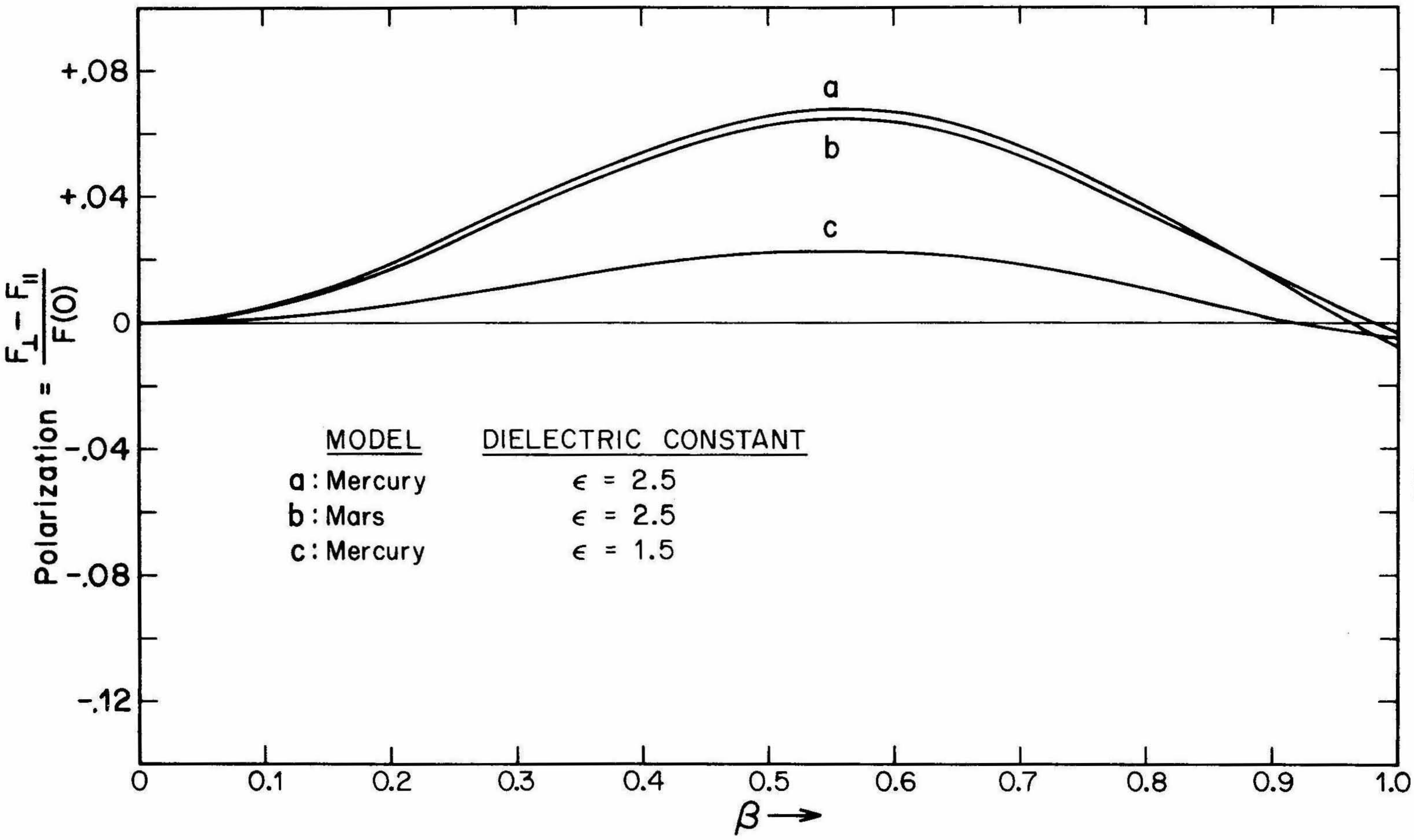

Fig. 56: Model-generated polarization difference functions illustrating the effective independence of this function on surface temperature distribution. These were computed with the use of brightness maps similar to those shown in figures 39-40 and fig. 22.

APPENDIX VI

Parameter Estimation and Error Analysis

A complete discussion of the method is given by Hamilton (1964). A brief sketch will be given here. Given a set of N_T observed values of a function f (= $f_1, f_2, \ldots . f_N$) which is linearly dependent on a set of M parameters (= $x_1, x_2, \ldots . x_M$), one may define a set of observational equations

$$\begin{array}{l}
f_1 = a_{11}x_1 + a_{12}x_2 + \cdots\cdots a_{1M}x_M + e_1 \\
f_2 = a_{21}x_1 + a_{22}x_2 + \cdots\cdots a_{2M}x_M + e_2 \\
\vdots \\
f_N = a_{N1}x_1 + a_{N2}x_2 + \cdots\cdots a_{NM}x_M + e_N
\end{array}$$

which may be written in matrix form as

$$\overline{F} = \overline{A}\,\overline{X} + \overline{E} \quad .$$

Then if the errors on the data are independent and the measurement process is stationary (the errors have a joint distribution with mean zero) the data covariance matrix

$$\overline{M}_f = \begin{bmatrix} \sigma_1^2 & \sigma_1\sigma_2\rho_{12} & \cdots\cdots & \sigma_1\sigma_N\rho_{1N} \\ \sigma_1\sigma_2\rho_{12} & \sigma_2^2 & \cdots\cdots & \cdot \\ \vdots & & & \vdots \\ \sigma_1\sigma_N\rho_{1N} & & \cdots\cdots & \sigma_N^2 \end{bmatrix}$$

will be diagonal ($\rho_{ij} = 0$) with $\sigma_i^2 = \langle e_i^2 \rangle = \mathrm{var}(f_i)$. No assumption of a Gaussian distribution is necessary, only that $\langle e_i^2 \rangle$ is defined. It may then be shown that the usual method of least squares analysis (minimizing the summed squares of residuals) which is the best possible estimator of the parameter set $\tilde{X}^*$ given the data f_i, is equivalent to the following matrix solution:

$$X^* = [A^T M^{-1} A]^{-1} A^T M^{-1} F \quad , \tag{1}$$

In the event that the errors are uncorrelated, ($M_{ij} = 0$, $i \neq j$) the following "brute force" technique is equivalent to the above and does not require knowledge of the exact form of A or M. The method was pointed out by Dr. D. Muhleman for the case of fitting one parameter.

The sum of residuals, weighted by the inverse squares of the errors on the respective data points, is for the j^{th} test value of the parameter X (= x_j)

$$S_j = \sum_i \frac{\left(f_{oi} - f_{ji}\right)^2}{\sigma_i^2}$$

where f_{ji} is the theoretical value of the observed function at sample point i for test parameter j, and f_{oi} is the observed value with associated error σ_i. By definition,

$$f_{ji} = A_{ji} \, x_j$$

then

$$S_j = \sum_i \frac{\left(f_{oi} - A_{ji} x_j\right)^2}{\sigma_i^2} \tag{2}$$

$$= \sum_i \frac{f_{oi}^2 - 2 f_{oi} A_{ji} x_j + A_{ji}^2 x_j^2}{\sigma_i^2}$$

but $\sigma_i^2 = M_{ii}^{-1} = (M^{-1})_{ii}$

$$S_i = \sum_i f_{oi}^2 M_{ii}^{-1} - 2x_i \sum f_{oi} A_{ji} M_{ii}^{-1} + x_i^2 \sum A_{ji}^2 M_{ii}^{-1}$$

which is in the form of a parabola in x_i:

$$S_i = a_o + a_1 x_i + a_2 x_i^2 \tag{3}$$

The best value of X is then X*, where (for the one-parameter case)

$$\left.\frac{\partial s_i}{\partial x_i}\right|_{X^*} = 0 = a_1 + 2a_2 X^*$$

or $X^* = -\dfrac{a_1}{2a_2}$

since

$$a_o = \sum_i f_{oi}^2 M_{ii}^{-1} \tag{4}$$

$$a_1 = -2 \sum_i f_{oi} A_{ji} M_{ii}^{-1} = -2 \sum f_{oi} M_{ii}^{-1} A_{ji} \tag{5}$$

$$a_2 = \sum_i A_{ji}^2 M_{ii}^{-1} \tag{6}$$

then

$$X^* = -\frac{a_1}{2a_2} = \frac{\sum_i f_{oi} M_{ii}^{-1} A_{ji}}{\sum_i A_{ji}^2 Mii^{-1}} \tag{7}$$

which is equivalent to

$$X^* = (A^T M^{-1} A)^{-1} (A^T M^{-1} F) \tag{8}$$

if the matrix M is diagonal.

It is also shown by Hamilton that a knowledge of the relative errors in the data is all that is necessary; i.e., if the elements M_{ii} are unequal but uncertain by a factor of σ^2, where σ is the (unknown) true standard deviation that would obtain in an infinite sample, then the matrix M may be replaced by the matrix P, where

$$P = \sigma^2 M^{-1} \quad . \tag{9}$$

Thus, (8) becomes

$$X^* = (A^T PA)^{-1} A^T PF \tag{10}$$

which is of course the real method used precisely because the real standard deviation of the data is not known from the limited data set.

Errors in the parameter estimates

Defining the covariance matrix of the parameter set x_M as

$$C_x = C_{ij} = \begin{bmatrix} \mathrm{Var}\ x_1 & \mathrm{cov}\ x_1 x_2 & \ldots\ldots\ldots & \mathrm{cov}\ x_1 x_M \\ \mathrm{Cov}\ x_2 x_1 & \mathrm{var}\ x_2 & \ldots\ldots\ldots & \\ \vdots & & & \\ \mathrm{Cov}\ x_M x_1 & \ldots\ldots & \ldots\ldots\ldots & \mathrm{var}\ x_M \end{bmatrix}$$

the desired formal error (variance) in x_i is then merely

$$\sigma_{x_i} = \sqrt{c_{ii}}$$

which is given at the best set of values of $X = X^*$ by

$$C_{X^*} = \langle (X^* - X^o)(X^* - X^o)^T \rangle$$

where X^o is the "true" (unknown) value of X of which X^* is our best estimate and the average is an expectation value.

We define F° such that

$$F^\circ = A X^\circ \text{ (noiseless experiment)}$$

and B, where

$$B = A^T M^{-1} A \tag{11}$$

noting that $B = B^T$.

Then

$$C_{X^*} = \langle (X^* - X^\circ)(X^* - X^\circ)^T \rangle$$

$$\left.\begin{aligned} X^* &= (A^T M^{-1} A)^{-1} A^T M^{-1} F \\ X^\circ &= (A^T M^{-1} A)^{-1} A^T M^{-1} F^\circ \end{aligned}\right\} \quad \text{from} \quad (1)$$

$$\begin{aligned} C_{X^*} &= \left\langle \left[(A^T M^{-1} A)^{-1} A^T M^{-1} (F - F^\circ)\right] \left[(A^T M^{-1} A)^{-1} A^T M^{-1} (F - F^\circ)\right]^T \right\rangle \\ &= \left\langle B^{-1} A^T M^{-1} (F - F^\circ) \left[B^{-1} A^T M^{-1} (F - F^\circ)\right]^T \right\rangle \\ &= \left\langle B^{-1} A^T M^{-1} (F - F^\circ)(F - F^\circ)^T M^{-1} A B^{-1} \right\rangle \end{aligned}$$

(since $B^{-1} = (B^{-1})^T$ and M has been assumed to be diagonal) then

$$C_{X^*} = B^{-1} A^T M^{-1} \left\langle (F - F^\circ)(F - F^\circ)^T \right\rangle M^{-1} A B^{-1} \quad ,$$

but $M = \langle (F - F^\circ)(F - F^\circ)^T \rangle$ (variance on the data set).

So,

$$\begin{aligned} C_{X^*} &= B^{-1} A^T M^{-1} M M^{-1} A B^{-1} \\ &= B^{-1} (A^T M^{-1} A) B^{-1} \\ &= B^{-1} \quad \text{from (11)} \\ &= \sigma^2 (A^T P A)^{-1} \quad \text{from (9).} \end{aligned}$$

It may be shown that the unbiased best estimate of σ^2 is given by σ^{*2}, where

$$\sigma^{*2} = \frac{V^T P V}{N_I - M} \tag{12}$$

where V = F - AX*, the matrix of lowest residuals, M is the number of parameters, and N_I is the number of independent data points. Thus

$$C_{X^*} = \frac{V^T P V (A^T P A)^{-1}}{N_I - M}$$

and the variance of parameter x_i^* is

$$\mathrm{Var}\ (x_i^*) = C_{ii}$$

$$\sigma_{x_i^*}^{\ *} = \sqrt{C_{ii}} \quad .$$

Recalling the definitions of the parabola coefficients a_o, a_1, a_2 given in (4) - (6), and going to the single parameter case ($x_i = X$, $A_{ji} = A_i$)

$$a_o = \sum_i f_{oi}^{\ 2} M_{ii}^{\ -1} = \sum_i f_{oi} M_{ii}^{\ -1} f_{oi}$$

$$a_1 = -2 \sum_i f_{oi} A_i M_{ii}^{\ -1} = -2 \sum_i f_{oi} A_i M_{ii}^{\ -1}$$

$$a_2 = \sum_i A_i^{\ -2} M_{ii}^{\ -1} = \sum_i A_i M_{ii}^{\ -1} A_i$$

we see that a_2 is equivalent to the matrix $a_2 = (A^T P^{-1} A)^{-1}$ and thus

$$C^* = \mathrm{Var}\ X^* = \frac{V^T P V}{(N_I - 1) a_2} \qquad (M = 1) \ .$$

But V = F - AX* and

$$S(X^*) = \sum_i \frac{(f_{oi} - A_i X^*)^2}{\sigma_i^2} = V^T P^{-1} V \quad \text{if P is diagonal.}$$

Thus $$\mathrm{Var}\,(X^*) = \frac{S(X^*)}{(N_I-1)a_2} = \frac{a_o + a_1X^* + a_2X^{*2}}{(N_I-1)a_2} \quad .$$

It may be seen that, if errors in the data set are uncorrelated, and if the relation giving the observable function in terms of the parameter set $\bar{X}$ is linear, one may get both the best estimate of the parameter and the best estimate of the variance of the parameter by fitting a parabola to the curve of residuals. Non-linear functional dependence will produce a non-parabolic residual curve due to the presence in (2) of higher order terms. If the region of interest (determined by the variance) on this curve is small, the parabolic approximation applied near the minimum is likely to be valid. This method was used in Section 5.1 to obtain the best-fitting value of the surface dielectric constant and its associated formal error. The parabolic assumption appears to be valid in a region near the minimum of this curve larger than the resultant error range.

In the difference method used, differences were taken between alternate data points in orthogonal polarizations, not only between alternate pairs of points. This was done in order to average out gain drifts over time scales of several records. Of course, if there is a total of N_T points (both polarizations) there are really only $\sim \frac{N_T}{2}$ independent differences. If the same point is used in adjacent differences, the differences will not be independent. Consequently in equation 13 the value of N_I refers to the number of independent difference points which is $N_I = N_T/2$. This factor is a standard approximation, and is included in the error given in Section 5.1.

BIBLIOGRAPHY

Allen, C.W., 1963, *Astrophysical Quantities*, Athlone Press, London, 2nd Ed.

Allen, R.J., and Barrett, A.H., 1967, "Absolute Measurements of the Radio Flux from Cassiopeia A and Taurus A at 3.64 and 1.94 cm.", *Ap.J.*, *149*, 1.

Aller, H.D., 1970, "The Polarization of Variable Radio Sources at 8 GHz." *Ap.J.*, *161*, 1.

Campbell, M.J., and Ulrichs, J., 1969, "Electrical Properties and their Significance for Lunar Radar Observations.", *J. Geophys. Res.*, *74*, 5867.

Capen, C.F., and Capen, V.W., 1970, "Martian North Polar Cap 1962-1968.", *Icarus*, *13*, 100.

Christiansen, W.N., and Högbom, J.A., 1969, *Radiotelescopes*, Cambridge University Press, Chap. 8.

Clegg, P.E., Bastin, J.A., and Gear, A.E., 1966, "Heat Transfer in Lunar Rock", *M.N.R.A.S.*, *133*, 63.

Crank, J., and Nicholson, P., 1947, "A Practical Method for Numerical Integration of Solutions of Partial Differential Equations of Heat Conduction Type.", *Proc. Camb. Phil. Soc.*, *43*, 50.

Cross, C.A., 1971, "The Heat Balance of the Martian Polar Caps.", *Icarus*, *15*, 110.

Cuzzi, J.N., and Muhleman, D.O., 1972, "The Microwave Spectrum of Mars and the Nature of Its Subsurface", to be published in *Icarus*, Oct. 1972.

Day, G.A., Shimmins, A.J., Ekers, R.D., and Cole, D.J., 1969, "The Parkes Catalogue of Radio Sources.", *Aus. J. Phys.*, *19*, 35.

Dent, W.A., 1972, "A Flux-Density Scale for Microwave Frequencies", *Ap.J.*, *177*, 93.

Dent, W.A., and Haddock, F.T., 1966, "The Extension of Non-Thermal Radio-Source Spectra to 8000 MC/S.", *Ap.J.*, *144*, 568.

deVaucouleurs, G., 1963, "Physical Parameters of Planets and Satellites.", *Icarus*, *3*, 187.

Epstein, E.E., Dworetsky, M.M., Fogarty, W.G., Montgomery, J.W., and Cooley, R.C., 1970, "Mercury: Epilith Physical Parameters and a Hermocentric Longitude Dependence of its 3.3 mm Radiation.", *Radio Sci.*, *5*, 401.

Epstein, E.E., 1971, "Mars: A Possible Discrepancy Between the Radio Spectrum and Elementary Theory.", Icarus, 14, 214.

Fountain, J.A., and West, E.A., 1970, "Thermal Conductivity of Particulate Basalt as a Function of Density in Simulated Lunar and Martian Environments.", J. Geophys. Res., 75, 4063.

Gierasch, P., and Goody, R., 1968, "A Study of the Thermal Dynamical Structure of the Martian Lower Atmosphere.", Planetary and Space Science, 16, 615.

Gold, T., Campbell, M.J. and O'Leary, B.T., 1970, "Optical and High Frequency Electrical Properties of Lunar Samples.", Science, 167, 707.

Goldstein, R.M., 1971, "Radar Observations of Mercury.", A.J., 76, 1152.

Golovkov, V.K., and Losovskii, B. Y., 1968, Sov. Astron - A.J., 12, 229.

Hagfors, T., 1968, Radar Astronomy, McGraw, Hill, Inc.

Hagfors, T., and Evans, J., 1968, Radar Astronomy, McGraw, Hill, Inc.

Hamilton, W.C., 1964, Statistics in Physical Science, Ronald Press, N.Y.

Hansen, O., 1970, Personal Communication.

Hansen, O., and Muhleman, D.O., 1970, unpublished.

Hardebeck, E., 1971, "Accurate Position Measurements in the 1720-MHz Line of OH.", Ap.J., 170, 281.

Harris, D., 1971, "Photometry of Planets and Satellites.", The Solar System, Vol. III, Kuiper and Middlehurst, Ed.

Haystack Observatory Staff, 1971, Quarterly Report of the Haystack Observatory, July 15, 1971.

Hobbs, R.W., and Knapp, S.L., 1971, "Planetary Temperatures at 9.55 mm Wavelength.", Icarus, 14, 204.

Hovis, W.A., and Callahan, W.R., 1966, "Infrared Reflectance Spectra of Igneous Rocks, Tuffs, and Red Sandstone from 0.5-22μ.", J. Opt. Soc. Am., 56, 639.

IAU, 1970, Transactions of the International Astronomical Union, 1970, Vol. XIV A, "Reports on Astronomy."

Ingersoll, A.P., 1970, "Mars: Occurrence of Liquid Water.", Science, 168, 972.

Jaeger, J.C., and Harper, A.F.A., 1950, "Nature of the Surface of the Moon.", *Nature*, *166*, 1026.

Kaftan-Kassim, M.A., and Kellermann, K.I., 1967, *Nature*, *213*, 272.

Kellermann, K.I., Pauliny-Toth, I.I.K., and Williams, P.J.S., 1969, "The Spectra of Radio Sources in the Revised 3C Catalogue.", *Ap.J.*, *157*, 1.

Klein, M.J., 1968, "The Planet Mercury: Measurements of Variations in the Microwave Disk Temperature.", Ph.D. Thesis, Univ. of Michigan, 1968.

Klein, M.J., 1971, "Mars: Measurements of Its Brightness Temperature at 1.85 and 3.75 cm Wavelength.", *Icarus*, *14*, 210.

Klein, M.J., 1972, Private Communication.

Kraus, J.D., 1966, *Radio Astronomy*, 1966, McGraw Hill, Inc., New York.

Lastochkin, V.P., Sorin, Y.M., and Stankevitch, K.S., 1964, "The Spectrum of Radio Emission of Cyg. A.", *Astr. Zh.*, *41*, 770.

Leighton, R.B., and Murray, B.C., 1966, "Behavior of Carbon Dioxide and Other Volatiles on Mars.", *Science*, *153*, 136.

Leovy, C.B., and Mintz, Y., "A Numerical General Circulation Experiment for the Atmosphere of Mars.", *NASA Memorandum* RM-5110-NASA. December, 1966, Rand Corp., Santa Monica

Liu, H-S., 1972, "Orientation and Resonance Locks for Satellites in the Elliptic Orbits.", to be published in *Celestial Mechanics Journal*.

Linsky, J.L., 1966, "Model of the Lunar Surface Including Temperature-Dependent Thermal Properties.", *Icarus*, *5*, 606.

Medd, W.J., 1972, "Absolute Flux Density Measurements at Centimeter Wavelengths.", *Ap.J.*, *171*, 41.

Minnaert, M., 1961, "Photometry of the Moon.", *The Solar System, Vol. III*, Kuiper and Middlehurst, Eds.

Moffet, A.T., 1962, "Brightness Distribution in Discrete Radio Sources, I. Observations with an East-West Interferometer.", *Ap.J.*, *Supp. 7*, 93.

Morrison D., and Sagan, C., 1968, "Interpretation of the Microwave Phase Effect of Mercury.", *Ap.J.*, *73*, 527.

Morrison, D., 1969, "Thermal Models and Microwave Temperatures of the Planet Mercury.", *Smithsonian Astrophys. Obs. Spec. Rept.*, *No. 292*.

Morrison, D., Sagan, C., and Pollack, J.G., 1969, "Martian Temperatures and Thermal Properties.", Icarus, 11, 36.

Morrison, D., 1970, "Thermophysics of the Planet Mercury.". Space Science Rev., 11, 271.

Morrison, D., and Klein, M.J., 1970, "The Microwave Spectrum of Mercury.", Ap.J., 160, 325.

Muhleman, D.O., 1964, "Radar Scattering from Venus and the Moon.", Ap.J., 69, 34.

Muhleman, D.O., 1966, "Planetary Characteristics from Radar Observations", Space Science Reviews, 6, 341.

Muhleman, D.O., Berge, G.L., and Cuzzi, J.N., 1971, in preparation.

Muhleman, D.O., 1972, "Microwave Emission from the Moon.", in Thermal Characteristics of the Moon, Lucas, Ed., MIT Press.

Muhleman, D.O., 1972, private communication.

Murdock, T.L., and Ney, E.P., 1970, "Mercury, The Dark Side Temperature." Science, 170, 535.

Murray, B.C., 1967, "Infrared Radiation from the Daytime and Nighttime Surfaces of Mercury.", (Abstract), Trans. Amer. Geophys. Union, 48, 148.

NEROC Quarterly Report, July 15, 1971.

Neugebauer, G., Münch, G., Kieffer, H., Chase, S.C. and Miner, E., 1971, "Mariner 1969 Infrared Radiometer Results: Temperatures and Thermal Properties of the Martian Surface.", A.J., 76, 719.

Olsen, E., 1972, private communication.

Pauliny-Toth, I.I.K., and Kellermann, K.I., 1968, "Measurements of the Flux Density and Spectra of Discrete Radio Sources at Centimeter Wavelengths. II. The Observations at Ghz (6 cm)." A.J., 73, 953.

Peale, S.J., 1969, "Generalized Cassini's Laws.", A.J., 74, 483.

Pettengill, G.H., Dyce, R.B., and Campbell, D.B., 1967, "Radar Measurements at 70 cm of Venus and Mercury.", A.J. , 72, 330.

Piddington, J.H., and Minnett, H.C., 1949, "Microwave Thermal Radiation from the Moon.", Aust. J. Sci. Res., SerA. 2 , 63.

Rayleigh, Lord (J.W. Strutt), 1892, "On the Influence of Obstacles Arranged in Rectangular Order on the Properties of a Medium.", *Phil. Mag.*, *34*, 481.

Read, R.B., 1963, "Two Element Interferometer for Accurate Position Determinations at 960 MC.", *IRE Trans. AP-9*, 31.

Sagan C. and Veverka, J., 1971, "Microwave Spectrum of Mars, an Analysis." *Icarus*, *14*, 222.

Sheuer, P.A.G., and Williams, P.J.S., 1968, "Radio Spectra.", *Annual Reviews of Astronomy and Astrophysics*, *Vol. 6*, 1968, p. 321.

Shimmins, A.J., and Bolton, J.G., 1972, "Accurate Flux Densities at 5009 MHz of 1007 Radio Sources.", *Aust. J. Physics, Astrophysical Supp.* *#23* , June 1972.

Sinton, W., and Strong, J., 1960, "Observations of the Infrared Emission of Planets and Determinations of Their Temperatures.", *ONR Contract Rept.*, *#248(01)*.

Smith, B., 1972, private communication.

Soter, S., and Ulrichs, J., 1967, "Rotation and Heating of the Planet Mercury.", *Nature*, *214*, 1315.

Stankevitch, K.S., 1962, "Precise Measurements of the Spectrum of the Discrete Source Cas A on Centimeter Wavelengths.", *Astr. Zh.*, *39*, 610.

Stratton, J.A., 1941, *Electromagnetic Theory*, McGraw, Hill Inc., New York, Chap. V.

Strezhneva, K.M., and Troitskii, V.I., 1960, "The Phase Dependence of Radio Emission of the Moon at 3.2 cm.", *The Moon*, Kopal and Mikhailov, Ed., Academic Press, N.Y.

Troitskii, V.S., Bondar, L.N., Zelinskaya, M.R., and Strezhneva, K.M., 1970, "Comparison of the Chemical Composition of Lunar Surface Material Determined by Radioastronomical Observations with the Results of Chemical Analysis Obtained by Surveyor.", *Radio Sci.*, *5*, 247.

Troitskii, V.S., and Tseytlin, N.M., 1960, *Radiophysics*, *3*, 667.

Troitskii, V.S., 1967, "Investigation of the Surfeces of the Moon and Planets by Means of Thermal Radiation.", *Proc. Roy. Soc. (London)*, *A296*, 366.

Troitskii, V.S., 1970, "On the Possibility of Determining the Nature of the Surface Material of Mars from its Radio Emission.", *Radio Sci.*, *5*, 481.

Ulich, B.L., Cogdell, J.R., and Davis, J.H., Paper given at Spring URSI Meeting, Washington, D.C., April 1972.

Ward, W.R., 1972, private Communication.

Watson, L., 1964, "I. Thermal Conductivity Measurements of Selected Silicate Powders in Vacuum from 150-350°K. II. An Interpretation of the Moon's Eclipse and Lunation Cooling Curve as Observed through the Earth's Atmosphere from 8-14 Microns.", Thesis, California Institute of Technology, Pasadena.

Wechsler, A.E., and Glaser, P.E., 1965, Pressure Effects on Postulated Lunar Materials.", Icarus, 4, 335.

Wechsler, A.E. Glaser, P.E., and Fountain, J.A., 1972, "Thermal Properties of Granulated Materials.", Thermal Characteristics of the Moon, Lucas, Ed. MIT Press.

Wesselink, A.J., 1948, Heat Conductivity and the Nature of the Lunar Surface Material.", Bull. Ast. Inst. Neth., 10, 351.

Winter, D.F., and Saari, J.M., 1969, "A Particulate Thermophysical Model of the Lunar Soil.", Ap.J., 156, 1135.

Winter, D.F., 1972, "Infrared Emission from the Surface of the Moon", Advances in Astronomy and Astrophysics, Vol. 9.

Wrixon, G.T., Welch, W.J., and Thornton, D.D., 1971, "The Spectrum of Jupiter at Millimeter Wavelengths.", Ap.J. 169, 171.